FEMTOSECOND OPTICAL PARAMETRIC OSCILLATORS FOR THE MID-INFRARED

Cathrine McGowan

A Thesis Submitted for the Degree of PhD
at the
University of St Andrews

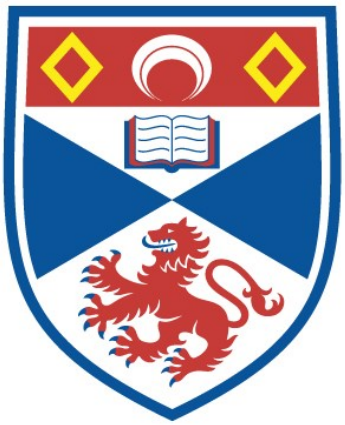

1998

FEMTOSECOND OPTICAL PARAMETRIC OSCILLATORS FOR THE MID-INFRARED

A thesis submitted to
the University of St Andrews
for the degree of
Doctor of Philosophy

by

Cathrine McGowan, B.Sc., M.Sc.

September 1997

J. F. Allen Physics Research Laboratories
School of Physics & Astronomy
University of St Andrews
North Haugh
St Andrews
Fife KY16 9SS

declarations

I, Cathrine McGowan, hereby certify that this thesis, which is approximately 55,000 words in length, has been written by me, that it is a record of work carried out by me and that it has not been submitted in any previous application for a higher degree.

date 2 Sept 1997 signature of candidate .....

I was admitted as a research student in October 1994 and as a candidate for the degree of Doctor of Philosophy in October 1994; the higher study for which this is a record was carried out in the University of St Andrews between 1994 and 1997.

date 2 Sept 1997 signature of candidate .....

I hereby certify that the candidate has fulfilled the conditions of the Resolution and Regulations appropriate for the degree of Doctor of Philosophy in the University of St Andrews and that the candidate is qualified to submit this thesis is application for that degree.

date 2 Sept 1997 signature of supervisor .....

copyright

וַיֹּאמֶר אֱלֹהִים יְהִי אוֹר וַיְהִי־אוֹר׃
וַיַּרְא אֱלֹהִים אֶת־הָאוֹר כִּי־טוֹב
וַיַּבְדֵּל אֱלֹהִים בֵּין הָאוֹר וּבֵין הַחֹשֶׁךְ׃

Genesis 1:3-4

abstract

The research presented in this thesis is concerned with the generation and characterisation of femtosecond pulses in the near and mid-infrared spectral regions. The three optical parametric oscillators which were constructed were synchronously-pumped by a self-modelocked femtosecond Ti:sapphire laser.

Noncollinear critical birefringent phasematching was used in an oscillator based on $KTiOAsO_4$, which was tunable from 1.03 to 1.2 μm and 2.51 to 4.1 μm by varying the crystal angle. The mid-infrared pulses were sub-100 fs, and essentially free from frequency chirp. With appropriate dispersion compensation the near-infrared signal pulses were temporally compressed to 69 fs. Theoretical models of noncollinear phasematching were derived and the results agreed closely with experiment.

A novel optical parametric oscillator design based on a semi-monolithic noncritically phasematched $RbTiOAsO_4$ crystal was implemented. This unique cavity configuration allowed independent focussing of the pump and signal beams within the crystal. It facilitated a reduction in cavity length to bring the signal pulse repetition rate into synchronism with the second (172 MHz) and fourth (344 MHz) harmonics of the pump pulse repetition frequency. Extraction efficiencies as high as 55% were observed.

Quasi-phasematched femtosecond optical parametric oscillation was demonstrated in periodically poled lithium niobate. This device offered extensive tunability, covering 0.975 to 1.54 μm in the signal branch and 1.67 to 4.55 μm in the idler branch, from a combination of grating, pump wavelength and cavity length tuning. A theoretical model indicated that a very broad gain bandwidth allowed the wide tuning range. An attractively low oscillation threshold of 45 mW was recorded, and a visible output of 70 mW at 540 nm was observed, caused by simultaneously phasematched frequency-doubling of the signal output.

The pulses from the Ti:sapphire laser and from the optical parametric oscillators were characterised by autocorrelation and frequency-resolved optical gating techniques. A highly advantageous autocorrelator arrangement based on quadratic nonlinearity in light-emitting diodes and photodiodes was demonstrated, and a novel second harmonic generation frequency-resolved optical gating system allowed real-time monitoring of pulsed outputs and complete characterisation of the intensity and phase of pulses.

contents

chapter one

NEAR AND MID-INFRARED ULTRASHORT PULSE SOURCES

UT NUCIA LASERIS TOTO TEMPORE UTARIS
(To make a little laser go a long way)
Apicius (fl. 20 BC), *Cooking and Dining in Imperial Rome*

1.1 Introduction

In an ideal world, there would be an ideal laser source, capable of producing any wavelength, any output power, and any pulse duration at the mere flick of a switch. Of course, our world is far from ideal, and the reality of laser sources is very different from this. There is a staggering array of coherent optical systems currently available, generating widely varied, but nonetheless limited, outputs. Since the advent of the laser in 1960 [1], research into source development has been impressive, both in terms of the generation of light at many different wavelengths, and the production of pulses of ever-shorter duration, but there are still a number of regions of the spectrum not yet readily accessible, and the shortest pulses currently possible are only available in a very few spectral bands.

One area of laser research that is receiving much attention at the present time aims to fill one of these gaps in the spectrum. Light in the mid-infrared (MIR) spectral region, especially in the 3 to 5 μm range, is desirable for a number of applications. More specifically, femtosecond pulses at these wavelengths are generally regarded as being very valuable, but are not currently very readily attainable. The aim of the work presented in this thesis was to attempt to identify reliable sources of mid-infrared femtosecond pulses, to construct such sources, and to fully characterise the pulses.

In the remainder of this chapter the applications of these pulses will be

discussed, and the research relevant to their generation will be summarised. Potentially suitable optical materials will be described, followed by a brief summary of the work presented in subsequent chapters.

1.2 Applications of mid-infrared femtosecond pulses

The requirement for femtosecond mid-infrared pulses stems from a number of applications, one of which is spectroscopy. Pulses of such short duration can be used to achieve remarkable time-resolution of processes occurring in semiconductors, such as band-to-impurity transitions, intraband free carrier absorption, intersubband transitions in quantum wells, and coherent phonon effects. Because many of these materials have intervalance band transitions in the 3 to 5 μm region [2], there is a strong desire to have access to pulses in this wavelength range. They can be used for photoexcitation, and the kinetics (such as relaxations and recombination dynamics) of the subsequent energetic states may be then studied by pump-probe spectroscopy [3, 4]. Reasonably high power pulses are needed, and tunability is also desirable so that a variety of kinetic processes can be easily examined with a single system [5, 6]. Time-resolved spectroscopy is also used to analyse the dynamics of chemical processes and reactions, and many vibrational frequencies in molecular solids and liquids occur between 3 and 5 μm [2]. For instance, the fundamental stretching modes of the important $-OH_x$, $-CH_x$ and $-NH_x$ chemical groups are near 3 μm, as shown in Fig. 1.1. These modes can be studied by using time-resolved non-linear coherent methods such as photon echoes [7]. Examples of processes studied with femtosecond pulses to date include transient bleaching in hexadibenzocyanine-3, by optical bleaching spectroscopy, which has a much reduced observation time compared to conventional pump-probe spectroscopy [3]; CO stretching vibration during photodissociation of CO from carboxyhaemoglobin [8]; coherent pulse propagation in CD_3I to determine the phase relaxation time of the molecular vibration of the stretching mode in CD_3 [6]; and the stretching modes of certain bonds in the free radicals HOCO, DOCO, and HCCN by measuring their spectra with so-called infrared kinetic spectroscopy [9]. Such photochemical spectroscopy tends to require lower pulse powers and repetition rates than those used for studying semiconductors, so different design criteria need to be employed to develop suitable

laser sources.

Mid-infrared wavelengths can also be used to record absorption spectra of atmospheric gases [10], which leads to the possibility of long range atmospheric sensing and environmental and pollution monitoring [11 - 13]. For example, light at 4 μm has good atmospheric transmission in all weathers, and 4 μm also corresponds to an absorption band in SO_2.

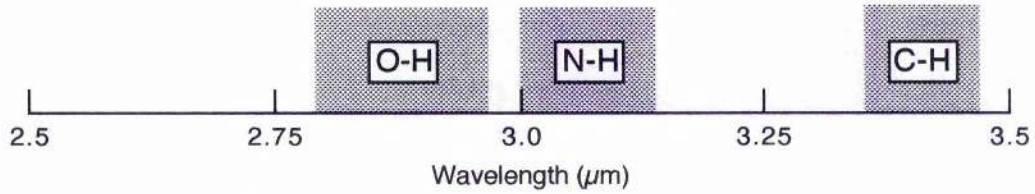

Figure 1.1 Mid-infrared fundamental stretching modes of some important chemical groups.

Other potential applications of femtosecond mid-infrared pulses include fibre-based chemical sensors, industrial process monitoring and biomedical technology [11]. Additionally, for some applications a femtosecond pulse sequence can be regarded as a quasi-continuous source if the pulse repetition rate is high enough.

The route followed by laser development towards the production of femtosecond mid-infrared pulses may be considered from two perspectives – the progress of femtosecond technology towards mid-infrared wavelengths, and the progress of mid-infrared sources into the femtosecond regime. The resulting sources depend almost entirely on nonlinear optical processes. The theory underlying these processes will be described in some detail in Chapter 2.

1.3 Progress of mid-infrared sources towards the femtosecond time domain

The majority of schemes reported to produce mid-infrared radiation rely on nonlinear optical processes. There are a number of existing lasers which have outputs directly in the mid-infrared, but these tend to be continuous wave devices, or have relatively long pulse durations, and are mentioned here only briefly, for the sake of completeness. Laser diodes based on lead chalcogenides are commercially available at wavelengths from 3 to 25 μm, but power levels are low (typically <1 mW) and

operation requires cooling to below 100 K [14]. Another such class of devices is the diode-pumped mid-infrared solid-state laser, reviewed by Stoneman and Esterowitz in 1991 [15]. A number of trivalent rare-earth materials have laser transitions in the 2 to 3 μm region, which if pumped by diode lasers provide more efficient and compact sources than if flashlamp pumped. However, diode-pumped devices depend heavily on diode quality, and to date better progress in the mid-infrared has been made by exploiting nonlinear interactions. Other alternatives are the Ho:YAG-pumped InAsSb and GaSb lasers developed by Le et al [16], which operate around 4 μm. The major drawback is that such devices require cooling; even when pulsed pumping was used to reduce heating, operation was only sustained up to 211 K. Hydrogen halide gas lasers have proved useful for mid-infrared production, although they have limited lifetimes and poor tunability, and tend to be bulky [17]. Additionally, pumping is conventionally achieved by electrical discharge, which is inefficient. A recent improvement was made by Miller et al [18] who achieved optical pumping of a HBr laser by using the output of a commercial Nd:YAG-pumped optical parametric oscillator. The HBr output was at 4 μm, with a 50 ns pulse duration, still a long way from the desired femtosecond pulses.

Nonlinear parametric processes seem to hold the key to the production of mid-infrared pulses, via optical parametric generation and oscillation and difference frequency mixing. Back in 1970, Goldberg [19] built an optical parametric oscillator (OPO) from lithium iodate ($LiIO_3$) pumped by a Q-switched ruby laser. Angle tuning produced an idler output of 2.5 to 4 μm, with approximately a 10 ns pulse duration. This was followed by the first proposal for the now common synchronously pumped OPO [20], a technique required for the successful generation of picosecond and femtosecond pulses. The method was immediately recognised as a source of high energy, highly tunable ultrashort pulses. However, the development of the OPO was then delayed for a number of years due to a lack of suitable nonlinear crystals and pump sources with sufficient intensity to drive the nonlinear interaction [21].

The related process of optical parametric generation was used in 1987 by Jedju and Rothberg as part of a series of experiments to obtain mid-infrared femtosecond sources for time-resolved spectroscopy [22]. Early work produced picosecond pulses tunable from 2 to 5 μm by mixing a dye laser with a white light continuum source in $LiIO_3$, which were successfully used to obtain the first picosecond

transient spectrum at these wavelengths of trans-polyacetylene.

The amount of published work in the area has increased dramatically since the turn of the decade, in line with the development of widely tunable powerful pulsed pump sources such as the self-modelocked titanium-sapphire (Ti:sapphire) laser [23], and improved nonlinear materials. The possibilities available have been contemplated by a number of authors [17, 24], leading to some successful experimental work. Two of the new materials are β-barium borate (BBO) and lithium triborate (LBO), the availability of which prompted much renewed interest in OPOs, although their transparency ranges cut off before 3 μm so they are of no use for mid-infrared generation directly. However, Zhang et al [25] used the idler output of a BBO optical parametric generator (OPG) to mix with Nd:YAG output in $AgGaS_2$ to cover 3 to 8 μm in the picosecond domain. In fact, the inability of many materials to give mid-infrared radiation directly by optical parametric generation or oscillation has prompted a number of researchers to consider difference frequency mixing (DFM) as an alternative. Recent examples of this work include mixing 1.064 μm and 1.444 μm Nd:YAG Q–switched pulses in $LiNbO_3$ to produce 20 ns pulses at 4.043 μm [13], and mixing Nd:YAG and tunable Ti:sapphire outputs in bulk periodically poled $LiNbO_3$ to give an output tunable from 3 to 4.1 μm [11]. Optical parametric oscillation and DFM have been combined by Laenen et al [6] by using a frequency-doubled modelocked Nd:YLF laser to pump a $KTiOPO_4$ (KTP) OPO, and then mixing the OPO output with the Nd:YLF fundamental in two $LiNbO_3$ crystals to produce 2 ps pulses tunable from 2.3 to 4.2 μm. $ZnGeP_2$ has been used [26] in an extension of previous work by the same authors and others as the crystal in a Er:Cr:YSGG-pumped travelling wave OPG to give picosecond pulses in the range 3.9 to 10 μm.

The family of titanyl arsenate crystals and their isomorphs have proved popular for nonlinear work. These materials have transparencies extending out to 4 and 5 μm, so are potentially of use as mid-infrared sources. DFM has been used in $KTiOAsO_4$ (KTA) to produce 2 ns pulses continuously tunable from 3 to 5 μm [10, 12]. Optical parametric oscillation in $KTiOPO_4$ (KTP) has generated nanosecond pulses at 3.2 μm from a Nd:YAG pump source [27], and 12 ps pulses tunable over the range 3.22 to 3.28 μm from a Nd:YLF pump [28]. However, more recently 3 ps pulses tunable over the wider range of 2.6 to 4.5 μm have been obtained from a combination of optical parametric generation and amplification in

$MgO:LiNbO_3$ crystals [29].

1.4 Progress of femtosecond sources into the mid-infrared spectral range

The generation of ultrashort pulses, that is, picosecond and femtosecond pulses, is made possible by the technique of modelocking, first demonstrated in the mid-1960s [30]. Active and passive modelocking methods originally produced picosecond pulses only, until passive modelocking was sufficiently improved by Shank and Ippen [31] to enable them to demonstrate the first femtosecond pulses, from a composite medium dye laser. By today's standards, these pulses were relatively long, having durations between between 500 fs and 1 ps. Further significant progress was then made thanks to the discovery of self-modelocking, first seen in a titanium-doped sapphire (Ti:sapphire) laser in 1991 [23, 32]. This phenomenon depends on the third-order optical nonlinearity known as the Kerr effect, hence the technique's alternative name of Kerr lens modelocking. Its use has led to reliable and robust femtosecond sources, so that pulses as short as just a few femtoseconds are now achievable, and 10 fs sources are available commercially [33].

Self-modelocked lasers are based on solid-state vibronic gain media having broad emission bandwidths in the near infrared (see Table 1.1). These broad bandwidths are necessary for the generation of very short pulses, because there is a fundamental limit on the product of the pulse duration and the frequency bandwidth of the pulse, so that the wider the bandwidth, the shorter the possible pulse duration. However, dispersion effects in the laser gain media tend to broaden pulses, so some form of compression is required. Traditionally this has been accomplished by inserting a pair of prisms inside the laser cavity to provide intracavity dispersion compensation, and produce chirp-free bandwidth-limited pulses. Prisms are unable to compensate for third- and fourth-order dispersion effects, though, so are not suitable for the production of the very shortest pulses now available. Instead, these pulses are generated from cavities containing multilayer dielectric mirrors, so-called "chirped mirrors" to provide compensation out to third-order dispersion. These mirrors were first proposed by Szipöcs et al in 1994 [35], who used them to generate 11 fs pulses from a Ti:sapphire laser [36], and then went on to produce the first sub-10 fs laser pulses, in the shape of near-bandwidth-limited 8 fs Ti:sapphire pulses from a linear cavity [37]. A ring cavity was then implemented to generate 7.5 fs

pulses more closely approaching the bandwidth limit [38]. The shortest pulses ever produced directly from a laser have been reported recently, using a combination of prisms and chirped mirrors to generate 6.5 fs pulses [39]. The record for the shortest pulses of any kind currently stands at 4.5 fs [40]. These pulses were produced by spectral broadening and subsequent compression of 20 fs pulses from a chirped mirror Ti:sapphire laser. An alternative use of chirped mirrors is to exploit the broad bandwidth to enhance tunability instead of pulse compression. This has been done by Mayer et al [41], who used a single set of chirped mirrors in a Ti:sapphire laser to generate 85 fs pulses tunable from 693 to 978 nm, which represents a substantial amount of the emission bandwidth of Ti:sapphire (see Table 1.1).

Gain media	**Pump band** (nm)	**Tuning range** (nm)	**Fluorescence peak** (nm)
Ti:sapphire	450 - 600	660 - 1180	780
Cr^{3+}:LiSAF	400 - 750	760 - 920	830
Cr^{3+}:LiCAF	350 - 750	720 - 840	780
Cr^{4+}:forsterite	850 - 1200	1167 - 1345	1000
Cr^{4+}:YAG	880 - 1100	1300 - 1600	1400

Table 1.1 Absorption and emission properties of some important solid-state vibronic laser gain media [34].

Other Ti:sapphire-based research has looked at the production of dual-wavelength femtosecond lasers, for use in two-colour spectroscopy. The most recent example of this is a system which emits two synchronous outputs of transform-limited pulses tunable over 220 nm [42]. Dual-wavelength Ti:sapphire lasers have also formed the basis of femtosecond mid-infrared sources. De Barros et al have used difference frequency mixing in AgGaS between the two outputs to generate 450 to 650 fs pulses tunable from 7.5 to 12.5 μm [43].

The early successes of the modelocked Ti:sapphire laser led researchers to investigate the possibilities of other vibronic gain media. One such material that caught the attention was chromium-doped $LiSrAlF_6$ (Cr^{3+}:LiSAF), a colquiriite which has one significant advantage over Ti:sapphire. Ti:sapphire is tunable over 660 to 1180 nm, but has to be pumped in the narrow wavelength band of 450 to 600 nm. This meant that until the recent introduction of powerful solid-state diode-

pumped green sources, such as the Spectra-Physics *Millennia* series [44], Ti:sapphire lasers had to be pumped with main-frame argon-ion lasers, which are notoriously costly and cumbersome. Cr^{3+}:LiSAF, on the other hand, emits over the similar range of 760 to 920 nm, but has a pump bandwidth extending from 400 to 750 nm. These much longer wavelengths mean that Cr^{3+}:LiSAF can be pumped in the red region of the spectrum, a wavelength range well covered by commercially available laser diodes such as those based on AlGaInP. Thus there has been much interest in diode-pumped Cr^{3+}:LiSAF as a potential compact all-solid-state laser system, and self-modelocked femtosecond Cr^{3+}:LiSAF systems are regularly reported. Dymott and Ferguson [45] achieved 34 fs pulses at an average power of 42 mW, while more recent work by Uemura and Miyazaki [46] has produced 26 fs pulses, the shortest pulses yet claimed from a single-diode-pumped solid-state laser. Other recent work by Robertson et al [47] has produced 94 fs pulses at 50 mW by pumping with a diode-pumped master oscillator power amplifier (MOPA). Such pump sources are likely to lead to higher power outputs in the future. However, doubts exist regarding the ultimate power capabilities of Cr^{3+}:LiSAF because it has poor thermal properties which can limit output powers. Possible alternative gain media are its close relatives Cr^{3+}:$LiCaAlF_6$ [48] and Cr^{3+}:$LiSrGaF_6$ [49], both of which have been successfully modelocked to produce femtosecond pulses.

Self-modelocking is now a widely accepted technique, but unfortunately is self-starting in only a small number of laser systems. It also places quite stringent demands on alignment and cavity design in some systems. For these reasons, alternative modelocking techniques tend to be favoured in another group of solid-state gain media, that of chromium-doped YAG and forsterite. These materials generate longer wavelengths than those available from Ti:sapphire and the colquiriites, as shown in Table 1.1, and have pump bandwidths in the approximate range of 850 to 1200 nm, so are often pumped by Nd:YAG lasers. Mode-locking methods based on saturable absorbers are popular, such as saturable Bragg reflectors and anti-resonant Fabry-Perot saturable absorbers. Such techniques have produced 120 fs pulses from Cr^{4+}:YAG [50] and 110 fs pulses from Cr^{4+}:forsterite [51]. Saturable absorbers have also been applied to Cr^{3+}:LiSAF, resulting in 50 fs pulses and average powers as high as 500 mW [52]. Conversely, self-modelocking has been successively achieved in Cr^{4+}:YAG and Cr^{4+}:forsterite systems [53].

Colour-centre lasers may also be modelocked to provide femtosecond pulses in

the near infrared, at slightly longer wavelengths than those available from Cr^{4+}:YAG and Cr^{4+}:forsterite. KCl:Tl may be tuned from 1.45 to 1.55 μm, and previous modelocking techniques used with it were improved by Kean et al [54] by the insertion of a length of optical fibre into an external control cavity to provide positive group velocity dispersion. The resulting pulses were 260 fs long. Higher powers are available from the $NaCl^-$:OH colour-centre laser, which tunes from 1.42 to 1.85 μm, and may be reliably modelocked by synchronous pumping to produce pulse durations of order 100 fs [55]. However, these systems require cryogenic cooling so are not as practical as the laser systems mentioned previously. Another alternative is the fibre laser, which is potentially cheaper and more compact and stable than OPOs or materials like Cr^{4+}:YAG for producing femtosecond pulses at 1.5 μm. Lenz et al [56] recently achieved diode-pumping of an erbium-doped fibre laser to produce 90 fs pulses at 1.55 μm.

The above-mentioned lasers are generally good sources of femtosecond pulses in the near infrared, but to extend their outputs to longer wavelengths it is necessary to use them to drive nonlinear interactions. All the nonlinear materials discussed in Section 1.3 have been successfully applied to the femtosecond regime, a potentially more difficult problem than working with nanoseconds or picoseconds since group velocity dispersion with such short pulses limits gain. Aiming to improve the availability of sub-100 fs pulses for spectroscopy, Laenen et al [5, 57] built a singly-resonant OPO based on BBO. Pumped with microsecond pulse-trains from frequency-doubled Nd:glass it achieved 160 to 260 fs pulses tunable from 0.7 to 1.8 μm. Travelling wave optical parametric generation [58] has been demonstrated in LBO and more successfully in BBO, producing an output tunable from 0.75 to 3.1 μm [59]. Difference frequency mixing in BBO has also been used, whereby a colliding pulse modelocked dye laser was mixed with an amplified portion of a white light continuum to produce 500 fs pulses at 2.5 μm [60].

The titanyl arsenate and phosphate crystal group has proved to be something of a success story in the femtosecond regime. Relatively new materials, they first attracted attention by their relatively high nonlinearities, and subsequently a large body of work has been published about them, a frequent arrangement being a Ti:sapphire synchronously pumped OPO. KTP has seemingly received the most attention, including being the basis for the first femtosecond synchronously pumped OPO in 1989 [61]. This device was pumped at the intracavity focus of a colliding

pulse modelocked dye laser and without dispersion compensation produced non-transform-limited 220 fs pulses, tunable over a signal branch of 820 to 920 nm and an idler branch of 1.9 to 2.54 μm. The system was later improved by the addition of prisms to give 120 fs signal pulses tunable from 0.75 to 1.04 μm, with the idler branch extended to 1.5 to 3.2 μm [62]. Ti:sapphire pumping was then introduced, changing the output to 1.0 to 1.8 μm (signal) and 1.5 to 2.75 μm (idler) at 100 fs pulse duration [63], subsequently reduced to 75 fs by using higher output coupling [64]. Extra-cavity prisms were used by other researchers [65] to produce signal pulses as short as 62 fs, although extra-cavity dispersion compensation cannot produce transform-limited pulses. These arrangements all used a critical phase-matching geometry, a situation which was improved by Dudley et al [66] who achieved Ti:sapphire pumped non-critical phase matching (pumping along a crystal axis) in KTP. This geometry eliminates walk-off between the interacting pulses, allowing pulse durations to be shorter; in this case intracavity prisms produced 40 fs near-transform-limited pulses, from 1.1 to 1.3 μm in the signal branch. The most recent development [67] has been the demonstration of self-modelocking in a KTP OPO. This resulted in pulses of 460 fs at 1.3 μm, which are obviously far longer than previous results, but the pump laser was a 3.5 ps frequency-doubled Nd:YLF laser. Thus the Kerr effect in the OPO produced significant pulse compression, which is highly desirable since picosecond pump pulses place less stringent demands on pumping conditions than femtosecond pump pulses.

The titanyl arsenates have also been used in Ti:sapphire pumped OPOs. A KTA OPO was first demonstrated by Powers et al [68], with a noncollinear pumping geometry producing a signal of 1.29 to 1.44 μm and an idler of 1.83 to 1.91 μm. At 150 fs the idler pulse was the shortest infrared idler pulse then recorded. Powers et al [69] were also the first to demonstrate optical parametric oscillation in $CsTiOAsO_4$ (CTA), this time using non-critical phase-matching with Ti:sapphire pumping to obtain continuous tuning from 1.46 to 1.73 μm, with a signal pulse duration of 62 fs. $RbTiOAsO_4$ (RTA) was the next titanyl arsenate to be addressed [70], such that with a noncritical geometry the signal branch tuned from 1.03 to 1.3 μm in 58 fs near-transform-limited pulses and the idler branch from 2.15 to 3.65μm in 68 fs pulses. Transform-limited pulses were later achieved by Reid et al [71, 72] with tuning from 1.32 to 1.34 μm and 2.1 to 2.43 μm, and the lowest oscillation threshold at that time for a femtosecond OPO, leading to the general

conclusion that RTA is a better OPO material than KTP.

The niobate materials have also been used to produce femtosecond infrared pulses. In 1990 Kurokawa and Nakazawa [73] mixed 80 ps Nd:YAG pulses with sub-picosecond dye laser pulses in $LiNbO_3$ to produce 1.4 to 1.6 μm by angle tuning. The pulse duration was estimated to be 300 fs. $KNbO_3$ has received more recent attention, by Spence et al [74], who demonstrated the first high repetition rate femtosecond OPO in the material, selected for its high non-linearity and high damage threshold. Ti:sapphire pumping gave 90 fs signal pulses at 1.2 to 1.4 μm and 105 fs idler pulses (the shortest idler pulses recorded up to that time) at 1.76 to 2.2 μm.

1.5 Current femtosecond mid-infrared sources

The research described in the previous two sections has culminated in a number of solutions to the quest for femtosecond mid-infrared pulses, the vast majority of which rely on nonlinear difference frequency mixing. These devices will now be reviewed, concentrating on the 3 to 5 μm region.

Prior to 1987, all tunable femtosecond infrared sources operated at wavelengths shorter than 1.6 μm. Desiring to extend this wavelength range to longer wavelengths with the aim of providing a source to study vibrational energy relaxation rates in molecules, Moore and Schmidt [75] performed a difference frequency mixing experiment in $LiNbO_3$. The two input waves came from an amplified colliding pulse modelocked ring dye laser at 613 nm and a sub-picosecond continuum source. By angle tuning, the device emitted 1.7 to 4 μm with an estimated pulse duration of 200 fs, at 2 nJ per pulse. More recently $LiNbO_3$ has been used by a number of other researchers. Emmerichs et al [76] used it to mix picosecond Nd:YLF pulses and tunable Ti:sapphire pulses (750 to 830 nm), resulting in 200 fs, 10 nJ pulses tunable from 2.6 to 4 μm. They selected $LiNbO_3$ since group velocities at 800 nm and 3 to 4 μm are nearly equal, which minimises walk-away, making the material good for generating mid-infrared light from an 800 nm input.

$LiIO_3$ has also been much used to produce femtosecond mid-infrared pulses by mixing. In an extension of their 1987 work, previously mentioned in section 1.3 [22], Jedju and Rothberg produced 350 fs pulses tunable from 2 to 5.5 μm by using a fibre compressor to shorten the initial Nd:YAG pulses used to pump their dye laser, thus

achieving the shortest mid-infrared pulses then recorded [77]. These pulses were successfully used to perform a number of time-resolved spectroscopy experiments on silicon and germanium, although the pulses had too large a bandwidth to be used for vibrational spectroscopy. However, this difficulty was soon resolved by amplifying the relevant frequency from the white light continuum in a two-stage dye amplifier [8], allowing accurate vibrational spectroscopy measurements on a 500 fs timescale. A more recent series of experiments using $LiIO_3$ has been performed by Elsaesser, Woerner and co-workers. They aimed to improve on the low efficiency and large intensity fluctuations of systems which mix dye lasers with white light continua, by mixing amplified and compressed pulses from a colliding pulse modelocked dye laser with pulses from a travelling wave dye cell [78], thus producing 400 fs pulses at 5.2 μm, with 10% conversion efficiency and less than 20% intensity fluctuations. The system was later improved by pumping and angle tuning two $LiIO_3$ crystals in parallel [4], resulting in the first parametric system to provide two synchronous (300) femtosecond pulse sequences independently tunable from 2.5 to 5 μm, an ideal source for pump-probe spectroscopy. Further improvements compressed the pulses to 250 fs [79].

A more complicated device utilized difference frequency mixing in $AgGaS_2$ [6], chosen to circumnavigate the problem that some crystals, otherwise suitable for difference frequency mixing, absorb at dye laser wavelengths. Frequency doubled 1 ps Nd:glass laser pulses pumped a BBO OPO, the idler of which was mixed with the Nd:glass fundamental frequency in two $AgGaS_2$ crystals to give 700 fs, 1 μJ, bandwidth-limited pulses tunable from 3.3 to 10 μm. This output was used in spectroscopy measurements, providing excellent time resolution.

KTP has also proved useful in a number of cases. Following extensive modelling to simulate walk-off, dispersion and chirp in a range of nonlinear systems designed to potentially produce sub-100 fs pulses in the 3 to 5 μm range, Cavallari et al [2] successfully tested the results of the model by mixing two Ti:sapphire outputs (100 fs at 720 nm and 35 fs tunable from 850 to 920 nm) in KTP, resulting in 100 fs pulses tunable over the range of 3.3 to 4.8 μm.

Until the last couple of years, the OPO was rather under-represented as a method of producing mid-infrared femtosecond pulses. The main example prior to 1995 was follow-up work to reference 60, the dye laser-pumped KTP OPO produced by Edelstein et al. The introduction of prisms to reduce pulse duration, and

active cavity length stabilisation via a photodiode comparison circuit gave 105 fs pulses and seemingly extended the tuning range to 0.72 to 4.5 μm [80]. Subsequently, though, researchers have found ways to generate mid-infrared wavelengths from synchronously-pumped OPOs, using a variety of materials. KTP was used by McCahon et al [81] in a critically phasematched interaction using near-collinear beam propagation to reduce idler walk-off at the longer wavelengths. This method produced idler pulses of 175 fs duration, tunable over the range 2.9 to 3.96 μm. Holtom et al favoured CTA [82], after concluding that it has better gain at long wavelengths than may be had from KTP, RTA or KTA. They generated idler pulse covering 2.59 to 4.12 μm. However, the most widely tunable idler output came from the $KNbO_3$-based OPO of Spence et al [83], which generated 60 fs pulses from 2.3 to 5.2 μm, using critical phasematching.

Fig. 1.2 illustrates the mid-infrared wavelengths achieved from OPOs and DFM systems in the femtosecond domain to date.

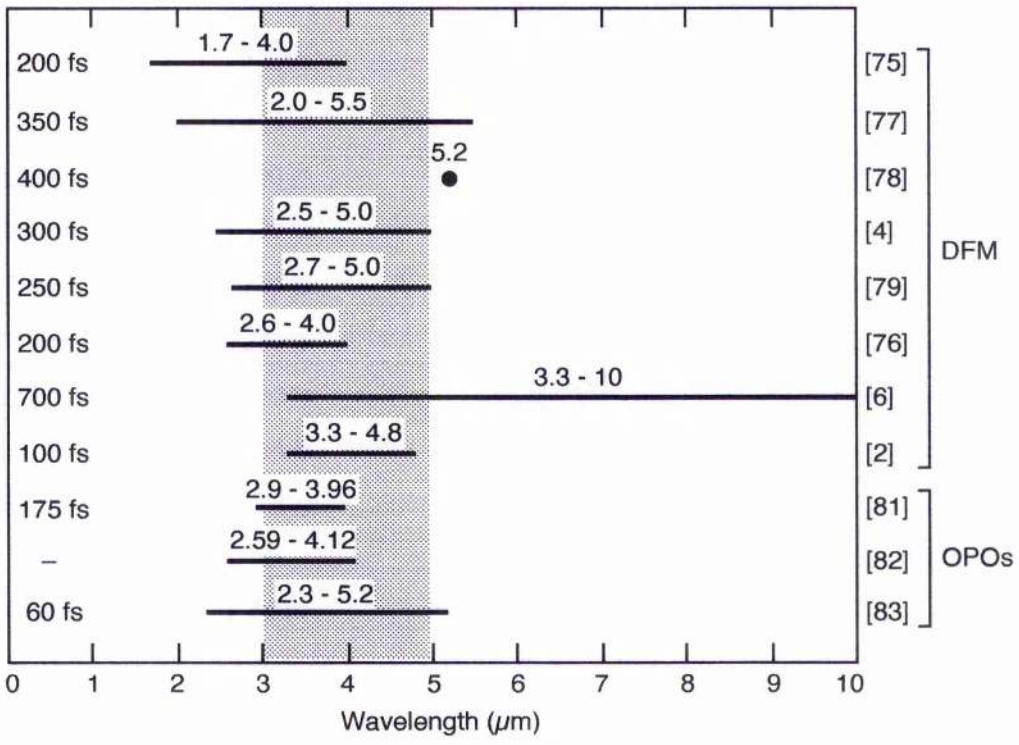

Figure 1.2 Mid-infrared wavelengths generated in the femtosecond domain to date, utilising difference frequency mixing and optical parametric oscillation.

Future mid-infrared femtosecond systems are unlikely to be based on the materials mentioned in the preceding sections. Three materials having wide

transparency ranges extending far into the mid-infrared offer some potential; these are silver gallium sulphide, silver gallium selenide and proustite. However, the greatest promise is offered by the newest nonlinear materials available, periodically poled ferroelectrics such as periodically poled lithium niobate and periodically poled RTA. All these crystals will be discussed in the next two sections.

1.6 Mid-infrared materials

Silver gallium sulphide ($AgGaS_2$), also known as silver thiogallate, silver gallium selenide ($AgGaSe_2$) and proustite ($AgAsS_3$) were introduced as nonlinear crystals in the late 1960s and early 1970s [84 - 86]. Interest in them was fuelled by their wide transparency ranges and high nonlinearities. They were investigated by a number of researchers and enjoyed a reasonable popularity at the time, but subsequently fell out of favour. This was partly because they suffer from low damage thresholds, and partly because they were usurped by newer and more reliable materials such as the titanyl arsenates. However, a few years ago these materials began to attract a renewed interest. Improved manufacturing techniques mean that the crystals available now are of superior quality to those of twenty years ago. In addition, they belong to what is a relatively small group of materials having extended transparency in the mid-infrared. Table 1.2 compares their transparency ranges with those of other materials discussed in this chapter.

Material	**Transparency range** (μm)
LBO	0.16 - 2.6
BBO	0.198 - 2.6
KTP	0.35 - 4.5
KTA	0.35 - 4
$LiNbO_3$	0.33 - 5.5
$KNbO_3$	0.4 - 4.5
$AgGaS_2$	0.5 - 13
$AgGaSe_2$	0.17 - 18
$AgAsS_3$	0.6 - 13

Table 1.2 Transparency ranges of some near and mid-infrared nonlinear optical materials [87].

All three materials have been successfully used for a variety of nonlinear interactions, including optical parametric generation [88], amplification [89] and oscillation [90], second harmonic generation [91], and sum [92] and difference frequency mixing [93]. Some of these devices demonstrated substantial tunability in the mid-infrared, as illustrated in Fig 1.3, which shows the wavelengths generated by optical parametric oscillators and generators. Although picosecond and nanosecond operation have been frequently demonstrated, none of these devices are femtosecond sources, although femtosecond difference frequency mixing has been achieved [102, 103].

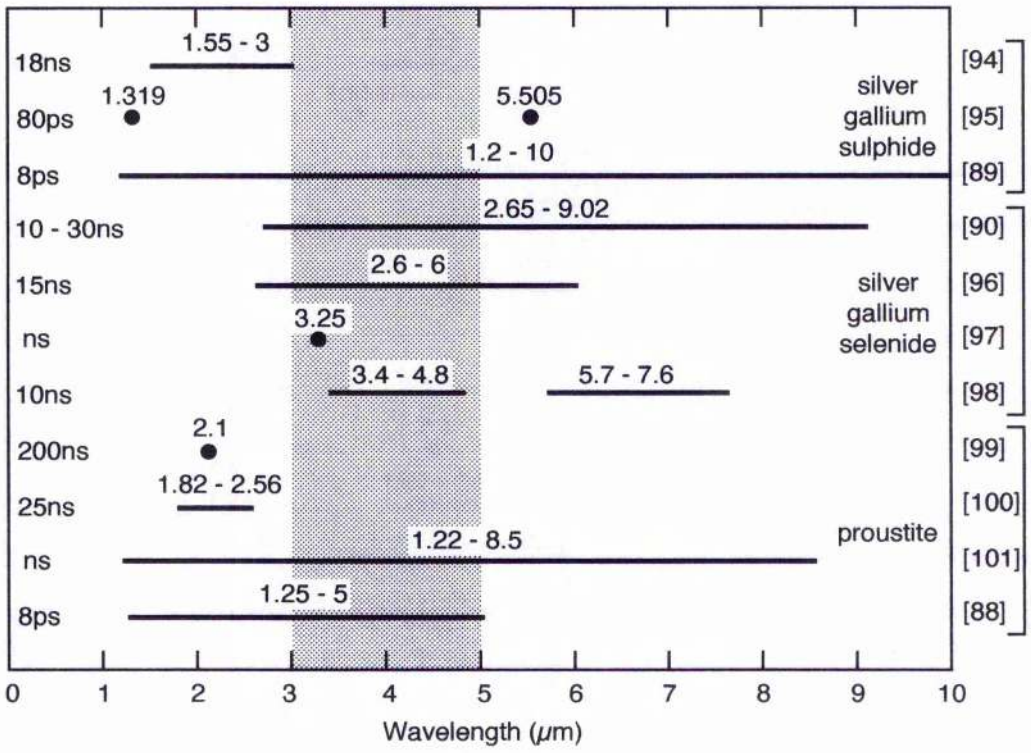

Figure 1.3 Summary of reported wavelengths generated from OPOs based on the mid-infrared materials silver gallium sulphide, silver gallium selenide and proustite. None of these sources produced femtosecond pulses.

In the context of the work presented in this thesis, $AgGaS_2$, $AgGaSe_2$ and $AgAsS_3$ were studied and compared in some detail to determine their suitability for use in a femtosecond OPO. This led to the conclusion that $AgGaSe_2$ was the most appropriate material, a conclusion also reached by Barnes [17] in his extensive

comparison of six mid-infrared materials. The OPO was never built, however. Just as these materials seemed to poised to solve the problem of the mid-infrared source, they were all but abandoned. The new periodically poled materials had arrived and captured everyone's attention, and it now appears probable that they will ultimately provide the best mid-infrared source.

1.7 Periodically poled materials

The nonlinear devices described in the previous sections have all utilised the technique of birefringent phasematching, which will be discussed theoretically in Chapter 2. Birefringence is a property relating to the magnitude of the difference between the various refractive indices of a nonlinear material, and determines which nonlinear interactions can be successfully phasematched. Hence the usefulness of a material is governed by the fixed fundamental properties of its refractive indices, over which the user has no control. This fact dominated the field of nonlinear optics for many years, and was one of the reasons for the difficulties faced in developing mid-infrared sources. Not only did a material have to be transparent in the mid-infrared, it had to have suitable phasematching properties there, too. Not many materials fall into this category.

Birefringent phasematching is not the only technique available, though. In fact, before it was even postulated, an alternative method was proposed, that of quasi-phasematching (QPM). [104]. This allows for the phasematching of any interaction within the transparency range of a material. If an interaction is not birefringently phasematched, the interacting waves become out of phase with each other after propagating only a very short distance through the material, known as the coherence length. Consequently the interaction becomes highly inefficient, and back conversion occurs. Quasi-phasematching overcomes this by reversing the sign of the nonlinearity of the material after every two coherence lengths to bring the waves back in phase and allowing the interaction to build up. Unfortunately, difficulties in engineering this sign reversal, or periodic poling, as it is known, held up the widespread implementation of QPM for many years. The most obvious approach of taking thin wafers of a material and then stacking them with alternate slices in opposing directions is not often practical, because most interactions require the slices to be

only a few micrometres thick. However, this has been successfully demonstrated with gallium arsenide (GaAs) to achieve second harmonic generation of a carbon dioxide laser, an interaction requiring a relatively long poling period of 106 μm [105]. This highlights a further advantage of QPM. GaAs, like many semiconductors, has a high nonlinearity but lacks birefringence, so this useful property can only be exploited by utilising QPM. Currently, the most popular poling technique involves the application of an electric field through a mask [106], the technology for which is improving rapidly at the present time, with finer and more complex masks becoming practicable. Poling by an applied electric field was first proposed in 1972 by Ballman and Brown, who used it to produce domain reversal in lithium tantalate [107]. The principle drawback to this is that only ferroelectric materials are suitable for poling in this way. To date, as far as bulk material is concerned (as opposed to waveguides), lithium niobate [108], KTP [109], RTA [110] and strontium barium niobate [111] have all been electrically poled and used successfully, with lithium niobate receiving the lion's share of the attention.

Second harmonic generation in electrically poled periodically poled lithium niobate (PPLN) was demonstrated as long ago as 1985 [112], and for a long time afterwards frequency doubling was the only interaction reported, used to generate green light [113, 114] and blue light [115, 116]. Many early PPLN devices were configured as waveguides, but now sources based on the bulk material are becoming more common. Optical parametric generators [117], amplifiers [118] and oscillators [119] and sum and difference frequency mixing [120] have all been reported recently. OPOs have been demonstrated in the nanosecond [119] and picosecond [121] regimes, and most recently in the femtosecond domain, as described in Chapter 6 of this thesis [122]. Part of the interest in PPLN OPOs stems from their potential in the mid-infrared; the transparency of lithium niobate extends out to 5.5 μm, so with an appropriate pump source and poling period, the crucial 3 to 5 μm spectral region is achievable.

Given the enormous versatility of periodically poled crystals and quasi-phase matching, it seems likely that they will prove to be the materials of choice for a great many nonlinear applications in the future. Given also the current quest for more powerful and robust laser diodes, this suggests that the future of the coherent light source will be the compact, efficient diode-pumped all-solid-state laser coupled with the quasi-phasematched nonlinear frequency converter.

1.8 Concluding remarks

A summary of recent and current research pertinent to the stated aim of constructing mid-infrared femtosecond sources has been presented in this chapter. A number of linear and nonlinear optical concepts have been introduced; these will be explained in more detail in Chapter 2, which includes the theory of frequency conversion techniques such as optical parametric oscillation and second harmonic generation, and some details relating to ultrashort pulse propagation. In Chapter 3, a description of the Ti:sapphire laser used as a pump source for the OPOs presented later will be given, and measurement techniques used to characterise ultrashort pulses will be considered. Experimental results from two techniques – autocorrelation and second harmonic generation frequency-resolved optical gating – are given. Experimental work will be presented in Chapters 4, 5 and 6, covering the three synchronously-pumped femtosecond OPOs built in the course of the research presented in this thesis. A KTA-based OPO is detailed in Chapter 4, which utilised critical phasematching and noncollinear beam propagation, and was tunable out to 4.1 μm. In Chapter 5, a high power, compact, ultrahigh repetition rate OPO based on a semi-monolithic RTA crystal is presented. A quasi-phasematched OPO based on periodically poled lithium niobate is discussed in Chapter 6, which includes results showing extensive tunability out to 5 μm, as well as a simultaneously phasematched visible output. A brief summary and some concluding remarks appear in Chapter 7.

References

1. T. H. Maiman, Nature **187**, 493 (1960).
2. M. Cavallari, G. M. Gale, F. Hache, L. I. Pavlov and E. Rousseau, Opt. Commun. **114**, 329 (1995).
3. S. Adachi, S. Takeyama and Y. Takagi, Opt. Commun. **117**, 71 (1995).
4. C. Ludwig, W. Frey, M. Woerner and T. Elsaesser, Opt. Commun. **102**, 447 (1993).
5. R. Laenen, K. Wolfrum, A. Seilmeier and A. Laubereau, J. Opt. Soc. Am. B **10**, 2151 (1993).
6. R. Laenen, K. Wolfrum and A Laubereau, Proc. SPIE **2138**, 41 (1994).
7. G. R. Holtom, R. A. Crowell and X. S. Xie, J. Opt. Soc. Am. B 12, **1723** (1995).
8. T. M. Jedju, L. Rothberg and A. Labrie, Opt. Lett. **13**, 961 (1988).
9. U. Simon and F. K. Tittel, Infrared Phys. Tech. **36**, 427 (1995).
10. A. H. Kung, Appl. Phys. Lett. **65**, 1082 (1994).
11. L. Goldberg, W. K. Burns and R. W. McElhanon, Opt. Lett. **20**, 1280 (1995).
12. A. H. Kung, Opt. Lett. **20**, 1107 (1995).
13. S. K. Wong, R. Oliver, K. L. Schepler and D. L. Fenimore, Opt. Lett. **19**, 1433 (1994).
14. Laser Components GmbH, Werner-von-Siemens-Str. 15, D-82140 Olching, Germany.
15. R. C Stoneman and L. Esterowitz, Opt. Phot. News **1**, 10 (1990).
16. H. Q Le, G. W. Turner, J. R. Ochoa and A. Sanchez, Electron. Lett. **30**, 1944 (1994).
17. N. P. Barnes, Int. J. Nonlinear Opt. Phys. **1**, 639 (1991).
18. H. C. Miller, D. T. Radzykewycz and G. Hager, IEEE J. Quantum Electron. **30**, 2395 (1994).
19. L. S. Goldberg, Appl. Phys. Lett. **17**, 489 (1970).
20. K. Burneika, M. Ignatavicius, V. Kabelka, A. Piskarskas and A. Stabinis, IEEE J. Quantum Electron. **8**, 574 (1972).
21. H. M. van Driel, A. Hache and G. Mak, Proc. SPIE **2041**, 50 (1994).
22. T. M. Jedju and L. Rothberg, Appl. Opt. **26**, 2877 (1987).
23. D. E. Spence, P. N. Kean and W. Sibbett, Opt. Lett. **16**, 42 (1991).
24. E. C. Cheung and J. M. Liu, J. Opt. Soc. Am. B **8**, 1491 (1991).
25. J. Y Zhang, J. Y. Huang. Y. R. Shen and C. Chen, J. Opt. Soc. Am. B **10**, 1758 (1993).
26. K. L. Vodopyanov and V. G. Voevodin, Opt. Comm. **117**, 277 (1995).
27. K. Kato, IEEE J. Quantum. Electron. 27, **1137** (1991).
28. Ch. Grässer, D. Wang, R. Beigang and R. Wallenstein, J. Opt. Soc. Am. B 10, **2218** (1993).
29. S. Lin and T. Suzuki, Opt. Lett. 21, **579** (1996).
30. L. E. Hargrove, R. L. Fork and M. A. Pollock, Appl. Phys. Lett. **5**, 4 (1964).
31. C. V. Shank and E. P. Ippen, Appl. Phys. Lett. **24**, 373 (1974).
32. D. E. Spence, J. M. Evans, W. E. Sleat and W. Sibbett, Opt. Lett. **16**, 1762

(1991).
33. *Femtosource* range from Stingl OEG, Kleinengersdorferstr. 24, A-2100 Korneuberg, Austria.
34. M. P. Critten, *All-solid-state femtosecond Cr:LiSAF and Cr:LiSGaF lasers*, PhD thesis, University of St Andrews (1996).
35. R. Szipöcs, K. Ferencz, C. Spielmann and F. Krausz, Opt. Lett. **19**, 201 (1994).
36. A. Stingl, Ch. Spielmann, F. Krausz and R. Szipöcs, Opt. Lett. **19**, 204 (1994).
37. A. Stingl, M. Lenzner, Ch. Spielmann, F. Krausz and R. Szipöcs, Opt. Lett. **20**, 602 (1995).
38. L. Xu, Ch. Spielmann, F. Krausz and R. Szipöcs, Opt. Lett. **21**, 1259 (1996).
39. I. D. Jung, F. X. Kärtner, N. Matuschek, D. Sutter, F. Morier-Genoud, U. Keller, V. Scheuer, M. Tilsch, T. Tschudi and R. Szipöcs, in *Conference on Lasers and Electro-Optics,* Vol. 11 of 1997 OSA Technical Digest Series (Optical Society of America, Washington, DC, 1997), p. 35, paper CMI3.
40. M. Nisoli, S. de Silvestri, O. Svelto, R. Szipöcs, K. Ferencz, Ch. Spielmann, S. Sartania and F. Krausz, Opt. Lett. **22**, 522 (1997).
41. E. J. Mayer, J. Möbius, A. Euteneur, W. W. Rühle and R. Szipöcs, Opt. Lett. **22**, 528 (1997).
42. P. Langot, N. del Fatti, R. Tommasi and F Vallée, Opt. Commun. **137**, 285 (1997).
43. M. R. X. de Barros, R. S. Miranda, T. M. Jedju and P. C. Becker, Opt. Lett. **20**, 480 (1997).
44. Spectra-Physics Lasers Inc., 1335 Terra Bella Avenue, Mountain View, CA 94043, USA.
45. M. P. J. Dymott and A. I. Ferguson, Opt. Lett. **20**, 1157 (1995).
46. S. Uemera and K. Miyazaki, Opt. Commun. **138**, 330 (1997).
47. A. Robertson, R. Knappe and R. Wallenstein, J. Opt. Soc. Am. B **14**, 672 (1997).
48. P. LiKamWa, B. H. T. Chai and A. Miller, Opt. Lett. **17**, 1439 (1992).
49. V. P. Yanovsky, F. W. Wise, A. Cassanho and H. P. Jenssen, Opt. Lett. **20**, 1304 (1995).
50. M. J. Hayduk, S. T. Johns, M. F. Krol, C. R. Pollock and R. P. Leavitt, Opt. Commun. **137**, 55 (1997).
51. P. T. Guerreiro, S. Ten, E. Slobodchikov, Y. M. Kim, J. C. Woo and N. Peyghambarian, Opt. Commun. **136**, 27 (1997).
52. D. Kopf, G. Zhang, U. Keller, M. Moser, M. A. Emanuel, R. J. Beach and J. A. Skidmore, in *Conference on Lasers and Electro-Optics*, Vol. 11 of 1997 OSA Technical Digest Series (Optical Society of America, Washington, DC, 1997), p. 11, paper CMC3.
53. Y. P. Tang, P. M. W. French, J. R. Taylor and J. O. Fujimoto, Opt. Commun. **136**, 235 (1997).
54. P. N. Kean, X. Zhu, D. W. Crust, R. S. Grant, N. Langford and W. Sibbett, Opt. Lett **14**, 39 (1989).
55. G. T. Kennedy, R. S. Grant, W. E. Sleat and W. Sibbett, Opt. Lett. **14**, 208 (1993).
56. G. Lenz, K. Tamura, H. A. Haus and E. P. Ippen, Opt. Lett. **20**, 1289 (1995).

57. R. Laenen, H. Graener and A. Laubereau, Opt. Lett. **15**, 971 (1990).
58. A. G. Akmanov, S. A. Akhmanov, R. V. Khokholv, A. I. Kovrigin, A. S. Piskarskas and A. P. Sukhorukov, IEEE J. Quantum Electron. **4**, 828 (1968).
59. R. Danielus, A. Piskarskas, A. Stabibis, G. P. Banfi, P. Di Trapani and R. Righini, J. Opt. Soc. Am. B **10**, 2222 (1993).
60. P. C. M. Planken, E. Snoeks, L. D. Noordam, H. G. Muller, H. B. van Linden van den Heurell, Opt. Commun. **85**, 31 (1991).
61. D. E. Edelstein, E. S. Wachman and C. L. Tang, Appl. Phys. Lett. **54**, 1728 (1989).
62. E. S. Wachman, W. S. Pelouch and C. L. Tang, J. Appl. Phys. **70**, 1893 (1991).
63. W. S. Pelouch, R. J. Ellington P. E. POwers and C. L. Tang, Proc. SPIE **1842**, 161 (1992).
64. W. S. Pelouch, P. E. Powers and C. L. Tang, Opt. Lett. **17**, 1070 (1992).
65. Q. Fu, G. Mak and H. M. van Driel, Opt. Lett. **17**, 1006 (1992).
66. J. M. Dudley, D. T. Reid, M. Ebrahimzadeh and W. Sibbett, Opt. Commun. **104**, 419 (1994).
67. R. Laenen, C. Rauscher and A. Laubereau , Opt. Commun. **115**, 533 (1995).
68. P. E. Powers, S. Ramakrishna, C. L. Tang and L.K. Cheng, Opt. Lett. **18**, 1171 (1993).
69. P. E. Powers, C. L. Tang and L.K. Cheng, Opt. Lett. **19**, 37 (1994).
70. P. E. Powers, C. L. Tang and L.K. Cheng, Opt. Lett. **19**, 1439 (1994).
71. D. T. Reid, M. Ebrahimzadeh and W. Sibbett, Appl. Phys. B **60**, 437 (1995).
72. D. T. Reid, M. Ebrahimzadeh and W. Sibbett, J. Opt. Soc. Am. B **12**, 1157 (1995).
73. K. Kurokawa and M. Nakazawa, Opt. Commun. **75**, 413 (1990).
74. D. E. Spence, S. Wielandy, C. L. Tang, C. Bosshard and P. Günter, Opt. Lett. **20**, 680 (1995).
75. D. S. Moore And S. C. Schmidt, Opt. Lett. **12**, 480 (1987).
76. U. Emmerichs, H. J. Bakker and H. Kurz, Opt. Commun. **111**, 497 (1994).
77. T. M. Jedju and L. Rothberg, Appl. Opt. **27**, 615 (1988).
78. T. Elsaesser and M. C. Nuss, Opt. Lett. **16**, 411 (1991).
79. M. Woener, W. Frey, M. T. Portella, C. Ludwig, T. Elsaesser and W. Kaiser, Phys. Rev. B **49**, 1707 (1994).
80. E. S. Wachmann, D. S. Edelstein and C. L. Tang, Opt. Lett. **15**, 136 (1990).
81. S. W. McCahon, S. A. Anson, D.-J. Jang and T. F. Boggess, Opt. Lett. **20**, 2309 (1995).
82. G. R. Holtom, R. A. Crowell and L. K. Cheng, Opt. Lett. **20**, 1880 (1995).
83. D. E. Spence, S. Wielendy, C. L. Tang, C. Bosshard and P. Günter, Appl. Phys. Lett. **98**, 452 (1996).
84. D. S. Chemla, P. J. Kupecek, D. S. Robertson and R. C. Smith, Opt. Commun. **3, 29** (1971).
85. G. D. Boyd, H. Kasper and J. H. McFee, IEEE J. Quantum Electron. **7**, 563 (1971).
86. E. O. Ammann and J. M. Yarborough, Appl. Phys. Lett. **17**, 233 (1970).
87. V. G. Dmitriev, G. G. Gurzadyn and D. N. Nikogosyan, *Handbook of Nonlinear Optical Crystals*, Springer-Verlag, Berlin (1991).

88. T. Elsaesser, A. Seilmeier and W. Kaiser, Opt. Commun. **44**, 293 (1983).
89. T. Elsaesser, A. Seilmeier, W. Kaiser, P. Koidl and G. Brandt, Appl. Phys. Lett. **44**, 383 (1984).
90. R. C. Eckardt, Y. X. Fan, R. L. Byer, C. L. Marquardt, M. E. Storm and L. Esterowitz, Appl. Phys. Lett. **49**, 608 (1986).
91. R. C. Eckardt, Y. X. Fan, R. L. Byer, R. K. Route, R. S. Feigelson and J. van der Lann, Appl. Phys. Lett. **47**, 786 (1985).
92. W. Jantz and P. Koidl, Appl. Phys. Lett. **31**, 99 (1977).
93. U. Simon, C. E. Miller, C. C. Bradley, R. G. Hulet, R. F. Curl And F. K. Tittel, Opt. Lett. **18**, 1062 (1993).
94. Y. X. Fan, R. C. Eckardt, R. L. Byer, R. K. Route and R. S. Feigelson, Appl. Phys. Lett. **45**, 313 (1984).
95. T. Dahinten, U. Plödereder, A. Seilmeier, K. L. Vodopyanov, K. R. Allakhvardiev and Z. A. Ibragimov, IEEE J. Quantum Electron. **29**, 2245 (1993).
96. T. Dahinten, U. Plödereder, A. Seilmeier, K. L. Vodopyanov, K. R. Allakhvardiev and Z. A. Ibragimov, IEEE J. Quantum Electron. **29**, 2245 (1993).
97. N. P. Barnes, K. E. Murray, M. G. Jani and S. R. Harrell, J. Opt. Soc. Am. B **11**, 2422 (1994).
98. J. Kirton, Opt. Commun. **115**, 93 (1995).
99. E. O. Ammann and J. M. Yarborough, Appl. Phys. Lett. **17**, 233 (1970).
100. D. C. Hanna, B. Luther-Davis, H. N. Rutt and R. C. Smith, Appl. Phys. Lett. **20**, 34 (1972).
101. D.C. Hanna, B. Luther-Davis and R. C. Smith, Appl. Phys. Lett. **22**, 440 (1973).
102. F. Seifert, V. Petrov and M. Woener, Opt. Lett. **19**, 2009 (1994).
103. A. Lohner, P. Kruck and N. W. Rühle, Appl. Phys. B **59**, 211 (1994).
104. J. A. Armstrong, N. Bloembergen, J.Ducuing and P. S. Pershan, Phys. Rev. **127**, 1918, (1962).
105. E. Lallier, M. Brevignon and J. LeHoux, in *Conference on Lasers and Electro-Optics*,Vol. 11 of 1997 OSA Technical Digest Series (Optical Society of America, Washington, DC, 1997), p. 61, paper CTuB6.
106. M. Houé and P. D. Townsend, J. Phys. D **28**, 1747 (1995).
107. A. Ballman and H. Brown, Ferroelectrics **4**, 189 (1972)
108. L. E. Myers, R. C. Eckardt, M. M. Feyer, R. L. Byer, W. R. Bosenberg and J. W. Pierce, J. Opt. Soc. Am. B **12**, 1202 (1995).
109. Q. Chen and W. P. Risk, Electron. Lett. **30**, 1516 (1994).
110. H. Karlsson, F. Laurell, P. Henriksson and G. Arvidsson, Electron. Lett. **32**, 556 (1996).
111. R. F. Xiao, Y. Y. Zhu, J. S. Fu and G. K. L. Wong, in *Conference on Lasers and Electro-Optics*,Vol. 11 of 1997 OSA Technical Digest Series (Optical Society of America, Washington, DC, 1997), p. 59, paper CTuB3.
112. A. Feisst and P. Koidl, Appl. Phys. Lett. **47**, 1125 (1985).
113. D. H. Jundt, G. A. Magel, M. M. Fejer and R. L. Byer, Appl. Phys. Lett. **59**, 2657 (1991).
114. J. Webjörn, V. Pruneri, P. St. J. Russell and D. C. Hanna, Electron. Lett. **31**, 669 (1995).

115. G. A. Magel, M. M. Fejer and R. L. Byer, Appl. Phys. Lett. **59**, 108 (1990).
116. J. Webjörn, V. Pruneri, P. St. J. Russell, J. R. M. Barr and D. C. Hanna, Electron. Lett. **30**, 894 (1994).
117. A. Galvanauskas, M. A. Arbore, M. M. Fejer, M. E. Fermann and D. Harter, Opt. Lett. **22**, 105 (1997).
118. J. J. Zayhowski,Opt. Lett. **22**, 169 (1997).
119. M. A. Arbore and M. M. Fejer, Opt. Lett. **22**, 151 (1997).
120. M. Asobe, I. Yokohama H. Itoh and T. Kaino, Opt. Lett. **22**, 274 (1997).
121. S. D. Butterworth, V. Pruneri and D. C. Hanna, Opt. Lett. **21**, 1345 (1996).
122. C. McGowan, D. T. Reid, Z. E. Penman, M. Ebrahimzadeh, W. Sibbett and D. H. Jundt, "Femtosecond optical parametric oscillator based on periodically poled lithium niobate", submitted to J. Opt. Soc. Am. B.

chapter two

LINEAR AND NONLINEAR OPTICS

2.1 Introduction

The field of nonlinear optics, to which the process of optical parametric generation belongs, is an extensive and complex one. A highly detailed treatment of the subject is beyond the scope of this thesis, but there are a number of topics which are referred to in later chapters and consequently require some discussion. The purpose of this chapter is therefore to provide a brief introduction to the origin of nonlinear optical effects, and the way in which they are described mathematically, and to present related material specifically relevant to the design and operation of ultrashort pulse optical parametric oscillators.

2.2 Nonlinear polarisation and the coupled wave equations

Nonlinear optical phenomena arise from the effects produced in certain materials when they are subject to intense electromagnetic radiation. Maxwell's equations, which describe the interaction of light with matter, are applicable to all materials, but the precise nature of any interaction is determined by properties of the light and the medium.

Consider a dielectric material in the presence of electromagnetic radiation. The field associated with the radiation causes the electrons in the dielectric to become polarised with respect to the nuclei, resulting in an overall induced polarisation in the medium. At low field strengths the amount of polarisation is proportional to the incident field, but when the applied field becomes comparable to the interatomic

electric field in the dielectric, the induced polarisation is nonlinearly related to the field strength. The low field proportional relationship describes the regime of linear optics, and can be written mathematically, in the scalar form, as

$$P = \varepsilon_0 \chi^{(1)} E \tag{2.1}$$

where P is the polarisation field vector, E is the electromagnetic field vector, and ε_0 is the permittivity of free space. $\chi^{(1)}$ is the linear susceptibility of the material, which connects P and E, and gives rise to linear optical effects such as refractive index, dispersion and birefringence (which will be discussed in more detail later). The nonlinear situation for high field strengths can be described by the related equation

$$P = \varepsilon_0 \chi^{(1)} E + \chi^{(2)} E^2 + \chi^{(3)} E^3 + \ldots \tag{2.2}$$

where $\chi^{(i)}$ is a tensor describing the nonlinear susceptibilities of the medium. It is necessary to use tensors to adequately describe these properties because in general the vectors P and E are not parallel. The magnitudes of $\chi^{(i)}$ decrease rapidly with increasing i, which is why high field strengths are required for optical nonlinearity to become significant. The generation of sufficiently high optical fields was not possible prior to the advent of the laser, so the subsequent evolutions of laser physics and nonlinear optics have been closely related. $\chi^{(2)}$ is the second order nonlinear susceptibility, and governs the three wave mixing phenomena of second harmonic generation, sum- and difference-frequency mixing, and parametric generation. The third order susceptibility, $\chi^{(3)}$, produces cubic nonlinear effects such as third harmonic generation and the Kerr effect. Higher order effects are seldom considered, and in the present case the second order effects are of primary interest so the cubic dependence will be neglected in the subsequent mathematics. Consequently, the nonlinear polarisation of the theoretical dielectric can be considered to be given by

$$P_{NL} = \chi^{(2)} E^2 \tag{2.3}$$

To describe nonlinear optical effects further it is necessary to consider the propagation of electromagnetic waves through the nonlinear medium. For a dielectric material, Maxwell's equation relates the time dependence of the polarisation and

electromagnetic fields via

$$\nabla^2 E = \mu\varepsilon_0 \frac{\partial^2 E}{\partial t^2} + \mu \frac{\partial^2 P}{\partial t^2} \tag{2.4}$$

For a nonlinear situation, the polarisation is described by equation 2.3. Substituting for this results in the second order nonlinear Maxwell equation:

$$\frac{\partial^2 E}{\partial z^2} = \mu\varepsilon \frac{\partial^2 E}{\partial t^2} + \mu \frac{\partial^2 (\chi^{(2)} E^2)}{\partial t^2} \tag{2.5}$$

where $\varepsilon = \varepsilon_0(1+\chi^{(2)})$, and the simplifying assumption that the electromagnetic waves are propagating in the z-direction has been made. This equation can be solved to determine the behaviour of the wave in question as it propagates through the medium. In general, second order nonlinear optical processes are concerned with the interaction of three waves, one or two of which are used to generate the remaining wave or waves. Conservation of energy requires that the frequencies of the three waves are related by

$$\omega_1 + \omega_2 = \omega_3 \tag{2.6}$$

where ω_3 is the highest frequency (shortest wavelength) and ω_1 is the lowest frequency (longest wavelength). Thus there are several different interactions which can occur. Equation 2.6 describes sum-frequency mixing, where two longer wavelengths result in a shorter one. Alternatively, the longest wavelength can be generated by difference-frequency mixing, where

$$\omega_3 - \omega_2 = \omega_1 \tag{2.7}$$

Optical parametric generation uses a single short wavelength to produce two longer ones,

$$\omega_3 = \omega_1 + \omega_2 \tag{2.8}$$

and if $\omega_1 = \omega_2$ the process is said to be degenerate. Similarly, second harmonic generation is a special case of sum-frequency mixing in which $\omega_1 = \omega_2$.

Returning to the discussion of Maxwell's equation, for the case of a three wave interaction the total instantaneous electric field is given by the sum of the individual

fields 1, 2 and 3, so that

$$E(z,t) = E_1(z,t) + E_2(z,t) + E_3(z,t) \tag{2.9}$$

If the waves $E_i(z, t)$ are plane, their spatial and temporal dependence can be written as

$$E_i(z,t) = \frac{1}{2}(E_i(z)e^{i(k_i z - \omega t)} + c.c.) \tag{2.10}$$

where k_i is the wave vector of wave *i*.

Equation 2.9 may be substituted into Equation 2.5, and the resulting equation then split into three components, each of which describes one of the waves. After some mathematics (which can be found in detail in many texts [1 – 5] but which is not necessary to repeat here), and the use of the slowly varying amplitude approximation, which assumes that the field amplitudes vary slowly over distances comparable to a wavelength, it can be shown that these components reduce to

$$\frac{dE_1(z)}{dz} = \frac{-i\omega_1}{2}\sqrt{\frac{\mu}{\varepsilon_1}}\chi^{(2)}E_3(z)E_2^*(z)e^{i\Delta kz} \tag{2.11a}$$

$$\frac{dE_2(z)}{dz} = \frac{-i\omega_2}{2}\sqrt{\frac{\mu}{\varepsilon_2}}\chi^{(2)}E_3(z)E_1^*(z)e^{i\Delta kz} \tag{2.11b}$$

$$\frac{dE_3(z)}{dz} = \frac{-i\omega_3}{2}\sqrt{\frac{\mu}{\varepsilon_3}}\chi^{(2)}E_2(z)E_1(z)e^{-i\Delta kz} \tag{2.11c}$$

where in each case $\chi^{(2)}$ describes the interaction of the other waves to generate the wave in question.

Equations 2.11a to c are known as the coupled wave equations, because the amplitudes of the fields are coupled to each other via the second order tensor $\chi^{(2)}$. They describe the propagation through a nonlinear medium of the waves involved in a three wave interaction, and their interaction one with another.

The quantity Δk in Equations 2.11 is the wave vector mismatch, given by

$$\Delta k = k_3 - k_2 - k_1 \tag{2.12}$$

where the individual wave momentum vectors k_i can be found from

$$k_i = \frac{n_i \omega_i}{c} = \frac{2\pi n_i}{\lambda_i} \tag{2.13}$$

where n_i is the refractive index, and λ_i the wavelength of wave i, and c is the speed of light.

Any combination of ω_1, ω_2 and ω_3 can interact during propagation through the nonlinear material. However, the only processes which can experience gain and hence generate light in significant quantities are those with the correct phase relationship to undergo constructive interference. This condition is met when $\Delta k = 0$. Achieving this is known as phasematching, and will be discussed in Section 2.4.

All of the second order interactions mentioned above can be used in a single pass arrangement, where the initial incoming wave or waves, typically provided by a laser beam, propagate once through the nonlinear medium to generate the other wave or waves. This is the case with an optical parametric generator. However, such a device can be modified by enclosing the medium within suitably reflecting mirrors so that one or more of the generated waves is sent back through the medium for multiple passes, thus increasing the interaction and the amount of light generated, via the process of oscillation. This converts an optical parametric generator into an optical parametric oscillator (OPO), several novel experimental examples of which are presented in later chapters of this thesis.

The waves 1, 2 and 3 of the preceding general discussion are given specific names in an OPO. By convention, the incident wave, having the shortest wavelength, is known as the pump, which generates two longer wavelengths known as the signal and idler. The idler is usually designated as the longest wavelength; this is the practice adopted here. Hence

$$\omega_p = \omega_s + \omega_i \tag{2.14}$$

The coupled wave equations can be solved to produce an equation describing the growth, or gain, of the signal and idler waves from the pump wave of an OPO [6, 7]:

$$G(\omega_s,\omega_i) \cong \frac{\omega_s\omega_i\mu_0(\chi^{(2)}_{eff})^2 l^2}{2n_p n_s n_i c} I_0(\omega_p)\frac{\sin^2(\Delta kl/2)}{(\Delta kl/2)^2} \tag{2.15}$$

where $\chi^{(2)}_{eff}$ is the effective second order susceptibility for the particular circumstances of the interaction, and l is the interaction length. This equation explains why a zero wave vector mismatch is an important condition for efficient operation; the sinc^2 dependence on Δkl means that the gain is maximised when $\Delta k = 0$, all other factors being equal.

2.3 Nonlinear crystals

It is evident from the previous section that a material must possess a second order nonlinear susceptibility, $\chi^{(2)}$, to be of use in an OPO, or for other second order effects. The origin of the susceptibility lies in the structure of a material. All crystalline materials fall into one of 32 possible structural categories, known as point groups. The various structures possess different levels of symmetry, which determine whether a crystal exhibits any of a number of physical properties, namely piezoelectricity, pyroelectricity and ferroelectricity. The lowest level of symmetry divides crystals into those which are centrosymmetric and those which are not. Non-centrosymmetry is a necessary condition for a non-zero second order susceptibility, so only these crystals can sustain optical parametric oscillation. Of the 32 crystal classes, 21 are non-centrosymmetric.

As mentioned previously, $\chi^{(2)}$ is actually a tensor. It is a third rank tensor, having 27 components, χ_{ijk}. However, the nonlinearity of a material is more commonly discussed in terms of the so-called piezoelectric tensor, which has elements defined as

$$d_{ijk} = \frac{\chi_{ijk}}{2} \tag{2.16}$$

Under many circumstances there is no distinction between the subscripts j and k, so that $d_{ijk} = d_{ikj}$. The tensor can therefore be replaced by a 3 x 6 matrix, d_{ij}, with elements d_{11} to d_{36}. A further simplification can be made if a lossless regime can be

assumed, as is the case in most nonlinear experimental work. This is Kleinman's conjecture [8], which states that the d_{ijk} coefficients that are related by a rearrangement of the subscripts are in fact equal. In this way, the 3 x 6 matrix is reduced to a maximum of only ten independent elements. Several of these are equal to zero in many crystals, so that often only a few values of d_{ij}, called the nonlinear coefficients, need be considered. The reduced matrix has the same form for all members of a given crystal class, and relates the polarisation and electric fields according to

$$\begin{bmatrix} P_x \\ P_y \\ P_z \end{bmatrix} = \begin{bmatrix} d_{11} & d_{12} & d_{13} & d_{14} & d_{15} & d_{16} \\ d_{16} & d_{22} & d_{23} & d_{24} & d_{14} & d_{12} \\ d_{15} & d_{24} & d_{33} & d_{23} & d_{13} & d_{14} \end{bmatrix} \begin{bmatrix} E_x^2 \\ E_y^2 \\ E_z^2 \\ 2E_zE_y \\ 2E_zE_x \\ 2E_xE_y \end{bmatrix} \tag{2.17}$$

The d_{ij} coefficients can be used to calculate an effective nonlinearity, d_{eff}, via equations which depend on the crystal class [9]. Equation 2.15 indicates that a large effective susceptibility, $\chi^{(2)}_{eff}$, will maximise the gain of an interaction, so given the relationship between $\chi^{(2)}$ and d_{ijk}, it is desirable to use a nonlinear material with large d_{ij} coefficients to maximise d_{eff}.

The d_{ij} matrices for the various crystal classes can be found in many textbooks [10 – 13].

2.4 Phasematching

Phasematching is the process whereby a nonlinear interaction is specifically configured by the user to have a zero wave-vector mismatch, ie. $\Delta k = 0$. This section will detail various methods for the attainment of phasematching.

The phase mismatch, Δk, was defined in general terms in Equation 2.12. For an OPO this becomes

$$\Delta k = k_p - k_s - k_i \tag{2.18}$$

so by using Equation 2.13. the phasematching condition is

$$\frac{n_p}{\lambda_p} - \frac{n_s}{\lambda_s} - \frac{n_i}{\lambda_i} = 0 \tag{2.19}$$

This equation in effect expresses conservation of photon momentum, and must be satisfied for phasematching. There is a further restriction, imposed by the conservation of energy condition of Equation 2.6. Given that $c = \nu\lambda$, and $\omega = 2\pi\nu$, for an OPO this is expressed as

$$\frac{1}{\lambda_p} - \frac{1}{\lambda_s} - \frac{1}{\lambda_i} = 0 \tag{2.20}$$

Equations 2.19 and 2.20 must be simultaneously satisfied for macroscopic amplification of the optical fields in any three wave mixing process.

2.4.1 Birefringent phasematching

The most common method of phasematching makes use of the fact that many materials are birefringent, that is to say, light of orthogonal polarisations propagating in an arbitrary direction through such a material experiences different values of refractive index. Given that refractive index also varies with wavelength, Equation 2.18 can be satisfied under certain circumstances. In general, nonlinear birefringent crystals have three optical axes, defined relative to the crystallographic structure,and designated x, y and z. Each axis has an associated refractive index, n_x, n_y and n_z. A wave propagating with its polarisation parallel to one of those axes will experience the index of that axis, and is referred to as an ordinary wave, or o-wave. Light propagating with the orthogonal polarisation, at an angle to an axis, will experience a value of refractive index which varies with angle, and is called an extraordinary wave, or e-wave. This situation is illustrated by the index ellipsoid, which is a surface defined by the equation

$$\frac{x^2}{n_x^2} + \frac{y^2}{n_y^2} + \frac{z^2}{n_x^2} = 1 \tag{2.21}$$

An example of this is depicted in Fig. 2.1. This shows that the refractive indices seen by an o-wave and an e-wave can be represented by the axes of an ellipse normal to a wave propagating at an angle θ. For the situation illustrated, n_e varies between n_x for θ = 0°, and n_z for θ = 90°, while n_o stays fixed at n_y. Hence, phasematching can be satisfied by choosing suitable polarisations and propagation angles.

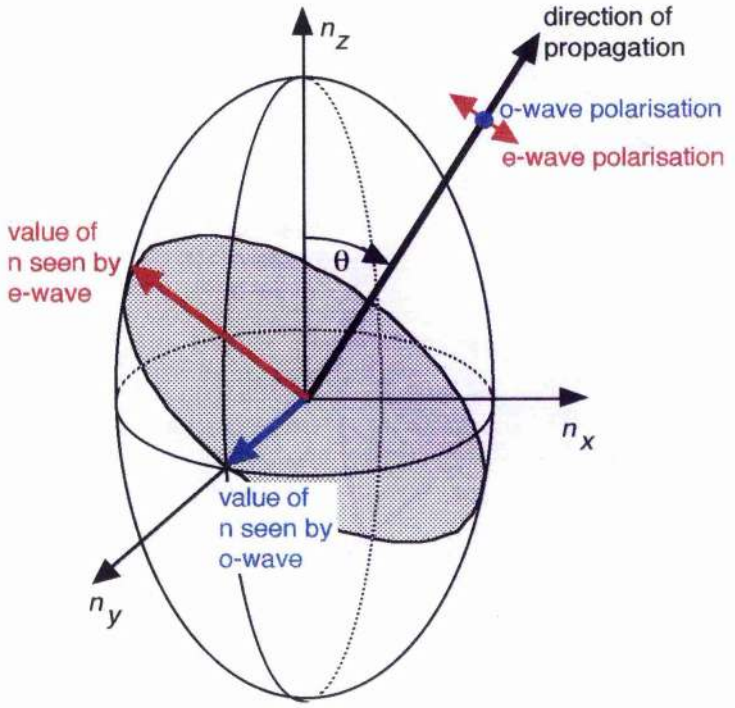

Figure 2.1 The index ellipsoid, illustrating the values of refractive index seen by an o-wave and an e-wave propagating at an angle in the birefringent crystal.

Birefringent crystals are divided into two categories: uniaxial and biaxial. Uniaxial crystals have two values of refractive index equal, so the three indices reduce to only two, known as n_o and n_e. A uniaxial crystal may be positive, where $n_e > n_o$, or negative, where $n_o > n_e$. A biaxial crystal has $n_x \neq n_y \neq n_z$, and either $n_x > n_y > n_z$, or $n_z > n_y > n_x$.

Different combinations of ordinary and extraordinary waves can be used to achieve the required effect; these combinations are referred to as Type I and Type II phasematching, and for parametric generation in positive and negative crystals are:

	Positive	**Negative**
Type I	o → e + e	e → o + o
Type II	o → e(o) + o(e)	e → o(e) + e(o)

The variations of refractive index with wavelength for crystals are described by Sellmeier equations, which are determined experimentally. Examples of Sellmeier equations for various materials can be found in Chapters 4, 5 and 6. After the selection of an appropriate nonlinear material, the Sellmeier equations can be used in the phasematching condition of Equation 2.19. By taking the angular variation of refractive index into account as well, the propagation angle required to generate specific signal and idler wavelengths from a given pump wavelength can be determined. For the configuration shown in Fig. 2.1, the angular variation of n_e is given by

$$n_e(\theta) = \sqrt{\frac{\cos^2\theta}{n_x^2} + \frac{\sin^2\theta}{n_z^2}}^{-1} \tag{2.22}$$

Tunability of the output of an OPO is frequently desirable, and this angular variation of index leads to the possibility of so-called angle tuning. The crystal in an oscillating OPO is slowly rotated, so that the incident pump beam experiences a varying refractive index, and the signal and idler wavelengths must alter to compensate for this and maintain phasematching. Other tuning methods include pump tuning, where the crystal is kept stationary while the pump wavelength is varied, and temperature tuning, which exploits the fact that some birefringent materials exhibit a significant variation of refractive index with temperature.

Birefringent phasematching can be further divided into the techniques of critical and noncritical phasematching. The latter method is configured such that the pump, signal and idler waves all propagate along a crystal optical axis, say the x-axis, and consequently see, in this case, either n_y or n_z. Under these conditions, the beams remain collinear throughout the crystal and can therefore interact over the whole crystal length. It is evident from Equation 2.15 that this is desirable, because of the dependence of gain on the square of the interaction length. This arrangement obviously precludes the use of angle tuning, so pump and temperature tuning must be relied upon. However, often these techniques are unable to generate the desired

wavelengths, and it becomes necessary to propagate the beams at an angle to one of the optical axes. This arrangement is called critical phasematching, and is unfortunately prey to a problem known as Poynting vector walk-off, or spatial walk-off, which is illustrated in Fig. 2.2. An ordinary wave propagates through a crystal with its momentum vector, k, parallel to its Poynting vector, S, with the wavefronts normal to both vectors. However, an extraordinary wave suffers walk-off, where the Poynting vector moves away from the k-vector by an angle ρ, the walk-off angle. The wave fronts remain normal to the k-vector. Thus an ordinary and extraordinary beam will overlap with each other for a short distance only, and the interaction between them will be greatly reduced, leading to low gain and poor efficiency. Since birefringent phasematching requires at least one extraordinary wave, Poynting vector walk-off affects a critically phasematched OPO, but not a noncritical OPO, where all the waves propagate along an optical axis in the crystal.

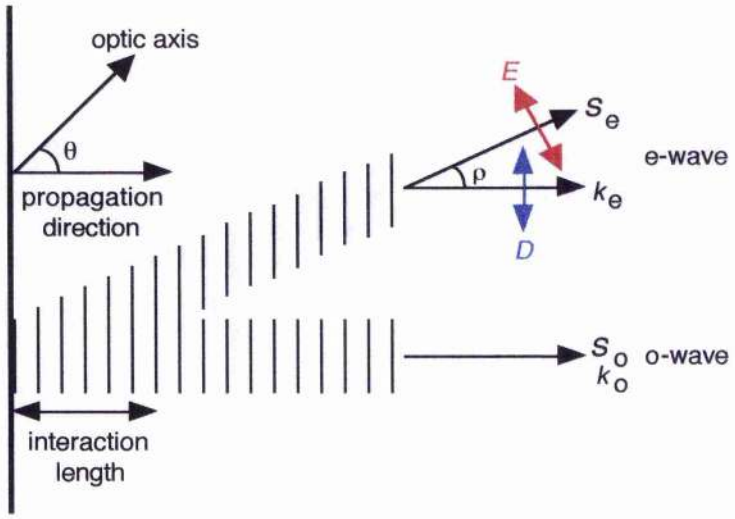

Figure 2.2 Poynting vector walk-off, whereby the Poynting vector of an e-wave moves away from the k-vector when the wave propagates at an angle to the optic axis, whereas those of an o-wave remain collinear.

One way of overcoming the problems of walk-off is to use noncollinear phasematching. The ordinary and extraordinary beams are propagated with their k-vectors at an angle to each other in such a way that the extraordinary S-vector walks onto the ordinary S-vector, increasing the interaction volume. This subject is dealt with in more detail in Section 4.3, with specific reference to a noncollinearly phasematched OPO based on $KTiOAsO_4$.

The walk-off angle for an extraordinary wave can be calculated from the dot product of the unit vectors of the electric field vector E, which is normal to the Poynting vector, and the displacement vector D, which is normal to the k-vector (Fig. 2.2):

$$\rho = \arccos(\hat{E}.\hat{D}) \tag{2.23}$$

A detailed calculation of the walk-off of an e-polarised signal wave in $KTiOAsO_4$ is given as an example in Appendix A.

2.4.2 Quasi-phasematching

Birefringent phasematching has been successfully demonstrated countless times, for the generation of a vast range of wavelengths from many varieties of nonlinear device. However, the fact that it relies on a physical property, namely, refractive index, means that it is limited and not viable for every application. This is particularly true for the generation of mid-infrared wavelengths; there are very few materials that are both transparent and phasematchable beyond 4 μm.

Ideally, researchers would like to be able to tailor nonlinear materials to fit any application. In effect, this means introducing some extra element into the wave vector mismatch equation to maintain $\Delta k = 0$ for any required combination of wavelengths. Happily, there is a way to do this – quasi-phasematching. This technique was originally suggested before that of birefringent phasematching, by Armstrong et al [14] in 1962, although they did not refer to it by that name.

Consider an OPO in which the pump, signal and idler propagate collinearly, but the interaction is not phasematched, so that $\Delta k \neq 0$. The waves slip out of phase and interact less strongly as they propagate through the crystal. Back conversion occurs until eventually the phase relation favours forward conversion again, and the process repeats itself. Over the length of a crystal the overall conversion efficiency is negligible, and no useful light is generated. The propagation distance after which the gain is reduced by half is referred to as the coherence length, l_c, given by

$$l_c = \frac{\pi}{k_p - k_s - k_i} = \frac{\pi}{\Delta k} \tag{2.24}$$

This detrimental process can be compensated for, however. If the sign of the nonlinear coefficient can be reversed after each coherence length (and is therefore modulated with a period equal to twice the coherence length), the interaction is brought back into phase, and continues to build up through the whole crystal length. This is the process of quasi-phasematching.

The sign reversal of the nonlinearity can be achieved by stacking plates of a nonlinear material in opposing orientations, but this is difficult to engineer on a small enough scale. A more useful technique is the periodic poling of ferroelectric crystals, whereby an electric field is applied to a crystal to periodically reverse the polarity, and hence the nonlinearity. This is discussed further in Section 6.4. Reliable fabrication methods for poled crystals are relatively new, so that the use of quasi-phasematching is only now becoming widespread, despite being based on an idea almost four decades old.

The modulation of the nonlinearity is referred to as a grating, so the period of the modulation is the grating period, Λ, where

$$\Lambda = 2l_c \tag{2.25}$$

It is the grating period that makes up the extra parameter required to balance the wave-vector mismatch, so that, for an OPO,

$$\Delta k_Q = k_p - k_s - k_i - k_m \tag{2.26}$$

where k_m is the grating vector, given by

$$k_m = \frac{2\pi m}{\Lambda} \tag{2.27}$$

and m is the order of the quasi-phasematched process, such that $m = 1, 3, 5\ldots$ $m = 1$ is referred to as a first order process, and so on. The appropriate grating period can therefore be chosen to produce phasematching.

Quasi-phasematching calculations can be carried out in the same way as for birefringent phasematching, provided that the grating vector is accounted for. The conservation of momentum condition for first order quasi-phasematching in an OPO is therefore given by

$$\frac{n_p}{\lambda_p} - \frac{n_s}{\lambda_s} - \frac{n_i}{\lambda_i} - \frac{1}{\Lambda} = 0 \tag{2.28}$$

while the conservation of energy condition of Equation 2.20 remains unchanged.

The advantages of quasi-phasematching over birefringent phasematching are manifold. The creation of a grating means that a nonlinear crystal can be tailored to phasematch any desired combination of wavelengths within the transparency range of a material, thus overcoming the limitations placed by birefringent properties. The lack of dependence on birefringence means that any propagation direction and polarisation combination can be used. Hence, beams can always be propagated along a crystal axis to avoid the problems caused by Poynting vector walk-off, outlined in the previous section. Also, larger nonlinearities can be accessed, leading to higher gain. The polarisation combinations imposed by birefringent phasematching mean that frequently the largest nonlinear coefficient in a crystal is not exploited, whereas a quasi-phasematched arrangement allows the use of the polarisations which access the largest coefficient. The effective nonlinearity of a quasi-phasematched process is given by

$$d_{eff_Q} = \frac{2\pi}{m} d_{eff} \tag{2.29}$$

where d_{eff} is the nonlinearity for the equivalent process in the absence of a grating, if such a process were phasematchable. Thus, a first order process is the most efficient.

All these reasons have contributed to the current meteoric rise in the popularity of quasi-phasematching, since the recent introduction of high quality poled crystals.

This section has described the three principal methods of phasematching: critical and noncritical birefringent phasematching, and quasi-phasematching. Experimental examples of each of these techniques are presented in subsequent chapters of this thesis. Chapter 4 describes a noncritically phasematched OPO based on $RbTiOAsO_4$; Chapter 5 discusses the use of noncollinear propagation to overcome walk-off in a critically phasematched $KTiOAsO_4$ OPO; and a quasi-phasematched OPO based on periodically poled lithium niobate is presented in Chapter 5.

2.5 Ultrashort pulse OPOs

All the points discussed so far in this chapter are applicable to all types of optical parametric oscillator devices, be they continuous wave or pulsed. However, the three devices referred to in the previous paragraph are all femtosecond systems, and ultrashort pulse OPOs have a unique set of characteristics caused by the temporal conditions and high peak powers, which must be considered in their design. These factors will be described in this section.

The envelope of an ultrashort pulse contains a large number of frequencies, so that ultrashort pulses have wide spectral bandwidths. This bandwidth determines the minimum possible duration of the pulse, according to a limit on the magnitude of the product of the spectral bandwidth and the temporal full-width half-maximum of the pulse. This is referred to as the time-bandwidth product, given by

$$\Delta\tau_p \Delta\nu = X \tag{2.30}$$

The minimum value of X depends on the shape of the pulse envelope. A pulse with this minimum value is said to be bandwidth-limited – that is, the spectral bandwidth is unable to support a shorter pulse duration. Femtosecond OPO pulses are frequently assumed to have a hyperbolic secant ($\mathrm{sech}^2(t)$) temporal profile; for this pulse shape, $X = 0.315$. Such a pulse can be described by the function [15]

$$U(t) = \mathrm{sech}(t / T_0)\exp\left[\frac{-iC}{2}\frac{t^2}{T_0^2}\right] \tag{2.31}$$

where T_0 is the temporal half-width of the pulse at the $1/e^2$ intensity level. It is related to the more usual full-width half-maximum, $\Delta\tau_p$, by

$$\Delta\tau_p = 2\ln(1+\sqrt{2})T_0 \tag{2.32}$$

The parameter C describes the frequency chirp across the pulse, which is a variation in the instantaneous frequency across the temporal profile of the pulse. Fig. 2.3 depicts an unchirped and a chirped pulse. Chirp may be positive, when the leading edge of the pulse is red-shifted with respect to the central wavelength and the trailing

edge is blue-shifted, or negative, which implies the reverse situation.

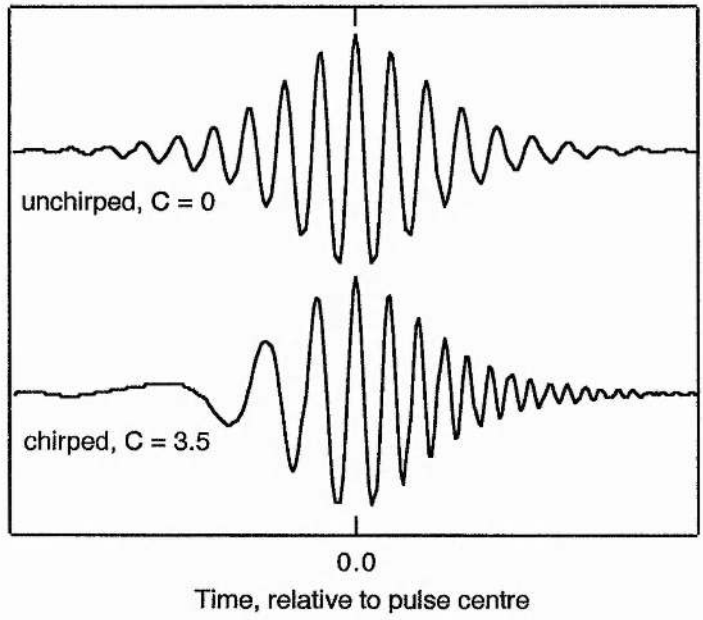

Figure 2.3 Unchirped and chirped $\text{sech}^2(t)$ pulses. The chirp factor, C, is that in Equation 2.31.

2.5.1 Linear refractive index

The discussion so far has been limited to second order nonlinear effects based on the susceptibility $\chi^{(2)}$. While being responsible for the origin of optical parametric generation, second order nonlinearity plays no role in the spectral and temporal evolution of ultrashort pulses once generated. These factors are governed by the linear susceptibility, $\chi^{(1)}$, which produces refractive index, and the third order susceptibility, $\chi^{(3)}$, which leads to the phenomenon of self-phase-modulation. Firstly, let us consider the linear refractive index [16].

It has been previously stated that refractive index is a function of wavelength, or frequency. This can be used to define a propagation constant, β, for a wave of frequency ω propagating in a medium with refractive index n:

$$\beta(\omega) = \frac{n(\omega)\omega}{c} \tag{2.33}$$

A Taylor series expansion of β about a centre frequency ω_0 gives

$$\beta(\omega) = \beta_0 + \beta_1(\omega - \omega_0) + \frac{1}{2}\beta_2(\omega - \omega_0)^2 + \frac{1}{6}\beta_3(\omega - \omega_0)^3 + \ldots \tag{2.34}$$

The various terms in this expansion describe different physical effects governing the propagation of pulses through the medium. Table 2.1 lists the mathematical expressions for each of the β coefficients, and the way in which they relate to their associated effects. Phase velocity is of little interest here, and third order dispersion will not be discussed further, since it is only of significance for pulses of shorter duration than were generated in the OPOs described later in this thesis.

β coefficient	**Related effect**
	Phase velocity
$\beta_0 = \frac{n\omega}{c}$	$v_\phi = \frac{\omega_0}{\beta_0}$
	Group velocity
$\beta_1 = \frac{1}{c}\left(n + \omega\frac{dn}{d\omega}\right)$	$v_g = \frac{1}{\beta_1}$
	Group velocity dispersion
$\beta_2 = \frac{1}{c}\left(2\frac{dn}{d\omega} + \omega\frac{d^2n}{d\omega^2}\right)$	$\beta_2 = \frac{d(1/v_g)}{d\omega}$
	Third order dispersion
$\beta_3 = \frac{1}{c}\left(3\frac{d^2n}{d\omega^2} + \omega\frac{d^3n}{d\omega^3}\right)$	$\beta_3 = \frac{d\beta_2}{d\omega}$

Table 2.1 Mathematical expressions for each of the coefficients of the propagation constant, β, and the related effects.

2.5.2 Temporal walk-away

Walk-away is the temporal equivalent of Poynting-vector walk-off, in that it

limits the interaction length in an OPO by moving the pulses away from each other in the temporal rather than the spatial domain. Table 2.1 shows the expression for group velocity, and indicates it to be frequency-dependent. Thus, the pump, signal and idler pulses will each propagate through an OPO crystal with different group velocities, so after some distance they cease to overlap in time and are unable to interact further. The walk-away, w, or the amount by which the pulses become separated, is often measured in terms of the difference in inverse group velocities, which for pulses of two different wavelengths, 1 and 2, is given by

$$w = \frac{1}{v_{g1}} - \frac{1}{v_{g2}} \tag{2.35}$$

This is generally expressed in fs/mm. It is important to take this into account when constructing a femtosecond OPO. Values of walk-away for common OPO materials are typically of the order of 100 fs/mm. For an OPO generating pulses of a few hundred femtoseconds duration or shorter, there is therefore little to be gained by using a crystal more than a few millimetres in length, because the pulses will walk away from each other to the extent that the bulk of the crystal will not contribute to the interaction. In fact, the extra material could prove detrimental, as it would lead to increased dispersion and pulse broadening, as discussed in the next section.

2.5.3 Group velocity dispersion

The temporal shape of an ultrashort pulse is principally governed by the presence of group velocity dispersion (GVD) [16, 17] in the propagation medium (Table 2.1). A dispersive medium is one in which different frequencies have different velocities, which has important ramifications for ultrashort pulses, with their wide spectral bandwidths. GVD changes the phase of each spectral component by an amount depending on the frequency, and thus produces chirp. The overall effect is to change the pulse duration, since each spectral component travels at a slightly different speed and so arrives at the end of the material at a different time. A material with positive ($\beta_2 > 0$), or normal dispersion, is one in which low, or red frequencies travel faster than blue ones. Hence a positively chirped pulse, in which the red

components lead, will be temporally broadened. This is the usual effect in an ultrashort pulse OPO crystal. The amount of dispersion, and therefore pulse broadening, increases with propagation distance, which is why an OPO crystal should be kept as short as possible, while still being long enough provide sufficient gain. An anomalously dispersive material ($\beta_2 < 0$) has the opposite effect of making blue frequencies travel faster then red ones.

Dispersive pulse broadening is generally undesirable in ultrashort pulses OPOs, since the purpose of such devices is to generate chirp-free and bandwidth-limited pulses. Dispersion is a fundamental material property and as such cannot be eliminated (although some nonlinear materials have very low dispersion), but it can be compensated for, as explained in the following section.

2.5.4 Dispersion compensation

The pulse broadening in ultrashort pulse OPOs and lasers is caused by the positive group velocity dispersion of the crystal. It is possible to shorten the pulses again by the introduction into the system of negative dispersion to balance the positive dispersion. This is known as dispersion compensation. One method of achieving this is to insert pairs of prisms into the cavity, as described by Fork et al in 1984 [18]. The prism material will itself have positive dispersion, but it is possible to configure the prisms in such a way that their overall contribution is negative. This configuration is illustrated in Fig. 2.4, using a sequence of four prisms. The prisms are cut and oriented such that the beams are incident at minimum deviation and Brewster's angle, to minimise losses. Spectral refraction in the prisms causes different wavelengths in a pulse to follow different optical paths through the sequence.

The total dispersion, D, available from a prism sequence is given by

$$D = (\lambda / cL)\frac{d^2P}{d\lambda^2} \tag{2.36}$$

where L is the physical length of the light path, and P is the optical path length. The derivative $d^2P/d\lambda^2$ is a function of the angular beam divergence α, the refractive index

of the prism material, and the prism apex separation *l*. It can be shown that for sufficiently large values of *l* the overall dispersion becomes negative. Thus, by adjusting the prism positions it is possible to vary the total dispersion of the cavity from positive to negative.

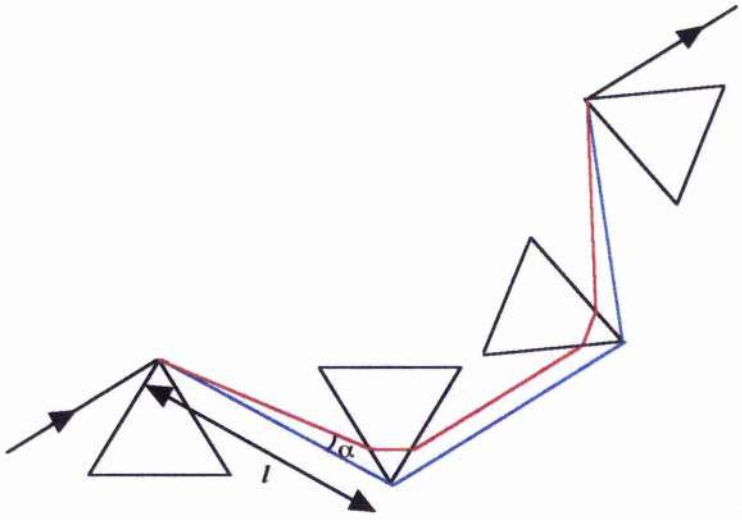

Figure 2.4 Prism sequence for dispersion compensation [18].

Maximum dispersion compensation is obtained from an intracavity prism position, because the pulses undergo multiple passes through the prisms. However, extra-cavity prisms can also provide some pulse shortening, although a very large separation is required to provide sufficient dispersion from a single pass.

Prisms are generally only able to compensate for second-order dispersion effects, and do not allow the generation of pulses much shorter than a few tens of femtoseconds. At these durations, third order dispersion (see Table 2.1) becomes the limiting factor. This can be compensated for by using specially coated dielectric cavity mirrors, known as chirped mirrors [19]. Such mirrors have facilitated the generation of sub-5 fs laser pulses [20], and have also been applied to a $KTiOAsO_4$-based OPO [21], leading to the generation of 50 fs pulses at 1.25 μm [22].

2.5.5 Self-phase modulation

Whereas group velocity dispersion is a linear, temporal effect, the other dominant pulse-shaping effect in OPOs, self-phase modulation (SPM) [23, 24], is a

third order ($\chi^{(3)}$), spectral effect. So far, the refractive index of a medium has been regarded as being dependent on wavelength only. However, there is also a nonlinear intensity dependence, caused by $\chi^{(3)}$, which comes into effect under the high electromagnetic field conditions of ultrashort pulses.

Ignoring terms higher than third order, and with no second order dependence ($\chi^{(2)}$ does not contribute to refractive index), the refractive index of a material can be written as [25]

$$n = n_0 + n_2|E|^2 \tag{2.37}$$

where n_0 is the linear refractive index considered so far, and n_2 is the nonlinear index. Time-averaging of the optical electric field E gives the intensity dependence:

$$n = n_0 + n_2 I \tag{2.38}$$

This is the optical Kerr effect, and n_2 is sometimes referred to as the Kerr coefficient. An ultrashort pulse has an intensity which varies in time, so different parts of the pulse experience different magnitudes of refractive index. This produces a change in phase across the pulse temporal profile, $\Delta\phi$, given by

$$\Delta\phi = \exp(2\pi i n_0 L/\lambda)\exp(2\pi i n_2 IL/\lambda) \tag{2.39}$$

where L is the propagation difference. Because frequency is the first time derivative of phase ($\omega = -d\phi/dt$), this phase shift results in a frequency shift, $\Delta\omega$, across the pulse profile:

$$\Delta\omega = -\frac{d(\Delta\phi)}{dt} \tag{2.40}$$

This induced phase and frequency shift is the phenomenon of self-phase modulation. The frequency shift produces new spectral components, so the spectral bandwidth is broadened. Fig. 2.5 shows the phase and frequency shift across a self-phase modulated pulse, and a typical corresponding spectrum. The multiple peaked nature of the spectrum is the signature of SPM; experimental examples of such spectra can be found in the experimental chapters of this thesis. The peaks arise from interference between equal spectral components occurring at different times, due to

the shape of the frequency shift. It is evident from Fig. 2.5 that the shift across the centre of the pulse is linear positive chirp, equivalent to the chirp produced by propagation through a positively dispersive material. Thus the spectral distortion effects of SPM can be removed by dispersion compensation. In fact, SPM produced by the nonlinear crystal in a dispersion compensated OPO can be beneficial, as the broadened spectrum can support shorter pulse durations in accordance with the time-bandwidth product (Equation 2.30).

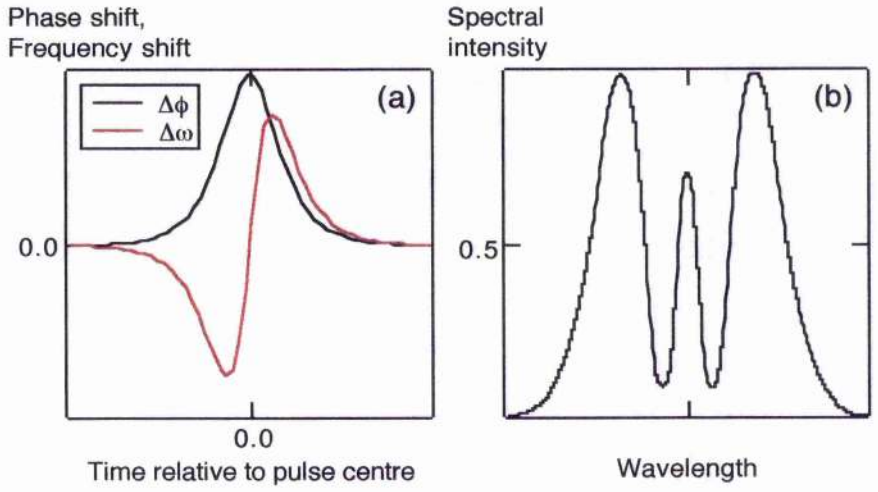

Figure 2.5 Phase shift and frequency shift induced across a pulse by self-phase modulation (a), and a typical resultant spectrum (b).

2.6 Concluding remarks

The discussion in this chapter has been concerned with the origin of various linear and nonlinear optical effects, with special reference to those relevant to ultrashort pulse parametric oscillators. The gain of an OPO, which determines the efficiency, is dependent on a number of parameters, as was shown in Equation 2.15. The wave vector mismatch, Δk, should be zero to maximise the gain; this is achieved by phasematching, as described in Section 2.4. If birefringent phasematching is used, the refractive index properties of the nonlinear crystal selected will determine the available output wavelengths. Quasi-phasematching, on the other hand, is much more versatile, and the possible wavelengths are limited only by the transparency of the material.

The effective nonlinearity should be as large as possible to maximise the gain. Careful choice of wave polarisations and propagation directions can usually select a reasonable nonlinearity, but in some cases the largest nonlinearity can only be accessed by quasi-phasematching. Conversely, some configurations, which apparently give desirable phasematching properties, correspond to a zero nonlinearity, and therefore can not be used.

The interaction length is also important, and Equation 2.15 implies that it should be large. This is, however, untrue in the specific case of ultrashort pulse OPOs. Section 2.5.2, about temporal walk-away, revealed the futility of having a crystal longer than a few millimetres for a femtosecond OPO; in addition, a short crystal is desirable for limiting dispersion. The effects of walk-away, and the need to minimise pulse broadening, mean that a long crystal is not a feasible way to increase the gain of a femtosecond OPO. This can be compensated for by using high pump power intensities, on which the gain also depends. Sufficient power is required initially to overcome losses in the system and exceed the oscillation threshold; above this point the generated output power increases with input power. Care must be taken, however, to keep the incident intensity below any threshold for optical damage which the OPO crystal may have.

There are thus a considerable number of parameters, some of them conflicting, which must be taken into account in the design of an OPO. It is therefore important to devote sufficient time to the selection of an appropriate crystal for an OPO, in order to obtain the best possible performance. Examples of this selection process are detailed in Chapters 4, 5 and 6, each of which presents experimental results from a different femtosecond OPO.

References

1. R. W. Boyd, *Nonlinear Optics* (Academic Press, San Diego, 1992).
2. A. Yariv, *Quantum Electronics* (third edition, Wiley, New York, 1989).
3. A. Yariv, *Optical Electronics* (fourth edition, Saunders College Publishing, USA, 1991).
4. R. L. Byer, "Parametric oscillators and nonlinear materials", Chapter 2, Nonlinear Optics: *Proceedings of the Sixteenth Scottish Universities Summer School in Physics*, P. G. Harper and B. S. Wherrett, ed. (Academic Press, London, 1977).
5. R. W. Munn, "Nonlinear optical phenomena", Chapter 2, and M. Ebrahimzadeh and A. I. Ferguson, "Novel nonlinear crystals", Chapter 6, *Principles and Applications of Nonlinear Optical Materials*, R. W. Munn and C. N. Ironside, ed. (Blackie Academic and Professional, 1993).
6. M. Ebrahimzadeh, "Pulsed parametric oscillators", *Laser Sources and Applications: Proceedings of the Forty Seventh Scottish Universities Summer School in Physics*, A. Miller and D. M. Finlayson, ed. (SUSSP Publications and Institute of Physics Publishing, Bristol, 1996) p. 235.
7. E. Harris, Proc. IEEE **57**, 2096 (1969).
8. R. W. Boyd, *Nonlinear Optics* (Academic Press, San Diego, 1992), p. 37.
9. V. G. Dmitriev, G. G. Gurzadyan and D. N. Nikogosyan, *Handbook of Nonlinear Optical Crystals* (second edition, Springer-Verlag, Berlin, 1997).
10. R. W. Boyd, *Nonlinear Optics* (Academic Press, San Diego, 1992), p. 44.
11. A. Yariv, *Quantum Electronics* (third edition, Wiley, New York, 1989), p. 381.
12. R. L. Byer, "Parametric oscillators and nonlinear materials", Chapter 2, Nonlinear Optics: *Proceedings of the Sixteenth Scottish Universities Summer School in Physics*, P. G. Harper and B. S. Wherrett, ed. (Academic Press, London, 1977), p. 55.
13. R. W. Munn, "Nonlinear optical phenomena", Chapter 2, and M. Ebrahimzadeh and A. I. Ferguson, "Novel nonlinear crystals", Chapter 6, *Principles and Applications of Nonlinear Optical Materials*, R. W. Munn and C. N. Ironside, ed. (Blackie Academic and Professional, 1993), p. 115.
14. J. A. Armstrong, N. Bloembergen, J. Ducuing and P. S. Pershan, Phys. Rev. **127**, 1918 (1962).
15. G. P. Agrawal, *Nonlinear Fibre Optics* (Academic Press, Inc., London, 1989), p. 59.
16. A. E. Siegman, *Lasers* (University Science Books, California, 1986), Chapter 9.
17. G. P. Agrawal, *Nonlinear Fibre Optics* (Academic Press, Inc., London, 1989), Chapter 3.
18. R. L. Fork, O. E. Martinez, J. P. Gordon, Opt. Lett. **9**, 150 (1984).
19. R. Szipöcs, K. Ferencz, C. Spielmann and F. Krausz, Opt. Lett. **19**, 201 (1994).
20. M. Nisoli, S. de Silvestri, O. Svelto, R. Szipöcs, K. Ferencz, Ch. Spielmann, S. Sartania and F. Krausz, Opt. Lett. **22**, 522 (1997).
21. J. Hebling, E. J. Mayer, J. Kuhl and R. Szipöcs, Opt. Lett. **20**, 919 (1995).
22. J. Hebling, H. Giessen, S. Linden and J. Kuhl, Opt. Commun. **141**, 229 (1997).

23. A. E. Siegman, *Lasers* (University Science Books, California, 1986), Chapter 10.
24. G. P. Agrawal, *Nonlinear Fibre Optics* (Academic Press, Inc., London, 1989), Chapter 4.
25. A. E. Siegman, *Lasers* (University Science Books, California, 1986), p. 378.

chapter three

ULTRASHORT PULSE GENERATION AND MEASUREMENT TECHNIQUES

3.1 Introduction

The optical parametric oscillators (OPOs) described in Chapters 4, 5 and 6 of this thesis were all synchronously-pumped by a self-modelocked femtosecond Ti:sapphire laser. This laser will be discussed in the first part of this chapter. A description of Ti:sapphire as a gain medium is given, followed by details relating to the process of self-modelocking, and then the specific configuration of the laser is presented.

At the current time, Ti:sapphire lasers are the most common pump source for ultrashort pulse OPOs. This is because of their broad tunability, relatively high powers, and ease of modelocking. The situation is unlikely to change until diode-pumped all-solid-state ultrashort pulse lasers such as Cr:LiSAF are further developed to produce sufficiently high output powers, which will lead to somewhat more compact systems. In the meantime, however, the Ti:sapphire laser has proved to be a highly reliable and suitable source for such applications, and is likely to continue as the pump laser of choice for some time to come.

Once ultrashort pulses have been generated, be they from a laser or an OPO, it is necessary to characterise them as completely as possible, both to fully understand their formation process, and to determine their suitability for particular applications. The main features of interest are the pulse duration, the spectral quality and the phase. The first two of these can be determined relatively straightforwardly. Commercial devices for spectral analysis are readily available. Pulse durations are commonly measured using the technique of autocorrelation, which will be described in this chapter, both in general terms and in terms of a novel arrangement which has

led to the development of a highly compact autocorrelator. The measurement of pulse phase is rather more challenging. Only a small amount of qualitative information about phase can be inferred from autocorrelation measurements; to accurately determine the phase requires simultaneous detailed measurement of both temporal and spectral information. One such technique for doing this is based on a frequency-resolved optical gating, which was used in this project to characterise pulses from one of the OPO systems. The experimental arrangement used to do this is presented in Section 3.3.

3.2 The self-modelocked Ti:sapphire laser

3.2.1 Ti:sapphire as a gain medium

Ti:sapphire is the common name for the solid-state vibronic laser gain medium titanium-doped sapphire, $Ti^{3+}:Al_2O_3$. Its use was first demonstrated by Moulton in 1982 [1], since when it has supplanted dye lasers as the most popular and convenient source of tunable near-infrared radiation. The broad and continuous tunability is the most attractive feature of Ti:sapphire; this is a characteristic of vibronic gain media, in which laser transitions occur between broad bands resulting from interaction between electrons of the active ions and vibrational modes in the host medium.

Ti:sapphire is a uniaxial crystal comprising the transparent host material of sapphire (Al_2O_3), doped with a small amount of Ti^{3+} impurity ions. The Ti^{3+} ions replace approximately 0.1% of Al^{3+} ions. The resulting structure is shown in Fig. 3.1; each Ti^{3+} or Al^{3+} ion is surrounded by an octahedral arrangement of six O^{2-} ions. The Ti^{3+} ions are the active ions in Ti:sapphire, and their electronic structure determines the laser properties of the material. The structure is that of a closed shell plus one outer 3d valence electron: $1s^2 2s^2 2p^6 3s^2 3p^6 3d^1$. This valence electron has a ^2D ground state, but when the Ti^{3+} ion is placed in the sapphire lattice, the cubic field from the O^{2-} ions splits the energy levels into a $^2T_2$ ground state and a ^2E excited state. Further interaction with the trigonal field resulting from the arrangement of the Al^{3+} ions splits the ground state into two, the lower of which is again split in two by spin-orbit coupling. The excited state is divided by Jahn-Teller splitting. The structure of these energy levels is illustrated in Fig. 3.2 [2], which

shows the broad energy bands which give the large bandwidth and tunability of Ti:sapphire lasers.

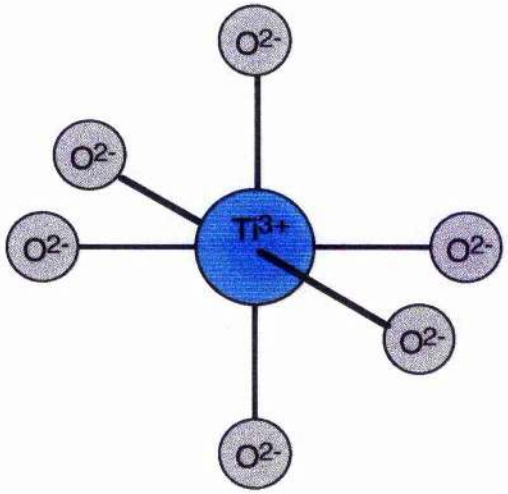

Figure 3.1 Octahedral arrangement of ions of Ti:sapphire.

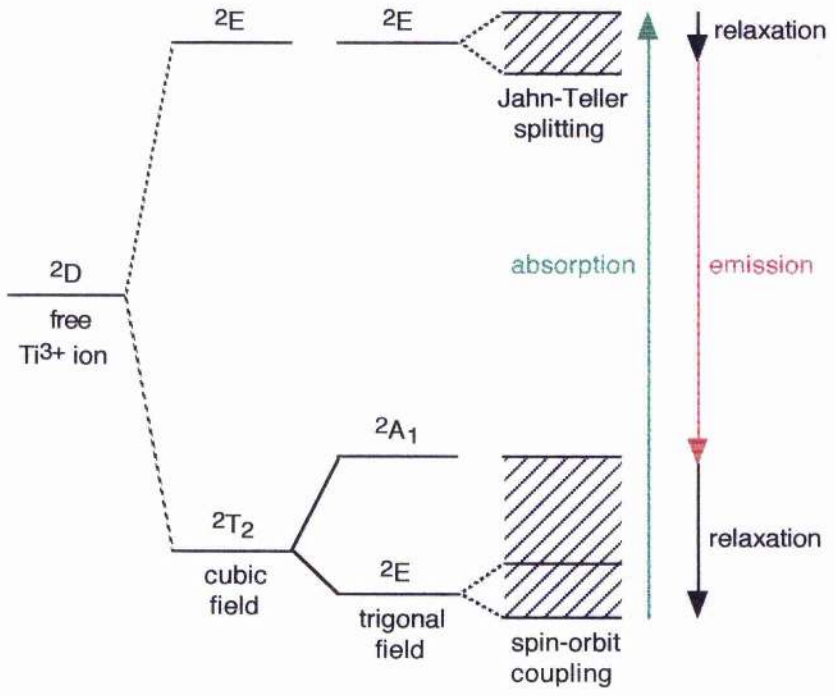

Figure 3.2 Energy level structure of Ti:sapphire, showing the optical absorption and emission bands.

Optical absorption from the $^2T_2$ to the ^2E state is centred near 500 nm, as shown in Fig. 3.3a [3]. This gives Ti:sapphire crystals their characteristic pink

colour. The π and σ polarisations indicated in the figure refer to light polarised parallel to (π) and perpendicular to (σ) the crystallographic *c*-axis. This absorption band is used for optical pumping into the excited state (upper laser level), so the much larger absorption of π-polarised light (2.3 times greater at the peak) indicates that pump light should be polarised in this direction for efficient operation of a Ti:sapphire laser. The peak wavelength of the absorption, in the blue-green spectral region, has meant that traditionally Ti:sapphire lasers have been pumped by argon-ion lasers. These lasers, while being capable of generating relatively high powers, are bulky and expensive to run, requiring a three-phase electrical supply and high pressure water cooling, so were always liable for replacement should a more practical alternative pump source become available. In recent months this has happened, with the development of high power, all-solid-state diode-pumped frequency-doubled Nd:YLF and Nd:YAG lasers, as typified by the commercially available Nd:YVO_4 Spectra-Physics *Millennia* [4], which delivers 5 or 10 W of green light at 532 nm, from a compact device powered by a single-phase electrical supply. The pumping of Ti:sapphire systems with these lasers is now becoming more common, and the demise of the argon-ion mainframe laser as a pump source is probably inevitable.

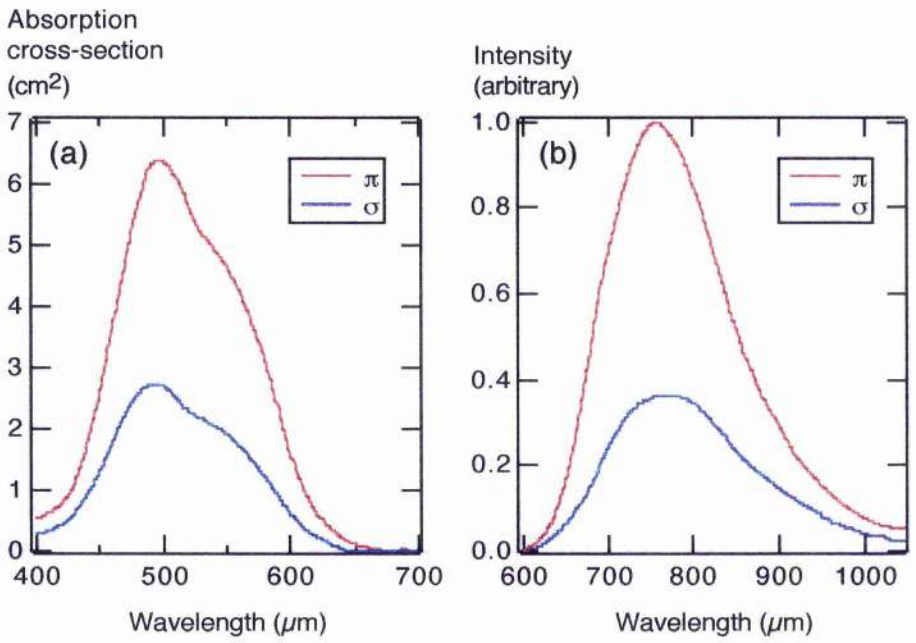

Figure 3.3 Absorption cross-section (a) and fluoresence emission spectrum (b) of Ti:sapphire [3].

The fluorescence band of Ti:sapphire resulting from blue-green pumping is shown in Fig. 3.3b [3], and covers in excess of 400 nm, with a peak at 790 nm. Thus the available tuning from a Ti:sapphire laser is extensive, and highly attractive for pump-tuning of an OPO.

Fig. 3.4 depicts the dependence of the upper-state lifetime of Ti:sapphire on temperature [5]. The reduction of lifetime with increasing temperature is due to undesirable non-radiative decay processes. Such decay is relatively modest at room temperature, and is not particularly detrimental to laser performance, so Ti:sapphire lasers require only simple, low pressure water cooling systems. A further advantage of Ti:sapphire is that the stimulated emission cross-section is large (3×10^{-19} cm^2) so that relatively short crystals can be used.

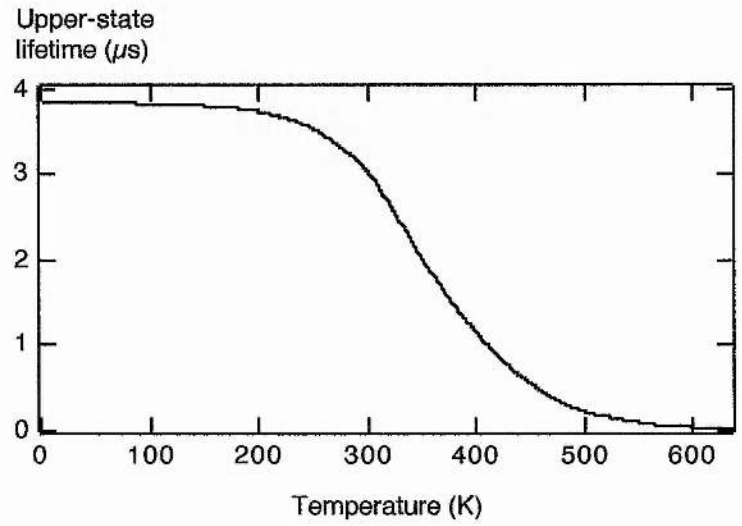

Figure 3.4 Variation with temperature of the upper-state lifetime of Ti:sapphire.

Ti:sapphire lasers are either operated as continuous wave systems, or used to generate picosecond or femtosecond pulses. A reasonably wide fluorescence bandwidth is a prerequisite for the generation of ultrashort pulses, due to the condition imposed by the time-bandwidth product $\Delta\tau_p \Delta\nu$, where $\Delta\tau_p$ is the temporal full-width half-maximum of the pulse, and $\Delta\nu$ is its frequency bandwidth. There is a lower limit on this product (see section 2.5), so that a very short pulse duration must be paired with an extended bandwidth. Ti:sapphire is therefore a near-ideal gain medium for ultrashort pulse generation; its fluorescence bandwidth is wide enough to support femtosecond pulses, and still allows significant wavelength tuning.

Ultrashort pulses are generated by the technique of modelocking, whereby the different longitudinal frequency modes of the laser are "locked" together in phase to produce a single, short pulse of highly intense radiation circulating around the laser cavity. There are numerous methods of doing this, but the only one which will be considered here is self-modelocking, since this was the technique applied to the Ti:sapphire laser used to pump the femtosecond OPOs. A detailed treatment of other types of modelocking, namely active and passive modelocking, can be found in Seigman's book, *Lasers* [6].

3.2.2 Self-modelocking

In the previous chapter, the subject of the nonlinear optical Kerr effect was introduced (Section 2.5.5). In suitable materials, having a non-zero third-order susceptibility, $\chi^{(3)}$, a sufficiently high electromagnetic field can induce a nonlinear refractive index response, such that the index, n, becomes intensity-dependent, and can be described by

$$n = n_0 + n_2 I \tag{3.1}$$

where n_0 is the linear refractive index, n_2 is the nonlinear refractive index, and I is the electromagnetic intensity. In Section 2.5.5, the Kerr effect was discussed in terms of its influence on optical parametric oscillators, via the phenomenon of self-phase modulation (SPM). This can also occur in laser gain media. The temporal profile of a laser pulse is such that the centre is more intense than the leading and trailing edges, and therefore sees an increased refractive index due to the Kerr effect. This variation of index across the pulse produces a change in phase, with a corresponding frequency shift. Thus extra spectral components are introduced, and the pulse spectrum is broadened. This is the effect of SPM, which is important in self-modelocked lasers because an increased spectral bandwidth can support shorter pulse durations.

The Kerr effect can also act in the spatial domain, where is produces the phenomenon of self-focussing. Consider a laser beam propagating through the laser gain medium. Typically, such a beam has a Gaussian spatial intensity profile, so that the centre of the beam has a higher intensity than the edges. In the presence of the Kerr effect, the centre of the beam will therefore induce a higher nonlinear refractive

index, and the phase velocity of the wavefront will be retarded more than at the edges of the beam. Thus, in effect, a weak positive lens is induced in the medium, and the beam becomes focussed, as illustrated in Fig. 3.5. This is self-focussing, and the lens is referred to as a Kerr lens.

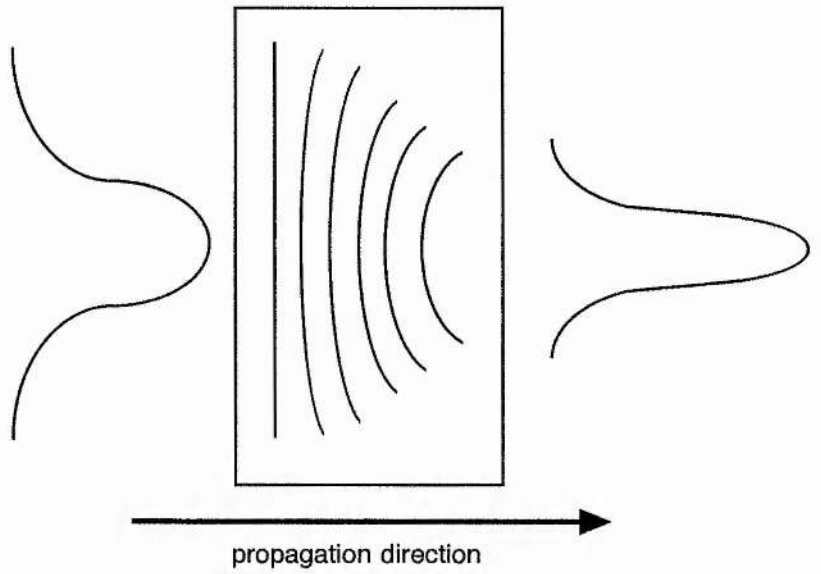

Figure 3.5 Self-focussing of an intense laser beam propagating through a Kerr medium.

The effects of self-phase modulation and self-focussing are the key processes in the self-modelocking of a solid-state laser, which was first observed in 1991 by Spence et al, in a Ti:sapphire laser generating 60 fs pulses [7, 8]. The key difference between self-modelocking and previously established modelocking techniques is the absence of an additional intracavity modelocking element; self-modelocking is due to the Kerr effect induced in the laser gain medium by the beam itself, whence comes the technique's alternative name of Kerr lens modelocking.

A laser gain medium such as Ti:sapphire has a gain bandwidth wide enough to be capable of supporting several modes of oscillation at once, between which mode beating occurs, producing self-amplitude modulation of the continuous wave (cw) laser output. This modulation can produce fluctuations, or primitive pulses, of sufficient intensity to induce the Kerr effect in the gain medium. The resulting Kerr lens and SPM modulate the spatial and spectral profile of the beam by self-focussing, thus producing a profile different from that of the cw beam. A suitable

configuration of the laser cavity elements can ensure that the modulated profile is smaller than the cw profile so that an aperture inserted into the cavity results in an increased loss for the cw beam, thus favouring pulsed operation and allowing a pulse sequence to build up. The aperture may be "hard" or "soft". Hard-aperture modelocking makes use of an actual physical aperture incorporated into one end of the laser cavity, to discriminate against the cw mode. Soft-aperture modelocking exploits the properties of the gain medium itself, whereby the cavity is configured such that the pulsed mode experiences a greater overlap with the pump beam in the laser crystal than the cw mode, and therefore experiences higher gain.

The requirement for a sufficiently intense primitive pulse to initiate the modelocked pulse sequence means that self-modelocking is generally not self-starting. In other words, pulsed operation does not spontaneously develop from cw operation. Some form of initiating action is required to produce an intense spike, be it a genuine pulse or a noise spike, which induces the Kerr lens and allows modelocked behaviour to develop. The simplest method of doing this is to tap one of the cavity mirrors, which produces a rapid variation in the length of the cavity and causes an intense amplitude fluctuation to occur. More sophisticated techniques rely on active or passive modelocking arrangements to produce long pulses sufficiently intense to induce self-focussing, thus leading to shorter pulses. Some passive methods rely on wavelength-dependent saturable absorbers so are not suitable for highly tunable lasers, whilst the common active modelocking element of an acousto-optic modulator requires the modulator to be regeneratively driven by the modelocked output to avoid conflict between the modulator frequency and the self-modelocked pulse repetition frequency determined by the length of the laser cavity.

A self-modelocked Ti:sapphire laser is an excellent pump source for femtosecond optical parametric oscillators. The absence from the laser cavity of any potentially loss-incurring modelocking elements means that maximum output power is available. In addition, the wide gain bandwidth of Ti:sapphire makes it a highly tunable gain medium, thus facilitating pump-tuning of an OPO. Mirror-tapping, and hard and soft apertures, were used very successfully to produce self-modelocked operation of the Ti:sapphire laser used here, which is described in the following section.

3.2.3 Configuration of the Ti:sapphire laser

The pump source for the femtosecond optical parametric oscillators presented in subsequent chapters was a commercial continuous-wave Ti:sapphire laser modified for self-modelocking. The original system was a Spectra Physics 3900S [4] four mirror resonator to which a number of elements were added to facilitate modelocking. Additionally, a birefringent filter used for cw tuning was removed. The resulting cavity is shown in Fig. 3.6. The modifications increased the cavity length from 0.8 m to approximately 1.75 m, so that several components lay outwith the original casing.

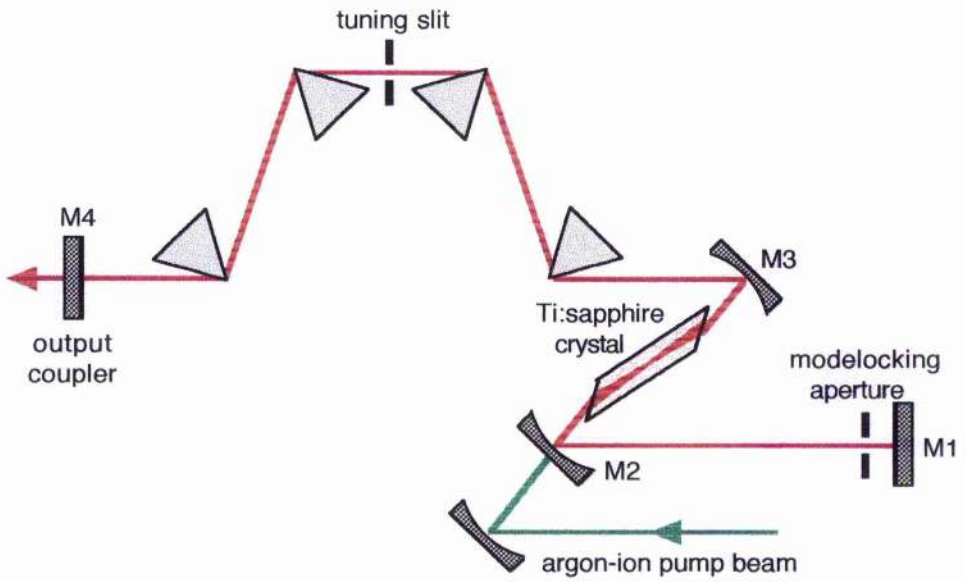

Figure 3.6 Configuration of the argon-ion-pumped self-modelocked Ti:sapphire laser used to pump the femtosecond optical parametric oscillators.

The Ti:sapphire laser was pumped with an argon-ion laser running on all lines (488 to 514 nm), in a TEM_{00} mode, and producing 15 W. After some beam steering optics the pump beam was coupled into the Ti:sapphire cavity through one of the curved mirrors, after focussing with a mirror of radius -228 mm. The two curved Ti:sapphire mirrors had radii of curvature of -100 mm; mirror M1 was a plane high reflector and mirror M4 a 20% output coupler; each was coated for broadband reflection from 750 to 900 nm. The Ti:sapphire crystal was a Brewster-cut 20 mm

long rod, cooled by a low pressure water supply.

The effects of group velocity dispersion and self-phase modulation on pulse propagation in OPOs have been discussed in Section 2.5. These phenomena also occur in ultrashort pulse lasers, leading to pulse broadening and spectral distortion which needs to be corrected. A sequence of four SF10 prisms were inserted into the Ti:sapphire laser cavity to achieve this; apex separations of 30 cm were sufficient to produce good quality transform-limited pulses. Evidence of this can be found in autocorrelation and spectral measurements presented in Section 3.2.1.

A hard aperture was positioned next to mirror M1 to facilitate modelocking. It was adjustable in the vertical direction to discriminate against the cw mode, which was typically TEM_{02}. The optimum cavity modelocking configuration could be found by altering the position of mirror M3 to change the mirror-crystal separation.

An additional aperture was placed between the second and third prisms, for tuning. At this point in the cavity, the beam was spectrally dispersed so by scanning the slit horizontally across the beam the desired spectral components could be selected.

The pulse repetition rate of a self-modelocked laser is determined by the cavity length. A single pulse circulates in the cavity, and part of it is transmitted through the output coupler each round trip, to produce a train of pulses. Given that the optical length of a cavity is nL, for $n = 1$ the pulse repetition rate, f, is related to the cavity length, L, according to

$$f = \frac{c}{2L} \tag{3.2}$$

Thus, the Ti:sapphire laser, having a cavity length of ~1.75 m, generated pulses at a repetition rate of ~83 MHz.

The laser produced average modelocked powers of between 1 and 2 W, with ~1.4 W corresponding to the most stable operation and easiest initiation of modelocking. Under these conditions modelocked operation could be sustained for several hours at a time in the absence of any external vibrations perturbing the system.

A more detailed discussion of the self-modelocked Ti:sapphire laser can be found in reference 9.

3.3 Autocorrelation

Pulse measurement by autocorrelation was carried out extensively during the research presented in this thesis, both to monitor the performance of the self-modelocked Ti:sapphire pump laser, and to characterise the pulses generated by the various optical parametric oscillators. It is therefore appropriate at this point to include a discussion of the underlying theory of autocorrelation, as it pertains to the conventional style of devices commonly used. Such devices suffer from a number of drawbacks, however, so a brief summary of alternative arrangements is given, as a preliminary to the presentation of the results relating to a novel solution to some of the problems, in the shape of using a light emitting diode to replace several standard components. This innovation led to the development of an extremely compact and inexpensive autocorrelator design, which will be discussed.

3.3.1 Theory of autocorrelation

Performing accurate measurements of the durations of ultrashort pulses produced by modelocked lasers presents a number of difficulties. Direct measurement by photodiode and oscilloscope, or by streak camera, is limited to pulse durations in the picosecond range due to inadequate electronic resolution and timing jitter problems, so when modelocking techniques led to sub-picosecond laser pulses, new measurement devices had to be developed. Techniques relying on detecting the correlation functions of pulses proved to be the answer; initially the two methods most often used were second harmonic generation (SHG) autocorrelation, and two-photon-fluorescence. The latter method enjoyed the most popularity with flashlamp-pumped modelocked lasers, because a measurement can be made on a single pulse, whereas the SHG method, first proposed in 1967 [10], requires a train of pulses, which was difficult to produce from early modelocked lasers. However, as the modelocking of continuous wave lasers became more advanced, pulse trains were more easily generated and the SHG autocorrelator came into its own.

Correlation functions can be classified in a number of ways, one of which is the distinction between *cross* correlation, where two or more separate signals are

correlated, and *auto*correlation, where two or more replicas (formed by splitting a pulse into equal parts) of a single pulse are used. The number of pulses correlated indicates the order of the correlation. In pulse measurement, it is usual to divide the intensity of a single pulse into two halves and correlate them, so the method therefore uses second order autocorrelation. The correlation, or overlap, of the pulses is designed to occur within a nonlinear crystal. The high intensities of ultrashort pulses are sufficient to produce nonlinear effects, and the crystal is chosen so that second harmonic generation takes place. The amount of second harmonic produced depends on how much the pulses overlap, ie. the level of correlation. The second harmonic is detected with a photomultiplier tube and the resulting electronic signal is displayed on an oscilloscope as a function of the overlap; this is the output of the autocorrelator. The width of the autocorrelation is related to the temporal extent of the original pulse, so pulse durations can be deduced.

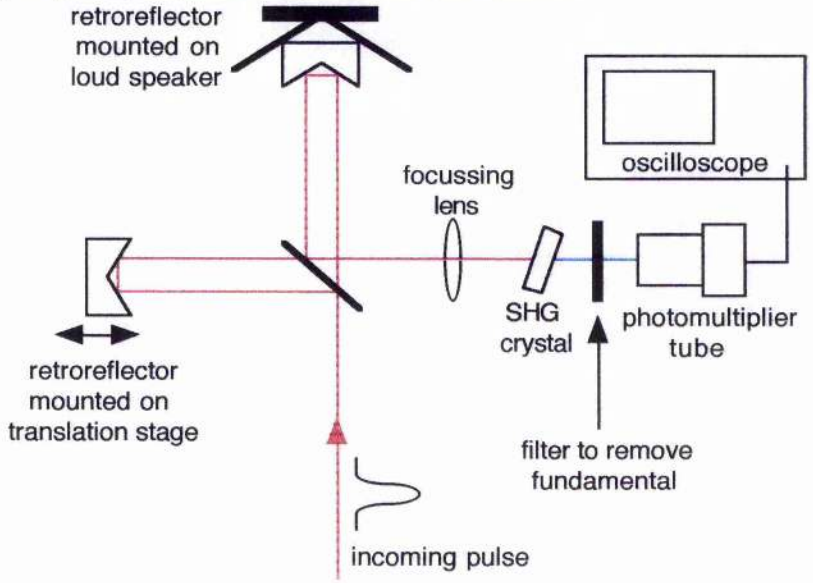

Figure 3.7 Configuration of a typical second harmonic generation autocorrelator.

A typical autocorrelator is shown in Fig. 3.7. The incoming pulse intensity is divided in two by a beam splitter; one part propagates to a retroreflector on a translation stage, the other to a retroreflector mounted on a loud speaker. They return to the beam splitter and are focused into the nonlinear crystal. The second harmonic output is detected by a suitable photomultiplier tube, and displayed on an

oscilloscope. The loud speaker operates at (typically) 20Hz, and the movement of it varies the overlap between the pulses. As the speaker moves in and out the path length for the second half of the pulse is changed, so a delay is introduced into its arrival time at the crystal. When the path lengths for the two pulses are equal, the pulses will exactly coincide at the crystal and the amount of second harmonic will be a maximum, but as the speaker increases and decreases the delay, the amount will drop. The speaker frequency is much less than the pulse repetition frequency, so the autocorrelation trace is made up from the second harmonic produced by many pulses, each subject to a different delay time.

Second harmonic generation is the nonlinear effect of choice for autocorrelation because it generally has a high conversion efficiency in crystals that are reasonably inexpensive and readily available. However, one drawback is that the demand for phase-matching puts a limit on the bandwidth of the fundamental for which SHG occurs; hence different crystals are needed for different pulse spectral bands. There is also the problem of Poynting vector walk-off, which can limit the thickness of crystal which can be used. Consideration of phase-matching also relates to a further distinction between types of correlation – the presence or absence of a background signal. Autocorrelations free from background can be obtained in one of two ways, both of which rely on the fact that under certain phase-matching geometries, SHG will only occur when both pulses are present in the crystal. Thus, when there is no pulse overlap, ie. a time delay above a certain limit, no second harmonic is produced so the output is zero. The two methods for achieving this are either to introduce polarising elements into the autocorrelator and chose a geometry such that phase-matching requires the two pulses to be orthogonally polarised and propagated collinearly, or alternatively, to have the pulses with parallel polarisation but propagating non-collinearly, with the second harmonic produced in a third direction. However, if a phase matching geometry is chosen such that the pulses are collinear and have parallel polarisation, SHG will occur for a single pulse as well as for two. Thus the autocorrelation signal has a background level produced by the small amount of second harmonic generated from one pulse, and a peak corresponding to the larger level of generation when the pulses overlap. One advantage of this method is that the ratio of the peak to the background – the so-called contrast ratio – for perfect modelocking is well-defined, so the laser system may easily be adjusted for optimum performance.

The final, and most important, distinction between types of autocorrelation used for pulse measurement is that between intensity and interferometric autocorrelations, sometimes called slow and fast respectively. In mathematical terms, the second-order autocorrelation function in terms of the delay between pulses, τ, for a pulse with a time-varying electric field $E(t)$, and a background level, is

$$g_2(\tau) = 1 + \frac{2\int_{-\infty}^{\infty} E^3(t)E(t+\tau)\mathrm{d}t + 2\int_{-\infty}^{\infty} E(t)E^3(t+\tau)\mathrm{d}t + 3\int_{-\infty}^{\infty} E^2(t)E^2(t+\tau)\mathrm{d}t}{\int_{-\infty}^{\infty} E^4(t)\mathrm{d}t} \tag{3.3}$$

If the electric field E(t) is described by

$$E(t) = \xi(t)[\cos\omega t + \phi(t)] \tag{3.4}$$

then $g_2(\tau)$ contains information arising from the phase variation with time within the pulse. However, if the response of the autocorrelator, determined by the photomultiplier tube and the oscilloscope, is slow compared to the duration of one optical cycle, this information cannot be resolved, and the output is limited to the time-average of $g_2(\tau)$, which can be shown to be

$$G_2(\tau) = 1 + \frac{2\int_{-\infty}^{\infty} E^2(t)E^2(t+\tau)\mathrm{d}t}{\int_{-\infty}^{\infty} E^4(t)\mathrm{d}t} \tag{3.5}$$

and contains no phase information. This output is called an intensity autocorrelation. Faster devices capable of resolving the phase information according to Equation 3.3 produce interferometric or fringe-resolved autocorrelations. The two types of autocorrelation provide different information about pulses, and when combined with information from spectrum analysis, can reveal much detail about a pulse. An intensity autocorrelation is obviously easier to measure, but since it contains no phase information it does not reveal whether or not a pulse is chirped. Information regarding chirp is present in an interferometric autocorrelation; the presence of chirp distorts the autocorrelation to a greater or lesser degree, depending on its level, although only qualitative phase information can be extracted. The presence of

satellite pulses and noise is also evident in autocorrelations, so they are useful for more than just pulse duration measurements. Examples of computer generated interferometric autocorrelations of hyperbolic secant pulses are given in Fig. 3.8, and illustrate the increasing distortion which arises from chirp.

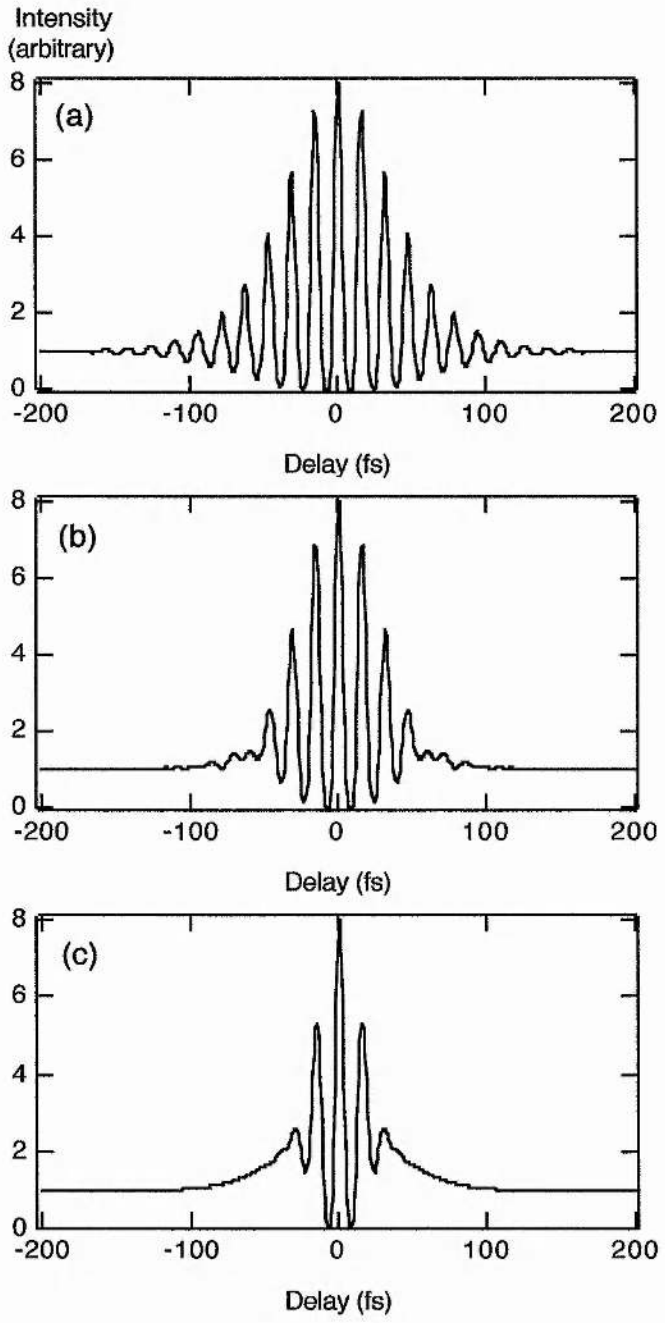

Figure 3.8 Computer-generated interferometric autocorrelations of a chirp-free pulse (a), and pulses with increasing amounts of chirp (b), (c). All pulses have the same temporal full-width half-maximum

As previously mentioned, the contrast ratio between peak and background is well-defined, and the value of this ratio for the two autocorrelation types is obvious from examination of Equations 3.3 and 3.5. In both cases, as τ becomes large, ie. there is a large delay between the pulses, and consequently SHG from one pulse only, the integrals involving τ approach zero so in both cases a background level of unity remains. On the other hand, for exact pulse overlap, and therefore maximum SHG, τ is zero. Consequently, in both equations each numerator integral is equal to the denominator integral, so we obtain total peak values of 8 and 3. Thus the contrast ratios are 8:1 for an interferometric autocorrelation, and 3:1 for an intensity autocorrelation. These values only apply to second-order autocorrelations. More general expressions are available to calculate the contrast ratios for higher order autocorrelations. For example, the ratio, *CR*, for an interferometric autocorrelation of order n is given by

$$CR(g_2) = n^{2n-1} \tag{3.6}$$

which evaluates to 8 for $n = 2$, in agreement with Equation 3.3 for $\tau = 0$. The contrast ratios for both types of autocorrelation increase rapidly with n. Ratios given by these equations are only valid for pulses with smoothly varying envelopes and phase variations; the situation is more complex for noise or pulses with substructure.

The rationale behind using autocorrelation techniques for the measurement of ultrashort pulses lies in the fact that an unmeasurably short time span is converted into a measurable distance. For example, a 100 fs pulse is 30 μm long, a length which can easily be measured on a micrometer. Since the autocorrelation trace represents the overlap between two pulses in space, which is varied by altering the time at which each pulse reaches a specified point, the two quantities of space and time become related via the constant of the speed of light. The first step in measuring a pulse duration is to calibrate the oscilloscope trace displaying the autocorrelation in terms of time. As mentioned, one of the retroreflectors in the autocorrelator is usually on a translation stage. The calibration is done by moving the reflector through a certain distance and noting how far across the screen the autocorrelation is shifted. This gives a calibration in terms of distance per screen division, which is converted to time per division by dividing by the speed of light. Thus the time width of the autocorrelation can be measured directly from the oscilloscope trace.

The full-width half-maximum of an autocorrelation, τ_{ac}, is related to the full-

width half-maximum of the original pulses, τ_p, by a constant, K, such that

$$\tau_p = \frac{\tau_{ac}}{K} \tag{3.7}$$

The value of K depends on the pulse shape. Unfortunately, the pulse shape is not obvious from the autocorrelation shape; for example, SHG autocorrelations are always symmetric functions, even when the pulses producing them are not. For this reason, if the pulse shape is not somehow known already, it is necessary to assume a pulse shape, and apply it to the data in the hope that it will fit established models. The quantity K is well-known for several common pulse shapes, as shown in Table 3.1, so a likely K value can be chosen and used to calculate the pulse width. Intensity autocorrelations are more accurate indicators of pulse width, because they are not liable to distortion by chirp, and should therefore be used where possible. The computer-generated autocorrelations of Fig. 3.8 indicate the problem arising from chirped interferometric autocorrelations; each of these was calculated for the same pulse duration, but have dramatically different widths.

Intensity profile	**Interferometric**	**Intensity**	**Time-bandwidth product**
	$\Delta\tau_{g(t)}/\Delta\tau_p$	$\Delta\tau_{G(t)}/\Delta\tau_p$	$\Delta\tau_p\Delta\nu_p$
Gaussian	1.697	1.414	0.441
$\text{sech}^2(t)$	1.897	1.543	0.315

Table 3.1 Constants relating full width-half-maximum pulse durations to the full-width half-maxima of intensity and interferometric autocorrelations, for different temporal intensity profiles.

Experimental SHG autocorrelations from the self-modelocked Ti:sapphire laser described earlier are presented in Fig. 3.9, with an accompanying spectrum. Assuming a $\text{sech}^2(t)$ pulse profile, the intensity autocorrelation implies a pulse width of 136 fs. This is in good agreement with that inferred from the interferometric autocorrelation, which indicates that the pulses were essentially chirp-free. This is confirmed by the time-bandwidth product of 0.36, which is close to the bandwidth limit for $\text{sech}^2(t)$ pulses. The Ti:sapphire laser typically produced pulses shorter than this (~80 fs), so these results suggest that the cavity was not optimally configured at the time when the measurements were made.

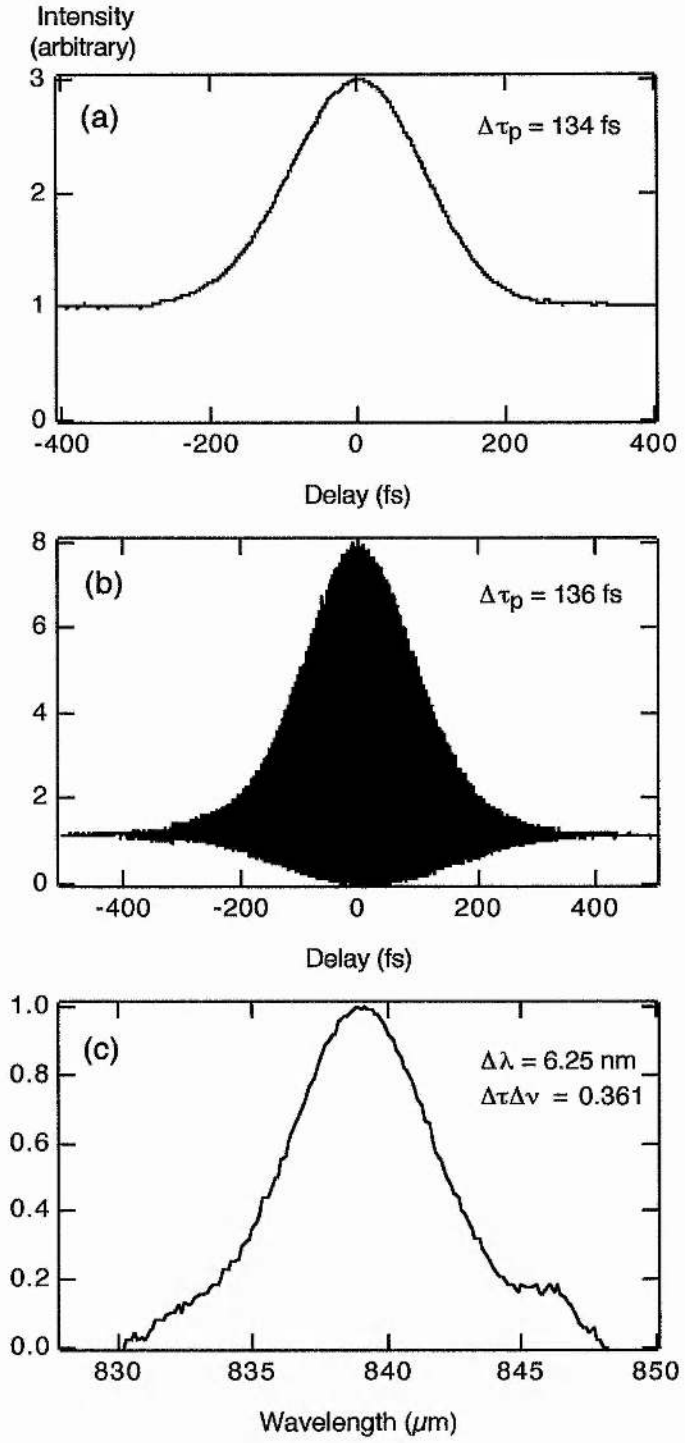

Figure 3.9 Intensity autocorrelation (a), interferometric autocorrelation (b) and spectrum (c) of pulses from self-modelocked Ti:sapphire laser. The good agreement between the pulse durations inferred from the two autocorrelations indicates that the pulses were essentially free from frequency-chirp.This is confirmed by the value of the time-bandwidth product.

3.3.2 Review of autocorrelation techniques

The second harmonic generation autocorrelator described in the previous section is a very widely used tool, and forms the basis of many commercially-available devices. The method has its drawbacks, though, and is not well-suited to all of the many ultrashort pulse systems currently in existence. The principal problem lies in the use of frequency doubling in a nonlinear crystal. Appropriate crystals are simply not available for the ultra-violet and mid-infrared wavelengths, and even in the remaining part of the spectrum, where SHG autocorrelators generally work well, there are disadvantages. The useful thickness of the crystal is limited by the effects of temporal walk-away and Poynting vector walk-off, leading to low conversion efficiencies. Additionally, the crystal must be thin to prevent dispersive broadening of the pulses being measured. The phasematching properties and spectral bandwidth of any particular nonlinear material make it suitable for only a specific wavelength range, so separate crystals are needed for different laser systems.

Detection of the second harmonic signal by a photomultiplier tube is far from ideal, but often necessary. Only a small portion of a laser's power output will be devoted to pulse diagnostics, so for a low power system, the input beam to the autocorrelator can be very weak. This, combined with the low conversion in a thin crystal, can result in a signal that is too low for accurate detection by a photodiode, so a photomultiplier tube has to be employed. The photomultiplier tubes are bulky, relatively expensive, require a high voltage power supply, and are very sensitive to ambient light so have to be carefully enclosed, none of which are desirable characterisitics.

The Michelson-type delay-line part of an autocorrelator can be of a considerable size as well, particularly if built in-house from standard components. This, of course, may not be a problem, but in the current climate of pulsed laser miniaturisation, by diode-pumping and the like, it surely defeats the purpose to have to use a bulky autocorrelator to monitor the laser output. Hence there is also the possibility of improving autocorrelators by reducing their size, perhaps leading to portable devices.

Research relating to the development and improvement of autocorrelators is regularly published, describing a myriad of potential solutions to the problems outlined above. An extensive review of this is not necessary here, but a brief

summary will be given, to place into context the experimental work relating to the light emitting diode and photodiode, which will be discussed later.

Potential improvements to the interferometer section of autocorrelators tend to centre on alternative scanning methods to provide the delay, generally by replacing the linear motion of a loud-speaker with rotational motion. A prism rotating on a wheel has been suggested [11, 12]. This gives sufficient delay for picosecond pulses, but the amount of glass involved makes it unsuitable for very short femtosecond pulses, because of pulse broadening by dispersion. A better arrangement from that respect is a pair of parallel spinning mirrors [13], the available delay from which is determined by the mirror size and separation. However, the state of the art in terms of miniaturisation of the interferometer is a surface-micromachined device, recently reported by Su et al [14]. They have machined the surface of a single silicon chip to produce an autocorrelator (minus detection) only 4 mm by 4.5 mm in size, complete with six mirrors, two beam splitters, and a moveable plate to produce the delay.

The ideal replacement for the frequency-doubling crystal would be a material producing a suitable nonlinear effect which did not require phasematching and would therefore be suitable for many wavelengths, in a small enough volume to minimise dispersion yet still maintaining efficiency. Surface second harmonic generation in metals [15] and semiconductors [16] is one solution. A surface effect by its very nature only uses a small volume (ultraviolet penetration of 10 nm has been observed in silicon [16]), so no phasematching is required, and no dispersion occurs. Cross-correlations can be conducted in a similar way, using surface sum-frequency mixing [17]. An intriguing possibility has been demonstrated by Bouevitch et al [18], who showed that thin films of bacteriorhodopsin were efficient at second harmonic generation at yellow to near-infrared wavelengths and could offer a low dispersion and inexpensive alternative to nonlinear crystals. Nonlinear effects are of course not limited to frequency mixing, which suggests that there might be suitable techniques for the autocorrelation of ultraviolet wavelengths, for which there are no frequency-doubling crystals. One solution is the use of two-photon absorption in diamond, as demonstrated by Dadap et al [19] who successfully measured femtosecond pulses at 310 nm by intensity autocorrelation. Another alternative to frequency doubling is to turn to third-order nonlinear effects like the Kerr effect. Sheik-Bahae has recently demonstrated autocorrelation of femtosecond Ti:sapphire pulses using a Kerr lens in zinc sulphide [20]. Two-photon absorption must be avoided in this situation, so the

lens material bandgap must be suitably large.

The drawbacks of photomultipliers as the detection device in autocorrelators have already been pointed out. An alternative for low power measurements has been suggested by Miyamoto et al [21], who used photon-counting detectors to record the signal from each arm of a Michelson delay line and measured autocorrelations via two-photon interference. This provides excellent time resolution, has no wavelength dependence, and the counting of individual photons means that the technique is even applicable to the monitoring of spontaneous fluorescence. It is, however, very slow.

It is possible to radically improve an autocorrelator by combining the nonlinearity and the detection in a single component, which can remove many of the problems. Early schemes for doing this relied on waveguides [22, 23] fabricated from, for example, GaAs/AlGaAs. The incoming pulses undergo two-photon absorption (in place of SHG in a nonlinear crystal) and the resulting conductivity is then detected in the same device if it is suitably biased. Two-photon absorption is relatively wavelength-insensitive, as long as two photons have sufficient energy to bridge the bandgap, and a waveguide is good for optical integration, but the length of a waveguide can lead to dispersion, so these devices are best suited to picosecond pulses. Femtosecond autocorrelation via two-photon absorption has been recently demonstrated in a zinc selenide photoconductive switch [24]. This material is suitable for wavelengths from 480 to 950 nm, and the small dimensions of a switch eliminate the dispersion problems found in waveguides. A further possibility is the use of quantum well devices. An unbiased GaAs/GaAlAs device has been used to measure picosecond pulses at 10.6 μm from a carbon dioxide laser, by exploiting two-photon quantum well ionisation [25]. The device required liquid nitrogen cooling, but nonetheless could prove useful, as the long wavelength of carbon dioxide laser pulses makes them notoriously difficult to characterise by autocorrelation.

Combining the nonlinearity and the detection of an autocorrelator into a single semiconductor component is very advantageous. Phasematching and dispersion problems can be avoided, allowing the measurement of a wide spectral range of femtosecond pulses. Elimination of the photomultiplier removes the need for a high voltage power supply, and the overall size of a correlator can be significantly reduced. However, the methods described in the previous paragraph all rely on specialist semiconductor devices, which require careful growth and engineering and can therefore be costly. If the same effects could be achieved in less elaborate

devices, the total cost of an autocorrelator could be considerably reduced. We have shown that simple light-emitting diodes and photodetectors are just as effective as switches and quantum wells, and can produce high quality interferometric autocorrelation traces. This subject will be addressed in the following section.

3.3.3 Light-emitting diodes for autocorrelation

The inspiration for using a light-emitting diode (LED) to replace the nonlinear crystal and detector in an autocorrelator came from a chance discovery which occurred during attempts to make autocorrelation measurements of 3.5 μm idler pulses generated by a KTA-based OPO (described in Chapter 4). Photomultipliers have a long wavelength cut-off at about 1 μm, so are unsuitable for the correlation of wavelengths much beyond 2 μm. An InGaAs photodiode was therefore used to measure the OPO pulses, in conjunction with a $LiNbO_3$ frequency doubling crystal. A rather poor autocorrelation trace was obtained, so in an effort to improve this, the crystal was removed to facilitate realignment of the correlator. However, the trace remained on the oscilloscope screen, and even improved somewhat, indicating that the $LiNbO_3$ had been contributing nothing to the process, and that the nonlinearity was occurring in the photodiode. High quality fringe-resolved autocorrelations of mid-infrared femtosecond pulses were obtained in this way (see Section 4.5.5), representing the longest wavelengths to be thus characterised at that time.

The excellent results obtained with the InGaAs detector suggested that similar success could be had with alternative photodiodes (as has subsequently been shown by Barry et al, who used a silicon photodiode to measure 1.5 μm pulses [26]), or, more interestingly, with LEDs, since an LED is, in effect, merely a photodiode in reverse, and should behave as a detector if suitably connected. This proved to be the case.

Fig. 3.10 shows the basic structure of an LED. The active semiconductor structure sits in a small metal cup, which reflects the emitted photons in the forward direction. The diode is connected to the other electrode via a fine bond wire, and the whole is encased in a plastic dome. The plastic needs to be removed down as close to the wire as possible for an autocorrelator; this allows maximum transmission of the pulses to the diode, and reduces group velocity dispersion.

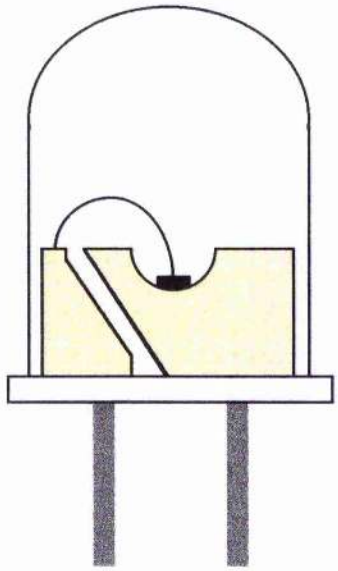

Figure 3.10 Basic structure of a light-emitting diode in its casing.

A double-heterostructure ultrahigh brightness AlGaAs LED [27] was selected for the autocorrelator experiments. Fig. 3.11 illustrates the difference between a standard LED and a high brightness LED, and shows that a standard device is not suitable for this application, because the incoming light would have to propagate through a layer of GaAs to reach the active region, and would suffer absorption. This layer is not present in a high brightness device.

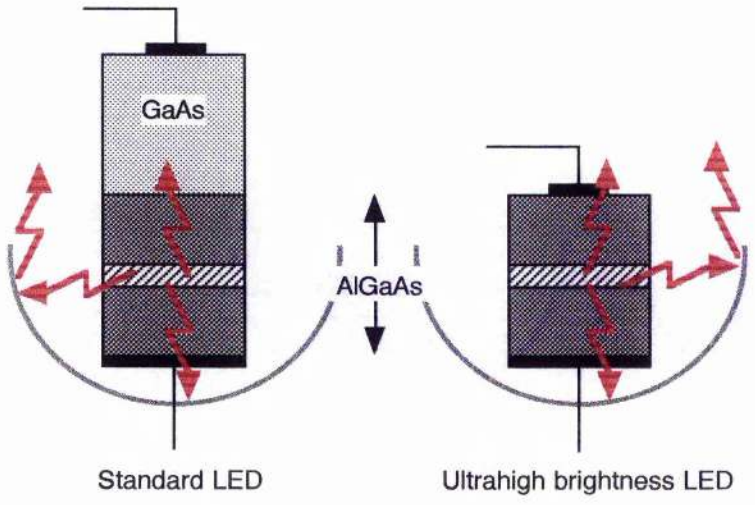

Figure 3.11 Structures of a standard AlGaAs LED and an ultrahigh brightness AlGaAs LED.

The choice of diode material is of crucial importance. The bandgap energy must be sufficiently large to prevent direct absorption of the pulse photons, otherwise no nonlinear response will be seen. The bandgap energy is roughly equivalent to the photon energy of the peak emission wavelength of the LED, so the wavelength to be correlated must be longer than the specified emission wavelength. The AlGaAs LED selected had a peak wavelength of 660 nm, so was entirely suitable for measuring Ti:sapphire pulses, for example. It was prepared for use by cutting off the front of the plastic casing, and polishing the resulting surface to obtain a suitably smooth and flat face. The electrodes were joined in unbiased mode to a coaxial cable connector, to allow direct connection to an oscilloscope.

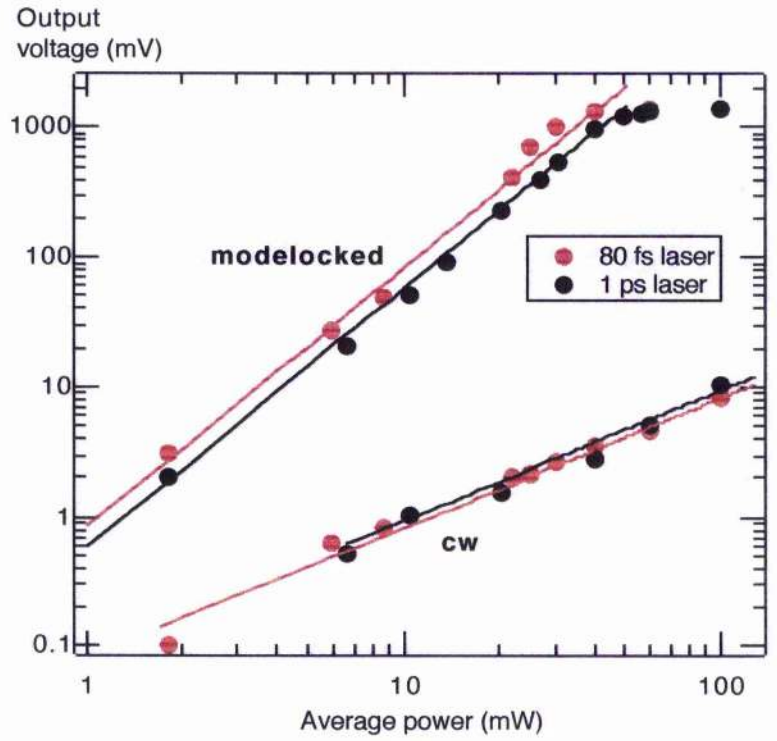

Figure 3.12 Response of the ultrahigh brightness LED, showing the variation of output voltage with incident average power, for femtosecond and picosecond pulses, and continuous wave outputs from same lasers.

A preliminary characterisation of the LED was carried out to determine its response to continuous wave and modelocked laser outputs. Two Ti:sapphire lasers were used to do this, with pulse durations of 80 fs and 1 ps. Both had pulse repetition rates close to 80 MHz. The light was focussed onto the LED using a microscope objective of 15 mm focal length. The incident optical power was

attenuated using a neutral density wheel, and the output voltage of the LED was recorded for various values of input power. This was done with each laser operating as a pulsed and as a continuous wave source. The results are presented in Fig. 3.12. The continuous wave measurements showed a weak and linear response of voltage with power, which can be attributed to very inefficient residual direct detection of the 800 nm photons. However, the increased intensity of the modelocked pulses induced a quadratic response, as would be expected for a second order process such as second harmonic generation or two-photon absorption. This indicated that the LED would be suitable for use in an autocorrelator. The response to modelocked power was approximately two orders of magnitude greater than to continuous wave power. The almost equal response to picosecond and femtosecond pulses was unexpected, given the much greater intensity of the femtosecond pulses. A possible explanation for this is that the femtosecond pulses created a higher carrier density in the diode, leading to more recombination, so that the overall number of carriers contributing to the photocurrent was of the same order for both pulse durations.

Following this successful test, the LED was incorporated into an autocorrelator similar to that shown in Fig. 3.7, with a loud speaker to provide the delay scanning, and the 15 mm microscope objective to focus the recombined beams onto the LED. This arrangement was used to obtain interferometric autocorrelations of the outputs of several different pulsed sources, examples of which are given in Fig. 3.13. The trace in Fig. 3.13b was obtained from the self-modelocked Ti:sapphire laser described earlier, running at a wavelength of ~800 nm. A pulse duration of 85 fs can be inferred if a $\mathrm{sech}^2(t)$ pulse shape is assumed. For comparison, Fig. 3.13a shows an autocorrelation of pulses from the same laser recorded using a nonlinear crystal and a photomultiplier tube, which implies an 81 fs pulse duration. It can be seen from this that the LED produced autocorrelations of as good quality as the more conventional method. The slight chirp evident on the LED trace is due to the fact that the measurement was made on a beam extracted from the opposite end of the laser cavity to that shown in Fig. 3.13a, which had experienced an additional pass through the intracavity laser optics. To demonstrate the broadband nature of the LED response, Fig. 3.13c shows an autocorrelation of femtosecond pulses at ~1.3 μm generated by an OPO.

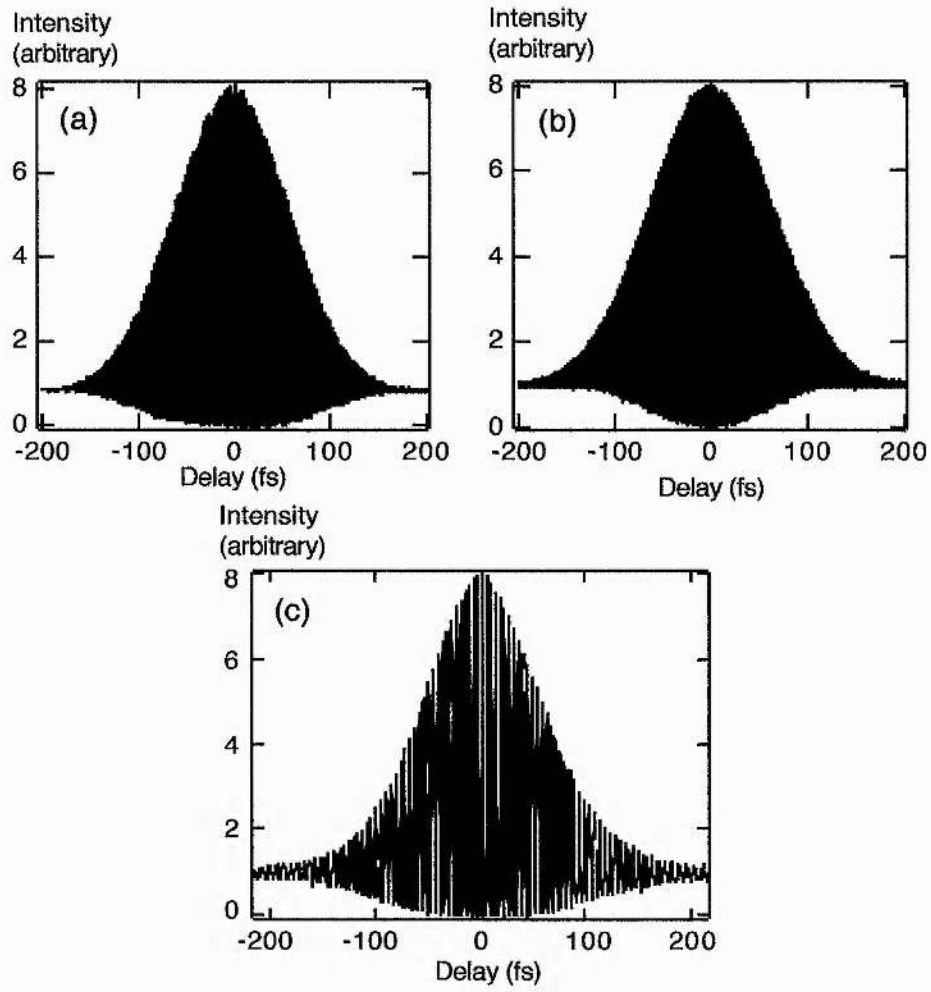

Figure 3.13 Interferometric autocorrelation traces of laser and OPO pulses. (b) shows an autocorrelation of pulses from the Ti:sapphire laser measured with the AlGaAs LED ($\Delta\tau_p$ = 85 fs), which should be compard with (a), which shows an autocorrelation of the same pulsed ouput measured with a conventional autocorrelator ($\Delta\tau_p$ = 81 fs). (c) shows an autocorrelation recorded with the LED of pulses at 1.3 μm generated from an RTA-based OPO ($\Delta\tau_p$ = fs).

It is evident from Fig. 3.13 that an unbiased LED works well as an alternative to a frequency-doubling crystal and photomultiplier. However, the exact mechanism of the nonlinear effect in LEDs and photodiodes has not as yet been fully established, and could either be second harmonic generation or two-photon absorption. Both of these are second order effects so would result in the quadratic response necessary for autocorrelation. Second harmonic generation can obviously not be phasematched, but the nonlinearity of bulk GaAs is so large (~90 pm/V) that sufficient SHG could occur over a single coherence length. The frequency-doubled photons would then be absorbed in the usual way, producing a photocurrent. The

wavelength limits for this process would be determined by the bandgap energy E_g. The lowest energy second harmonic photons that could be detected would require energy equal to E_g, and would therefore be generated from pulses with photons of energy $E_g/2$. At the other end of the scale, ~E_g is the maximum fundamental photon energy allowed to avoid direct detection. Thus SHG in a semiconductor device is limited to the measurement of pulses with photon energies between $E_g/2$ and E_g, or in terms of wavelength. between $\lambda = hc/E_g$ and $\lambda = 2hc/E_g$.

Two-photon absorption would work to convert the optical signal at the fundamental wavelength directly into the photocurrent. The process, which is a nonresonant nonlinear effect only observed at high light intensities, works by an electron in the valence band of a semiconductor absorbing two incident photons to acquire enough energy for promotion to the conduction band. Thus the photons must have a minimum energy of half the bandgap energy, so that two could move an electron from the very top of the valence band to the lowest level of the conduction band. Photons with more energy could excite electrons between other levels in the two bands, up to photons with energy equal to the bandgap, which would be absorbed directly. Thus the same wavelength limits apply to two-photon absorption as to second harmonic generation. For the AlGaAs LED, the emission peak at 660 nm corresponds to a bandgap energy of 1.878 eV, and indicates that the LED could correlate pulses from 660 nm to 1320 nm. Much of this range was demonstrated experimentally as shown in Fig. 3.13.

In my view, two photon absorption is more likely to be the nonlinearity at work in the LED and photodiode, given that it is the proven mechanism in so many related semiconductor devices, such as waveguide autocorrelators [22, 23]. However, knowledge of the exact nature of the nonlinear mechanism is interesting from a fundamental physical viewpoint, but it is largely irrelevant in terms of device application and usage, since the two possible processes have the same limitations and produce the same end result. Thus the numerous advantages of using an LED or a photodiode in an autocorrelator are still the same regardless of the underlying cause, and for most practical purposes it is the advantages which are important. Many advantages are in common with those of the other semiconductor devices discussed, but what is perhaps the most attractive advantage is unique to LEDs. This is the cost – the AlGaAs LED used here was purchased for a mere £1.75, which is orders of magnitude cheaper than a nonlinear crystal and a photomultiplier tube with

accompanying power supply. LEDs and photodiodes are also readily available from numerous commercial suppliers, and they are robust and compact. The very broad wavelength response makes the device applicable to many pulsed sources, and the lack of phasematching means that no tuning is required for different sources. Alignment of an autocorrelator is greatly simplified, both in terms of tuning and because there is no requirement to couple the light into an additional detector. The small volume of material involved eliminates dispersive pulse broadening, making these devices potentially suitable for the autocorrelation of sub-10 fs sources currently attracting so much research interest. And finally, low input powers can be used; the AlGaAs LED generated good quality autocorrelations from incident average powers as low as 350 μW. Hence, LEDs and photodiodes can be successfully used to characterise the outputs of a wide range of ultrashort pulse lasers and OPOs, with the minimum of expense and effort.

3.3.4 The Wollaston prism autocorrelator

The very small size of an LED, compared to a doubling crystal, photomultiplier tube and power supply, gives tremendous impetus to the ideal of miniaturising an autocorrelator. To take this further, it is necessary to reduce the size of the interferometer section, which is done most readily be replacing the traditional loud speaker with some other means of providing a temporal delay. Recent research has been reported on the development of a compact Fourier-transform spectrometer in which a Michelson-type of delay-line was replaced by a polarising interferometer based on a Wollaston prism [28]. It was decided to adopt a similar approach here, and a compact, unidirectional autocorrelator was developed as a result.

A Wollaston prism comprises two wedges of birefringent material, joined by their hypotenuses (Fig. 3.14). The wedges are oriented so that their optic axes are perpendicular to each other, and parallel to the entrance and exit faces of the prism. The effect of this on an incident beam of light is that ordinarily and extraodinarily polarised rays experience a different change in refractive index at the interface between the wedges, and hence are refracted differently, and leave the prism with an angular separation. This behaviour leads to the use of Wollaston prisms as polarising beam splitters. The angle of separation, or splitting angle, α, is given by [29]

$$\alpha = 2(n_e - n_o)\tan\theta \tag{3.8}$$

where n_o and n_e are the ordinary and extraordinary refractive indices of the prism material, and θ is the wedge angle.

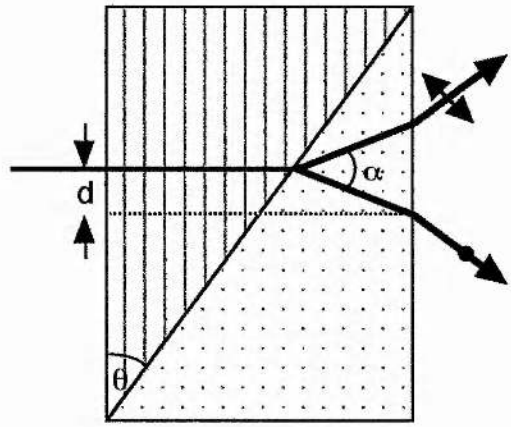

Figure 3.14 Wollaston prism, showing the beam splitting effect at the interface between the wedges, which have orthogonal optic axes.

The orientation of the optic axes in the two wedges is such that a beam which is ordinary in the first wedge becomes extraordinary in the second, and vice versa. Thus there is an optical path difference, Δ, between two orthogonal beams propagating through the prism, which varies with position along the prism due to the varying relative thickness of the wedges. This can be shown to be [29]

$$\Delta = 2d(n_e - n_o)\tan\theta \tag{3.9}$$

where d is the displacement from the centre of the prism, at which point the wedges are of equal thickness so there is no path difference. This path difference means that a Wollaston prism introduces a temporal delay between the two polarisation components of an incident ultrashort pulse, and this delay can be varied by scanning the prism across the incident beam. This is precisely the effect needed for autocorrelation, such that a Wollaston prism can replace the components of a Michelson delay-line in an autocorrelator.

The prism used here was made of quartz, with a wedge angle of 26° and a length of 20 mm. The birefringence (n_e - n_o) of quartz at 800 nm is approximately 0.0089 [30], so using the above dimensions in Equation 3.9 gives a change in path

length across the whole prism of ±87 μm, corresponding to a maximum available delay of approximately ±300 fs. This is perfectly adequate for the measurement of 100 fs pulses. Different amounts of delay may be readily attained by using larger or smaller prisms, and different prism materials, such a calcite or magnesium fluoride.

The autocorrelator was configured as shown in Fig. 3.15. A polariser was used to polarise the incident beam at 45° to the optic axes of the prism so that ordinary and extraordinary components would be present. The beam was then focussed into the prism with a 30 mm focal length lens to produce a spot size of 40 μm. To obtain full resolution of the fringes of an interferometric autocorrelation, the delay introduced across the beam due to its physical dimension must not exceed one-half of the wavelength. For 800 nm pulses a 40 μm spot size is sufficiently small. On exiting the prism, the two spatially separated and orthogonally polarised components were collimated by a second 30 mm focal length lens, and then passed through a further polariser to select a common 45° polarisation component to allow the necessary interference between the beams. Finally, a 15 mm microscope objective focussed the two beams on to the same place on the LED. The Wollaston prism was mounted on a translation stage driven by an electromagnetic actuator to scan it continuously across the incident beam. An electronic trigger signal was taken from the actuator to maintain synchronism between the prism motion and the oscilloscope trace displaying the LED output.

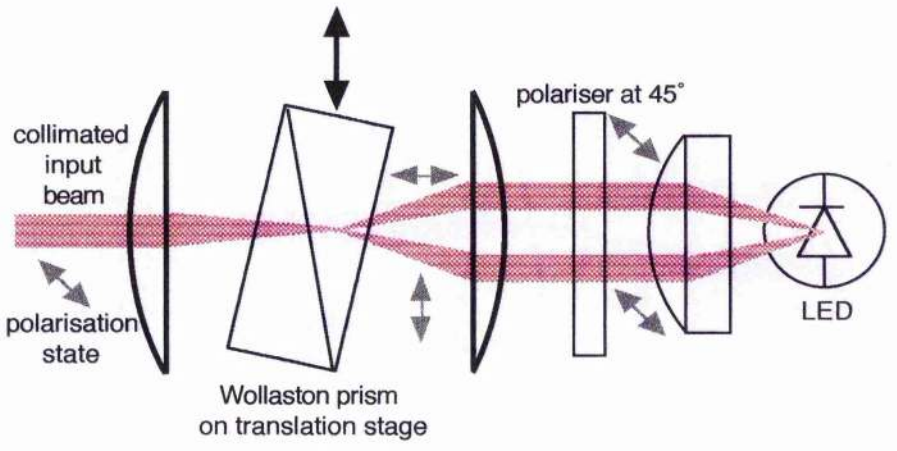

Figure 3.15 Configuration of the Wollaston prism and LED autocorrelator.

Note that in Fig. 3.15 the Wollaston prism is portrayed as being angled with respect to the incident beam. This was to compensate for the fact that the

polarisation components are refracted at both the interface and the exit face of a Wollaston prism. On leaving the prism, the two beams therefore appear to have split at a plane which can be shown to lie halfway between the interface and the exit face, as illustrated in Fig. 3.16. In the correlator, this plane was set normal to the beam propagation direction so that the two beams could be properly collimated by the second lens for all positions of the prism.

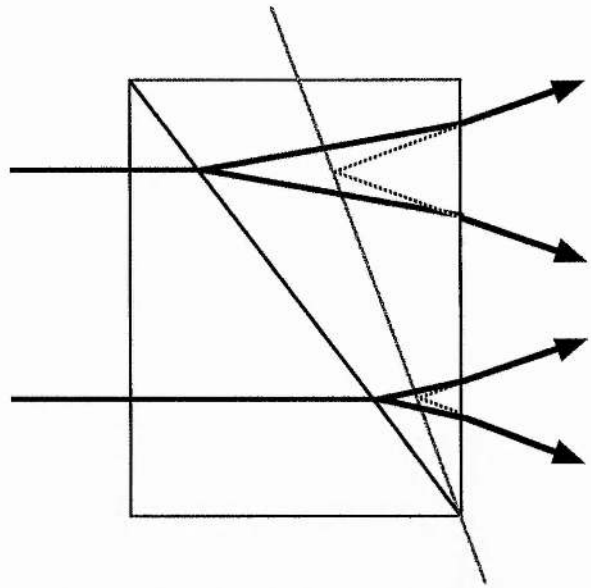

Figure 3.16 Beam-splitting effect in a Wollaston prism, illustrating how the beams appear to trace back to a common plane halfway between the prism exit face and the interface (blue line).

A fringe-resolved interferometric autocorrelation of the pulses from the self-modelocked femtosecond Ti:sapphire laser is presented as Fig. 3.17. The small level of chirp evident is due to the same cause as that given to explain the autocorrelation of Fig. 3.14b. A pulse duration of 88 fs can be inferred from Fig. 3.17; this is slightly longer than the pulses presented in Fig. 3.13, due to a small amount of pulse broadening induced by dispersion in the quartz prism. The noise on Fig. 3.17 may be related to the mechanical translation of the prism, or may have been caused by inhomogeneities in the prism material or at the prism interface.

There are several advantages and disadvantages to the Wollaston autocorrelator. It was a compact device, which was simple and straightforward to align. No attempt was made to calibrate it; instead the pulse duration was calculated from the wavelength and the number of interference fringes. However, the precise way in

which the delay relates to the properties of the prism means that an accurate calibration could be done. Improvements to the method of scanning the prism would probably result in reduced noise and a better quality output. The principal disadvantage lies in the dispersive pulse broadening of the prism glass, which suggests that a Wollaston prism autocorrelator would not be appropriate for measuring the hypershort pulses now becoming commonplace. However, judicious selection of the prism material can help to reduce this problem; the dispersive properties of various materials vary quite dramatically with wavelength so a material can be chosen to suit a particular application. Some values of pulse broadening in various materials at different wavelengths are given in Table 3.2.

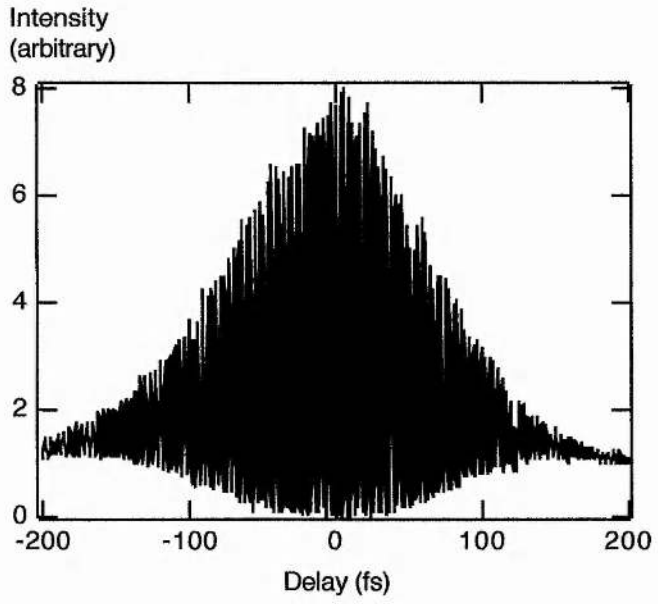

Figure 3.17 Interferometric autocorrelation trace of pulses from the Ti:sapphire laser, recorded with the Wollaston autocorrelator. The inferred pulse duration is 88 fs, due to a small amount of broadening induced by the prism glass.

Material	**Pulse broadening (%) at**		
	800 nm	**1000 nm**	**1200 nm**
quartz	8	2.7	0.6
calcite	1.6	0.04	0.01
Mg_2F	1.1	0.27	44

Table 3.2 Percentage pulse broadening at different wavelengths in different prism materials for propagation through a Wollaston prism giving a total temporal delay of ± 1 ps.

The main purpose of the Wollaston autocorrelator was to demonstrate the potential miniaturisation of autocorrelators which is made feasible by LEDs. In addition, it is a novel application of the Wollaston prism. However, many other compact autocorrelator designs exploiting LEDs are of course possible, and may be realised by other researchers in the future.

3.4 Frequency-resolved optical gating

The theoretical discussion of autocorrelation (Section 3.2.1) indicated that only a small amount of information regarding the pulses being measured can be derived in this way. The pulse duration may only be inferred by making an assumption of the pulse shape. An interferometric autocorrelation trace reveals a little qualitative information about phase, whereas an intensity autocorrelation contains no phase information at all. Spectral measurements can complement autocorrelations to some extent, but still contain no phase details. This is a basic problem stemming from the fact that most pulse measurement techniques rely on devices which only measure intensity. Consequently, the complete characterisation of the complex electric field of a pulse, that is, the intensity and phase in both the temporal and spectral domains, is something of a non-trivial task, but nonetheless a very important one.

For a long time, no satisfatory solution was available. In recent years, however, the technique of frequency-resolved optical gating (FROG) has been pioneered by Trebino and co-workers [31]; this allows the full characterisation of a pulse with no requirement for prior knowledge of its shape, phase or duration. The method has been extensively applied to many laser pulses, but the characterisation of pulses from optical parametric oscillators has been neglected. In the light of this, it was decided to consruct a FROG system and use it to study pulses from the femtosecond OPOs described elsewhere in this thesis.

3.4.1 Theory of FROG

In essence, the technique of FROG takes a pulse to be measured and a gate pulse, delays one with respect to the other, and subjects them to an instantaneous

nonlinear process. The resulting signal is then spectrally resolved and recorded, producing a plot of intensity as a function of both delay and frequency, which may be mathematically described as

$$S_E(\omega,\tau) = \left| \int_{-\infty}^{\infty} E(t)g(t-\tau)\exp(-i\omega t)\mathrm{d}t \right|^2 \tag{3.10}$$

where $E(t)$ is the electric field of the pulse, and $g(t - \tau)$ is the gate pulse, with a delay τ. Such a description is known as a spectrogram, and is a concept commonly used in acoustics to display sound waves, where the gate pulse is usually a known and simple function. FROG, however, removes the need for such a well-defined and independent gate pulse, and instead gates the optical pulses to be measured with replicas of themselves. It can be shown that the spectrogram includes all intensity and phase information of the pulse, and that the complex field of the pulse can be recovered from it, which is the purpose of FROG.

There are two separate parts to a FROG system. The first is the apparatus used to obtain the spectrogram, and the second is a computer algorithm used to extract the pulse information from the spectrogram. Various techniques for accomplishing these objectives have been presented in the literature, some of which will now be described.

The exact shape of the spectrogram, which is referred to as the FROG trace, depends on the nonlinear response used to gate the pulses, as this affects the form of the gate pulse, derived from a replica of the pulse to be measured. The resulting optical signal, after gating, is written as $E_{sig}(t,\tau)$, and has a mathematical form determined by the gating technique. Any suitable instantaneous nonlinearity can be used for this, but the most popular to date have proved to be polarisation gating (utilising the Kerr effect), self-diffraction, and second harmonic generation (SHG) [32]. They each have advantages and disadvantages. The beam geometries required for each of these methods are shown in Fig. 3.18, and the corresponding signal fields are given by

$$\begin{aligned}
&\text{polarisation gate} && E_{sig}(t,\tau) = E(t)\left|E(t-\tau)\right|^2 \\
&\text{self-diffraction} && E_{sig}(t,\tau) = E^2(t)E^*(t-\tau) \\
&\text{SHG} && E_{sig}(t,\tau) = E(t)E(t-\tau)
\end{aligned} \tag{3.11}$$

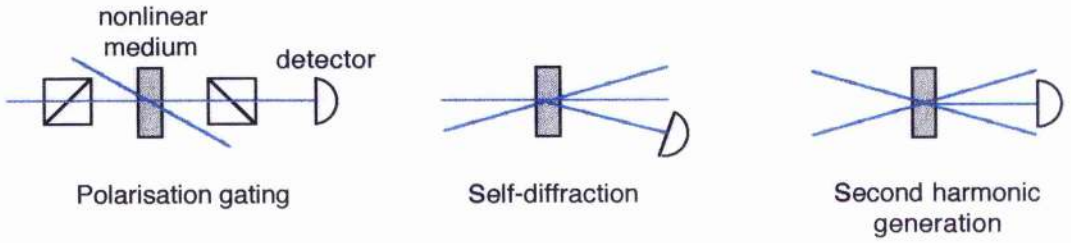

Figure 3.18 Beam geometries for three common gating methods for frequency-resolved optical gating.

The primary problem with polarisation gating and self-diffraction is that they are third-order nonlinear effects, and consequently require a high intensity to produce a significant signal field. SHG is therefore the technique best suited to lower power laser systems, and specifically to synchronously-pumped femtosecond OPOs, which frequently produce relatively low output powers. Thus SHG FROG was used here, and will be referred to in the remainder of this discussion.

Once generated, the signal field is spectrally dispersed and recorded as a function of delay, τ. For SHG FROG, the spectrogram of Equation 3.10 becomes the FROG trace

$$I_{FROG}(\omega,\tau) = \left| \int_{-\infty}^{\infty} E(t)E(t-\tau)\exp(-i\omega t)\mathrm{d}t \right|^2 \tag{3.12}$$

Because SHG is the nonlinearity commonly used in autocorrelation, the SHG FROG trace is effectively composed of individual spectra recorded for each value of delay used to obtain an autocorrelation. The method was therefore dubbed spectrally resolved autocorrelation when it was first demonstrated experimentally by Paye et al in 1993 [33]

It can be shown [34] that the pulse field $E(t)$ can be easily obtained from the signal field $E_{sig}(t,\tau)$, and hence from the FROG trace, $I_{FROG}(\omega,\tau)$. The quantities are related via two-dimensional Fourier transforms, so the problem of extracting $E_{sig}(t,\tau)$ from the measured FROG trace is a two-dimensional phase retrieval problem. Such retrieval problems are common to many fields of research, and hence it is well-known that two-dimensional phase retrieval is a solvable problem, and in fact always gives a unique result. In other words, a pulse and its FROG trace are uniquely related. This

is part of the power of FROG measurements; only one pulse can be retrieved from a particular trace, and must therefore have the exact form of the original pulse which produced the trace.

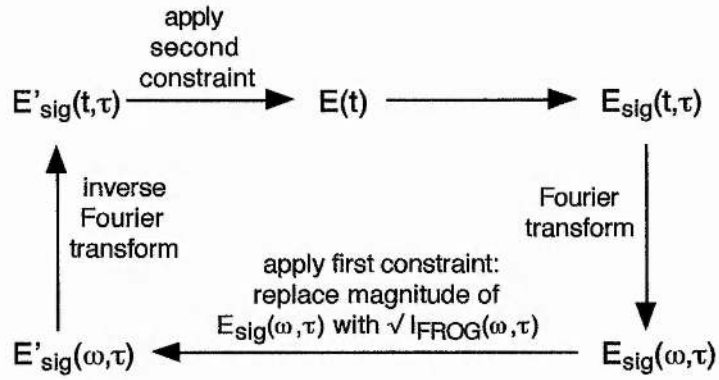

Figure 3.19 Fourier-transform retrieval algorithm for extracting pulse intensity and phase information from a FROG trace, $I_{FROG(\omega,\tau)}$.

The retrieval is done by an iterative Fourier-transform algorithm, with two constraints to force it to converge to the correct solution. The algorithm originally proposed by Trebino and Kane [34] produced good results, but it has since been further refined, particularly with regard to SHG FROG [35]. The form of the FROG algorithm is shown in Fig. 3.19, and starts off with a guess pulse, $E(\tau)$, which may or may not be similar to the pulse being measured. The signal field, $E_{sig}(t,\tau)$, of this guess pulse is calculated, and then this is Fourier-transformed to produce the signal field in terms of frequency, $E_{sig}(\omega,\tau)$. At this point, the first constraint is applied – the magnitude of $E_{sig}(\omega,\tau)$ is replaced by the magnitude of the measured FROG trace, to give $E'_{sig}(\omega,\tau)$. An inverse Fourier-transform returns the field to the time domain, $E'_{sig}(t,\tau)$, and then the second constraint is applied. The result of this then acts as a new guess pulse, and the algorithm repeats until satisfactory convergence is achieved. Convergence is monitored by calculating the FROG trace of the guess pulse after each iteration, and comparing this with the actual recorded FROG trace, to give an error G [35]:

$$G = \sqrt{(1/N^2)\sum_{\omega,\tau=1}^{N}\left[I_{FROG}(\omega,\tau) - \left|E_{sig}(\omega,\tau)\right|^2\right]^2} \tag{3.13}$$

where N^2 is the size of the array of frequency and delay data, ie. there are N frequency values to describe the spectrum at each of N delay times. A square data array is essential for the fast Fourier-transform routines required by the algorithm, because the increment in delay values, $\delta\tau$, must be related to the frequency increment $\delta\nu$ by $\delta\nu = 1/N\delta\tau$. Thus it can be necessary to scale experimentally recorded FROG traces before applying the algorithm, to obtain an N by N array.

The nature of the second constraint in the algorithm is the reason for the difference between the originally proposed algorithm [34], and the improved SHG algorithm [35]. It was found that the original basic algorithm frequently stagnated at a large error value, and thus failed to converge. By replacing the second constraint with one based on the mathematical phenomenon of generalised projections (GPs), many pulses which had previously stagnated were quickly retrieved [36]. However, some pulses which retrieved well from the basic algorithm failed to retrieve from the GP algorithm, so it was concluded that a composite of the two algorithms would be best. The algorithm monitors its progress via the error G, and if G fails to reduce significantly after a specified number of iterations, the algorithm swaps from the basic to the GP type, or vice versa. In this way, most pulse shapes can be successfully determined after a hundred or so iterations. Additional algorithmic improvements have also been investigated [37]. The mathematical particulars of various forms of the second constraint can be found in the relevant references.

SHG FROG is relatively straightforward to implement, particularly by those used to working with SHG autocorrelation, although it does have a number of drawbacks. Some of these are the same problems suffered by autocorrelation, as discussed in Section 3.2.2, namely the limitations of phasematching and bandwidth, and the problem of dispersive pulse broadening in the nonlinear crystal. However, the primary problem is a little more serious, although it is also a feature of autocorrelation. SHG FROG is symmetric in terms of delay, so that a delay of $-\tau$ produces the same signal field as a delay of τ. This can be seen from Equation 3.11 by performing a charge of variable so that $t' = t - \tau$, and then dropping the primes. Thus an SHG FROG trace is symmetric about $\tau = 0$ (as is the case with an autocorrelation trace) and it is not possible to determine the direction in time of a pulse (ie. $E(t)$ gives the same FROG trace as $E(-t)$). This is not true for polarisation gating FROG and self-diffraction FROG, so in some respects these techniques are

more useful than SHG FROG. However, this ambiguity can be overcome in some circumstances. For example, pulses from a particular source may be known to have positive chirp caused by, for example, group velocity dispersion, so this information can be used to identify the leading and trailing edges of the retrieved pulse.

Fig. 3.20 shows some theoretical FROG traces of a transform-limited pulse, a pulse with positive linear chirp and a pulse with self-phase modulation, obtained using the three different gating methods. These show how an SHG FROG trace is always symmetrical with delay, which removes information about the sign of chirp. This aside, much information can be visually gleaned from FROG traces, without the need to run the algorithm. This attractive feature of FROG was recognised by Delong, Trebino and Kane, who have published a detailed study of the traces of different pulse shapes and different gating geometries, from which the user of a FROG system can gain an intuitive grasp of trace interpretation [32].

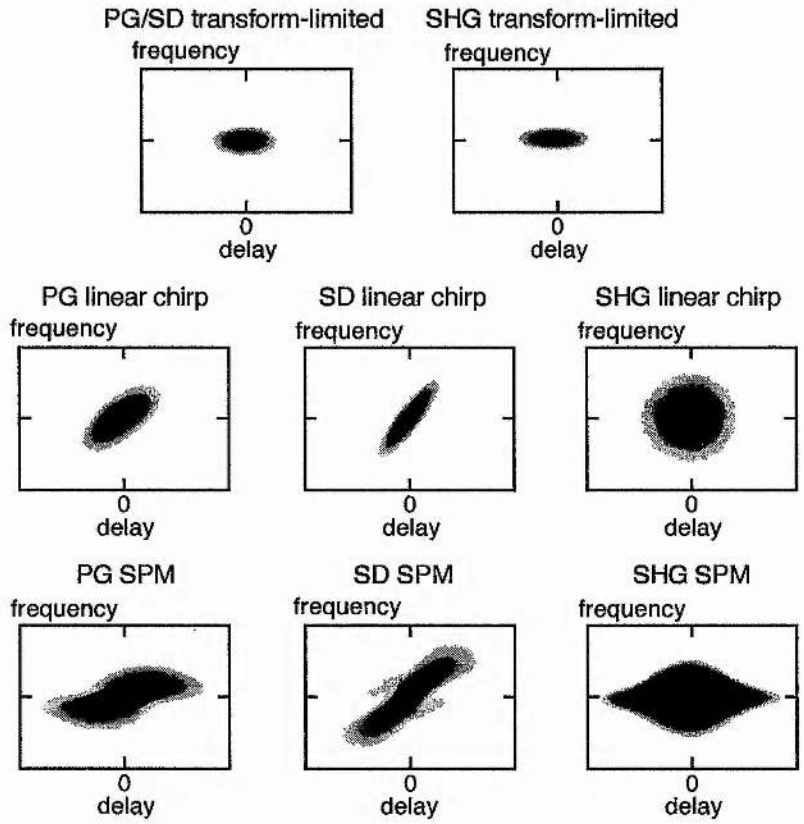

Figure 3.20 Examples of theoretical FROG traces of transform-limited pulses, linearly-chirped pulses and pulses with self-phase modulation (SPM), obtained using different gating geometries: PG = polarisation gating, SD = self-diffraction, SHG = second harmonic generation [32].

3.4.2 Experimental FROG

The majority of the experimental FROG arrangements reported to date have worked by incrementally adjusting the delay, recording an individual spectrum for each delay value, and building up the FROG trace from the spectra. This approach is satisfactory, but slow. Much more useful would be a real-time system, with a full and constantly updated display of the FROG trace. This would dramatically reduce data acquisition time, which is advantageous both practically and in terms of noise minimisation, and would also be a highly useful diagnostic tool, allowing constant monitoring of the spectral and temporal characteristics of a pulsed output during any optimisation of the source. These points are particularly applicable to high repetition rate femtosecond sources, producing as they do continuous pulse trains which can require constant monitoring. To this end, a real-time SHG FROG system was constructed to potentially characterise the output of the femtosecond OPOs described in later chapters.

The configuration of the FROG system is shown in Fig. 3.21. A conventional autocorrelator arrangement was used to provide a continuously scanning delay, comprising a beam splitter and two retroreflectors, one mounted on a loud speaker and one on a calibrated translation stage, followed by a 35 mm focussing lens and a BBO doubling crystal, 500 μm long with $\theta = 27°$. Whereas SHG autocorrelation typically has a background level and is therefore obtained via collinear phasematching, FROG must be background-free for successful retrieval by the algorithm, so an SHG FROG system must be aligned for noncollinear phasematching. The details of this can be seen in Fig. 3.21; the two halves of the input beam were laterally separated but collinear at the lens, so that on focussing they crossed at an angle in the crystal. A small amount of frequency doubling occurred along the beam directions, but when the pulses overlapped in the crystal the combined intensities of their forward propagating components was sufficient to generate second harmonic in the forward direction. A pinhole was used to block the two side beams, and the forward component, the required $E_{sig}(t,\tau)$, was spectrally dispersed using an SF11 prism. Continuous scanning of the frequency, to produce the other dimension of the FROG trace, was obtained by using a spinning mirror to sweep the dispersed spectrum across the surface of a CCD camera. The mirror was phaselocked to the loudspeaker so that the delay scan and the frequency scan were always synchronous.

This was done by spinning the mirror freely using a small motor, and comparing the frequency of spin with the frequency of the loudspeaker to derive an error signal. This signal was then used in a feedback loop to adjust the loudspeaker frequency to minimise the error. Thus the image detected by the camera was a full and continuously scanned FROG trace, which was displayed on a video monitor and updated at approximately 20 Hz.

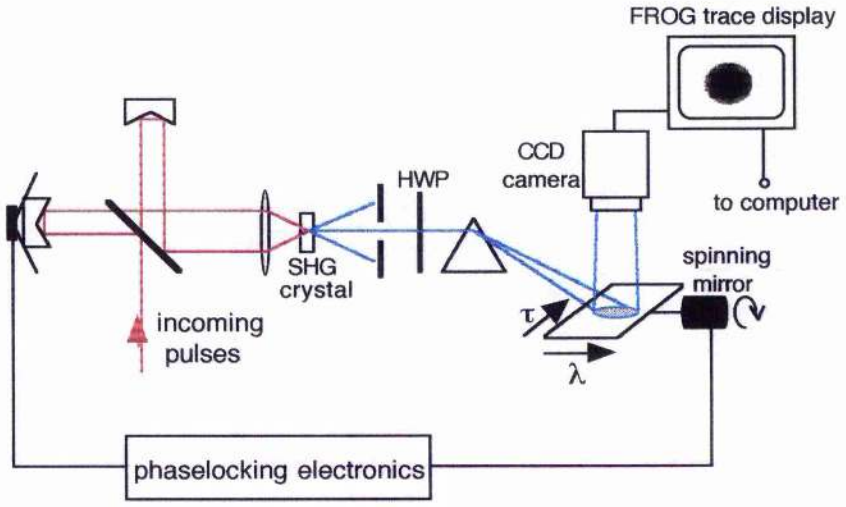

Figure 3.21 Configuration of the real-time second harmonic generation FROG system.

A frame-grabber was used to select and digitise a FROG trace to produce a 512 by 512 data array. Various image processing was performed to remove background noise, and to centre the trace in the middle of the array, and the trace was then calibrated. Temporal calibration was done in the same way as for an autocorrelation trace, and spectral calibration was achieved by measuring the dispersed output with a monochromator to determine the bandwidth and peak wavelength corresponding to a zero delay. A retrieval algorithm was then applied to the data set to obtain the pulse information. The algorithm, based on those of Trebino et al, was a composite of the basic and GP algorithms discussed earlier, and typically achieved satisfactory retrieval in 50 to 200 iterations, the whole process taking a few minutes. The results were returned in the form of graphical displays of the intensity and phase in the temporal and spectral domains.

The FROG system was used to characterise the output of the syncronously-pumped femtosecond OPP based on RTA; the details of this are given in Section 5.4.6.

Thus the FROG system proved to be a useful diagnostic tool, providing detailed and complete characterisation of pulses in a few minutes, and allowing for the continuous monitoring of the FROG trace from a source under scrutiny.

FROG is still a relatively new technique, and being more complex than autocorrelation, is still far from commonplace. Given the highly useful and detailed information that can be obtained, however, it is likely to become far more prevalent in the future, especially as reliable commercial systems become available.

3.5 Concluding remarks

The purpose of this chapter has been to provide theoretical and experimental details necessary as background material to the results presented in the following three chapters, which each deal with the design, construction, operation and characterisation of a different femtosecond optical parametric oscillator. These OPOs were all pumped by a self-modelocked femtosecond Ti:sapphire laser, so this device was described in some detail, along with details relating to Ti:sapphire as a laser gain medium, and to the technique of ultrashort pulse generation by self-modelocking.

Once generated, ultrashort pulses must be characterised, so two schemes for doing this were presented. Second harmonic generation autocorrelation, the most common pulse measurement technique, was described, preliminary to the presentation of a novel autocorrelation method based on the use of light emitting diodes or photodiodes. This arrangement offers numerous advantages over more conventional configurations; these were discussed and then exploited by the demonstration of a compact autocorrelator using an AlGaAs LED, and a Wollaston prism to replace the traditional Michelson interferometer.

The other pulse measurement method, frequency-resolved optical gating (FROG), was then addressed. FROG is a relatively new but extremely useful technique, and as such is currently attracting much interest, and is subject to continuing improvements and updates. An improved arrangement was presented here, which used a loudspeaker and spinning mirror to provide a real-time second harmonic generation FROG system, allowing continuous monitoring of femtosecond pulse trains. Successful characterisation of the intensity and phase of OPO pulses was achieved using this device, and the results are presented in Chapter 5.

References

1. P. Moulton, Opt. News **8**, 9 (1982).
2. R. R. Joyce and P. L. Richards, Phys. Rev. **179**, 375 (1969).
3. P. F. Moulton, J. Opt. Soc. Am. B **3**, 125 (1986).
4. Spectra-Physics Lasers Inc., 1335 Terra Bella Avenue, Mountain View, CA. 94043, USA.
5. P. Albers, E. Stark and G. Huber, J. Opt. Soc. Am. B **3**, 134 (1986).
6. A. E. Siegman, *Lasers* (University Science Books, California, 1986).
7. D. E. Spence, P. N. Kean and W. Sibbett, Opt. Lett. **16**, 42 (1991).
8. D. E. Spence, J. M. Evans, W. E. Sleat and W. Sibbett, Opt. Lett. **16**, 1762 (1991).
9. D. T. Reid, *Novel nonlinear techniques for femtosecond pulse generation in the visible and near-infrared*, PhD thesis, University of St Andrews (1994).
10. H. P. Weber, J. Appl. Phys. **38**, 2231 (1967).
11. H. Harde and H. Bruggraf, Opt. Commun. **38**, 211 (1981).
12. G. Xian, M. Lambsdorff, J. Kuhl and W. Biachang, Rev. Sci. Instrum. **59**, 2088 (1988).
13. Z. A. Yasa and N. M. Amer, Opt. Commun. **36**, 406 (1981).
14. G. D. Su, L. Y. Lin and M. C. Wu, in *Conference on Lasers and Electro-Optics*, Vol. 11 of 1997 OSA Technical Digest Series (Optical Society of America, Washington, DC, 1997), p. 286, paper CWL2.
15. N. A. Papadogiannis ans S. D. Moustaizis, Opt. Commun. **137**, 174 (1997).
16. E. J. Canto-Said, P. Simon, C. Jordna and G. Marowsky, Opt. Lett. **18**, 2038 (1993).
17. W. Plaß, H. Rottke, W. Heuer, G. Eichhorn and H. Zacharias, Appl. Phys. B **54**, 199 (1992).
18. O. Bouevitch and A. Lewis, Opt. Commun. **116**, 170 (1995).
19. J. I. Dadap, G. B. Focht, D. H. Reitze and M. C. Downer, Opt. Lett. **16**, 499 (1991).
20. M. Sheik-Bahae, Opt. Lett. **22**, 399 (1997).
21. Y. Miyamoto, T. Kuga, M. Baba and M. Matsuoko, Opt. Lett. **18**, 900 (1993).
22. F. R. Laughton, J. H. Marsh and A. H. Kean, Electon. Lett. **28**, 1663 (1992).
23. F. R. Laughton, J. H. Marsh, D. A. Barrow and E. L. Portnoi, IEEE J. Quantum Electron. **30**, 838 (1994).
24. W. Rudolph, M. Sheik-Bahae, A. Bernstein and L. F. Lester, Opt. Lett. **22**, 313 (1997).
25. A. Zavriyez, E. Dupont, P. B. Corkum, H. C. Liu and Z. Biglov, Opt. Lett. **20**, 1886 (1995).
26. L. P. Barry, P. G. Bollond, J. M. Dudley, J. D. Harvey and R. Leohardt, Electron. Lett. **32**, 1922 (1996).
27. Stock number 564-015, RS Components
28. M. J. Padgett and A. R. Harvey, Rev. Sci. Instrum. **66**, 2807 (1995).
29. M. Françon and S. Mallick, *Polarisation Interferometers* (Wiley Interscience, London, 1971), p. 25 - 31.

30. V. G. Dmitriev, G. G. Gurzadyan and D. N. Nikogosyan, *Handbook of Nonlinear Optical Crystals* (second edition, Springer-Verlag, Berlin, 1997).
31. D. J. Kane and R. Trebino, IEEE J. Quantum Electron. **29**, 571 (1993).
32. K. W. Delong, R. Trebino and D. J. Kane, J. Opt. Soc. Am. B **11**, 1595 (1994).
33. J. Paye, M. Ramaswamy, J. G. Fujimoto and E. P. Ippen, Opt. Lett. **18**, 1946 (1993).
34. R. Trebino and D. J. Kane, J. Opt. Soc. Am. A **10**, 1101 (1993).
35. K. W. Delong, R. Trebino, J. Hunter and W. E. White, J. Opt. Soc. Am. B **11**, 2206 (1994).
36. K. W. Delong, D. N. Fittinghoff, R. Trebino, B. Kohler and K. Wilson, Opt. Lett. **19**, 2152 (1994).
37 K. W. Delong and R. Trebino, J. Opt. Soc. Am. A,**11**, 2429 (1994).

chapter four

THE KTA OPTICAL PARAMETRIC OSCILLATOR

4.1 Introduction

Before the recent advent of readily available periodically poled crystals, $KTiOPO_4$ (KTP) and its crystal isomorphs were regularly used for the generation of infrared wavelengths via birefringent phasematching. These crystals are attractive for several reasons. They have wide transparency ranges, relatively large nonlinearities and high damage thresholds, and have been exploited for a wide variety of applications. The system described in this chapter is a synchronously-pumped femtosecond optical parametric oscillator (OPO) based on a $KTiOAsO_4$ (KTA) nonlinear crystal and tunable beyond 4 μm, which was constructed to provide a mid-infrared (MIR) source for detector testing. The choice of KTA as the nonlinear crystal is explained in Section 4.2, where a brief summary of the relevant linear and nonlinear optical properties is also presented, followed by a review of published KTA-based research. A theoretical analysis of the phasematching arrangement used in the OPO is given in Section 4.3. Sections 4.4 and 4.5 include details of the cavity construction and the experimental results. A conclusion of the chapter is included as Section 4.6.

Quasi-phasematching in periodically poled crystals is rapidly becoming the most prevalent method of MIR generation, in attempts to provide reliable sources operating in the desirable 3 to 5 μm range. However, the research described here dates back approximately two years to a time when quasi-phasematching was very much in its infancy, and birefringent phasematching in unpoled material was the only nonlinear interaction method available to most researchers. A large amount of work in

many laboratories was devoted to finding a material suitable for MIR generation, via optical parametric oscillation or difference frequency mixing. The KTP family, that is, the titanyl arsenates and phosphates, were generally well developed and commercially available at that time, so received a lot of attention to this end, and in the present case were selected as suitable candidates for a femtosecond MIR OPO. The next step was to determine which one would be best.

4.2 KTA

4.2.1 Choice of crystal

Of the many titanyl arsenates and phosphates, KTP, KTA and $RbTiOAsO_4$ (RTA) are probably the best developed in terms of crystal quality, and are certainly the most commonly used. A brief comparison of their qualities as regards use in a mid-infrared OPO will now be given, to justify the use of KTA.

The two primary criteria to consider when selecting a crystal for the generation of a specific wavelength range are the phasematching properties and the transparency. The material must phasematch such that the desired output can be generated via an interaction with a reasonable nonlinear coefficient, and must also be transparent to all waves involved in the interaction. If at all possible it is generally desirable to use noncritical phasematching to avoid the problems inherent in the Poynting vector walk-off which arises from critical phasematching. Noncritical phasematching removes the possibility of angle tuning, so for a device to be tunable it must exploit pump or temperature tuning. The temperature variation of the refractive indices of the KTP family is too slight for temperature tuning of these materials to be of much practical use, so pump tuning must be used. The pump source available for the femtosecond OPO was the self-modelocked Ti:sapphire laser discussed in Chapter 3, which was tunable over the approximate range 760 - 860 nm with the optics set available. For the crystals under consideration, the largest nonlinearity can be accessed by propagation along the x-axis, using type II phasematching (see Section 4.2.2). The infrared idler wavelengths available via this interaction from Ti:sapphire pumping of KTP, KTA and RTA are given in Fig. 4.1. The data for KTA and RTA were calculated from the relatively recent Sellmeier coefficients of Fenimore et al [1, 2], while those for KTP came from the Sellmeier

coefficients reported by Cheng et al [3] which are known to be somewhat inaccurate at longer wavelengths. This is the reason for the KTP curve crossing over that for KTA. The graph indicates that while over 400 nm of tuning can be obtained via noncritical phasematching, oscillation beyond 3 μm cannot be achieved.

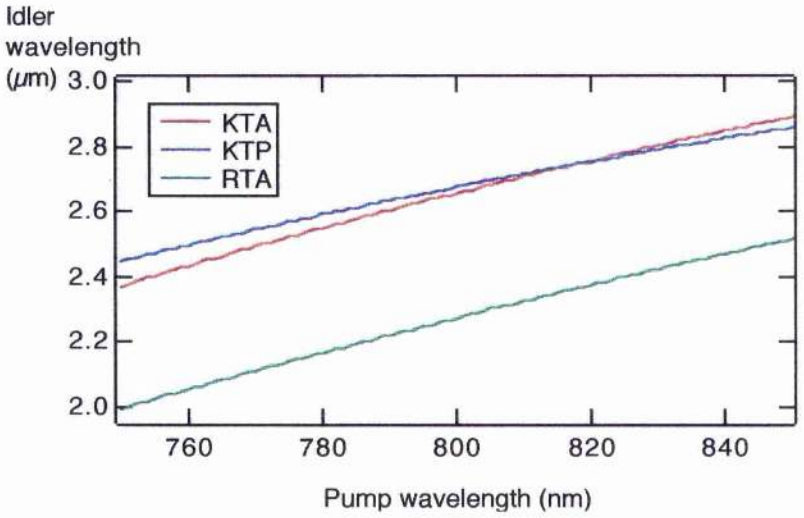

Figure 4.1 Idler wavelengths available from Ti:sapphire pump tuning of type II noncritically (*x*-axis propagation) phasematched OPOs based on KTA, RTA and KTP.

Hence it is necessary to turn to the more complex arrangement of critical phasematching to reach the crucial 3 to 5 μm range with these materials. From Fig. 4.2 it can be seen that angle tuning in the *xz*-plane ($\phi = 0°$) can achieve this. The curves are for a type II interaction ($o \rightarrow e + o$)[1] and a pump wavelength of 830 nm, and show that rotation of each of the crystals over only a couple of degrees near $\theta = 40°$ (internal angle) would cover the required tuning range. At this point, however, KTP can be rejected. Included in Fig. 4.2 is the transparency cut-off of KTP, at 4.3 μm [4]. KTA and RTA are both transparent beyond 5 μm; the shorter limit for KTP is due to the phosphate group. Thus only KTA and RTA are suitable for generation of the entire 3 to 5 μm region.

There is little to choose between these two materials as regards their other pertinent properties. They have similar nonlinearities and Poynting vector walk-off angles, and would be equally appropriate for a critically phasematched femtosecond MIR OPO. However, KTA is more readily available and less costly than RTA, so

[1] Type I interactions give a zero effective nonlinearity.

these were the determining factors in the final choice of KTA as the nonlinear medium for the MIR OPO. The expected signal and idler outputs for several degrees of angle tuning are shown in Fig. 4.3, for a pump wavelength of 830 nm. Pump tuning can be combined with angle tuning to enhance the output wavelength range. Based on this information, a crystal specified for propagation at θ=43°, and with dimensions of 3 mm by 5 mm aperture and 2 mm length was obtained from Crystal Associates [5]. It was antireflection coated at 1.1 μm.

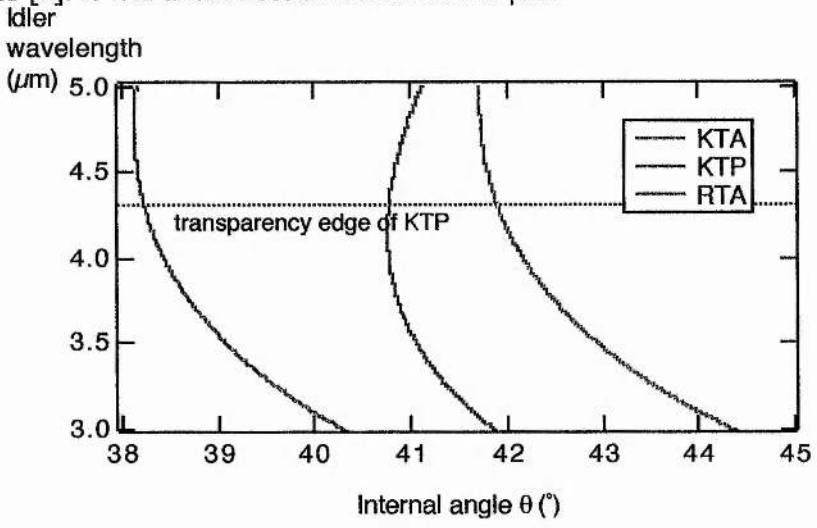

Figure 4.2 Idler wavelengths available from angle tuning of type II phasematched OPOs based on KTA, RTA and KTP, for a pump wavelength of 830 nm.

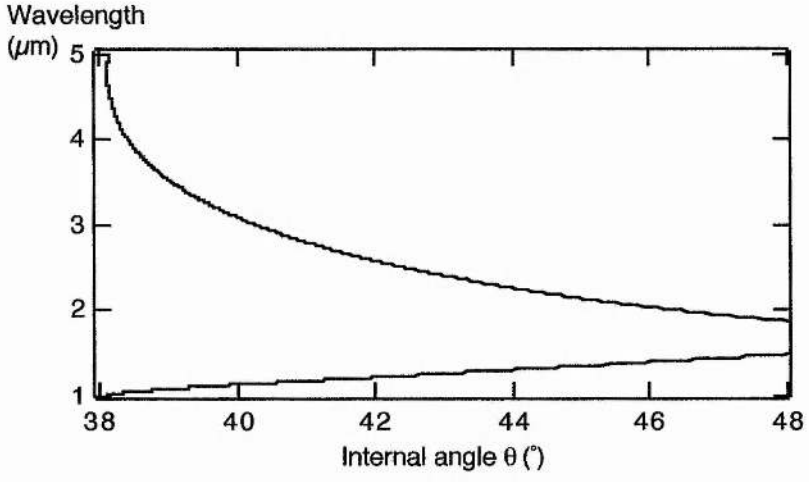

Figure 4.3 Signal and idler wavelengths available from angle tuning of a type II critically phasematched KTA OPO, for a pump wavelength of 830 nm.

4.2.2 Properties of KTA

Like the rest of the titanyl arsenates and phosphates, potassium titanyl arsenate, more commonly known as KTA, is a positive biaxial crystal ($n_z > n_y > n_x$) of crystallographic point group mm2, with an orthorhombic structure. All the crystals in the family have the chemical formula $M\mathrm{TiO}X\mathrm{O}_4$, where M is K, Rb, Cs, Tl or NH_4, and X is P or As. The origin of the optical nonlinearity in KTP has recently been investigated by Xue and Zhang [6], and some conclusions relating to KTA may be drawn from this work. Traditionally, the nonlinearity of KTP has been attributed to the Ti–O bonds, but this fails to explain the differences observed across the crystal family, since they all have these bonds in common. The crystals are complex, having 37 types of constituent chemical bonds. Xue and Zhang analysed the individual contributions of each these, and found that some of the PO_4 phosphate groups make a substantial contribution to the nonlinearity of KTP, so for KTA much of the nonlinearity must be due to certain of the AsO_4 arsenate groups.

KTA can be grown by both the flux growth method and the hydrothermal method. Flux growth has a tendency to produce multidomain crystals, as discussed by Liu et al [7], but technological advances have resulted in good quality single domain crystals in recent years. Both growth methods have been described in the literature [4, 7, 8, 9]. The KTA crystal from Crystal Associates was flux grown.

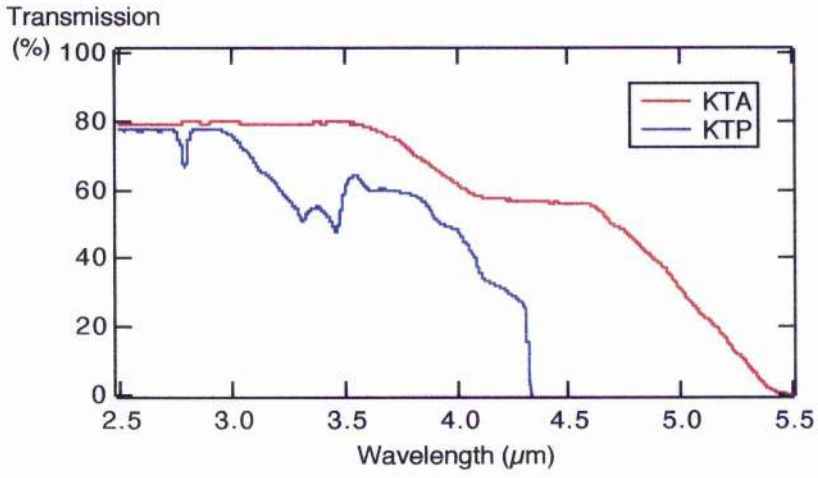

Figure 4.4 Mid-infrared transmission of KTA and KTP (from ref. 4).

As mentioned in the previous section, KTA is transparent to beyond 5 μm. Fig. 4.4 shows the transmission measurements of Loiacono et al [4], illustrating the transparency edge at ~5.3 μm. Measurements by Kung [10] show good agreement with these results. A transmission curve for KTP [4] is included for comparison, showing the reduced transparency beyond 4 μm, and also a strong dip near 3.5 μm which is caused by the phosphate group and is consequently absent in KTA. In addition, the absorption at ~2.8 μm in KTP, which is ascribed to a hydroxyl group, is shifted and very much reduced in KTA. Overall, the MIR transmission of KTA is vastly superior to that of KTP.

Several sets of Sellmeier coefficients describing the refractive indices of KTA have been published. Those of Cheng et al [3] date from 1993, and are based on measurements from 0.45 to 1.5 μm. They are known to be unreliable at longer wavelengths, so for mid-infrared work they have been supplanted by coefficients calculated by Fenimore et al [1] from measurements out to 3.6 μm. The variation of refractive index with wavelength, calculated from these coefficients, is illustrated in Fig. 4.5; the coefficients themselves are given in Table 4.1, and fit the equation

$$n^2 = A + \frac{B}{1-(C/\lambda)^2} - D\lambda^2 \qquad (4.1)$$

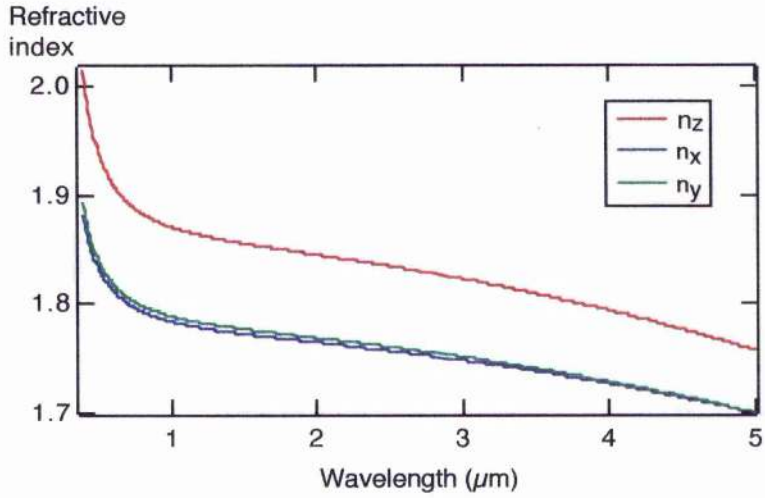

Figure 4.5 Infrared refractive indices of KTA, calculated from the Sellmeier coefficients of Fenimore et al [1].

An alternative set of coefficients can be found in a 1994 paper by Kato [11], but as these were calculated from second harmonic generation data, they are unlikely to be

accurate in the MIR. The coefficients of Fenimore et al [1] are used in the remainder of this chapter.

A_x	1.90713	A_y	2.15912	A_z	2.14786
B_x	1.23522	B_y	1.00099	B_z	1.29559
C_x	0.19692	C_y	0.21844	C_z	0.22719
D_x	0.01025	D_y	0.01096	D_z	0.01436

Table 4.1 KTA Sellmeier coeffients of Fenimore et al [1].

There are three non-zero nonlinear d_{ij} coefficients for crystals in the mm2 class: d_{31} (d_{15}), d_{32} (d_{24}) and d_{33}. These have been measured for KTA by both Kato [11] and Cheng et al [12]; the values are shown in Table 4.2. Unfortunately, type II phasematching in the principal crystal planes fails to access d_{33}, the largest coefficient. Instead, the effective nonlinearity, d_{eff}, depends only on d_{31} and d_{32}. The variation of d_{eff} with propagation angle, as calculated from the values of Cheng et al, can be seen in Fig. 4.6, which shows that the largest nonlinearity is available for propagation along the *x*-axis, and that for critical phasematching at θ=43°, a nonlinearity of 3.55 pm/V would be expected.

d_{15} (pm/V)	**d_{24}** pm/(V)	**d_{33}** pm/(V)	**Reference**
2.5	4.5	–	11
2.8	4.2	16.2	12

Table 4.2 Nonlinear coefficients of KTA.

The magnitude of the Poynting vector walk-off must be considered in the design of an OPO utilising critical phasematching. The KTA OPO was configured for type II phasematching (o→ e + o) in the *xz*-plane. Consequently, the pump and idler were both polarised parallel to the *y*-axis as ordinary waves and experienced no walk-off, but the extraordinary signal, polarised in the *xz*-plane, did suffer from it. The variation of walk-off angle, that is, the angle at which the Poynting vector walks off from the momentum vector, for the signal over the wavelength range of interest is

shown in Fig. 4.7. The signal wavelengths correspond to idler wavelengths of 2 to 5 μm and a pump wavelength of 830 nm, and are generated by angle tuning over the range $\theta = 38.1^\circ$ to 46.4°. The amount of walk-off stays approximately constant at just over 2.6° at all points, so the same level of walk-off had to be compensated for throughout the operating regime of the OPO.

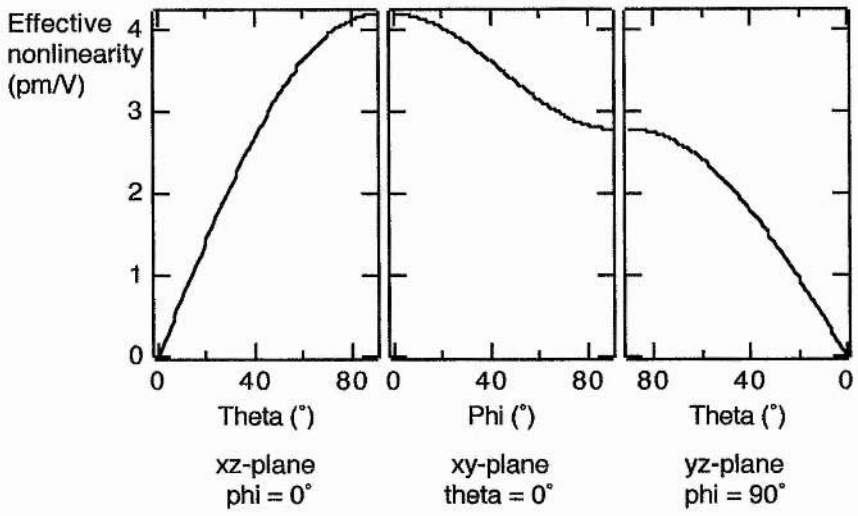

Figure 4.6 Variation with propagation angle of the effective nonlinearity of KTA in the principle planes (calculated from the nonlinear coefficients of Cheng et al [12]).

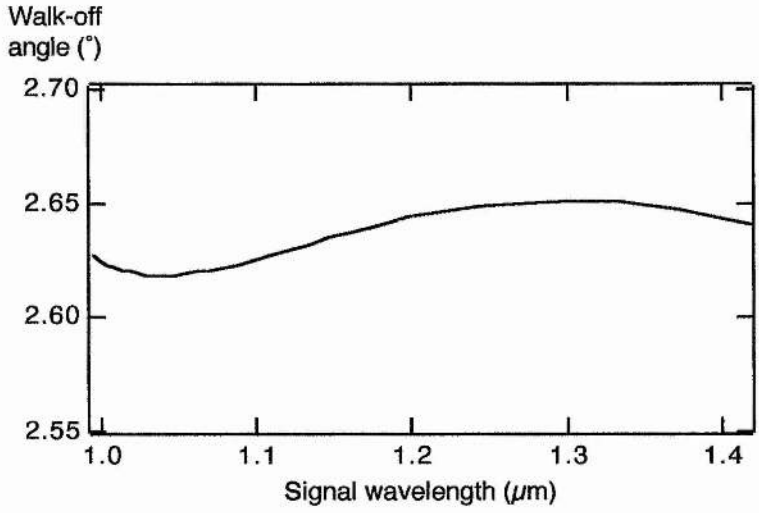

Figure 4.7 Variation of walk-off angle, ρ, with signal wavelength for the propagation angles shown in Fig. 4.3.

4.2.3 Review of KTA research

Optical parametric oscillation in KTA has been demonstrated many times, with both continuous wave (cw) and pulsed operation, and with a variety of pump sources. The first KTA-based OPO dates back to 1992, when Jani et al [13] used a nanosecond alexandrite pump laser, and type II phasematching at an angle of θ=53°. The doubly resonant system generated idler wavelengths out to 1.7 μm, so did not exploit the MIR capabilities of KTA. The first femtosecond KTA-based OPO was reported the following year by Powers et al [14]. Ti:sapphire pumping and angle tuning resulted in a signal branch of 1.29 to 1.44 μm and an idler branch of 1.83 to 1.91 μm from a crystal cut at θ=50°. Bosenberg et al [15] were the first to employ Nd:YAG pumping, in a nanosecond system using noncritical phasematching. They also used a θ=49° crystal to perform sum and difference frequency mixing of the output of an OPO based on KTP to verify the possibility of OPO phasematching out to 5 μm in KTA. A non-critically phasematched synchronously-pumped picosecond OPO was demonstrated by French et al [16], using Ti:sapphire pumping to generate near-bandwidth-limited pulses tunable over 1.13 to 1.26 μm and 2.37 to 3.10 μm. Longer MIR wavelengths were achieved by Rahlff et al [17], who used a nanosecond Nd:YLF pump laser to generate 3.44 μm, and more recently by Kato et al [18], from an OPO pumped by the 1.928 μm output of a Nd:YAG-pumped KTP-based OPO, which was continuously tunable from 3.4 to 4.3 μm. An intracavity cw KTA OPO was demonstrated by Colville et al [19] who used pump tuning to generate outputs covering 1.11 to 1.19 μm and 2.5 to 2.8 μm. Finally, Grässer et al [20] have recently reported the first observation of stimulated Raman scattering in a KTA-based OPO, in which the powers of the Raman-shifted pulses from the picosecond Nd:YLF-pumped device were high enough for it to be useful as a multiwavelength source.

More impressive MIR outputs have been obtained by difference frequency mixing. One of the first available hydrothermally-grown KTA crystals was used by Kung to generate 3 to 5.3 μm [21]. This was done by mixing a tunable Ti:sapphire laser with a Q-switched Nd:YAG laser to produce nanosecond pulses, but the conversion efficiency was only 7%, due partly to the poor quality of the KTA. A recent development of the system was to mix the frequency-doubled output of a Q-switched Nd:YAG laser with a pulsed dye laser to generate pulses tunable from

3.4 to 5.3 μm [22]. Lancaster and Dawes have also worked on difference frequency mixing, aiming to generate a narrowband nanosecond source at 3.43 μm for use in remote methane sensing [23, 24].

KTA has attracted little attention for use in second harmonic generation, despite the fact that KTP is the material of choice for frequency doubling of 1.064 μm Nd:YAG lasers. However, Boulanger et al recently presented an in-depth study of frequency doubling of 1.32 μm in $CsTiOAsO_4$ (CTA), KTA and KTP [25]. They concluded that CTA was the best material because it has the smallest walk-off, but that KTA was more efficient than KTP for this application. KTA waveguides have also been produced, inspired by the success of KTP as a waveguide material. Risk et al have fabricated such devices by ion exchange in a mixed $RbNO_3/Ba(NO_3)_2$ melt [26, 27].

It can be seen from this summary that although the wide transparency of KTA has been successfully exploited for MIR generation via difference frequency mixing, no KTA-based OPO has been extensively tunable in the MIR. However, the femtosecond OPO presented here demonstrated near-transform-limited idler pulses tunable beyond 4 μm, with the MIR tuning limited only by the reflectivity bandwidth of the cavity mirrors. These and other experimental results are discussed in a later section, following an analysis of the theory underlying the critical phasematching.

4.3 Noncollinear phasematching

As discussed earlier, the generation of MIR wavelengths from Ti:sapphire laser pumping of a KTA-based OPO requires the use of a critical crystal cut, leading to Poynting vector walk-off of the e-polarised signal beam. If, under such conditions, a collinear beam geometry is used, where the *k*-vectors of the pump and signal remain parallel, the Poynting vector of the signal walks off from the Poynting vector of the pump, which remains collinear with the pump *k*-vector, and hence there is little overlap between the two. It is interaction between the Poynting vectors which leads to oscillation of an OPO, so poor spatial overlap will result in low gain, a high threshold, and poor efficiency. It is therefore necessary to compensate for the walk-off in some way, to increase overlap of the vectors. One technique, used by

Bosenberg et al [28] in a Q-switched Nd:YAG-pumped BBO OPO, is to use two crystals with opposite orientations. The beams walk off from each other in the first crystal, and back onto each other in the second. Such an approach is unsuitable for a femtosecond OPO, though, because the second crystal would add extra dispersion to the system and consequently broaden the pulses. In addition, the increased temporal walk-away would reduce pulse interaction in the second crystal.

An alternative approach is to use a noncollinear geometry. The OPO cavity is configured so that the pump and signal propagate at an angle to each other and the signal Poynting vector walks onto that of the pump instead of away from it. This can be done by choosing to propagate the beams at an angle equal and opposite to the walk-off angle, as was demonstrated by Powers et al in their Ti:sapphire-pumped femtosecond OPOs based on KTA [14] and RTA [29]. This method works well at wavelengths near to degeneracy, but for MIR generation, far from degeneracy, the angle between the pump and the idler becomes too large. Generation of the signal is a pump-idler interaction, so if this is reduced the signal gain can fall below threshold. This is the reason given by Powers et al to explain the poor operation of their RTA-based OPO at longer wavelengths. Vector diagrams relating to these conditions are given in Fig. 4.8. Recalling that $k = 2\pi/\lambda$, a long idler wavelength corresponds to a short idler k-vector, and an increase in the pump-idler angle.

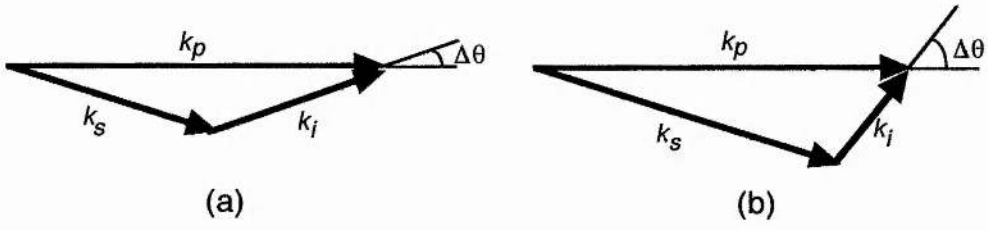

Figure 4.8 Vector diagrams of noncollinear propagation in an OPO, illustrating how the pump-idler angle increases with idler wavelength. (a) corresponds to a short idler wavelength, and (b) to a longer wavelength.

From the above considerations, it follows that a collinear geometry reduces gain due to signal-pump noncollinearity, and complete walk-off compensation reduces gain due to pump-idler noncollinearity. This suggests that there is an intermediate regime which minimises the effects of both noncollinearities – partial walk-off compensation where the pump and signal propagate at an angle less than the walk-

off angle. This situation is illustrated in Fig. 4.9, for phasematching in the *xz*-plane of KTA, where the signal walk-off is towards the *z*-axis. The angle $\Delta\theta$ between k_p and k_s will be referred to as the noncollinear angle throughout the remainder of this chapter. The walk-off angle, ρ, is between the signal Poynting vector, S_s, and the *k*-vector, k_s. θ_p is the pump propagation angle relative to the *z*-axis.

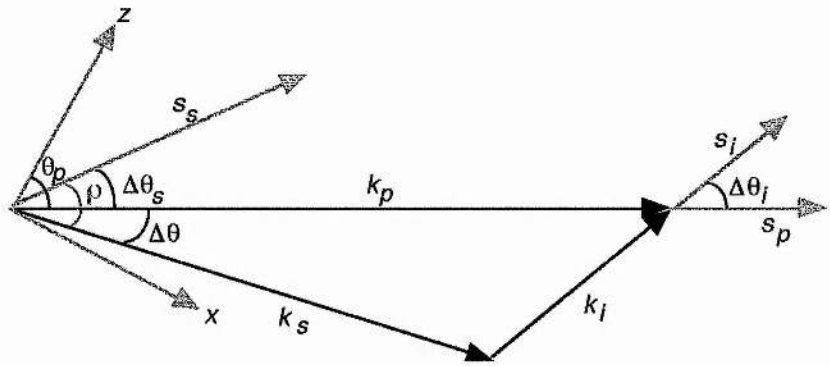

Figure 4.9 Vector diagram of the noncollinear propagation in the *xz*-plane used in the KTA OPO to provide partial compensation for Poynting vector walk-off of the signal. The angle $\Delta\theta$ between the pump and signal *k*-vectors is the noncollinear angle.

It is evident from Fig. 4.9 that the signal propagation angle, θ_s, is given by $\theta_p + \Delta\theta$. This must be accounted for in phasematching calculations for noncollinear propagation. As usual, phasematching is calculated by finding wavelength combinations that satisfy both the conservation of energy and conservation of momentum equations,

$$\frac{1}{\lambda_p} = \frac{1}{\lambda_s} + \frac{1}{\lambda_i} \tag{4.2a}$$

$$k_p = k_s + k_i \quad \equiv \quad \frac{n_p}{\lambda_p} = \frac{n_s}{\lambda_s} + \frac{n_i}{\lambda_i} \tag{4.2b}$$

where in this case the refractive indices n_p and n_i are functions of wavelength only since the pump and idler are o-waves, and n_s is a function of λ_s and θ_s for the extraordinary signal. The conservation of momentum condition (Equation 4.2b) can be solved by applying the cosine rule to Fig. 4.9, to obtain an expression for the idler

k-vector. Substituting for the idler wavelength using Equation 4.2a leads to the phasematching condition

$$\sqrt{\left(\frac{n_p}{\lambda_p}\right)^2+\left(\frac{n_s}{\lambda_s}\right)^2-2\left(\frac{n_p}{\lambda_p}\right)\left(\frac{n_s}{\lambda_s}\right)\cos\Delta\theta}=\frac{n_i(\lambda_p,\lambda_s)}{\left(\frac{1}{\lambda_p}-\frac{1}{\lambda_s}\right)^{-1}} \tag{4.3}$$

from which tuning curves may be calculated. Note that for collinear propagation ($\Delta\theta = 0°$), this reduces to the more usual expression of Equation 4.2b.

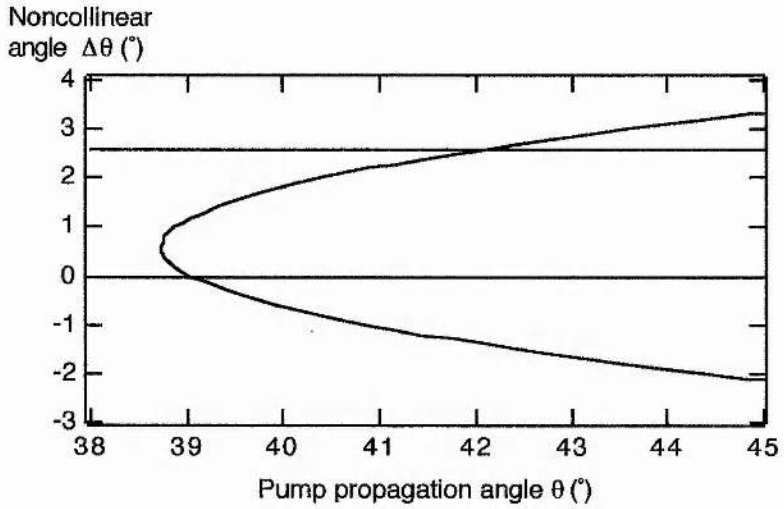

Figure 4.10 Variation of noncollinear angle with pump propagation angle for a pump wavelength of 816 nm, a signal wavelength of 1.064 μm and an idler wavelength of 3.5 μm. The straight lines represent the situations of collinear phasematching ($\Delta\theta = 0°$) and complete walk-off compensation ($\Delta\theta = 2.6°$).

A wide variety of curves can be generated from Equation 4.3, since it contains so many variables. For example, the combinations of pump propagation angle and noncollinear angle required to produce a given wavelength combination can be derived. The result of this is shown in Fig. 4.10 for a typical wavelength combination of the KTA OPO, λ_p = 816 nm, λ_s = 1.064 μm and λ_i = 3.5 μm. It is evident from this that phasematching for these wavelengths can be satisfied for a wide range of pump angles and noncollinear angles. It has already been stated that gain is poor for

collinear propagation ($\Delta\theta = 0°$) and for total walk-off compensation ($\Delta\theta \approx 2.6°$ for these wavelengths in KTA), so it was necessary to find a way to calculate the optimum noncollinear angle between these two limits. This was done by deriving a model for the increase in signal pulse energy after a single pass through the crystal which took account of spatial and temporal displacement of the pump, signal and idler beams. Since the gain of an OPO is determined by the temporal and spatial overlap of all three beams it was necessary to consider spatial walk-off, propagation angles, diffraction of the beams from their foci in the centre of the crystal, pulse durations, and temporal walk-away as determined by the group velocities. Using the mathematical analyses of Boyd and Kleinman [30] and Guha et al [31], expressions for the fields of each of the waves were derived, including all the above factors so that the fields are functions of x, y and z (dimensions in the crystal), and of time, t. The distance from the front face of the crystal at which the pump, signal and idler pulses exactly overlap in time is represented by z_0.

$$E^p(x,y,z,t) = \frac{E_0^p}{(1+i\tau_p)} \exp\left[\frac{-(x^2+y^2)}{w_{0p}^2(1+i\tau_p)} - \frac{2\ln 2\left(t - \frac{(z-z_0)}{u_p}\right)^2}{\Delta\tau_p^2}\right] \tag{4.4a}$$

$$E^s(x,y,z,t) = \frac{E_0^s}{(1+i\tau_s)} \exp\left[\frac{-((x-\Delta\theta_s(z-l/2))^2+y^2)}{w_{0s}^2(1+i\tau_s)} - \frac{2\ln 2\left(t - \frac{(z-z_0)}{u_s}\right)^2}{\Delta\tau_s^2}\right] \tag{4.4b}$$

$$E^i(x,y,z,t) = \frac{E_0^i}{(1+i\tau_i)} \exp\left[\frac{-((x-\Delta\theta_i(z-l/2))^2+y^2)}{w_{0i}^2(1+i\tau_i)} - \frac{2\ln 2\left(t - \frac{(z-z_0)}{u_i}\right)^2}{\Delta\tau_i^2}\right] \tag{4.4c}$$

where $\tau_j = 2(z - l/2)/b_j$

l = crystal length

b_j = confocal parameter = $w_{0j}k_j$

w_{0j} = radial beam waist

u_j = group velocity

$\Delta\tau_j$ = pulse duration

The factor $E_0 j$ is the electric field amplitude of wave j at the beam waist and is given by

$$\left|E_0^j\right|^2 = \frac{2P_{av}}{\pi n_j c \varepsilon_0 w_{oj}^2 f \Delta\tau_j} \tag{4.5}$$

where P_{av} is the average power of the modelocked pulse train, with repetition frequency f. All other symbols have their usual meanings. Assuming steady-state conditions, the preceding expressions for the electric fields can be used to calculate the single pass increase in signal pulse energy, ΔQ_s, by following the analysis of Guha et al:

$$\Delta Q_s = -\frac{1}{2}\omega_s d_{eff}\varepsilon_0 \,\mathrm{Im}\int E_s^* E_p E_i^* \, dx\, dy\, dz\, dt \tag{4.6}$$

The noncollinear angle $\Delta\theta$ is included in the spatial dependence of the beams, so Equation 4.6 can be used to evaluate the dependence of ΔQ_s on $\Delta\theta$. The resulting values only give the gain relative to the gain for the collinear case, $\Delta\theta = 0°$. No attempt was made to model the absolute value of the gain; such an analysis would have to include a solution of the coupled wave equations to account for varying pulse amplitude throughout the crystal. Equation 4.6 is best used simply to determine the optimum geometry for a critically phasematched ultrashort pulse OPO.

Fig. 4.11 shows the relative gain for the KTA-based OPO for a pump wavelength of 816 nm, which was used experimentally, requiring a pump propagation angle of 38.8° to generate an idler wavelength of 3.5 μm (see Appendix B for other parameters used in the model). It can be seen from these curves that the signal gain is optimised for a noncollinear angle of ~0.4°. This value was verified experimentally, as will be discussed later in this chapter. Note that this angle corresponds to the value of $\Delta\theta$ at which the tuning curve of Fig. 4.10 turns back on itself, ie. the minimum pump propagation angle at which phasematching can be sustained for a given wavelength combination. This implies that it is not necessary to

go through the complex calculations of Equations 4.4 to 4.6 to determine the optimum noncollinear angle for a given OPO. Instead, the simpler method of calculating a tuning curve from Equation 4.3 can be used to produce the same result.

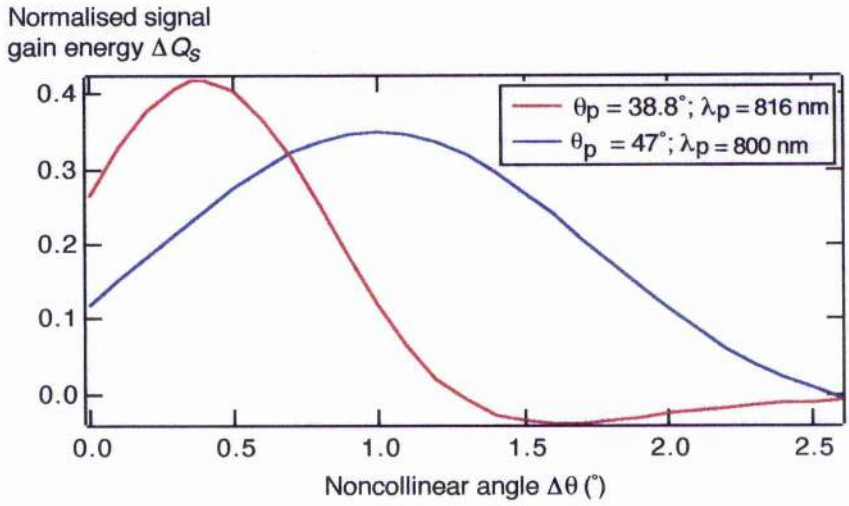

Figure 4.11 Variation of relative gain with noncollinear angle for the KTA-based OPO (red line), showing a maximum gain at a noncollinear angle of ~0.4°. Shown for comparison (blue line) is a curve modelling the OPO of Powers et al [14],which used complete compensation for walk-off.

The remaining curve on Fig. 4.11 represents the KTA-based OPO of Powers et al [14], mentioned earlier as using a noncollinear angle equal to the walk-off angle to achieve operation at shorter idler wavelengths. The peak of the gain curve occurs at a larger noncollinear angle, and is very much broader than for the mid-infrared KTA-based OPO, which explains how oscillation was maintained for a large noncollinearity.

The following section describes the alignment of the OPO cavity, to achieve oscillation in accordance with the above model.

4.4 Cavity configuration and alignment

The KTA-based OPO was configured as a symmetric x-cavity, pumped by the self-modelocked Ti:sapphire laser described in Chapter 3. All mirrors had highly reflecting coatings centred at 1.1 μm for resonance of the signal. The coatings were

also specified for high transmission at the pump wavelength (800 nm) and idler wavelengths from 2.5 to 4 μm. In addition, the curved mirrors, which had radii of curvature of -100 mm, were coated onto calcium fluoride substrates for maximum transmission of the idler. The crystal was mounted on an xyz-translation stage to allow optimum positioning in the stability region between the two curved mirrors. Rotational adjustment was provided about the vertical axis for angle tuning; the *xz*-plane of the crystal therefore lay horizontally. This arrangement required a vertically polarised pump beam, to generate a horizontally polarised signal beam for which dispersion compensation could be readily provided by a prism pair in the horizontal plane. Angular rotation of the crystal meant that it did not need to be oriented normal to the incident pump beam, so no isolator was required to prevent back reflections from reaching the Ti:sapphire laser. This was advantageous in that all the available laser power (~1.5 W) could be used to pump the OPO, with no losses being incurred in an isolator. The pump beam was introduced into the cavity through the first curved mirror via a lens of focal length 50 mm. A schematic of the cavity is depicted in Fig. 4.12.

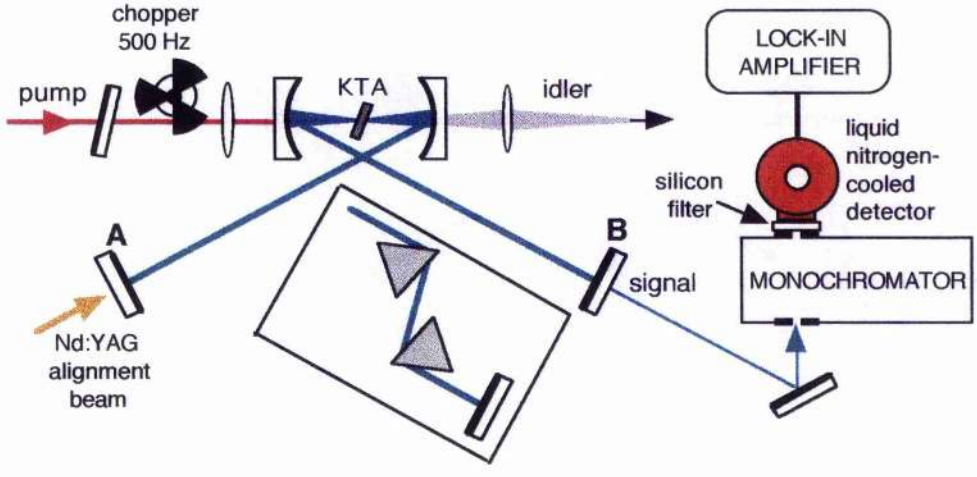

Figure 4.12 Cavity configuration of the KTA OPO, including the detector and Nd:YAG laser used for alignment. The inset shows the position of prisms used for dispersion compensation.

Alignment of a noncollinear OPO is rather more complex than for a collinear noncritically phasematched OPO (hence the general preference for noncritical phasematching). The noncollinearity implies that the pump and signal follow

different paths within the cavity, so the pre-existing pump beam cannot be used for accurate alignment. The path of the signal beam is unique, but obviously cannot be traced until oscillation is achieved. Instead, it is necessary to monitor the single pass spontaneous parametric fluorescence at the signal wavelength which is generated by the pump beam incident on the crystal. In this case, the fluorescence power was very weak (typically <1 pW), so very sensitive detection was needed. A liquid nitrogen-cooled germanium detector [32] was used in conjunction with a digital lock-in amplifier [33], positioned as shown in Fig. 4.12. The incoming pump beam was modulated by an optical chopper to enable the lock-in to isolate the required signal. A number of precautions were taken to ensure that nothing other than the signal fluorescence was detected. Firstly, a plane cavity mirror reflecting at 1.1 μm was inserted into the pump beam to block any long wavelength fluorescence from the Ti:sapphire laser. A scanning monochromator was placed before the detector to spectrally resolve the fluorescence, and lastly, a silicon filter was placed over the detector window to exclude any stray ambient light.

A relatively crude alignment of the cavity was adequate initially to observe the fluorescence signal. This was done partly with the pump beam and a small amount of blue light produced by non-phasematched second harmonic generation in the KTA, which were used to position the intracavity beams at the correct height. Walk-off occurred in the horizontal plane only, so the pump and signal would have the same position vertically. The alignment was then further improved by use of a low power diode-pumped Nd:YAG laser, the output of which was injected into the OPO cavity through mirror A (see Fig. 4.12). Having a wavelength of 1.064 μm, this beam experienced a similar amount of walk-off as the signal at 1.1 μm, so was used to check the beam path in the horizontal plane. Once this was done, a reasonable level of fluorescence was detected for a single pass through the crystal, there being no mirror in position B (Fig. 4.12) at this stage. The signal could be improved by adjustment of the three remaining mirrors and the crystal. The spectrum of the fluorescence was regularly recorded by scanning the monochromator grating, to monitor any tuning in the position of the peak due to rotation of the crystal. In this way the cavity could be adjusted for optimisation of the peak only, rather than other parts of the spectrum. Fig. 4.13 shows two typical fluorescence spectra; the very large bandwidth meant that maximisation of the fluorescence away from the peak was an easy error to make. Once the single pass signal was optimised, a 30%

Nd:YAG laser output coupler was placed in position B. This transmitted enough fluorescence for the level to be conveniently monitored, while reflecting enough for retroreflection to be achieved. A sudden increase in the detected fluorescence was observed when the output coupler was adjusted into the retroreflecting position, indicative of multiple passes around the cavity and implying that the cavity was properly aligned on the signal beam. However, the transmission of the output coupler was too high to permit oscillation, so it had to be replaced by a high reflector. This was done with great care to ensure that the position of the output coupler was exactly replicated by that of the high reflector, by reflecting a low power red diode laser alignment beam off the surface of the output coupler before it was removed, and then directing the reflected beam to the same location with the high reflector, whilst taking account of a slight difference in thickness between the two mirrors. Oscillation was then achieved by scanning the lateral position of the high reflector to bring the cavity period into synchronism with that of the pump laser.

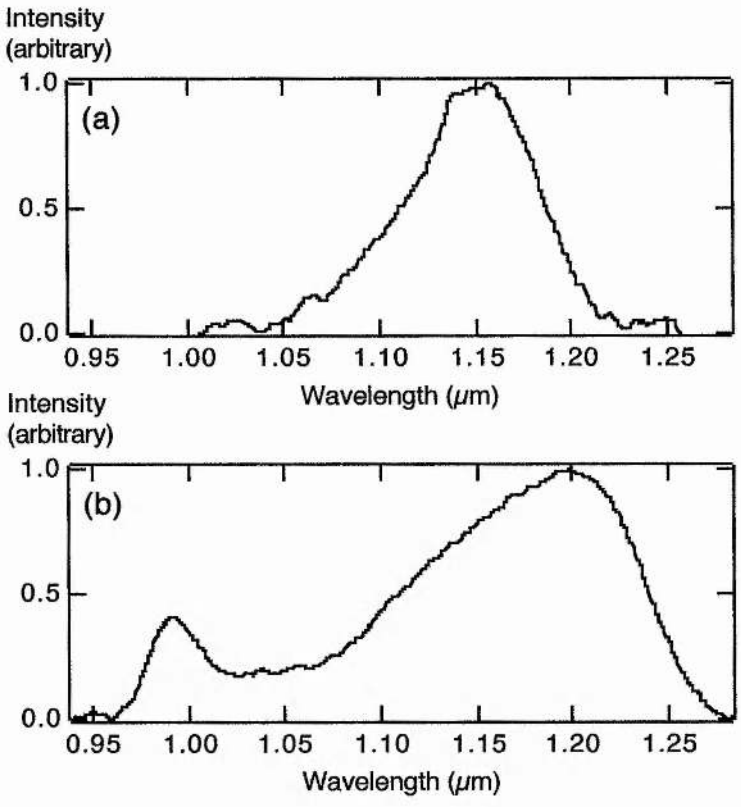

Figure 4.13 Spectra of spontaneous fluoresence at the signal wavelength, recorded during alignment of the OPO, and corresponding to different angular postions of the crystal, hence illustrating tuning. The two peaks of (b) are caused by the double-valued nature of phasematching in KTA – see Fig. 4.26.

4.5 Experimental results

4.5.1 Tuning

Angle tuning of the optical parametric oscillator produced an extensive output. Approximately 4° (internal angle) of crystal rotation covered the entire tuning range. Minor adjustments to the cavity length and the horizontal position of one of the curved mirrors were required to maintain oscillation during tuning. The results of this for two different pump wavelengths, 816 nm and 846 nm, are given in Fig. 4.14. The experimental data are compared with theoretical curves calculated from the Sellmeier coefficients of Fenimore et al [1], with which they show good agreement. The idler data were inferred from the signal wavelength measurements, which were made with a Rees Instruments laser spectrum analyser [34]. The total signal tuning illustrated here covered 1.027 to 1.195 μm, with the corresponding idler being 2.573 to 3.972 μm. Fig. 4.15 shows a set of signal spectra recorded across the tuning range, for a pump wavelength of 796 nm. The spectra all have the double-peaked shape indicative of self-phase-modulation, as would be expected from an OPO with no dispersion compensation. Superimposed over the spectra is a curve showing the transmission of the cavity mirrors, centred at 1.1 μm. From this it can be seen that tuning was achieved across the entirety of the mirror reflectivity bandwidth, so it was the bandwidth which limited the tuning.

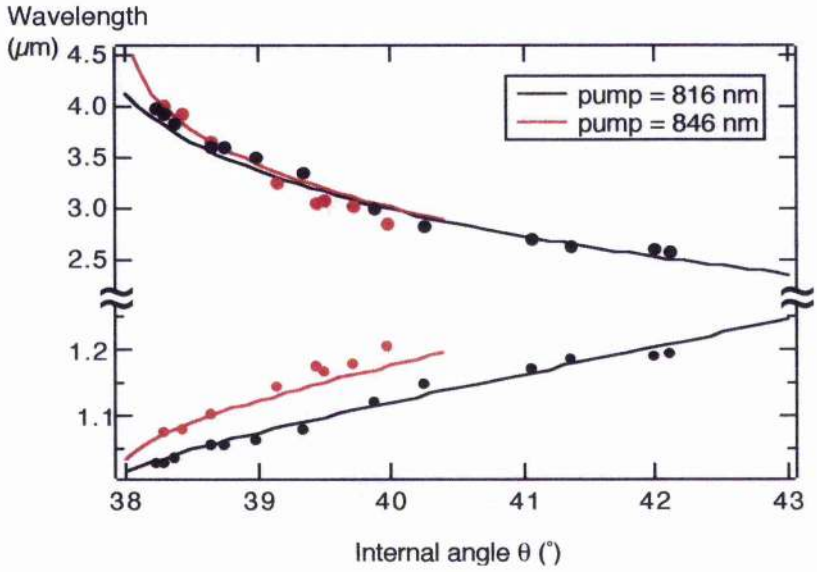

Figure 4.14 Experimental tuning results from the KTA OPO, for two pump wavelengths (circles). The lines are theoretical curves calculated from Sellmeier equations [1].

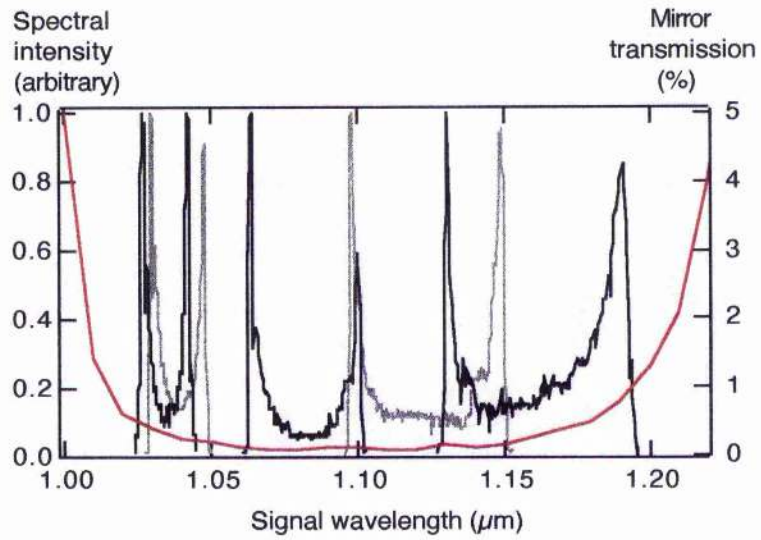

Figure 4.15 Signal spectra recorded across the tuning range of the KTA OPO, without dispersion compensation. The red line shows the bandwidth of the cavity mirrors. Pump wavelength = 796 nm.

4.5.2 Threshold

The oscillation threshold of the OPO, measured by using a neutral density wheel to attenuate the pump beam, was found to be 700 mW. This is in good agreement with a value that can be predicted from the gain model of Section 4.3. It can be seen from Fig. 4.11 that the maximum gain expected from the KTA-based OPO as operated with a noncollinear angle of ~0.4° was about 40% of that for a collinearly phasematched device. Hence the oscillation threshold of a collinear device should be approximately 40% of that of the noncollinear device. The nonlinear coefficients of KTA are similar to those of KTP [35], so a previously reported value of the threshold of a noncritically phasematched Ti:sapphire-pumped femtosecond KTP-based OPO [36] can be used for comparison. That device had a threshold of 300 mW, which is ~43% of the threshold for the KTA-based OPO, so there is good agreement between experiment and the model.

4.5.3 Signal pulse characterisation

No suitable output coupler was available for use in the OPO. Instead, a measurement of the signal power was made by introducing a Brewster-cut prism into

one arm of the oscillating cavity. The apex of a prism can be inserted into an intracavity beam sufficiently far to pick off part of the beam for measurement while leaving enough intensity to sustain oscillation. 80 mW of signal power were measured in this way. It has been previously noted [36] that a near-optimal output coupler can extract 40% to 50% more power than a prism. It can therefore be estimated that up to 120 mW would have been available from an appropriate output coupler.

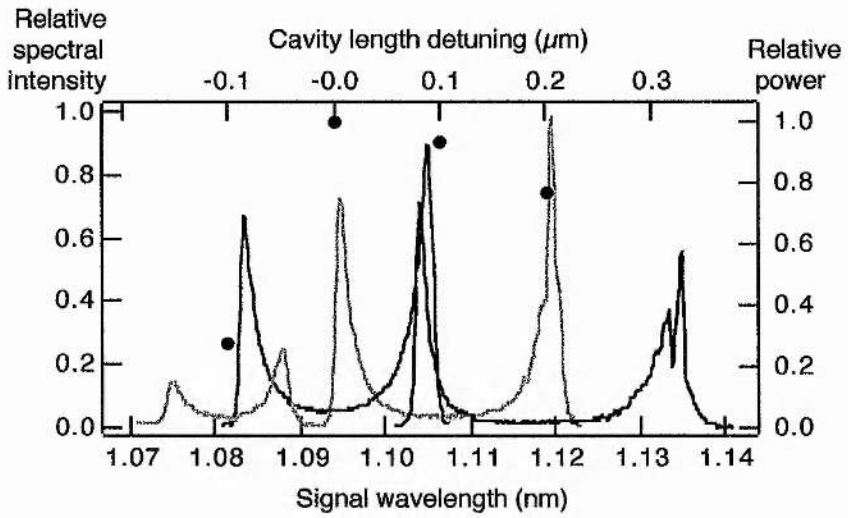

Figure 4.16 Cavity length tuning. The signal spectra were recorded for detuning of the cavity length by 100 nm increments. The circles represent the relative signal power for each cavity length.

As well as the angle and pump tuning evident from Fig. 4.14, a small amount of tuning was available by variation of the cavity length. Oscillation could be sustained over a change in length of ~500 nm, resulting in ~40 nm tuning of the signal. Fig. 4.16 shows a set of signal spectra recorded for de-tuning of the cavity length by 100 nm increments. Comparison of the areas under the spectra indicates that the OPO maintained a signal output power within 80% of the maximum over 200 nm of cavity length variation. This implies that the OPO was tolerant to quite large shifts in cavity length, and offered a stable output.

The signal pulses were further studied via autocorrelation measurements. A standard second harmonic Michelson interferometer autocorrelator set-up was used, with a 2 mm-thick BBO crystal to generate the frequency-doubled light which was then detected using a photomultiplier tube. An interferometric autocorrelation

recorded in this way is shown in Fig. 4.17, with a corresponding spectrum centred at 1.12 μm. As expected from the spectrum, the autocorrelation shows a high level of chirp. Correlations distorted in this way are unreliable indicators of pulse duration, so the width of the signal pulses was measured independently from an intensity autocorrelation (not shown here). A $\mathrm{sech}^2(t)$ pulse shape was assumed, leading to a pulse duration of 790 fs.

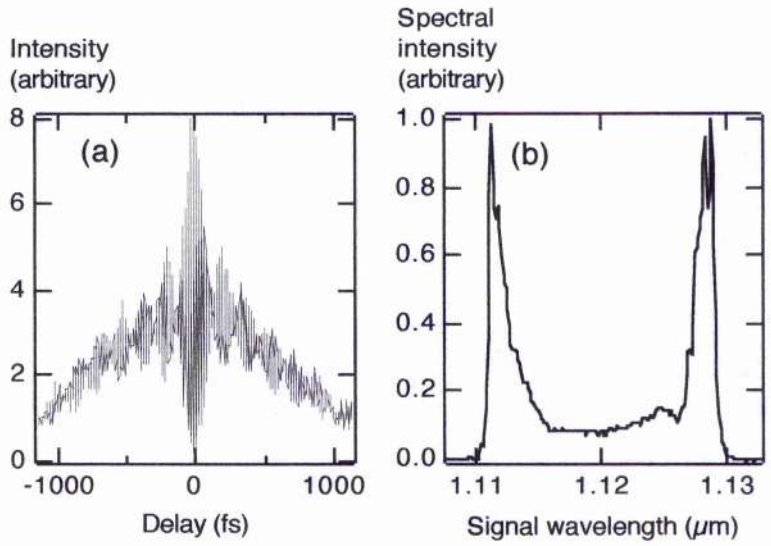

Figure 4.17 Autocorrelation of signal pulses from the uncompensated cavity (a), and accompanying spectrum (b). The pulse duration was 790 fs.

4.5.4 Dispersion compensation

The spectral and temporal quality of the signal pulses was vastly improved by the implementation of dispersion compensation, in the form of a pair of SF14 prisms inserted into one arm of the cavity (see inset of Fig. 4.12). The apex separation was 237 mm. An interferometric autocorrelation and corresponding spectrum of the resulting pulses are presented as Fig. 4.18. These measurements show essentially chirp-free pulses with a single-peaked spectrum. The autocorrelation implies a 69 fs pulse duration, for a $\mathrm{sech}^2(t)$pulse shape. The spectrum, centred at 1.13 μm, has a bandwidth of 20.5 nm; the combination of these results gives a time-bandwidth product of 0.33, thereby demonstrating that the pulses were near-bandwidth-limited.

Further signal spectra were recorded across the tuning range of the

compensated cavity; these appear as Fig. 4.19. The spectra are of good quality at all wavelengths, and as before, span the entire bandwidth of the cavity mirrors. These wavelengths were generated for a pump wavelength of 816 nm.

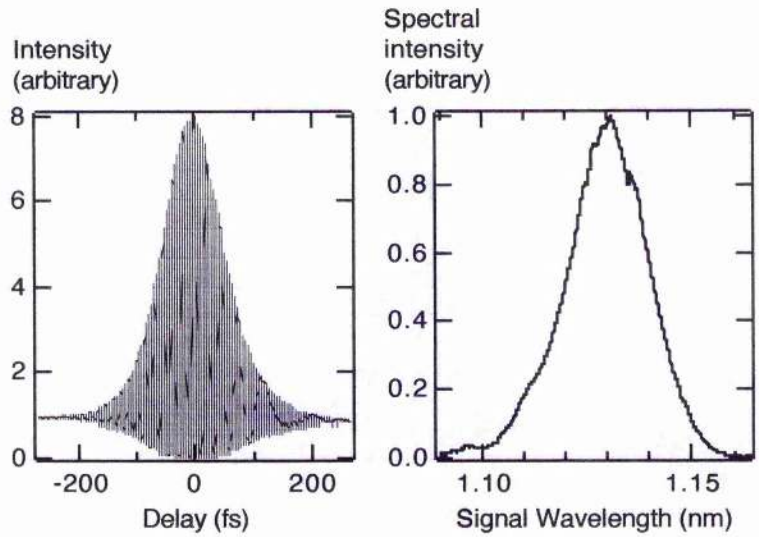

Figure 4.18 Autocorrelation of signal pulses from the compensated OPO cavity (a), and accompanying spectrum (b). The pulse duration was 69 fs, and the spectral bandwidth was 20.5 nm, which imply that the pulses were near-bandwidth-limited.

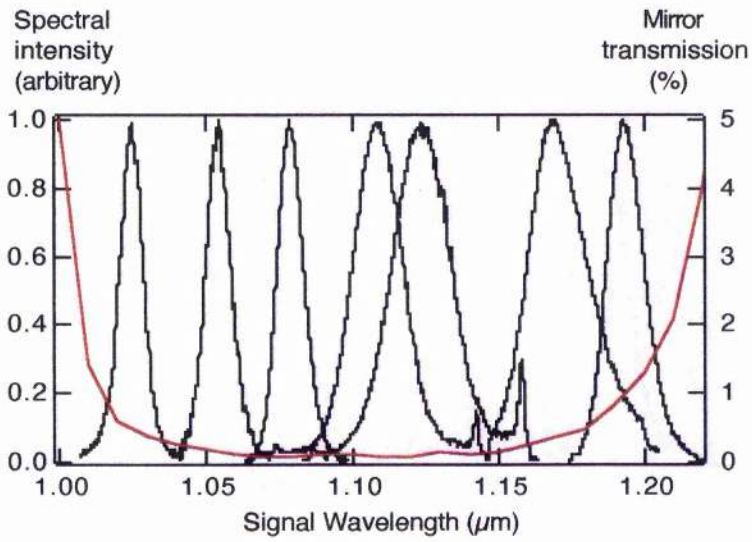

Figure 4.19 Signal spectra recorded across the tuning range of the dispersion compensated OPO. The red line represents the bandwidth of the cavity mirrors. Pump wavelength = 816 nm

4.5.5 Idler pulse characterisation

The idler output was studied in some detail, as the generation of mid-infrared wavelengths was the raison d'être of the OPO. The idler pulses were extracted from the cavity through the second curved mirror, as shown in Fig. 4.12. The small noncollinear angle used meant that the idler was not generated at an extreme angle, so there were no problems relating to clipping of the beam on the mirror mount. The output was highly divergent, and was collimated with a calcium fluoride lens.

Spectral measurements of the idler were made using a room temperature lead selenide detector [37] connected to a chart recorder via the lock-in amplifier. A scanning monochromator was used to obtain spectral resolution, and a germanium filter blocked light at the pump and signal wavelengths. Fig. 4.20 presents a number of idler spectra recorded from the uncompensated cavity, which were generated from a pump wavelength of 796 nm, and are counterparts of the signal spectra of Fig. 4.15. Also included is a longer wavelength spectrum at 3.8 μm which was obtained by tuning the pump laser to 840 nm. These results indicate that the idler spectra were single-peaked, rather than having the double-peaked shape of the uncompensated signal spectra. This is because the idler pulses had much less opportunity of acquiring self-phase-modulation. They only propagated once through the crystal, thus encountering little dispersion, and the idler intracavity peak power was very much less than that of the signal.

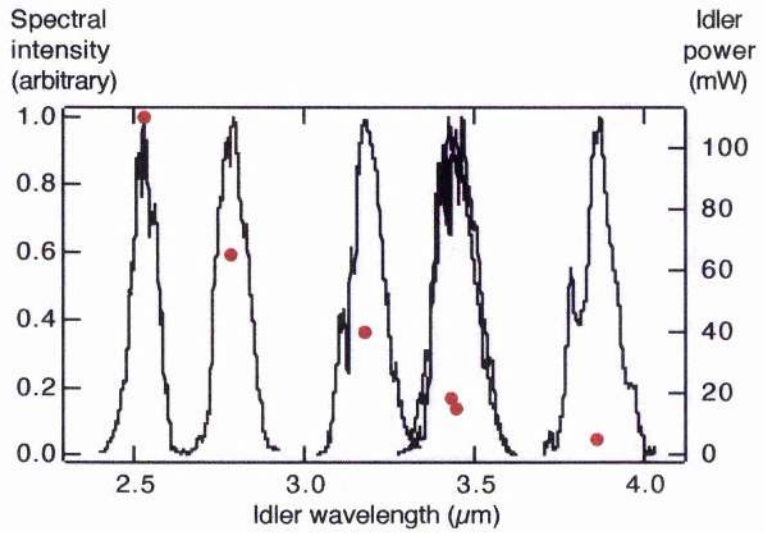

Figure 4.20 Idler spectra recorded across the tuning range, for a pump of 796 nm. The red circles show the power measured for each spectrum.

Fig. 4.21 shows a spectrum of the longest idler wavelength obtained from the OPO, with a peak at 4.1 μm, and a full-width-half-maximum bandwidth of 300 nm. The pump laser wavelength was 840 nm, and the central signal wavelength was measured to be 1.05 μm. These two values imply an idler wavelength of 4.2 μm, which is obviously not what was observed. This may be attributed to the double-peaked nature of the signal spectra, where the maximum signal power is shifted away from the spectral centre so that the maximum pump-signal interaction occurs at longer or shorter wavelengths. The result in this case suggests that the longer wavelength end of the signal pulses interacted with the pump, which would serve to produce a smaller pump-idler noncollinearity than interaction of the shorter wavelengths. Additionally, the group velocity walk-away within the KTA crystal was such that the longer wavelength end of the signal pulses had more temporal overlap with the idler pulses, resulting in a shorter idler wavelength than would be predicted from the centre of the signal spectrum. The conclusion to be drawn here is that direct measurement of the idler is the most accurate way of determining the idler wavelength.

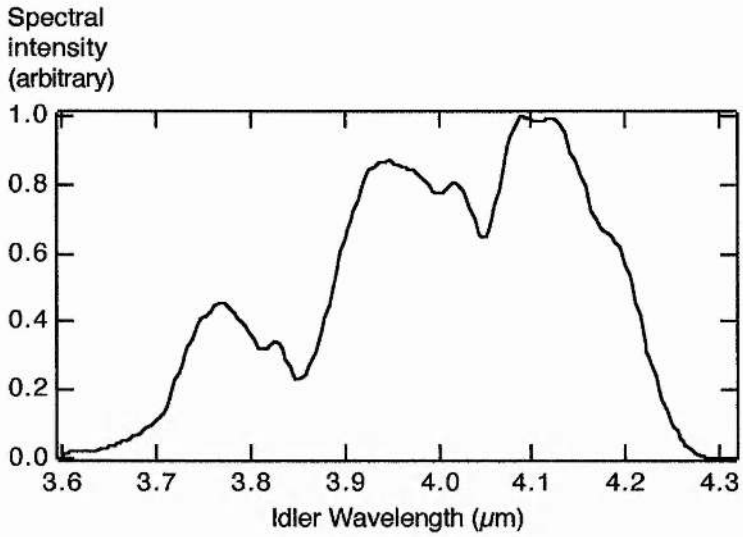

Figure 4.21 Spectrum of the longest idler wavelength measured from the KTA OPO.

The very broad spectral bandwidth of >300 nm is due to the phasematching properties of KTA. As will be seen in a later figure (Fig. 4.26), the signal and idler tuning curves turn back on themselves; this occurs for the idler at ~4 μm. This behaviour produces an increase in the angular acceptance bandwidth, and a wide range of idler wavelengths can be phasematched for a very small range of propagation

angles, which results in a wide spectral bandwidth. A wavelength of 4 μm and a bandwidth approaching 400 nm implied that pulses with sub-100 fs durations could be generated. This was confirmed by autocorrelation of the idler, as will be discussed shortly.

The modulation on the idler spectrum of Fig. 4.21 may be a real feature, but could be attributable to experimental causes. A relatively long acquisition time was used to record the spectrum, and any fluctuations in power, or in signal wavelength (due to minor instabilities in the cavity length) would have been translated into modulation of the idler. Additionally, the mildly periodic nature of the variations could be the result of anomalies in the monochromator grating.

Returning to Fig. 4.20, the data points shown represent measurements made of the average idler power across the tuning range. A maximum of 110 mW was observed at 2.5 μm, falling steadily to about 5 mW at 3.8 μm. This reduction is to be expected from the decrease in photon energies. These measurements are corrected for an 8% transmission loss in the calcium fluoride lens and mirror substrate, a 15% loss at the germanium filter used to block shorter wavelengths, and for the percentage transmission of the mirror coating at each relevant wavelength.

The autocorrelation of femtosecond idler pulses much longer than 2 μm presents practical problems not encountered in the measurement of signal pulses. The primary difficulty lies in the lack of suitable fast or sensitive detectors operating beyond 1 μm, with the result that interferometric autocorrelation is seldom employed. The less stringent time resolution demands of intensity autocorrelation make that technique somewhat less problematic. Holtom et al [38] published an intensity autocorrelation of 160 fs idler pulses centred at 2.75 μm from an optical parametric amplifier, while more recently, Spence et al [39] presented data for 150 fs pulses at 2.4 μm. An alternative technique is that of cross-correlation with near-infrared signal or pump pulses; the resulting wavelength of the correlated beam is short enough to be detected by a photomultiplier tube. This method has been used for femtosecond idler pulses at 3.3 μm [39] and 3.55 μm [40]. It is rather unsatisfactory, however, as it does not provide as much useful information as autocorrelation due to lack of interferometric detail. Also, the inferred pulse duration depends on the pulse durations of both pulse trains and on any timing jitter between them. Thus, a reliable technique for the interferometric autocorrelation of mid-infrared femtosecond pulses would be extremely useful, especially in light of the

current great interest in the construction of mid-infrared sources. Such a technique was developed to characterise the idler pulses of the KTA-based OPO, and will now be described.

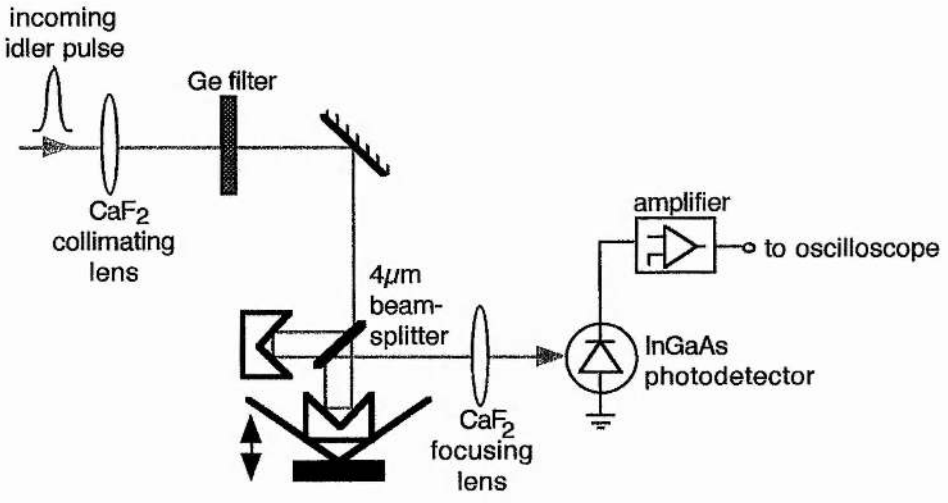

Figure 4.22 Configuration of the autocorrelator used to measure the idler pulses.

Fig. 4.22 depicts the arrangement of the autocorrelator, which was configured in a Michelson interferometer design, and worked in real time. After collimation of the idler, a gold mirror steered the beam into the correlator. The beam splitter was custom-coated for 50:50 performance at 3.5 μm onto a 1 mm-thick calcium fluoride substrate. Both retroreflectors were gold-coated, one being static and the other mounted on a loudspeaker cone for scanning at 10 Hz. The main feature of note is the lack of a frequency doubling crystal. It was found that by focussing the idler beam (with a calcium fluoride lens) onto the surface of a 1 mm-diameter InGaAs PIN detector [41] used in unbiased photovoltaic mode, a sufficient second-order nonlinear response occurred in the semiconductor for autocorrelation. In fact, it was this discovery that led to the development of the LED autocorrelator of Chapter 3. The detector was responsive out to 1.8 μm and was thus suitable for autocorrelation of pulses out to 3.6 μm, although a low noise high gain amplifier [42] had to be used to boost the output voltage for wavelengths above 2.8 μm. Below this, the interferometric autocorrelation trace could be viewed directly on a 1 MΩ input-impedance oscilloscope.

This autocorrelation scheme is advantageous for several reasons. Firstly, one of

the difficulties of autocorrelating mid-infrared pulses is in finding an appropriate frequency-doubling crystal with a suitably large phasematching bandwidth, because the idler pulse bandwidth can be very wide, as demonstrated here. The response of the InGaAs detector was not reliant on phasematching, and could be used to measure any pulses between 1.8 and 3.6 μm without realignment. Also, a single detector is much more straightforward to align than a doubling crystal and a photomultiplier tube, and makes for a more compact system. No high voltage supply is needed. Having the nonlinear interaction and the detection in the same component means that all the autocorrelation signal is detected, leading to a better efficiency. This is particularly beneficial for the low powers typically generated in the MIR. And finally, the absence of a nonlinear crystal substantially reduces the cost of a correlator.

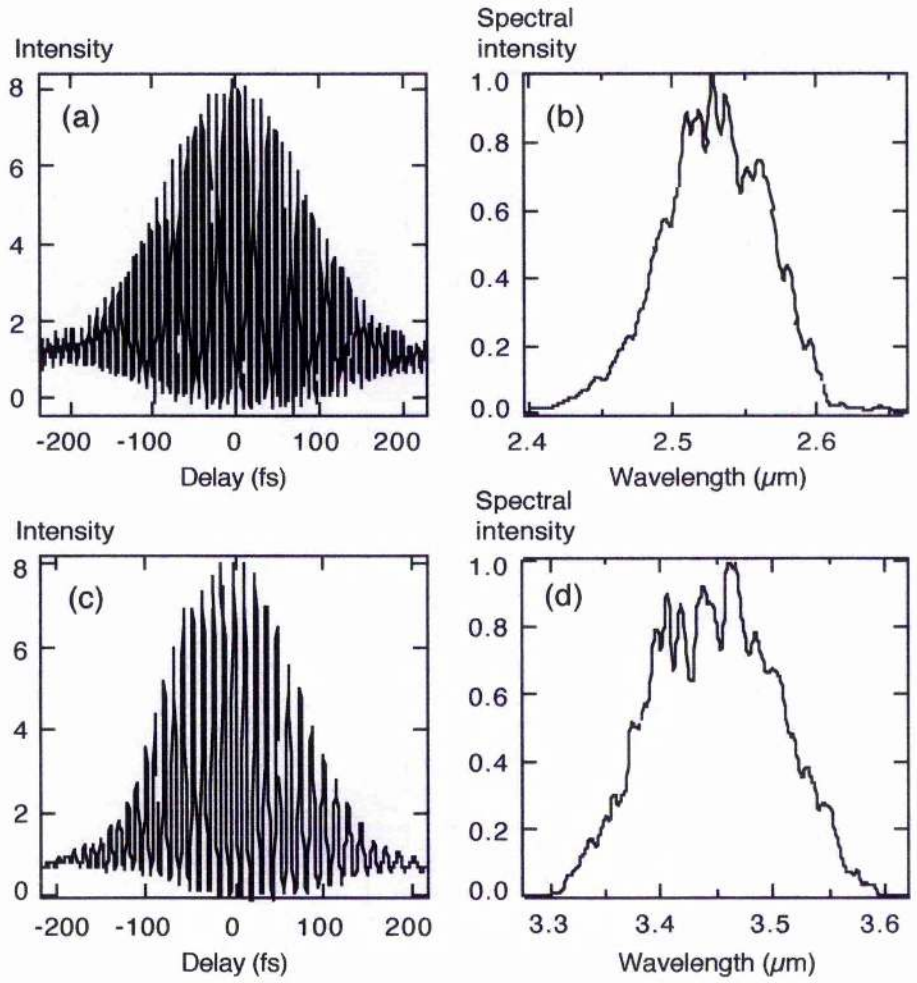

Figure 4.23 Autocorrelations of idler pulses and corresponding spectra. The pulses at 2.52 μm ((a) and (b)) had a duration of 116 fs and a time-bandwidth product of 0.53. The pulses at 3.45 μm ((c) and (d)) were 94 fs long, with a time-bandwidth product of 0.35.

Idler autocorrelations made with this system are shown in Fig. 4.23, for idler wavelengths of 2.52 and 3.45 μm, as indicated by the accompanying spectra. The pulses were from the uncompensated cavity. Assuming a $\mathrm{sech}^2(t)$ pulse shape, the shorter wavelength pulses had a duration of 116 fs. The time-bandwidth product is 0.53, implying a small amount of frequency chirp. However, at 3.45 μm, the pulse duration was 94 fs, leading to a time-bandwidth product of 0.35, which indicates near-transform-limited pulses. The autocorrelations confirm what was suggested by the spectral data of Fig. 4.20 – little of the phase distortion of the highly chirped uncompensated signal pulses was transferred to the idler pulses. Hence, it is possible to generate high quality, sub-100 fs, near-chirp-free MIR pulses from an OPO without the need for dispersion compensation. Prisms tend to introduce loss into an OPO cavity, reducing output powers, and also increase the spatial extent of a cavity in terms of laboratory space, so it is all to the good if they are not needed in certain circumstances.

Given the increased spectral bandwidth at longer idler wavelengths, it is likely that the pulses at 4 μm were shorter than those characterised here, but the limitations of the InGaAs detector did not permit measurements to the extreme of the tuning range.

4.5.6 Noncollinear angle

Once the OPO was oscillating it was possible to make an experimental measurement of the noncollinear angle. This was done by examining the spatial separation of the pump and signal beams transmitted through the second curved mirror, which implied an angle between the two beams of 0.76°. This was outside the crystal, whereas the internal angle was the value of interest. Taking 1.8 as the refractive index of KTA at the wavelengths of interest gives an internal noncollinear angle of 0.42°. This is in excellent agreement with the value predicted by the theoretical models in Section 4.3. It can thus be concluded that these models are reliable tools to use when designing a noncollinear critically phasematched OPO.

4.5.7 Visible light generation

In addition to the infrared wavelengths generated by the OPO, a small amount of visible light was produced from non-phasematched nonlinear interactions between the pump, signal and idler. Four processes were observed: frequency doubling of the pump (~400 nm), frequency doubling of the signal (~515 to 600 nm), sum-frequency-mixing of the pump and signal (~450 to 480 nm), and sum-frequency-mixing of the pump and idler (~600 to 670 nm). The frequency doubling of the signal was the dominant interaction. These visible outputs were recorded photographically, as shown in Fig. 4.24. This is a multiple exposure photograph. The visible beams, leaving the cavity through the second curved mirror, were spatially separated using a prism. Between each exposure the OPO was angle-tuned, and the extracavity position of the beams altered slightly using a silver mirror. The photograph is a vivid illustration of the tuning capabilities of the OPO. The pump-idler mixing output tuned in the opposite direction to the other outputs because long signal wavelengths correspond to short idler wavelengths. The static blue beam at the top of the picture is the frequency-doubled pump, which was not tuned during the photographic procedure.

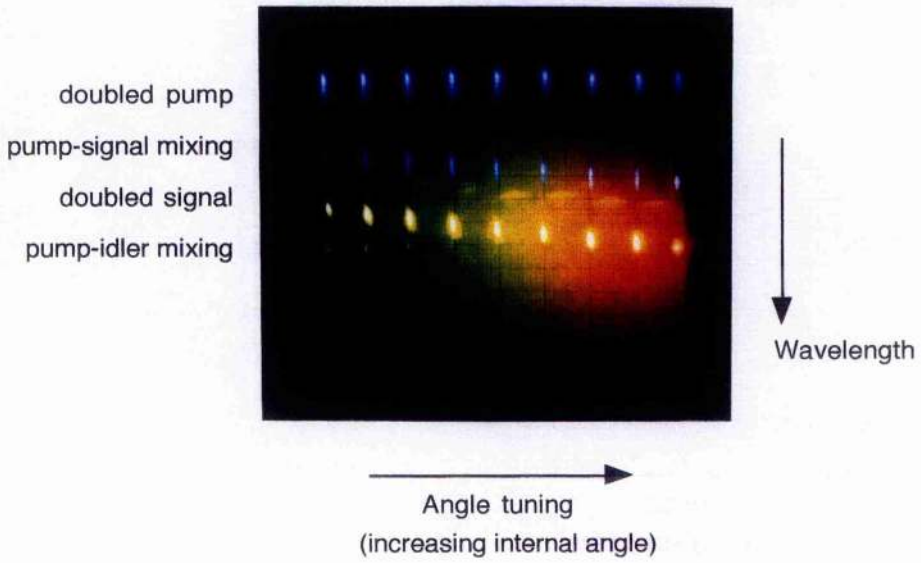

Figure 4.24 Visible light generated by unphasematched mixing processes in the OPO. The OPO was tuned between each exposure of this multiple exposure photograph.

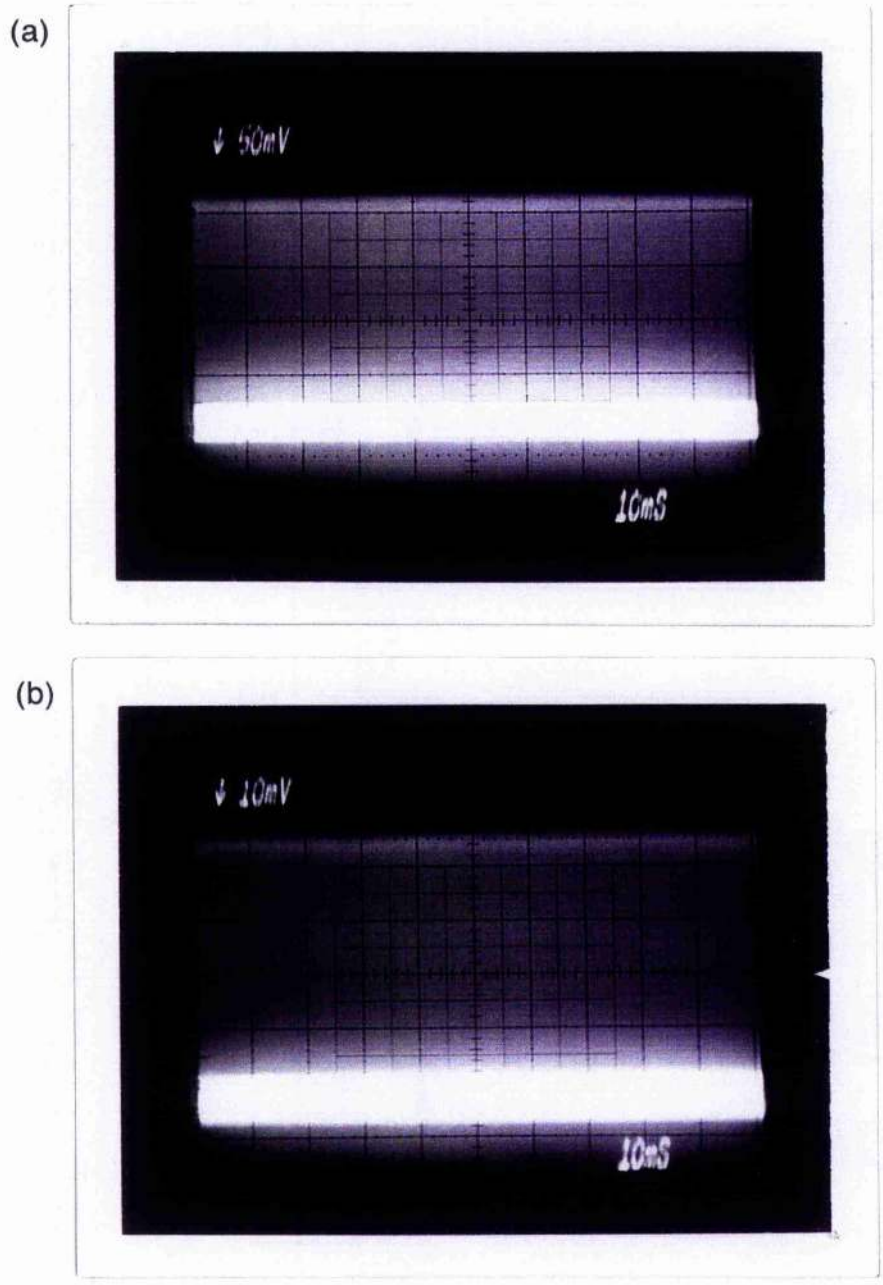

Figure 4.25 Oscillograms of the pump (a) and signal (b) pulse trains from the OPO.

4.5.8 Amplitude noise

The amplitude noise of the OPO was investigated. Both the pump and signal pulse trains were studied using a fast response germanium photodiode. Oscillograms of the pulse trains can be seen in Fig. 4.25, and indicate amplitude noise of between 5% and 10%. No suitable detector was available to study the idler pulses, but it is likely that they had a similar noise level. The amplitude fluctuations of the OPO

were probably primarily caused by those of the pump, so stabilising the pump would have improved the performance of the OPO. Amplitude noise of the pump pulses was mainly due to air currents caused by air-conditioning and draughts, and could therefore have been reduced by covering the Ti:sapphire system with a box. This was not done because it would have interfered with daily maintenance of the laser.

4.6 Concluding remarks

4.6.1 Future work

The KTA-based optical parametric oscillator demonstrated good performance in most respects, but is still open to further improvement. This is especially true in respect of the tuning range, since the generated idler wavelengths covered only half of the 3 to 5 μm mid-infrared objective. It was stated earlier in the chapter that the tuning was limited by the bandwidth of the cavity mirrors, which only allowed the generation of signal wavelengths from ~1.05 to 1.2 μm. The shortest of these was too long for the production of idler longer than 4 μm from the pump wavelengths used. There are two solutions to this problem, which would extend the tuning range of the OPO.

The first solution would be to increase the pump wavelength. Given that the existing mirrors constrain the signal wavelength to be no shorter than ~1.05 μm, a pump of ~870 nm would be required. This is really beyond the limit of good performance available from the existing Ti:sapphire laser. However, the fluorescence bandwidth of Ti:sapphire extends far beyond this point, to ~1.18 μm [43], and with suitable cavity optics it is possible to achieve oscillation at wavelengths well over 1 μm [44].

A less drastic option than reconfiguring the Ti:sapphire laser would be to replace the OPO mirrors with alternatives having a reflectivity bandwidth centred at a shorter wavelength. For example, supposing the pump laser ran at 830 nm, an idler of 5 μm could be obtained for a signal of just below 1 μm. Hence a change of less than 100 nm in the bandwidth of the cavity mirrors would extend the tuning to 5 μm.

The picture is complicated somewhat by the phasematching behaviour of KTA. Fig. 4.26 illustrates the tuning of the signal and the idler for various Ti:sapphire pump wavelengths. From this it can be seen that the tuning curves turn

back on themselves, such that for each propagation angle there are two available signal-idler pairs. The top half of the signal branch corresponds to the bottom half of the idler branch, and vice versa. The turning point of the idler occurs between 4 and 5 μm, so that in most instances it is necessary to push the operation of the OPO round the turn onto the top branch to tune out to 5 μm. Unfortunately, however, given the opportunity to oscillate at either of the signal-idler pairs (by an appropriate mirror bandwidth) it is more likely that the OPO would run at the long signal/short idler combination since this minimises the pump-idler noncollinearity and hence maximises the signal gain. It is therefore necessary to force oscillation onto the longer idler branch, by having cavity mirrors with a reflectivity cut-off at the signal branch turning point so that only oscillation of the shorter signal wavelengths can be sustained. The blue curve on Fig. 4.26 shows that for the existing mirrors, which have a cut-off at ~1.19 μm, a pump wavelength of ~935 nm would be required. Hence, new OPO mirrors would be needed for such a regime with the Ti:sapphire laser as it is currently configured. The wavelength at which the signal branch turns back varies quite rapidly with pump wavelength and propagation angle, so careful control of the mirrors, pump and crystal would be needed to achieve oscillation at 5 μm from an OPO based on KTA.

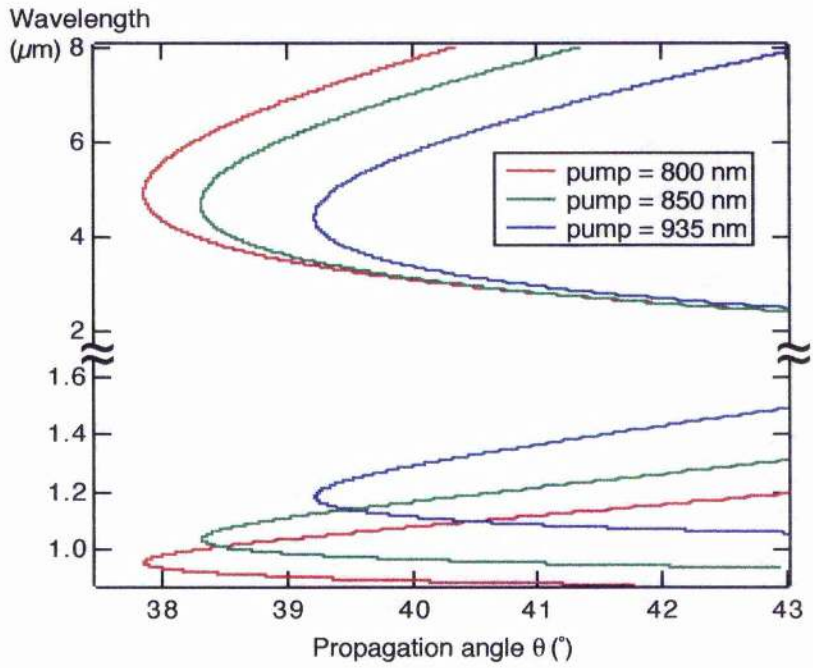

Figure 4.26 Theoretical tuning curves for type II critical phasematching of a KTA OPO, for three pump wavelengths.

The study of the cavity length tuning (Section 4.5.3) showed that the OPO was reasonably tolerant to changes in cavity length as far as the output power was concerned. However, the signal wavelength varied quite substantially over the same range of cavity lengths. The length of the cavity was subject to small fluctuations caused by draughts and temperature variations in the laboratory environment, which produced small variations in the output wavelength which would be unacceptable for some applications. A problem of this sort can be readily solved by the implementation of electronic cavity stabilisation. A simple technique for doing this involves mounting one end mirror of the cavity onto a piezoelectric transducer. Part of the output beam is dispersed by a prism or grating onto a pair of photodiodes. If a change in the cavity length causes the wavelength to shift, the dispersion angle will change and the signals detected by the photodiodes will alter relative to each other. The detection of this change can be configured so that the transducer voltage is increased or decreased appropriately to bring the cavity back to the original wavelength.

4.6.2 Conclusions

The construction, operation and characterisation of a noncollinear, critically phasematched tunable mid-infrared femtosecond OPO based on KTA have been described in this chapter. The choice of KTA as the nonlinear media was justified, and a short review of other KTA-based nonlinear devices was given, to put this work into context. Two models to calculate the optimum noncollinear angle for operation of a critically-phasematched OPO were discussed, one of which was very simple, and the other, more complex model, gave predictions of the expected gain. The theoretical values were in good agreement with the experimental results of this device and those of other researchers [14, 36], so the models can be taken to be accurate and reliable.

Extensive tuning was obtained from the OPO. A signal output of 1.03 to 1.2 μm, and an idler output of 2.51 to 4.1 μm were generated from angle tuning over ~4°, supplemented with some tuning of the Ti:sapphire pump laser. A maximum signal power of 80 mW was extracted with a Brewster-cut prism, which suggested that over 100 mW would have been available from an optimum output coupler. Idler

power varied from 110 mW to 5 mW with tuning to long wavelengths. The threshold of 700 mW agreed well with the theoretical model – the high value is due to the noncollinear phasematching. Highly chirped signal pulses of 790 fs duration were measured from the uncompensated cavity, but these were significantly improved by the use of a prism pair to provide intracavity dispersion compensation. This resulted in near-bandwidth-limited pulses of 69 fs. Amplitude noise of the signal pulses was low, and was probably caused by noise on the pump pulse train.

A novel autocorrelator was constructed to obtain interferometric autocorrelations of the idler pulses. The correlator was based on a quadratic nonlinearity in an InGaAs detector, which removed the need for a frequency-doubling crystal, was suitable for the autocorrelation of pulses from 1.8 to 3.6 μm, and offered a number of advantages over a conventional autocorrelator. This device was used to produce fringe-resolved autocorrelations of idler pulses at 2.52 μm and 3.45 μm, which revealed the idler output of the uncompensated cavity to be sub-100 fs and essentially chirp-free. Little of the phase modulation of the uncompensated signal pulses was transferred to the idler, indicating that good quality idler pulses can be generated from an OPO without the need for dispersion compensation. To my knowledge, these wavelengths were the longest to have been characterised by interferometric autocorrelation at that time. Techniques to extend the tuning range out to 5 μm were discussed.

Overall, the KTA-based OPO has been shown to be a reasonable source of femtosecond mid-infrared pulses, which could have been developed further. However, since the date of the research presented here, periodically poled nonlinear crystals have come into their own and seem to offer an excellent basis for tunable MIR femtosecond optical parametric oscillators (this subject is addressed further in Chapter 6). Consequently, the main achievement of the work described in this chapter was the development of the MIR autocorrelator. This device is more advantageous than a conventional correlator in several respects, and similar arrangements should allow the characterisation of all-important MIR femtosecond pulses to become common-place.

References

1. D. L. Fenimore, K. L. Schepler, U. B. Ramabadran and S. R. McPherson, J. Opt. Soc. Am. B **12**, 794 (1992).
2. D. L. Fenimore, K. L. Schepler, D. Zelmon, S. Kück, U. B. Ramabadran, P. Von Richter and D. Small, J. Opt. Soc. Am. B **13**, 1935 (1996).
3. L. -T. Cheng. L. K. Cheng and J. D. Bierlein, Proc. SPIE **1863**, 43 (1993).
4. G. M. Loiacono, B. N. Loiacono, J. J. Zola, R. A. Stolzenberger, T. McGee and R. G. Norwood, Appl. Phys. Lett. **61**, 895 (1992).
5. Crystal Associates Inc., 15 Industrial Park, Waldwick, NJ 07463, USA.
6. D. Xue and S. Zhang, Appl. Phys. Lett. **70**, 943 (1997).
7. W. J. Liu, S. S. Jiang, X. R. Huang, X. B. Hu, C. Z. Ge, J. Y. Wang, J. H. Jiang and Z. G. Wang, Appl. Phys. Lett. **68**, 25 (1996).
8. J. D. Bierlein, H. Vanherzeele and A. A. Ballman, Appl. Phys. Lett. **54**, 783 (1989).
9. L. K. Cheng, L. T.Cheng, J. Galperin, P. A. Morris Hotsenpiller and J. D. Bierlein, J. Crystal Growth **137**, 107 (1994)
10. A. H. Kung, Opt. Lett. **20**, 1107 (1995).
11. K. Kato, IEEE J. Quantum Electron. **30**, 881 (1994).
12. L. K. Cheng, L. T. Cheng, J. D. Beirlein, F. C. Zumsteg and A. A. Ballman, Appl. Phys. Lett. **62**, 346 (1993).
13. M. G. Jani, J. T. Murray, R. R. Petrin, R. C. Powell, D. N. Loiacono and G. M. Loiacono, Appl. Phys. Lett. **60**, 2327 (1992).
14. P. E. Powers, S. Ramakrishna, C. L. Tang and L. K. Cheng, Opt. Lett. **18**, 1171 (1993).
15. W. R. Bosenberg, L. K. Cheng and J. D. Beirlein, Appl. Phys. Lett. **65**, 2765 (1994).
16. S. French, M. Ebrahimzadeh and A. Miller, Opt. Lett. **21**, 131 (1996).
17. C. Rahlff, Y. Tang, W. Sibbett and M. H. Dunn, in *Conference on Lasers and Electro-Optics,* Vol. 19 of 1996 OSA Technical Digest Series (Optical Society of America, Washington, DC, 1996), p. 267, paper CWF16.
18. K. Kato, N. Umemura and E. Tanaka, Japan. J. Appl. Phys. part 2: Letters, **36**, L403 (1997).
19. F. G. Colville, T. J. Edwards, G. A. Turnbull, M. H. Dunn and M. Ebrahimzadeh, in *Conference on Lasers and Electro-Optics*, Vol. 11 of 1997 OSA Technical Digest Series (Optical Society of America, Washington, DC, 1997), p. 341, paper CThG3.
20. Ch. Grässer, R. Beigang and R. Wallenstein, in *Conference on Lasers and Electro-Optics*, Vol. 11 of 1997 OSA Technical Digest Series (Optical Society of America, Washington, DC, 1997), p. 201, paper CWB6.
21. A. H. Kung, Appl. Phys. Lett. **65**, 1082 (1994).
22. A. H. Kung, S. L. Fei and H. L. Strauss, Appl. Spectroscopy **50**, 790 (1996).
23. D. G. Lancaster and J. M. Dawes, Opt. Commun. **120,** 307 (1995).
24. D. G. Lancaster and J. M. Dawes, Appl. Opt. **35**, 4041 (1996).

25. B. Boulanger, J. P. Fève, G. Marnier, G. M. Loiacono and D. N. Loiacono and C. Bonnin, IEEE J. Quantum Electron. **33**, 945 (1997).
26. W. P. Risk and G. Loiacono, in *Conference on Lasers and Electro-Optics,* Vol. 19 of 1996 OSA Technical Digest Series (Optical Society of America, Washington, DC, 1996), p. 461, paper CThQ4.
27. W. P. Risk and G. Loiacono, Appl. Phys. Lett. **69**, 4157 (1996).
28. W. R. Bosenberg, W. S. Pelouch and C. L. Tang, Appl. Phys. Lett. **55**, 1952 (1989).
29. P. E. Powers, C. L. Tang and L. K. Cheng, Opt. Lett. **19**, 1439 (1994).
30. G. D. Boyd and D. A. Kleinman, J. Appl. Phys. **39**, 3597 (1968).
31. S. Guha, F. -J. Wu and J. Falk, IEEE J. Quantum Electron. **18**, 907 (1982).
32. Model J16D, EG & G Judson, 2211 Commerce Dr., Montgomeryville, PA 18936, USA.
33. Model SR810, Stanford Research Systems Inc., 1290 D Reamwood Avenue, Sunnyvale, CA 94089, USA
34. Rees Instruments Ltd., Thornbrook, Weyside Park, Catteshall Lane, Godalming, Surrey, GU7 1XE.
35. V. G. Dmitriev, G. G. Gurzadyan and D. N. Nikogosyan, *Handbook of Nonlinear Optical Crystals* (second edition, Springer-Verlag, Berlin, 1997).
36. J. M. Dudley, D. T. Reid, M. Ebrahimzadeh and W. Sibbett, Opt. Commun. **104**, 419 (1995).
37. Model P791-02, Hamamtsu Photonics UK Ltd, Lough Point, 2 Gladbeck Way, Windmill Hill, Enfield, Middlesex, EN2 7JA.
38. G. R. Holtom, R. A. Crowell, and X. S. Xie, J. Opt. Soc. Am. B **12**, 1723 (1995).
39. D. E. Spence, S. Wielandy, C. L. Tang, C.Bosshard and P. Günter, Appl. Phys. Lett. **68**, 452 (1996).
40. S. W. McCahon, S. A. Anson, D. -J. Jang and T. F. Boggess, Opt. Lett. **20**, 2309 (1995).
41. Model G3476-10, Hamamtsu Photonics UK Ltd, Lough Point, 2 Gladbeck Way, Windmill Hill, Enfield, Middlesex, EN2 7JA.
42. Model PA-9, EG & G Judson, 2211 Commerce Dr., Montgomeryville, PA 18936, USA.
43. M. P. Critten, *All-solid-state femtosecond Cr:LiSAF and Cr:LiSGaF lasers*, PhD thesis, University of St Andrews (1996).
44. K. Oppo, *Tunable femtosecond lasers with low pump thresholds*, PhD thesis, University of St Andrews (1996).

chapter five

THE SEMI-MONOLITHIC ULTRAHIGH REPETITION RATE FEMTOSECOND OPTICAL PARAMETRIC OSCILLATOR

5.1 Introduction

The research discussed in this chapter concerns the design and operation of a novel femtosecond optical parametric oscillator (OPO) based on the nonlinear material rubidium titanyl arsenate ($RbTiOAsO_4$), or RTA, as it is more commonly known. One of the aims behind the construction of this source was to produce an OPO with a threshold sufficiently low that the device could be pumped by a diode-pumped all-solid-state laser, such as Cr:LiSAF. There is a considerable amount of interest at the present time in developing all-solid-state ultrashort pulse OPOs, because they will be more compact and cost-effective than systems relying on main-frame gas pump lasers. However, the power levels currently available from diode-pumped femtosecond Cr:LiSAF lasers and the like are at best of the order of 100 mW, so an OPO would need to have a threshold of only a few tens of milliwatts to run sufficiently above threshold.

The two principal criteria to consider when contemplating the construction of such an OPO are the choice of nonlinear material, and the design of the cavity. The next sections of this chapter present the results of such considerations. Section 5.2 includes the reasons for choosing RTA as the nonlinear crystal, a description of some of the properties of the material and a summary of some of the uses to which it has been put, while the contents of Section 5.3 are concerned with a novel cavity design which was implemented in an attempt to produce a low oscillation threshold. Experimental results are presented and discussed in the remainder of the chapter,

which concludes with suggestions for further development of the system.

5.2 RTA

5.2.1 Why RTA?

RTA was chosen as the nonlinear crystal best suited for a low threshold OPO. This choice was based on the results of experiments conducted by the St Andrews femtosecond OPO group before the commencement of the work presented in this thesis. Two OPOs were built, based on the then new nonlinear materials potassium titanyl phosphate (KTP) and RTA, and a detailed comparison of the relative merits of the two systems was undertaken [1, 2]. Both systems were three-mirror resonators, and used non-critical phasematching along the x-axis of the crystal to maximise the nonlinear coefficient. The results most relevant here are the threshold measurements; the KTP-based OPO had a threshold of 230 mW, while that of the RTA-based OPO was only 50 mW. This value represented the lowest threshold reported for a femtosecond OPO up to that time. It was this fact that determined the choice of RTA in the present case. Some linear and nonlinear optical properties of the material are now given.

5.2.2 Properties of RTA

Like KTA, described in Chapter 4, RTA is an isomorph of KTP, but was developed more recently than that material. Consequently its chemical formula is of the form $M\mathrm{TiO}X\mathrm{O}_4$, where M is K, Rb, Cs, Tl or NH_4, and X is P or As. All the crystals of the group are orthorhombic, belonging to the crystallographic point group mm2. Their structures are based on chains of TiO_6 tetrahedra, which are joined at two corners, with $X\mathrm{O}_4$ tetrahedra in between [3]. The way in which such a structure produces an optical nonlinearity is described in Section 4.2.2. A detailed illustration of the chemical structure of RTA can be found in a paper by Hu et al [4].

The first study of the optical properties of RTA was published by Han et al in 1993 [5], and a surprising lack of information has appeared since then. There, are however, a small number of reported measurements of the main properties of

interest, those being refractive index, transparency and nonlinearity.

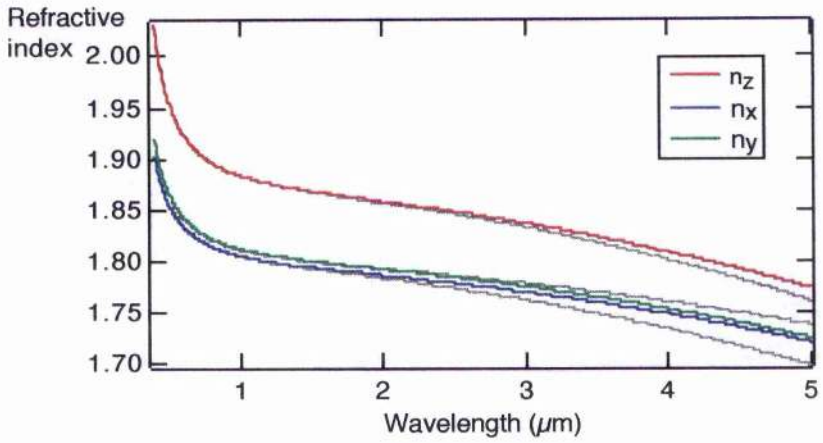

Figure 5.1 Refractive indices of RTA, calculated from the Sellmeier coefficients of Fenimore et al [7] (coloured lines). Shown for comparison are indices calculated from the coefficients of Cheng et al [6] (grey lines).

RTA is a positive biaxial crystal, so that $n_z > n_y > n_x$. Among the KTP family, it has been found that while the arsenate members have higher refractive indices, the phosphate crystals are more birefringent [6]. Typically, the birefringence n_y - n_x is about 10% of the n_z - n_x value. Han et al [5] conducted a series of refractive index measurements in the wavelength region 656 to 1064 nm, but made no attempt to derive Sellmeier equations from their data. Shortly afterwards, Sellmeier coefficients were published by Cheng et al [6], calculated from measurements in the 458 to 1500 nm range. These coefficients were used by a number of researchers, but as interest grew in the generation of mid-infrared (MIR) wavelengths, the equations were found to be highly inaccurate at longer wavelengths. This situation was subsequently rectified by Fenimore and co-workers [7], who made measurements and derived coefficients applicable from 403 to 3600 nm. Fig. 5.1 shows a comparison between refractive index values calculated from the two sets of coefficients, illustrating how radically they differ in the MIR. The coefficients themselves are given in Table 5.1, and fit the equation

$$n^2 = A + \frac{B}{1-(C/\lambda)^2} - D\lambda^2 \qquad (5.1)$$

Thus for nonlinear work using RTA in the MIR, it would be advisable to use the

coefficients of Fenimore et al. However, the OPO presented here was not investigated particularly in terms of tuning, since it would have behaved in the same way as the previous femtosecond RTA OPO [1].

	Cheng et al [6]	**Fenimore et al** [7]
A_x	2.22681	2.04207
B_x	0.99616	1.77850
C_x	0.21423	0.20157
D_x	0.01369	0.01035
A_y	1.97756	2.14941
B_y	1.25726	1.09267
C_y	0.20448	0.21462
D_y	0.00865	0.01067
A_z	2.28779	2.18962
B_z	1.20629	1.30103
C_z	0.23484	0.22809
D_z	0.01583	0.01390

Table 5.1 Sellmeier coefficients of RTA, to fit Equation 5.1.

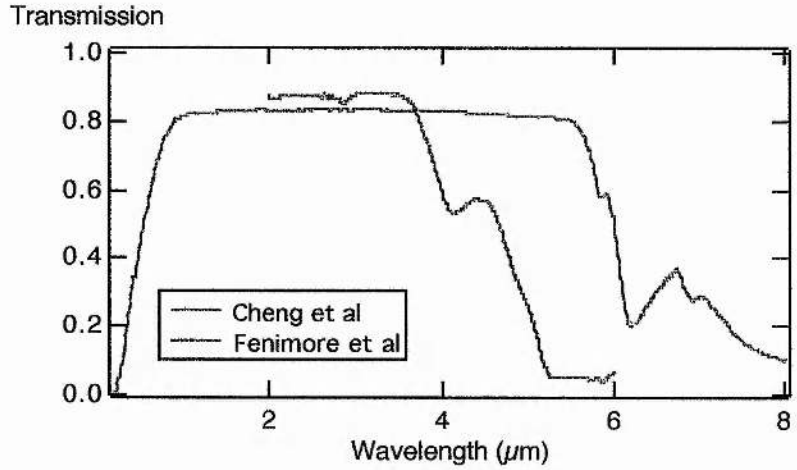

Figure 5.2 Infrared transmission of RTA, as measured by Cheng et al [6] and Fenimore et al [7].

RTA is transparent out to about 5 μm, so is suitable for the generation of MIR wavelengths. Unfortunately, these are not available from noncritical birefringent

phasematching, meaning that walk-off compensation must be used to generate longer wavelengths from a birefringent RTA OPO. This fact tended to exclude RTA from the list of crystals deemed suitable for a MIR source. Recently, though, periodic poling of RTA has been achieved, removing this problem and making it a prime candidate for MIR generation. It is more suitable than its relative KTP, also recently poled, since it is free from absorption bands at 3.4 and 3.8 μm caused by the phosphate group. Fig. 5.2 shows transparency measurements of RTA from two different groups of researchers [6, 7]. The rather large discrepancy between 3 and 5 μm suggests that this property warrants further investigation.

Like the rest of the KTP family, RTA has relatively large nonlinear d_{ij} coefficients, leading to potentially higher efficiencies. This was one of the reasons for the original popularity of the materials when they were first introduced. There are three non-zero coefficients: d_{15} (d_{31}), d_{24} (d_{32}) and d_{33}. Several widely-varying values for these have been reported, as shown in Table 5.2. The values from Reference 8 are average values calculated by Reid, partly from values for KTP and the relative magnitude of the coefficients of KTP and RTA as measured by Han et al [5]. It is these values which are used in subsequent calculations in this chapter.

d_{15} (pm/V)	d_{24} pm/(V)	d_{33} pm/(V)	Reference
2.24	7.73	19.62	5
2.3	3.8	15.8	6
4.1	1.7	13.7	8

Table 5.2 Effective nonlinearities of RTA.

The nonlinear coefficients can be used to calculate the effective nonlinearity, d_{eff}, as it varies with propagation direction through a crystal, as shown for RTA in Fig. 5.3. This indicates that propagation along the x-axis ($\theta = 90°$, $\phi = 0°$) yields the maximum value of nonlinearity, and consequently the highest efficiency. For this reason, propagation in this direction was chosen for the OPO. In addition, the cavity design chosen for low threshold operation (Section 5.3) was suitable only for noncritical phasematching, and would have been unable to operate in the presence of the Poynting vector walk-off which would have originated from propagation at an angle through the crystal.

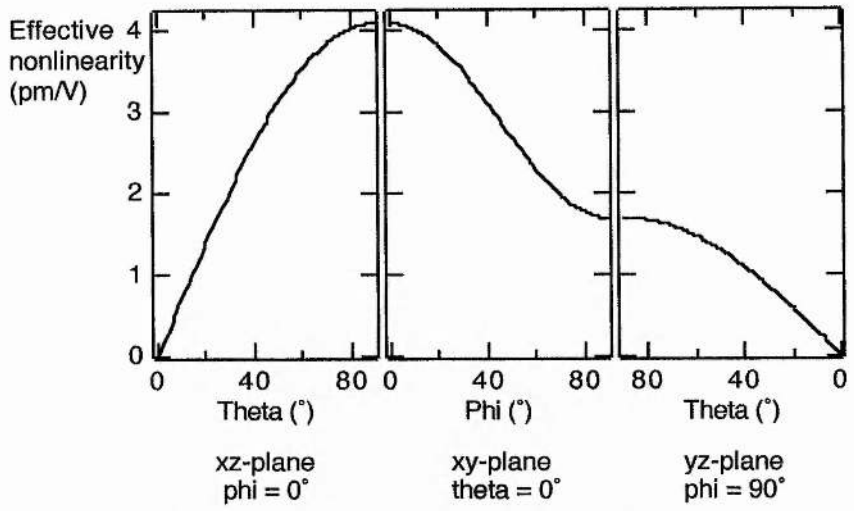

Figure 5.3 Variation with propagation angle of the effective nonlinearity of RTA in the principle planes (calculated from the nonlinear coefficients of reference 8).

In view of this, an RTA crystal cut for type II (o → o + e) noncritical phasematching along the *x*-axis was obtained from Crystal Associates [9]. It had an aperture of 5 mm by 5 mm and was 3 mm in length.

5.2.3 Review of RTA research

Given the enormous popularity of KTP, the body of published work relating to RTA is surprisingly small. Their optical properties do not differ significantly enough to account for this, but nonetheless, whilst reference to RTA has almost completely disappeared from the journals in recent months, KTP is still the material of choice for many OPO and frequency-doubling applications.

Optical parametric oscillators make up the largest group of nonlinear devices represented in the body of published work pertaining to RTA. The first was a synchronously pumped femtosecond device, demonstrated by Powers et al in 1994 [10]. Using a critically phasematched noncollinear geometry and a Ti:sapphire pump, they achieved signal tuning from 1.03 to 1.3 μm and idler tuning from 2.15 to 3.65 μm. Dispersion compensation compressed the signal pulses to 58 fs. The system obviously suffered from walk-off, leading to a high threshold at longer idler wavelengths. The first noncritically phasematched RTA OPO was the St Andrews

device of Reid et al [11], mentioned previously as providing some of the inspiration for the OPO presented here. This was also a synchronously Ti:sapphire-pumped femtosecond OPO, and utilised pump tuning to generate an output of 1.23 to 1.34 μm signal and 2.1 to 2.43 μm idler. A continuous wave (cw) Ti:sapphire system has recently been demonstrated by Scheidt et al [12], who have also achieved continuous-wave diode-pumping of doubly resonant and triply resonant RTA OPOs [13]. The related process of optical parametric amplification has been investigated by Petrov et al [14] who compared systems based on KTP, RTA and KTA. Seeded amplifiers were pumped by a femtosecond Ti:sapphire laser and tuned over the spectral range 2.9 to 3.8 μm. RTA gave the highest powers for wavelengths greater than ~3.3 μm.

Difference frequency mixing has also been demonstrated. Fenimore et al selected RTA over KTP for its superior transparency in the MIR [7]. They generated nanosecond pulses tunable from 3.18 to 4.16 μm by mixing the output of a Q-switched Nd:YAG laser with the signal of a $LiNbO_3$ OPO pumped by the same laser, thus producing an all-solid-state tunable MIR source. A rather different motivation was behind the work of Pfister et al [15], who mixed a 1.064 μm Nd:YAG laser output with the 3.192 μm output of a CO overtone laser to generate 1.596 μm in an attempt to build a source for an optical frequency standard.

The above represent much of the RTA-based work published since 1994, and is obviously not a vast amount. RTA now looks set for an up-swing in popularity, though, following the development of periodically poled RTA in 1996 [16, 17]. Hydrothermally-grown KTP had previously been poled [18], but RTA was the first flux-grown member of the crystal family to be successfully poled. Flux-grown RTA has a three times lower ionic conductivity than flux-grown KTP, meaning that much lower fields are needed for electric-field poling [16]. Quasi-phasematched frequency doubling of Ti:sapphire lasers has been demonstrated in both bulk [16] and waveguide [18] devices. The most recent development is that of a femtosecond Ti:sapphire-pumped OPO tunable out to 4.5 μm, demonstrated at St Andrews [19].

5.3 Cavity design

In an OPO, as in a laser oscillator, threshold is achieved when the gain exceeds

the losses. Thus threshold can be reduced either by increasing the gain or by reducing the losses. Gain depends partly on the effective nonlinearity, so can be enhanced by choosing a material with a high nonlinearity, or a crystal geometry to maximise the available nonlinearity in a given material, as was done here by selecting type II propagation along the x-axis in the RTA crystal. Losses in an OPO cavity are due to absorption in the crystal, reflection losses from any prisms used for dispersion compensation, and primarily by transmission losses at the cavity mirrors, since perfect 100% reflection across the entire bandwidth of a mirror set is impossible to manufacture. Hence, reducing the number of mirror reflections per round trip should reduce loss. This can be done by moving from a four-mirror cavity, or x-cavity (as used for the KTA-based OPO of Chapter 4), to a three-mirror cavity, or v-cavity (see the PPLN-based OPO of Chapter 6). Reducing the number of cavity elements in this way is also advantageous in that it makes for easier alignment and increased compactness. To this end, a three-mirror cavity can be further simplified by replacing one of the curved focusing mirrors with a highly reflecting (HR) surface deposited directly onto the surface of the crystal, and pumping through it. The intracavity focus is positioned at the HR end of the crystal, so the cavity becomes in effect a four mirror cavity folded back on itself (Fig. 5.4). As far as a synchronously pumped OPO is concerned, this is analogous to the four mirror cavity receiving two pump pulses per resonant wave round trip, thus increasing the gain to loss ratio.

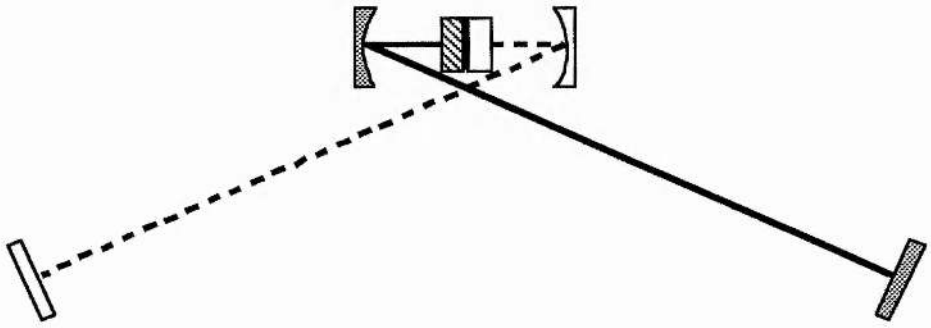

Figure 5.4 A semi-monolithic optical cavity design, which is in effect a four-mirror cavity folded back on itself at the mirror coating on the crystal face.

A crystal having an HR coating on one end like this is referred to as semi-monolithic. Such crystals have been extensively used by Fujimoto and co-workers

[20, 21] in Ti:sapphire lasers, in attempts to improve self-modelocking conditions by moving from the conventional four mirror, two prism ultrashort pulse laser cavity to configurations using only three elements, one of them being a semi-monolithic crystal. Such an arrangement had not been reported in a synchronously-pumped OPO, but it seemed that such a simplified cavity design would be likely to produce a low threshold, so it was implemented in the RTA OPO. The crystal was coated on one side to give high reflection at the signal wavelength of 1.274 μm and high transmission of the pump wavelength (the system was pumped by the Ti:sapphire laser described in Section 3.2.3) and the opposite face had an antireflection coating at the signal wavelength.

The threshold of an OPO is also dependent on the focusing of the pump beam and the intracavity resonant beam. The modes of these two beams within the crystal must be carefully matched to allow maximum interaction between them, and therefore maximum gain. A number of theoretical studies of the effects of focusing on gain have been published. The most general of these is that of Guha et al [22] who give an analysis of pump threshold intensity for both singly and doubly resonant oscillators. According to their model, the pump threshold intensity for a singly resonant oscillator, as the RTA OPO was, is given by

$$P_t = \frac{\varepsilon_s}{K h_s} \tag{5.2}$$

where ε_s is the fractional loss per cavity round trip, and the factor K, which accounts for a range of parameters, is given by

$$K = \frac{128\omega_s\omega_i\chi^2\pi^2 l}{n_s n_i n_p c^3}\frac{k_s k_p}{k_s + k_p} \tag{5.3}$$

where χ is the effective nonlinearity in e.s.u. units, and the other symbols have their usual meanings and are in S.I. units [8].

Returning to Equation 5.2, it can be seen that the threshold is inversely proportional to a parameter h_s. This is a dimensionless quantity which describes the efficiency of the parametric interaction in terms of focusing, and is a function of, amongst other things, a factor ξ which is the ratio of the crystal length, l, to the confocal parameter, b, and is defined for both the pump and signal (where the signal

is the resonant wave), so that

$$\xi_p = \frac{l}{b_p} \qquad \xi_s = \frac{l}{b_s} \tag{5.4}$$

The quantity b_j is the confocal parameter and is defined as

$$b_j = \frac{2\pi(w_{oj})^2}{\lambda_j} \tag{5.5}$$

where w_{oj} is the radius of the focused beam waist of the pump or signal within the crystal.

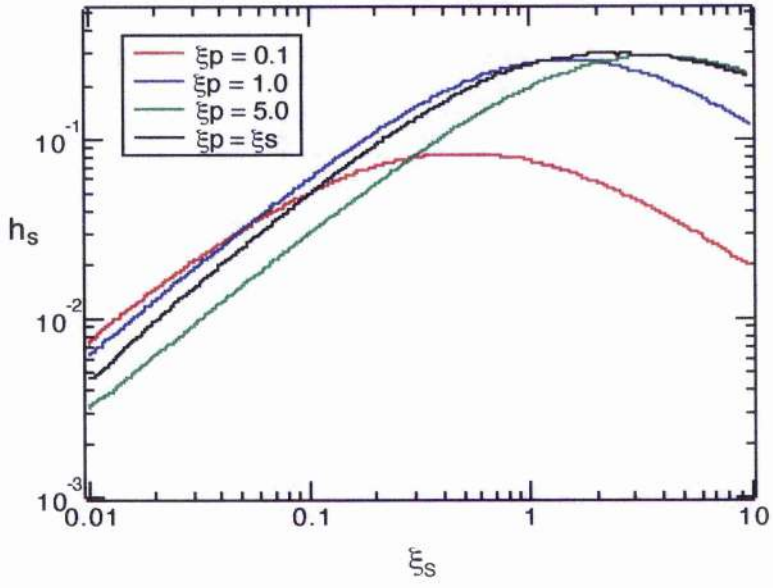

Figure 5.5 Variation of focussing parameter h_s with ξ_s, the ratio of the crystal length to signal confocal parameter,for various values of the pump ratio ξ_p.

Fig. 5.5 shows graphs of the value of h_s, which must be evaluated numerically, (taken from the Guha paper) for various combinations of ξ_s and ξ_p in the absence of walk-off. Equation 5.2 implies that a large value of h_s is required to minimise the threshold, and it can be seen from Fig. 5.5 that the maximum value is obtained when $\xi_s = \xi_p \approx 2.4$. Given the definition of ξ (Equation 5.4), this means that as far as minimising the threshold is concerned, optimum focusing occurs when the confocal

parameters of both the pump and signal are equal to 0.41 times the crystal length. The same crystal length obviously applies to both beams, so in effect, the confocal parameters must be equal. Since the pump wavelength is shorter than the signal wavelength, to achieve this condition the pump beam waist must be smaller than that of the signal. Three OPO design problems arise at this point. Firstly, the very short crystal length required in a femtosecond OPO makes it technically difficult to focus sufficiently tightly to achieve $b = 0.41l$. The other problems stem from the conventional configuration of a collinearly-pumped noncritically phasematched OPO. This is normally realised by introducing the pump beam, via a lens, into the cavity through a curved cavity mirror, as depicted in Fig. 5.6, but such an arrangement is problematic on two counts. The curved mirror acts to expand the pump beam waist over the focusing which would be achieved from the lens alone, thus making it difficult to produce a pump beam waist smaller than the signal beam waist. Also, the fact that the pump and signal focussing are both affected by the curved mirror (which serves, after all, to focus the signal beam intracavity) means that they are intrinsically coupled together, and cannot be separately adjusted to achieve optimum mode matching.

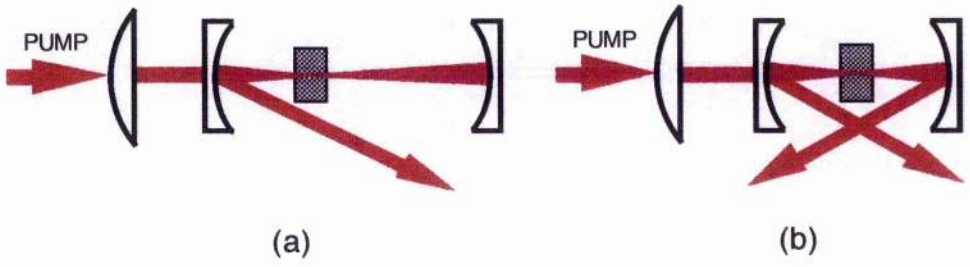

Figure 5.6 Focussing arrangements in conventional three- and four-mirror OPO cavities.

Happily, a semi-monolithic OPO design removes these problems. The removal of the curved mirror allows totally independent focusing of the pump and signal, because the pump focusing can be controlled wholly by a lens, and the signal is focused solely by the remaining curved mirror. Therefore it should be possible to adjust the confocal beam parameters to optimise the mode matching at any wavelength, hence improving the gain over that of a standard three-mirror cavity. Given a Ti:sapphire pump wavelength of 830 nm, a typical signal wavelength from

RTA is 1.274 μm, and for a 3 mm long crystal the above conditions indicate that beam waist radii of 31 μm and 38 μm for the pump and signal respectively are required to minimise the threshold.

There is an additional advantage to a synchronously-pumped semi-monolithic OPO with independent focusing. It is usual to construct a synchronously-pumped OPO so that its pulse repetition rate matches that of the pump laser. However, it may be possible to reduce the length of the OPO cavity by half or more, so that it runs at the second or higher harmonic of the pump repetition rate. Not only would this be a more compact arrangement, but much higher repetition rates than usual could be achieved, which have applications in their own right, and are also more quasi-continuous than a lower repetition rate and thus more suitable for continuous wave applications. A semi-monolithic OPO is ideally suited to such a modification. The cavity length can be altered simply by moving the plane mirror. Moreover, the independent focusing is advantageous here too. Moving to a shorter cavity length results in an increased intracavity beam waist, which requires adjustments to the focusing to maintain stability. This can easily be done via the lens and the single curved mirror.

The OPO described in the chapter was operated at the fundamental of the pump repetition rate, and then modified to operate at the second and fourth harmonics, resulting in a compact tunable ultrahigh-repetition rate femtosecond source. The experimental results from these configurations are now presented.

5.4 The length-matched semi-monolithic RTA OPO

5.4.1 Cavity configuration and alignment

The specification of the RTA crystal used in the semi-monolithic OPO has been described in the previous two sections. The cavity was configured in a simple design, illustrated in Fig. 5.7. The pump laser was the Ti:sapphire system described in Chapter 3, having a repetition rate of 86 MHz. The pump beam was introduced via an optical isolator to prevent feedback to the laser, and focused using a lens of focal length 63 mm. Both cavity mirrors had highly reflecting coatings centred at 1.274 μm, the middle of the expected signal wavelength range. The radius of curvature of the focusing mirror was -100 mm.

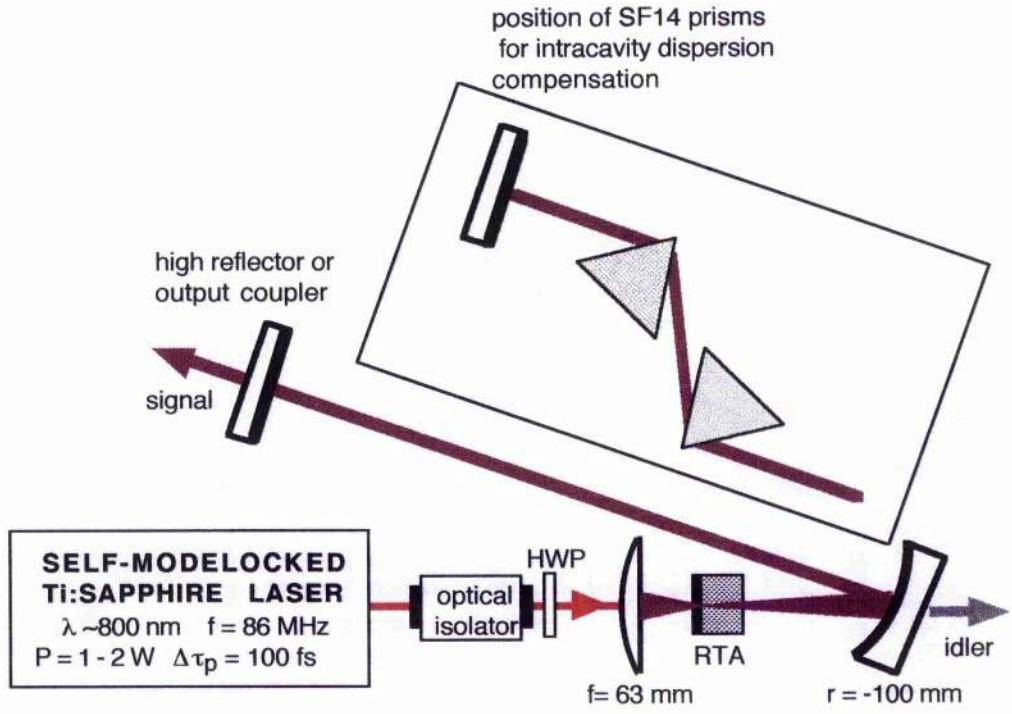

Figure 5.7 Cavity configuration of the semi-monolithic RTA-based OPO. The inset shows the position of prisms used for dispersion compensation.

The OPO was aligned by making use of the small amount of blue light produced in the RTA crystal by non-phasematched second harmonic generation of the pump. This is a tried and tested alignment method developed previously in the femtosecond OPO group [8], and suitable for use in noncritically phasematched OPOs. Under such a geometry no walk-off occurs, and all beams propagate collinearly along a crystal axis. This includes the non-phasematched blue, which therefore follows the same path round the OPO cavity as the signal beam, and can consequently be used for alignment. The blue beam is centred on each cavity mirror, and retroreflected from them by the use of pinholes. This is repeated iteratively until all reflections overlap at all points in the cavity, and the beam is collimated. Oscillation can then be achieved by adjustment of the lateral position of the end mirror, so bringing the cavity length into synchronism with the pump laser. In the case of the semi-monolithic OPO this method was particularly simple due to the small number of cavity elements to be adjusted, and oscillation was achieved very quickly. Initially, the mode of the signal beam was poor; several high order modes were observed as the angular positions of the mirrors were changed. This problem

was rectified by lateral adjustment of the curved mirror to change the mirror-crystal separation. It was necessary to simultaneously walk the end mirror to maintain the correct cavity length. In this way a high quality TEM_{00} mode was generated.

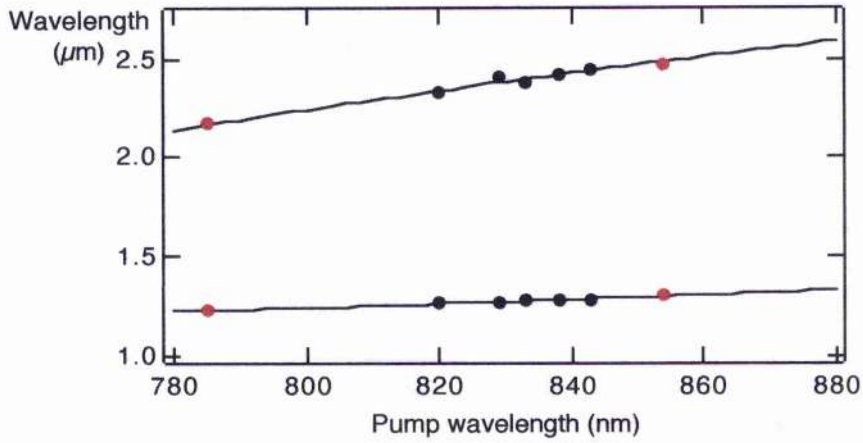

Figure 5.8 Experimental pump tuning results from the length-matched semi-monolithic OPO (black circles). The tuning limits of the noncitically phasematched pump-tuned RTA OPO of Reid et al [11] are shown for comparison (red circles). The curves are theoretical, calculated from the Sellmeier coefficients of Cheng et al [6].

5.4.2 Tuning

A noncritical phasematching geometry limits the tuning of an OPO to that available from pump tuning. Using the Sellmeier coefficients of Cheng et al [6]quoted in Section 5.2, it is possible to calculate the tuning expected from the *x*-axis of the RTA, for pump wavelengths available from the Ti:sapphire laser. This is shown in Fig. 5.8, and was verified experimentally by Reid et al, using the the St Andrews femtosecond RTA-based OPO mentioned previously [11]. That system was pumped by the same Ti:sapphire laser used here, so there was no reason to expect that the tuning behaviour of the semi-monolithic OPO would be any different. Consequently, only a handful of pump tuning results were taken from the OPO. These are presented in Fig. 5.8, and show good agreement with the theoretical curves. The limits of the tuning obtained by Reid et al are included for comparison. Spectral measurements of the signal were made using a Rees Instruments laser spectral analyser [23]; the idler values were inferred from them. It is clear from Fig 5.8 that Ti:sapphire-pumping of *x*-cut RTA is unable to generate MIR wavelengths. This is

true for all non-critical phasematching geometries in KTP and its isomorphs. It is necessary to use a critical cut to extend the tuning range, as explained in Chapter 4.

A number of non-phasematched nonlinear processes generating visible light were also observed, as is typical in an infrared OPO. The most prominent of these were second harmonic generation of the signal producing red light at ~630 nm, sum-frequency-mixing of the pump and signal generating green light at ~500 nm, and sum-frequency-mixing between the pump and idler resulting in orange light at ~600 nm. These outputs provided a useful visible indicator of oscillation. No power measurements were conducted, but it is to be expected that power levels were negligible.

5.4.3 Power measurements

Disappointingly, after all the consideration given to the design of a low threshold system, the OPO proved to have a high oscillation threshold, considerably larger than the 50 mW measured from the previous RTA OPO [11]. However, this was compensated for by very high output powers.

Initial brief measurements of the signal power were made after the highly reflecting end mirror. 55 mW were recorded, indicating that a total signal power of 165 mW was exiting the cavity through the three high reflectors. Approximately 270 mW of power was extracted by introducing a Brewster-cut prism into the long arm of the cavity; this implied that it should be possible to extract as much as 400 mW by using an optimised output coupler [24]. The most appropriate output couplers available were coated for transmission at 1.32 μm, but there were no data regarding their specification at 1.274 μm. The input pump power was 1.15 W; from this, 350 mW were extracted via a 10% output coupler, and 340 mW via a 12.5% output coupler. Thus the 10% output coupler gave the best performance, and was used for subsequent measurements. The fact that this did not quite give the predicted 400 mW suggests that it was not truly optimal for the OPO, but no more suitable output coupler was available. By increasing the pump power to 1.7 W, a total of 600 mW of signal power was recorded. These measurements were made at a signal wavelength of 1.25 μm.

Measurements of the idler power were equally encouraging. As shown in Fig.

5.7, the idler beam left the cavity through the curved mirror, since it was the non-resonant beam. With the 10% output coupler in the cavity, 50 mW of idler power were measured directly. A germanium filter was used to block shorter wavelengths; this had a transmission of 85% at idler wavelengths. Correcting the measured power for both this loss and a 29% absorption loss in the substrate of the curved mirror implies a total idler power of 83 mW.

5.4.4 Signal pulse measurements

Autocorrelation measurements of the signal pulses were conducted. A standard second harmonic autocorrelator arrangement was used, with a beam splitter coated for 50:50 performance at 1.2 μm, a 300 μm long BBO crystal cut for frequency doubling of 1.2 μm, and a photomultiplier tube. An example of the resulting interferometric autocorrelation traces is given in Fig. 5.9, along with a corresponding spectrum of the signal at 1.24 μm. As expected from an OPO with no dispersion compensation, the autocorrelation shows some chirp and the spectrum is distorted. Assuming a $\mathrm{sech}^2(t)$ pulse shape, the full-width-half-maximum of the autocorrelation implies a pulse duration of 360 fs.

No measurements of the idler pulses were made.

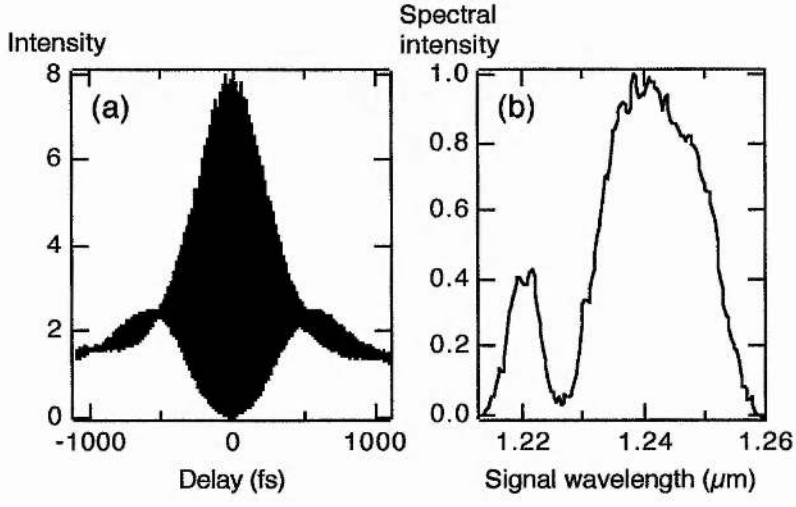

Figure 5.9 Autocorrelation (a) and spectrum (b) of the signal pulses from the uncompensated length-matched OPO. The pulse duration was 360 fs.

5.4.5 Dispersion compensation

Intracavity dispersion compensation was implemented in order to improve the quality of the signal pulses. A pair of SF14 prisms, separated by ~300 mm, was inserted into the long arm of the cavity, as depicted in the inset of Fig. 5.7. Oscillation was achieved with both the high reflector and the 10% output coupler in the end mirror position. The prisms introduced some loss into the cavity, resulting in a decrease in the signal power extracted through the output coupler. An incident pump power of 1 W generated 200 mW of signal power, and 116 mW of idler power. These measurements are summarised in Table 5.3, where they are compared with the powers provided by the uncompensated cavity. Figures for the conversion efficiencies are also given, indicating that the OPO was highly efficient. The unbracketed numbers were calculated directly from the measured signal and idler powers. For comparison, the bracketed figures are derived from the signal power measurements only, using the Manley-Rowe relations. These relations are a statement of the principle of conservation of energy in an OPO, and basically state that each pump photon creates one signal and one idler photon in such a way that the total photon energy is conserved. A mathematical derivation of the relations can be found in Boyd's book on nonlinear optics [25]. The energy of a photon is inversely proportional to its wavelength, so the ratio of signal and idler energies, or powers, generated in an OPO is equal to the inverse ratio of their wavelengths. The efficiency, E, of an OPO can therefore be calculated from the pump and signal powers only, and can be shown to be given by

$$E = \frac{P_s(1+\lambda_s/\lambda_i)}{P_p} \tag{5.6}$$

where P_j is the power of wave j and the subscripts have their usual meanings. This was done in the present case to provide a check on the accuracy of the power measurements. The idler measurements were particularly prone to error because the idler was emitted in a divergent beam. The efficiency figures of Table 5.3 indicate that the power measurements from the compensated cavity were reasonable accurate, but the discrepancy between the values for the uncompensated cavity imply an error, probably due to under-measurement of the idler power. All the efficiency

figures are high, though, and increase with increasing pump power.

	Pump power (W)	Signal power (mW)	Idler power (mW)	Conversion efficiency
Uncompensated cavity	1.15	350	83	40% (47%)
	1.7	600	–	(55%)
Compensated cavity	1	200	116	33% (31%)

Table 5.3 Measured powers and calculated efficiencies from the uncompensated and compensated length-matched cavities. The efficiencies in brackets are calculated using Equation 5.6.

Fig. 5.10 presents a fringe-resolved autocorrelation trace of the signal from the compensated cavity, and the corresponding spectrum at 1.27 μm. Assuming a $\text{sech}^2(t)$ pulse shape implies a pulse duration of 70 fs. The spectral bandwidth is 25 nm, which combined with the pulse duration gives a time-bandwidth product of 0.32, so the signal pulses were virtually bandwidth-limited.

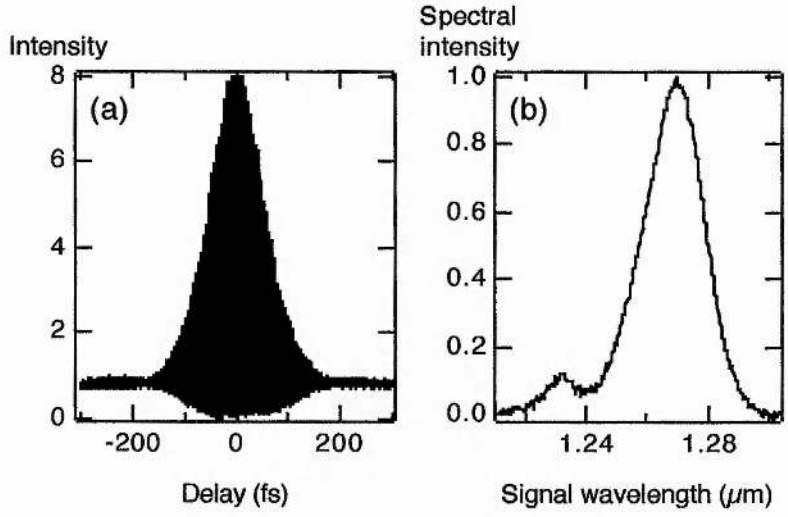

Figure 5.10 Autocorrelation (a)and spectrum (b) of the signal pulses from the compensated length-matched OPO. The pulse duration of 70 fs and the spectral bandwdith of 25 nm imply a time-bandwidth product of 0.32.

5.4.6 Frequency-resolved optical gating measurements

To further characterise the signal pulses in a more comprehensive way, they were analysed using the technique of second harmonic generation frequency-resolved optical gating (FROG). As discussed in Section 3.3, FROG is a relatively new innovation [26], which can be used to measure full intensity and phase information of pulses. It has been used by many researchers to study the pulses from ultrashort pulse lasers, but to date it has not been applied to OPO pulses. FROG is a powerful tool which can be used to provide important insights into pulse evolution in OPOs, which is a complex and as yet poorly-understood subject.

A second harmonic generation FROG system is essentially a spectrally-resolved autocorrelator, in that it records traces of intensity against wavelength and time delay between two replicas of a pulse sequence, which are composed of pulse spectra measured for each value of autocorrelation delay. Such a trace can be shown to contain all the intensity and phase information relating to the pulses being measured, and this information can be retrieved from the trace by use of an appropriate iterative Fourier-transform computer algorithm. The FROG system used in this case was the arrangement described in Chapter 3. This was a novel real-time system, in which the frequency-doubled output of an autocorrelator was dispersed by a prism, and then swept across the surface of a CCD camera by a spinning mirror moving in synchronism with the scanning loudspeaker in the autocorrelator. The camera image, or FROG trace, was displayed on a video monitor to allow continuous monitoring. Further details of the system can be found in Section 3.3.2. It was used to obtain a FROG trace of the signal pulses from the dispersion compensated semi-monolithic OPO, which is shown in Fig. 5.11. The intensity and phase of the pulses in both the temporal and spectral domains were retrieved from this using an algorithm based on those of Trebino and co-workers [27]. The retrieval error of the FROG algorithm was G = 0.009, which is sufficiently small to imply accuracy of the retrieved results. Fig. 5.12(a) presents the spectral data. The retrieved spectrum as shown is compared to an experimental spectral measurement taken at the same time, and shows excellent agreement, implying that the retrieved data are genuinely representative of the actual pulses. The phase profile, with two turning points, is characteristic of the presence of third-order dispersion. A polynomial fit to the phase data gave a value for this of $d^3\phi/d\omega^3$ = 260,000 fs^3, while the second-order

dispersion was only residual, $d^2\phi/d\omega^2 = -160$ fs^2. The temporal pulse data can be seen in Fig. 5.12(b). The phase change across the centre of the pulse is of the order of 0.1 rad, indicating essentially the absence of frequency chirp. The retrieved temporal intensity profile was fitted to theoretical profiles of a sech$^2(t)$ pulse and a Gaussian pulse. As is evident from the figure, the Gaussian pulse is a poor fit in the wings of the pulse, but the sech$^2(t)$ profile, of a pulse with duration 78 fs, is an excellent fit over most of the pulse.

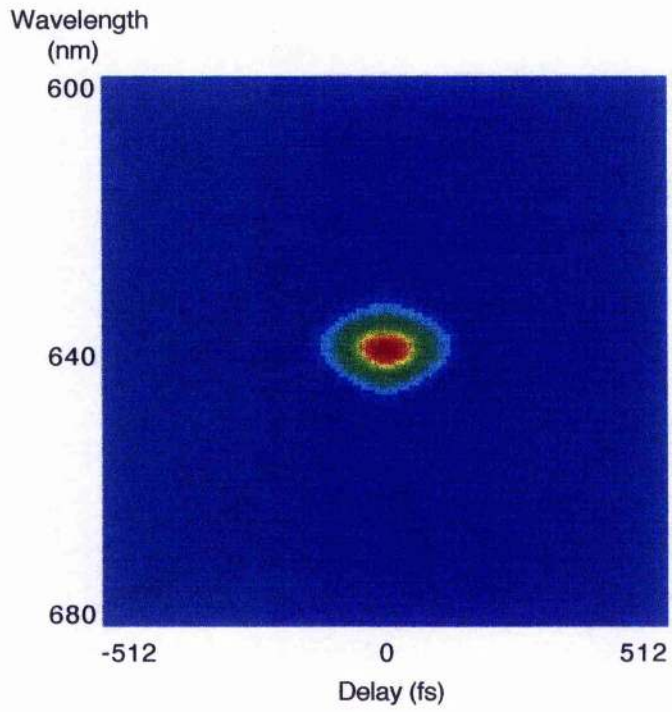

Figure 5.11 FROG trace of 1.28 μm signal pulses from the dispersion compensated length-matched OPO.

The pulse characteristics revealed by the FROG analysis are in reasonable agreement with those deduced from the autocorrelation, indicating that in this instance at least, it was appropriate to assume a sech$^2(t)$ pulse shape.

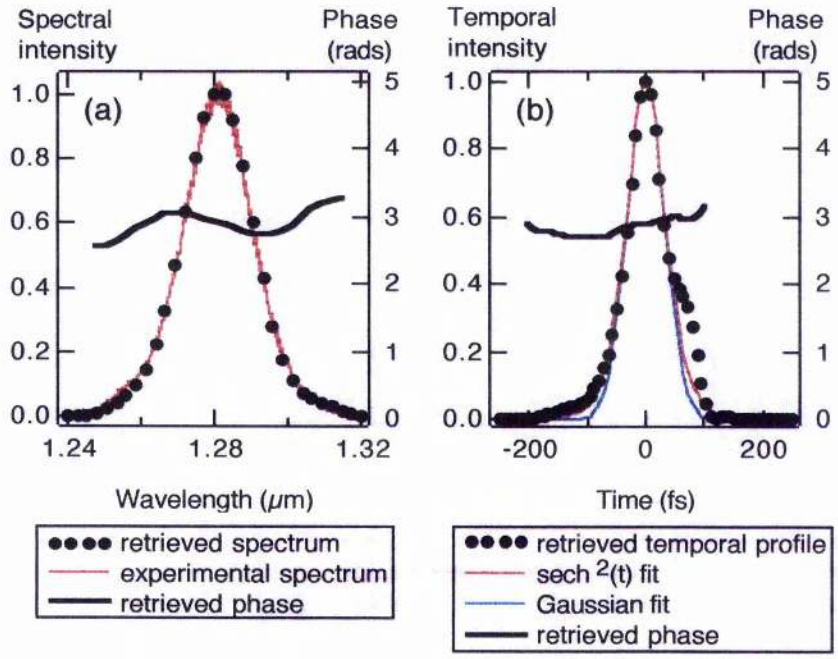

Figure 5.12 Intensity and phase in the spectral (a) and temporal (b) domains of the signal pulses from the dispersion compensated length-matched OPO, as retrieved from the FROG trace of Fig. 5.11.

5.5 The half-length semi-monolithic RTA OPO

The first step in increasing the repetition rate of the OPO was to decrease the length of the cavity by half, to 87 cm. In this condition, each signal pulse propagates twice around the cavity before the arrival of the next pump pulse, and would leave the cavity with a repetition rate of 172 MHz.

The change to a shorter cavity length was very straightforward. Stability could be achieved with the same pump lens (f = 63 mm) and curved mirror (r = -100); the only adjustment needed was a small increase in the mirror-crystal spacing to compensate for the change in beam waist due to shortening the cavity. After alignment, the signal beam was initially a TEM_{01} mode. This was improved to a TEM_{00} mode by walking the curved and plane mirrors as before, but the range of crystal-mirror spacings corresponding to this regime was very much smaller than that which produced TEM_{01} operation.

The OPO did not oscillate with the 10% output coupler. This is not a surprising result, because the signal pulses met the output coupler twice per pump

pulse, so in effect the output coupling was doubled to 20%, and the OPO was unable to tolerate such a high loss. Returning to the high reflector, 60 mW of signal power were coupled out from it, from a pump power of 1.2 W. At the same time, 190 mW of idler were measured after the curved mirror, taking into account the transmission losses at the germanium filter and the mirror substrate.

Once again, the signal pulses were characterised by autocorrelation. Intensity and interferometric autocorrelation traces are given in Fig. 5.13, with a signal spectrum centred at 1.25 μm showing the double peaks indicative of self-phase-modulation. A pulse duration of 408 fs was inferred from the interferometric trace, assuming a $\mathrm{sech}^2(t)$ pulse profile. No dispersion compensation was implemented in the half-length cavity, so any improvement this would have had on the pulses is not known.

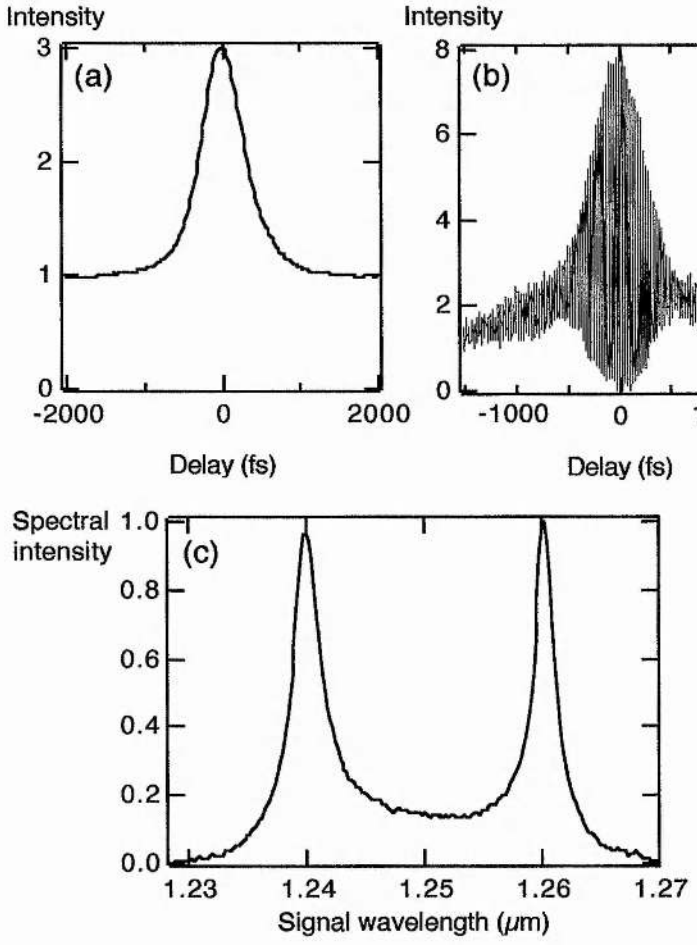

Figure 5.13 Intensity (a) and interferometric (b) autocorrelations and spectrum of the signal pulses from the uncompensated half-length OPO. The pulse duration was 408 fs.

The performance of the OPO was also characterised in terms of the repetition frequency. With the signal pulses interacting with a pump pulse only every second round trip it was to be expected that some modulation of the signal pulses would be evident. The question was whether this would be detrimental to the overall performance to such an extent that the OPO could not properly be claimed as a 172 MHz source.

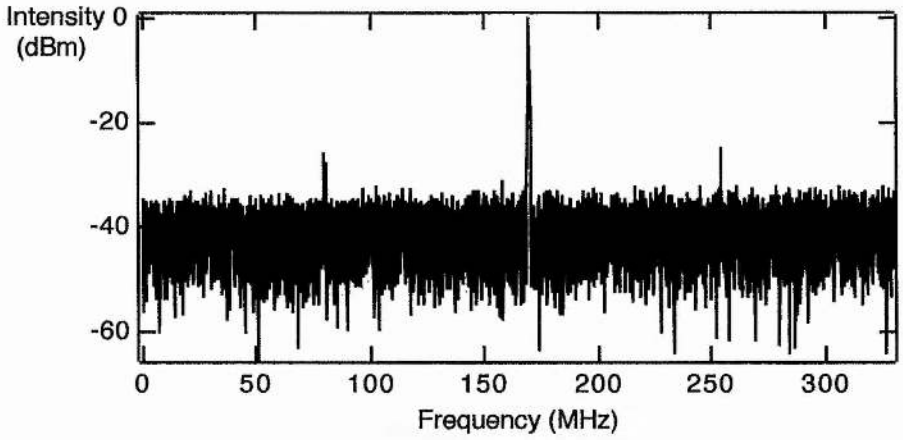

Figure 5.14 Microwave spectrum of the signal pulse sequence generated by the half-length OPO, showing the repetition frequency of 176 MHz, and slight modulation at ±86 MHz, the pump pulse repetiton frequency.

A fast InGaAs photodiode was used to detect the signal, and the output studied using a microwave spectrum analyser. The spectrum is shown in Fig. 5.14, and clearly shows a large centre peak at 172 MHz and sidebands at ±86 MHz due to modulation at the pump frequency. However, the sidebands are 25 dBm below the main peak on a logarithmic scale, which means that the amplitude modulation on the signal pulses was less than 1%, which would be perfectly acceptable for most purposes. The photodiode output was also fed into a fast oscilloscope so that the pulse sequence could be observed directly. The resulting oscillogram is depicted in Fig. 5.15 and verifies the very low amplitude modulation. Thus the half-length semi-monolithic OPO could genuinely be described as a 172 MHz near-infrared femtosecond source.

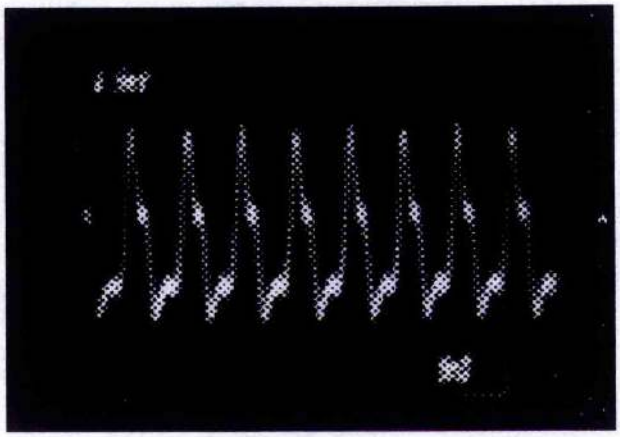

Figure 5.15 Oscillogram of the signal pulse sequence from the half-length OPO, indicating negligible amplitude noise.

5.6 The quarter-length semi-monolithic RTA OPO

The success of the half-length cavity prompted a move to a quarter-length cavity, which would operate at a repetition frequency of 344 MHz. The cavity length needed in this case was just 43.5 cm, producing a highly compact source.

Oscillation of the OPO could not be achieved with the pump lens and curved mirror combination used for the full and half-length cavities. However, changing to a curved mirror with a radius of -50 mm produced the correct signal spot size in the crystal, and oscillation was achieved. The signal beam had a good quality TEM_{00} mode, but oscillation could be sustained over only a few hundreds of microns variation in the crystal-curved mirror separation. A high reflector was initially used for the end mirror.

Autocorrelation measurements of the signal pulses were made from the beam transmitted through the high reflector. An interferometric autocorrelation trace is shown in Fig. 5.16, accompanied by a spectrum of the signal. A pulse duration of 370 fs can be inferred if a $sech^2(t)$ pulse shape is assumed. In the absence of dispersion compensation, the interferometric trace shows chirp, and the spectrum has the double peaks induced by self-phase-modulation.

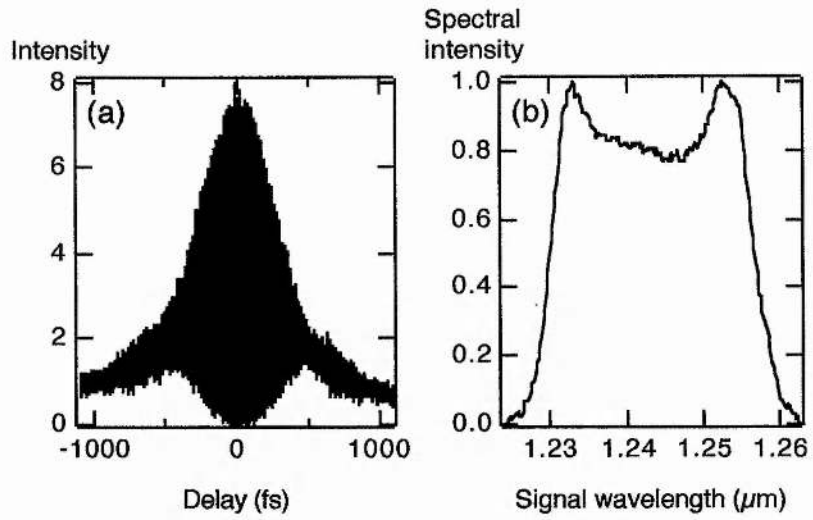

Figure 5.16 Autocorrelation (a) and spectrum (b) of the signal pulses from the uncompensated quarter-length OPO, with a high reflector as the end mirror. The pulses duration was 370 fs.

The long arm of the cavity was too short to allow the introduction of a prism pair for intracavity dispersion compensation. However, it is possible to compress pulses by passing the beam through prisms external to a cavity. Such an arrangement does not remove chirp, because the prisms are not working in tandem with the crystal to provide a net reduction in the intracavity dispersion, but significant pulse shortening can be achieved in this way. To this end, extracavity dispersion compensation was implemented in the quarter-length OPO by positioning a pair of SF14 prisms in the output beam, as indicated in Fig. 5.17. Much larger prism separations are needed in the single pass arrangement of extracavity dispersion compensation compared to an intracavity set-up where pulses propagate many times through the prisms before exiting the cavity. A prism spacing of 175 cm was used in this case, which compressed the signal pulses to 280 fs (Fig. 5.18a). Adjustment of the amount of prism glass in the beam had no significant effect on the pulse duration, and so the spacing was extended to 310 cm. This resulted in 177 fs pulses (Fig. 5.18b). The interferometric autocorrelations show that the pulses were still chirped, as expected. Space restrictions prevented any additional increase in the prism spacing, so it was not possible to determine whether the pulses could be further compressed.

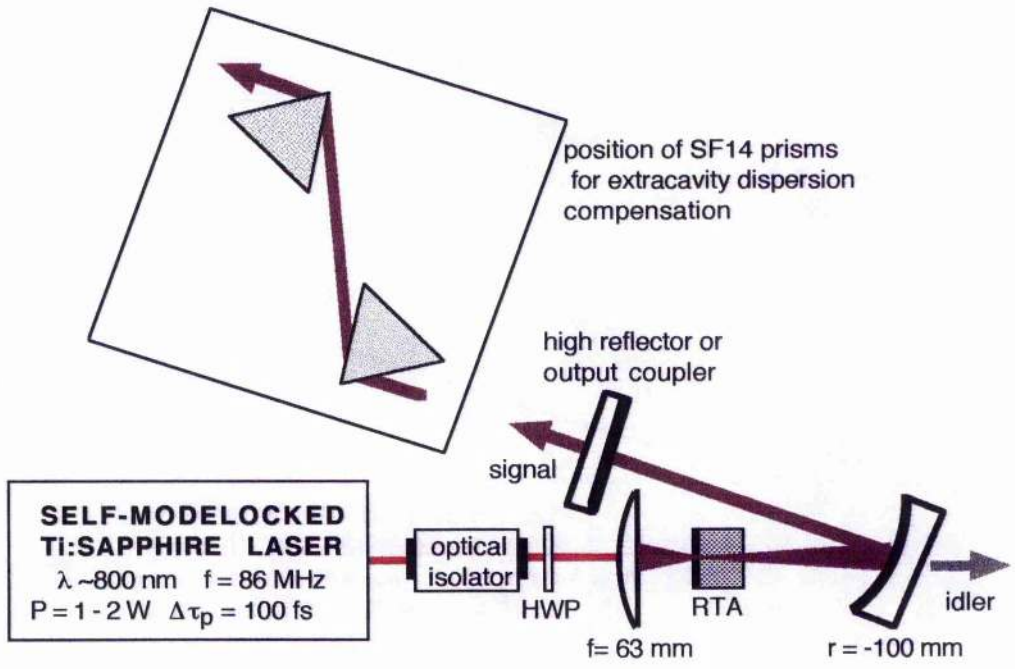

Figure 5.17 Cavity configuration of the quarter-length semi-monlithic OPO, showing the position of the extra-cavity prisms used for dispersion compensation (inset).

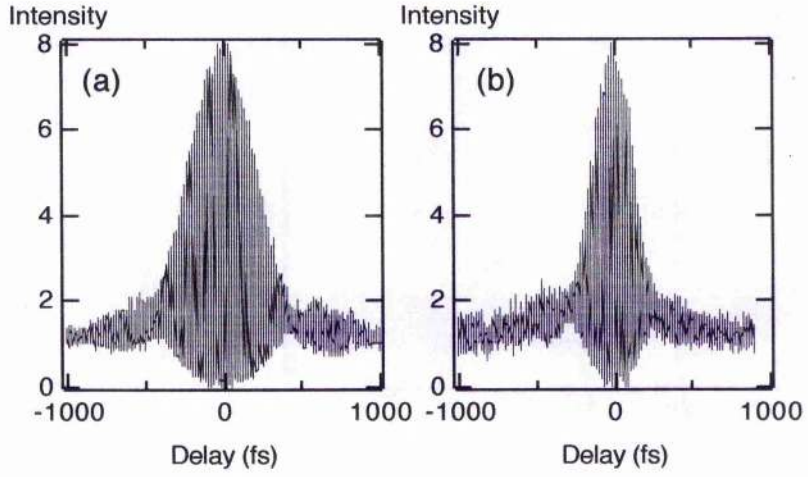

Figure 5.18 Autocorrelations of the signal pulses from the extra-cavity dispersion compensated quarter-length OPO. A prism separation of 175 cm produced 280 fs pulses (a), while a separation of 310 cm compressed the pulses to 177 fs (b).

The percentage transmission of an output coupler is effectively quadrupled in a quarter-length OPO cavity, because the resonant beam undergoes four round trips per pump pulse. Thus a small output coupler was needed for the OPO, such that the

overall loss would not be so high as to prevent oscillation. Such an output coupler was available in the shape of one specified as having 1% transmission at 1.2 μm. Its reflectivity curve implied a transmission of 1.75% at 1.25 μm, and so it acted as a 7% output coupler in the OPO. Power measurements were made once the output coupler was in place. A pump power of 1.3 W generated 175 mW of signal power and 230 mW of idler power (corrected for transmission losses), which implies a 31% conversion efficiency. The low amount of signal power as compared to the idler power suggests that the output coupling was not optimised. An autocorrelation of the signal pulses from the cavity with the output coupler but no dispersion compensation is included as Fig. 5.19. This measurement implies a pulse duration of 288 fs, significantly shorter than the pulses generated by the uncompensated cavity with the high reflector (c.f. Fig. 5.16), which suffered more broadening from additional passes through the crystal.

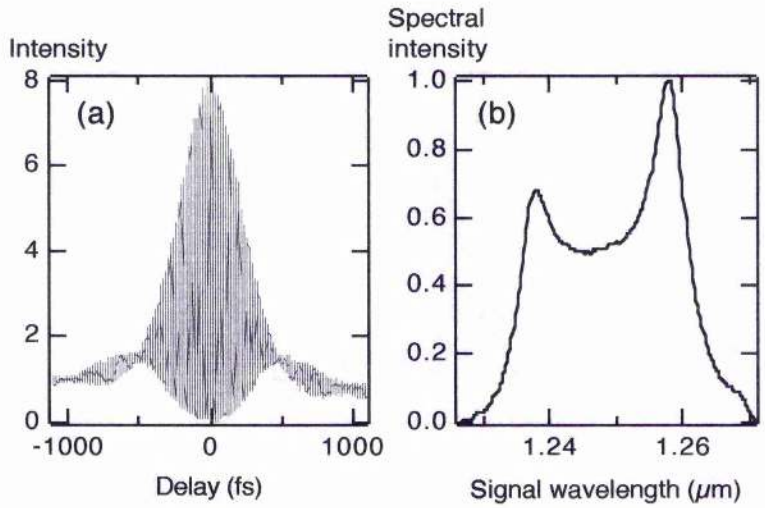

Figure 5.19 Autocorrelation (a) and spectrum (b) of signal pulses from the uncompensated quarter-length OPO, with a 7% output coupler. The pulses duration was 288 fs.

As with the half-length cavity, it was important to investigate the pulse amplitude modulation. The signal was once again detected with the fast InGaAs photodiode, and fed to the microwave frequency analyser. The resulting frequency spectrum appears as Fig. 5.20, and shows a main peak at the OPO repetition frequency of 344 MHz, with sidebands at multiples of the pump laser frequency of 86 MHz. The 25 dBm difference in magnitude between the centre peak and the sidebands indicates an amplitude modulation of the order of only 1%. An oscillogram

of the signal pulse sequence is shown in Fig 5.21a and shows a very small decrease in amplitude over each set of four pulses, until the next pump pulse interaction.

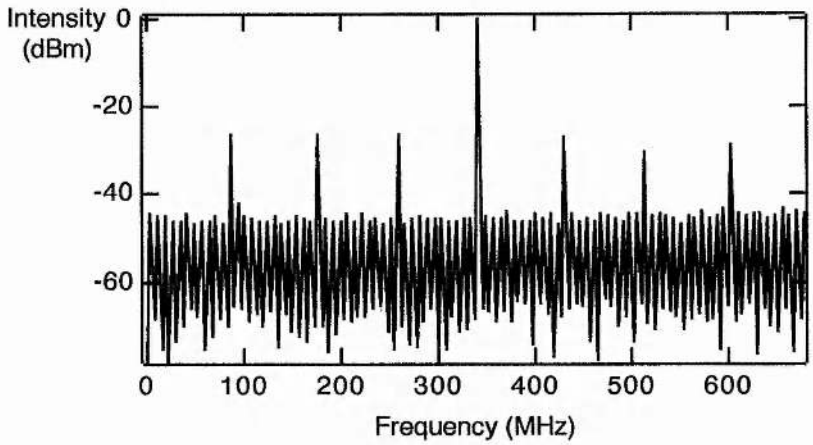

Figure 5.20 Microwave frequency spectrum of the signal pulses from the quarter length cavity, showing the 344 MHz repetition rate, and a slight modulation at harmonics of the 86 MHz pump pulse repetiton frequency.

The idler pulse sequence, on the other hand, shared the pump pulse repetition rate. Idler pulses could only be generated in the presence of both the signal and the pump, and as only every fourth signal pulse coincided with a pump pulse in the crystal, there was only one idler pulse for every four signal pulses. No fast detector was available suitable for monitoring the idler pulses at 2.4 μm, so it was decided to investigate the idler pulse train by frequency doubling it in a $LiNbO_3$ crystal, and then looking at the resulting 1.2 μm pulse train with a fast germanium detector. However, the $LiNbO_3$ proved to be redundant. When the idler beam was focused onto the detector, a signal was seen, presumably originating via the same second order nonlinear effect that enabled the LED autocorrelator of Chapter 3 to function. An oscillogram of the idler pulses recorded in this way is given as Fig. 5.21b. Three small and decreasing pulses can be seen between each major idler pulse, so the cavity mirrors must have had a small level of reflectivity at the idler wavelength. Thus the quarter-length cavity acted as a 344 MHz source at ~1.25 μm, and a 76 MHz source at ~2.4 μm.

An acronym was coined for the quarter-length cavity, to convey its principal characteristics of an ultrahigh repetition rate and a semi-monolithic cavity. The system is known as the SMURRF OPO, standing for semi-monolithic ultrahigh

repetition rate femtosecond optical parametric oscillator.

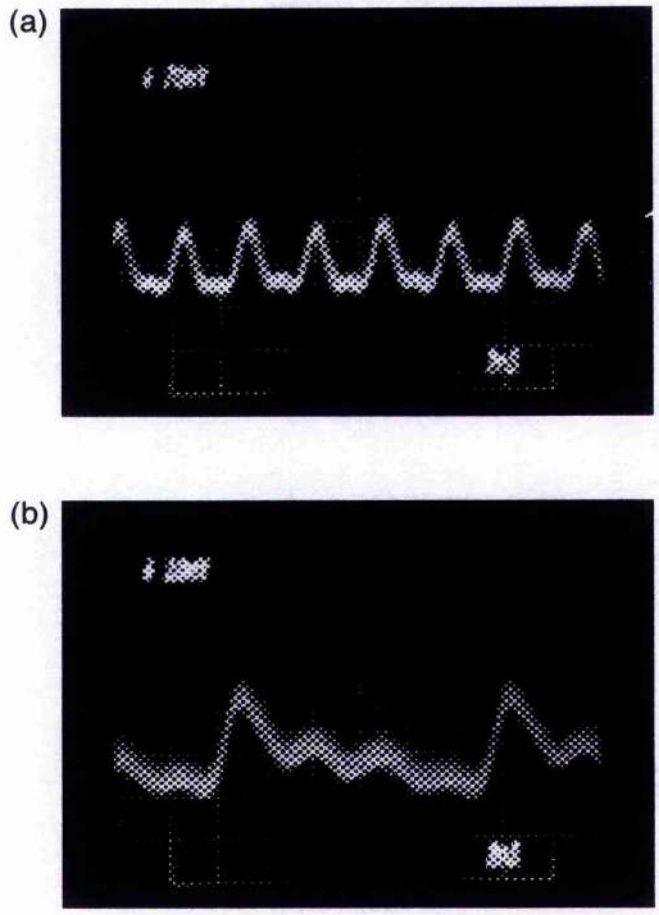

Figure 5.21 Oscillograms of the pulse sequences from the quarter-length OPO. The signal pulse sequence, with a repetition rate of 344 MHz, and negligible amplitude noise, is shown in (a), while (b) shows the idler pulse sequnce, which shared the pump pulse repetiton rate of 86 MHz.

5.7 Concluding remarks

5.7.1 Future work

There is ample scope for further development and refinement of this SMURRF design of an optical parametric oscillator. As discussed in Section 5.6, no intracavity dispersion compensation was implemented in the system, because the cavity was too short to allow sufficient spacing between a prism pair. The compactness and

simplicity of the source is one its main advantages, and would be compromised by changing to prisms with a higher refractive index to reduce the required spacing. However, there are a number of more appealing solutions which would help to maintain the compactness. One answer is still to use prisms, but in the form of a prismatic output coupler. This is an arrangement suggested by Fujimoto and co-workers [20, 21] in their work on semi-monolithic three-mirror laser cavities. The conventional plane end mirror of the cavity is replaced by a right-angled prism, such that the hypoteneuse is Brewster-angled in the cavity, and the opposite side is coated as a high reflector or output coupler as required. Full dispersion compensation can then be provided by either a single prism within the cavity, or by having the anti-reflection-coated side of the crystal cut at Brewster's angle. These two configurations are illustrated in Fig. 5.22.

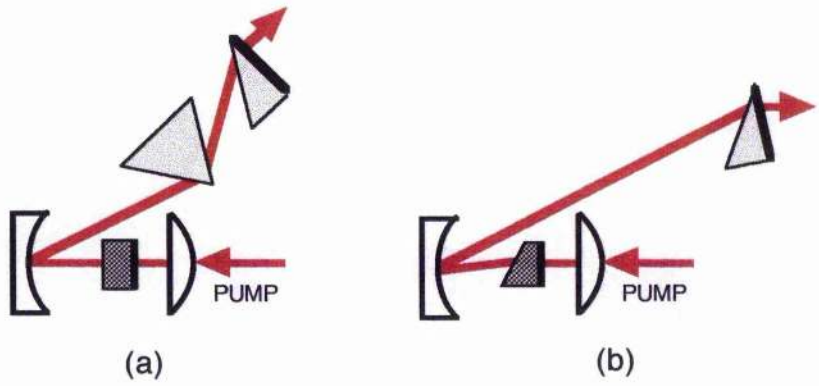

Figure 5.22 Intracavity dispersion compensation schemes for semi-monolithic cavities, utilising prismatic output couplers. (a) has a full prism and a prismatic output coupler, while (b) uses a Brewster-cut crystal and a prismatic output coupler [20, 21].

An alternative method of providing intracavity compensation would be to use the chirped mirrors introduced by Szipöcs and co-workers [28], which were described in Chapter 1. Already applied successfully to a range of ultrashort pulse Ti:sapphire and Cr:LiSAF lasers, mirrors of this type have yet to be utilised in an OPO. They are ideally suited to the SMURRF OPO, and would maintain the simplicity of the system while allowing the generation of sub-100 fs transform-limited ultrahigh repetition rate pulses.

There is, of course, no reason why the development of an ultrahigh repetition rate source should stop at the fourth harmonic of the pump laser frequency. Given

suitable cavity optics to allow the focusing required for mode matching, the SMURRF OPO could be further reduced in size to produce operation at even higher harmonics. A gigahertz source could be constructed by using the sixteenth harmonic of the Ti:sapphire laser, which would result in a cavity length of less than 11 cm, and a repetition rate of 1.376 GHz. The logical conclusion of progression in this direction is an all-monolithic femtosecond OPO. The crystal length would be chosen to match a high harmonic of the pump laser, and both ends of the crystal would be coated as high reflectors, with the possibility of chirped mirrors to provide dispersion compensation. This would be as compact as a synchronously-pumped OPO could get.

It would also be advantageous to extend the tuning range of the SMURRF OPO. The constraint of noncritical phasematching would have hampered this somewhat, were it not for the recent introduction of periodically poled materials. Quasi-phasematching in poled crystals is always noncritical, and allows extensive tuning over the entire transparency range of the material. Consequently the application of a poled crystal to a SMURRF OPO configuration would produce a widely tunable, highly compact, ultrahigh repetition rate source. To date, femtosecond optical parametric oscillation has been demonstrated in periodically poled RTA [19] and lithium niobate [29], so either of these would be a suitable choice of crystal. The wide transparency ranges of these materials would facilitate the generation of near and mid-infrared wavelengths. It would be necessary to resonate the idler to produce ultrahigh repetition rate MIR pulses, but resonance of the signal would still result in a highly compact MIR source. Moreover, it has been shown that parametric processes generating visible light can be simultaneously phasematched with optical parametric oscillation in PPLN [29, 30], so there is the possibility of a visible SMURRF OPO as well. A compact multi-wavelength source should be feasible although it would not be possible to have ultrahigh repetition rates at all wavelengths due to the difficulties of resonating all the waves simultaneously.

A possible explanation for the unexpectedly high oscillation threshold of the semi-monolithic OPO is that some kind of thermal effect in the RTA crystal was to blame. For example, any non-uniform thermal expansion of the crystal would have distorted the highly reflecting coating and impaired the performance of the OPO. A solution to this is to decouple the crystal from the mirror surface, by having an anti-reflection-coated crystal placed almost in contact with a mirror deposited on a very

thin plane substrate. Such a mirror would not interfere with the pump beam focusing, and would not be affected by thermal changes in the crystal.

5.7.2 Conclusions

A femtosecond OPO based on a semi-monolithic crystal has been described in this chapter. The cavity was designed primarily for low threshold operation, and although this goal was not achieved, the system proved to have other useful attributes. Very high output powers were generated; 600 mW of signal power was the maximum recorded, implying a highly efficient conversion of 55%. Intracavity dispersion compensation facilitated the generation of 70 fs, near-transform-limited signal pulses, which were characterised by both a conventional autocorrelation method and the technique of second-harmonic generation frequency-resolved optical gating. The measurement techniques showed good agreement. The main feature of the semi-monolithic design was the fact that the cavity length could easily be reduced to produce operation at harmonics of the pump laser repetition frequency. In this way, the OPO was operated at 172 MHz and 344 MHz, these being the second and fourth harmonics of the Ti:sapphire pump. The 344 MHz cavity was extremely compact, having a total cavity length of only 43 cm. In terms of actual laboratory bench space the length was even less due to the fold in the cavity. Extracavity dispersion compensation was implemented, resulting in 177 fs pulses. A number of possible arrangements for intracavity dispersion compensation in compact cavities have been discussed. Investigation of the amplitude noise of the high repetition rate configurations showed it to be very low, leading to the conclusion that these designs were genuine high repetition rate sources.

The OPOs described elsewhere in this thesis had as their primary purpose the demonstration of oscillation in particular crystals, namely KTA and PPLN, with the aim of generating mid-infrared wavelengths. In contrast to this, the main achievement of the research based on the RTA OPO has been the development of a cavity configuration for the production of high repetition rate pulse sequences. In some ways, the choice of RTA as the nonlinear medium was immaterial to the ultimate results. Because of this, the final cavity design lends itself well to modification by the use of alternative materials to generate different wavelength ranges.

Consequently, the SMURRF OPO configuration could pave the way for a selection of compact, widely tunable, high power, high efficiency, low noise and ultrahigh repetition rate femtosecond sources.

References

1. D. T. Reid, M. Ebrahimzadeh and W. Sibbett, Appl. Phys. B **60**, 437 (1995).
2. D. T. Reid, M. Ebrahimzadeh and W. Sibbett, J. Opt. Soc. Am. B **12**, 2168 (1995).
3. D. Xue and S. Zhang, Appl. Phys. Lett. **70**, 943 (1997).
4. Z. W. Hu, P. A. Thomas, J. Webjörn and G. M. Loiacono, J. Phys. D **29**, 1681 (1996).
5. J. Han, Y. Lui, M. Wang and D. Nie, J. Crystal Growth, **128**, 864 (1993).
6. L. -T. Cheng. L. K. Cheng and J. D. Bierlein, Proc. SPIE **1863**, 43 (1993).
7. D. L. Fenimore, K. L. Schepler, D. Zelmon, S. Kück, U. B. Ramabadran, P. Von Richter and D. Small, J. Opt. Soc. Am. B **13**, 1935 (1996).
8. D. T. Reid, *Novel nonlinear techniques for femtosecond pulse generation in the visible and near infrared*, PhD thesis, University of St Andrews (1994).
9. Crystal Associates Inc., 15 Inductrail Park, Waldwick, NJ 07463, USA.
10. P. E. Powers, C. L. Tang and L. K. Cheng, Opt. Lett. **19**, 1439 (1994).
11. D. T. Reid, M. Ebrahimzadeh and W. Sibbett, Opt. Lett **20**, 55 (1995).
12. M. Scheidt, B. Beier, K. -J. Boller and R. Wallenstein, in *Conference on Lasers and Electro-Optics,* Vol. 19 of 1996 OSA Technical Digest Series (Optical Society of America, Washington, DC, 1996), p. 341, paper CThA4.
13. K. -J. Boller, M. Scheidt, B. Beier, C. Becher, M. E. Klein and D. H. Lee, Quantum and Semiclass. Opt. **9**, 173 (1997).
14. V. Petrov, F. Noack and R. Stolzenberger, in *Conference on Lasers and Electro-Optics Europe* (Institute of Electrical and Electronics Engineers, Inc., Piscataway, NJ, 1996), p. 303, paper CThN1.
15. O. Pfister, M. Mürtz, J. S. Wells, L. Hollberg and J. T. Murray, Opt. Lett. **21**, 1387 (1996).
16. H. Karlsson, F. Laurell, P. Henriksson and G. Arvidsson, Electron. Lett. **32**, 556 (1996).
17. Q. Chen and W. P. Risk, Electron. Lett. **30**, 1516 (1994).
18. W. P. Risk and G. M. Liaocono, Appl. Phys. Lett. **69**, 311 (1996).
19. D. T. Reid, Z. E. Penman, M. Ebrahimzadeh and W. Sibbett, "Broadly-tunable infrared femtosecond optical parametric oscillator based on periodically-poled $RbTiOAsO_4$", accepted by Opt. Lett.
20. M. Ramaswamy-Paye and J. G. Fujimoto, Opt. Lett. **19**, 1757 (1994).
21. B. E. Bouma and J. G. Fujimoto, Opt. Lett. **21**, 134 (1996).
22. S. Guha, F. -J. Wu and J. Falk, IEEE J. Quantum. Electron. **18**, 907 (1982).
23. Rees Instruments Ltd., Thornbrook, Weyside Park, Catteshall Lane, Godalming, Surrey, GU7 1XE.
24. D. T. Reid, C. McGowan, M. Ebrahimzadeh and W. Sibbett, IEEE J. Quantum Electron. **33**, 1 (1997).
25. R. W. Boyd, *Nonlinear Optics* (Academic Press, San Diego, 1992).
26. D. J. Kane and R. Trebino, IEEE J. Quantum. Electron. **29**, 571 (1993).
27. R. Trebino and D. J. Kane, J. Opt. Soc. Am. A **10**, 1101 (1993).
28. R. Szipöcs, K. Ferencz, C. Spielmann and F. Krausz, Opt. Lett. **19**, 201 (1994).

29. See Chapter 6, and also C. McGowan, D. T. Reid, Z. E. Penman, M. Ebrahimzadeh, W. Sibbett and D. H. Jundt, "Femtosecond optical parametric oscillator based on periodically poled lithium niobate", submitted to J. Opt. Soc. Am. B.
30. S. D. Butterworth, P. G. R. Smith and D. C. Hanna, Opt. Lett. **22**, 618 (1997).

chapter six

THE PPLN OPTICAL PARAMETRIC OSCILLATOR

6.1 Introduction

The work presented in this chapter concerns a synchronously-pumped femtosecond optical parametric oscillator (OPO) based on periodically poled lithium niobate (PPLN). As a preliminary to the reported experimental work, a brief review of recent research relating to PPLN is presented, followed by a summary of the properties of lithium niobate and a short discussion on the principle technique for poling crystals. The subsequent sections describing the PPLN OPO commence with some phasematching properties of PPLN, leading to the design of the OPO. A comprehensive range of results is then presented, and placed in the context of the observations of other researchers. The chapter concludes with remarks pertaining to potential future work.

6.2 Recent PPLN research

The past couple of years have seen an enormous increase in the quantity of reported research using PPLN as the nonlinear material in frequency conversion experiments. It is no exaggeration to say that at the present time more papers are published about PPLN than about any other nonlinear crystal. The sudden surge in interest has a number of causes. The seeming difficulty of other materials to perform well in the mid-infrared (MIR) led researchers to search for alternatives. The versatility of quasi-phasematching (QPM) meant that periodically poled materials in general created a lot of interest, but the high nonlinearity and wide transparency range

of PPLN made it the most popular candidate for a wide selection of applications. Improved poling techniques mean that high quality, reliable PPLN crystals are now commercially available, and are being utilised for almost every conceivable nonlinear frequency process.

The majority of early work used PPLN for second harmonic generation, to produce green and blue light. Of course, this does not take advantage of the infrared transparency, but the wide variety of laser wavelengths converted in this way are testimony to the versatility of periodic poling in allowing the user to engineer phasematching properties. Also, the high nonlinearity of PPLN, and therefore the high conversion efficiencies available, made it popular with many researchers. Blue light has been generated by the frequency doubling of a dye laser at 820 nm [1], a Ti:sapphire laser running at 832 nm [2] and a Nd:YAG laser at 946 nm [3]. Both first order and third order phasematching have been used, highlighting the necessary trade-off between the higher efficiencies available from first order processes, and the increased difficulty of making the shorter grating periods required for them. Green light has also been produced in a number of ways, most often by the frequency doubling of 1.064 μm Nd:YAG systems. Pruneri et al used an intracavity configuration [4], whereas Miller et al achieved highly efficient doubling by using a single pass arrangement [5]. These systems were both continuous wave (cw), whereas 2.4 ps pulses have been generated from frequency doubling of a modelocked Nd:YLF laser at 1.047 μm [6]. Moving to longer wavelengths and shorter pulses, Arbore et al recently reported the generation of 190 fs pulses at 777 nm, produced by frequency doubling of a modelocked Er:fibre laser [7].

Difference frequency mixing in PPLN has received some attention, as a technique for producing tunable mid-infrared radiation. The first demonstration of this was in 1995 by Goldberg et al [8], who mixed Ti:sapphire and Nd:YAG laser wavelengths to produce a continuous wave output tunable from 3 to 4.1 μm by rotating the crystal to change the effective grating period. Steps towards more compact sources were taken by both Sanders et al [9] and Wang et al [10]. The first of these systems generated 7.1 μW of light tunable from 3.6 to 4.3 μm by mixing two 0.5 W tunable laser diodes. Higher powers were achieved by Wang et al, who mixed the output of a tunable Cr:LiSAF laser with its laser diode pump source to produce 50 mW of light tunable from 3.3 to 4.2 μm.

Pump	Grating period (μm)	Pulse duration	Tuning method	Output (μm)	Ref.
Q-switched Nd:YAG 1.064 μm	31	ns	temperature	1.664 - 2.95	15
MOPA 977.6 nm	28.5	cw	cavity length	1.85 - 2.08	16
Frequency doubled Q-switched Nd:YAG 532 nm	6.8, 6.85	ns	temperature and grating	0.97 - 1.175	17
Q-switched Nd:YAG 1.064 μm	26 - 31.75	ns	grating	1.36 - 4.83	18
Nd:YAG 1.064 μm	28 - 30	cw	temperature and grating	1.45 - 1.62 3.11 - 3.98	19
modelocked Q-switched Nd:YAG 1.064 μm	29.75	ps	none	1.51 and 3.59	20*
Nd:YAG 1.064 μm	28 - 29.75	cw	grating	1.45 - 1.6 3.25 - 3.95	21
modelocked Nd:YLF 1.047 μm	30.5	2.65 ps (signal)	temperature	1.67 - 1.96 2.24 - 2.8	22
Nd:YAG 1.064 μm	29.75	cw	none	1.57 and 3.3	23
Nd:YAG 1.064 μm	29.75	cw	none	3.2	24
modelocked Ti:sapphire 784 - 804 nm	19, 20	1.4 ps (signal)	pump	1.15 - 1.53 1.68 - 2.4	25
Millennia 532 nm	6.5	cw	temperature	0.953 - 1.0 1.16 - 1.234	26
Q-switched Nd:YAG 1.064 μm	26 - 31	ns	temperature and grating	1.43 and 4.18 1.99 and 5.04	27†

* First synchronously-pumped PPLN OPO

† Two OPOs simultaneously phasematched in one crystal, one pumped by the signal of the other.

Table 6.1 Summary of PPLN-based optical parametric oscillator research.

Optical parametric processes have also been addressed. While the volume of research devoted to parametric generation [11] and amplification [12, 13] is small, a great number of PPLN OPOs have been reported, and a commercial device has just appeared on the market [14]. Continuous wave, nanosecond, and picosecond oscillation have all been demonstrated, based on a variety of pump sources operating in the visible and near infrared. Tuning has been achieved by varying the pump wavelength, crystal temperature, grating period and cavity length. The first PPLN OPO was reported in 1995 [15] and Table 6.1 summarises a number of systems reported since then, in approximately chronological order. From this it can be seen that extensive tunability in the mid-infrard has been achieved in very few systems, and that no OPO operating at pulse lengths shorter than picosecond durations has yet been reported. The OPO described in this chapter addresses both of these shortcomings, offering widely and continuously tunable femtosecond pulses in the near and mid-infrared.

Various optical properties of lithium niobate are relevant to the understanding of PPLN OPOs in general and the femtosecond OPO in particular. These are discussed in the next section.

6.3 Lithium niobate

Lithium niobate, $LiNbO_3$, is a ferroelectric crystal. It is this property that partially determines its use as a periodically poled material; only ferroelectrics can be poled by the application of an external electric field, the current most common method of poling, which is described in Section 6.4.

The property of ferroelectricity [28] is a dielectric phenomenon first discovered in the 1920s, although lithium niobate was not reported to be ferroelectric until several decades later, by Matthias and Remeika in 1949 [29]. The occurrence of the property depends on crystallographic structure, and only a small number of the total of 32 crystal symmetry classes (see Section 2.3) are ferroelectric. The phenomenon is related to electric polarisation and is therefore only found in crystals having a non-centrosymmetric structure. Crystals with a centre of symmetry possess no polarisation properties and consequently cannot be ferroelectric, pyroelectric or piezoelectric. Nonlinear optical properties similarly depend on a lack of

centrosymmetry. Fig 6.1 shows the break-down of the crystal classes by these properties, illustrating how ferroelectric materials have the highest degree of non-symmetry and are therefore also piezoelectric and pyroelectric. A detailed treatment of ferroelectricity is beyond the scope of this thesis, but a brief description is appropriate.

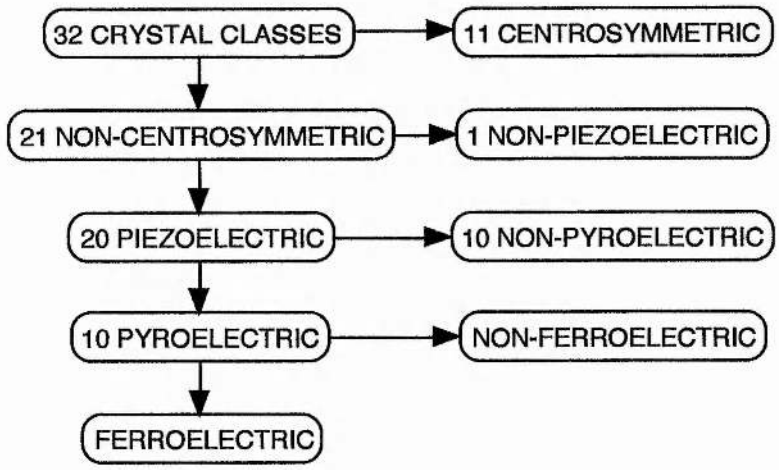

Figure 6.1 Break-down of the 32 crystal symmetry classes according to property.

In essence, a ferroelectric is a material which possesses a permanent spontaneous electric polarisation which can be reversed by an applied electric field. The crystalline structure is such that the internal potential field allows more than one equilibrium position for some of the ions, so that an external electric field can displace ions and hence change the overall polarity. Local regions with homogeneous polarity different from the polarities of neighbouring regions may exist – these regions are called domains. The grating in a periodically poled crystal is simply made up of a number of sequential regions having alternating opposing polarities (and therefore opposing optical nonlinearities). Thus a ferroelectric crystal can be periodically poled by the appropriate application of an electric field to form domains of opposite polarity along the length of the crystal. This is known as a grating, and the width of each domain is half of the grating period, Λ. Fig 6.2 illustrates the structure of opposing domains in lithium niobate, whereby the positions of the lithium and niobium ions are shifted relative to the planes of oxygen ions. A specific relationship exists between the magnitude of the applied electric field, E, and the net polarisation, P, as shown graphically in Fig. 6.3. The relationship forms a hysteresis

loop and it is this that gives the propertyof ferroelectricity its name, because such behaviour is directly analogous to the hysteresis loop relationship between magnetic induction and magnetic field displayed by ferromagnetic materials. Extrapolation of the linear part of the loop back to the polarisation axis gives the value of the spontaneous polarisation, P_s. This property is measured in units of Coulombs per metre squared, C/m^2, and for most ferroelectrics has a value between 10^{-3} and 1 C/m^2. The spontaneous polarisation of lithium niobate is 0.7 C/m^2 [4].

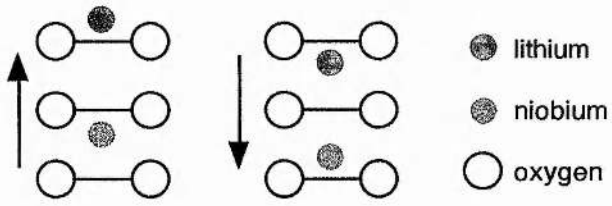

Figure 6.2 Structure of lithium niobate, showing the two equilibrium positions of the lithium and niobate ions which give oppposite polarisations.

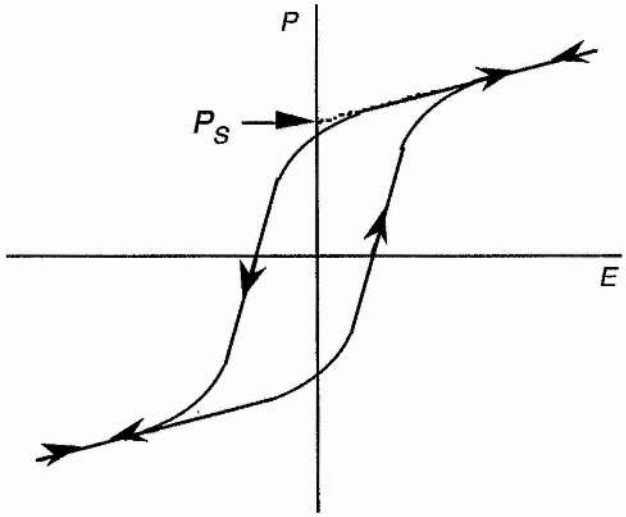

Figure 6.3 Hysterisis loop relationship between applied electric field, E, and net polarisation, P, in a ferroelectric. P_S is the spontaneous polarisation.

Lithium niobate is a uniaxial crystal of symmetry point group 3m, and therefore has a trigonal unit cell and a single three-fold axis of symmetry. Consequently its nonlinear optical tensor, d_{ij}, taking Kleinman's conjecture into account, is given by [30]

$$d_{ij} = \begin{bmatrix} 0 & 0 & 0 & 0 & d_{31} & -d_{22} \\ -d_{22} & d_{22} & 0 & d_{31} & 0 & 0 \\ d_{31} & d_{31} & d_{33} & 0 & 0 & 0 \end{bmatrix} \tag{6.1}$$

Thus there are only three non-zero nonlinear coefficients, d_{22}, d_{31} (or d_{15}) and d_{33}. A number of values for these coefficients have been published. Some of these are given in Table 6.2, which indicates reasonable agreement between the various measurements.

d_{22} (pm/V)	d_{31} (pm/V)	d_{33} (pm/V)	**Wavelength** (μm)	**Ref.**
3.1	5.8	41	–	31
4.0	5.9	34	–	32
2.76	5.44	–	1.06	33
–	5.95	34.4	1.06	33
–	5.77	33.4	1.15	33
–	–	31.8	1.318	33
–	–	29.1	2.12	33

Table 6.2 Published values of the nonlinear coefficients of lithium niobate.

The efficiency of a nonlinear optical interaction is proportional to the square of the effective nonlinear coefficient, d_{eff}, which in turn is related to the d_{ij} coefficients by equations determined by the type of interaction and the type of crystal. Hence d_{eff} should ideally be as large as possible. As Table 6.2 shows, the d_{33} coefficient in lithium niobate is significantly larger than the d_{22} and d_{31} coefficients. Unfortunately, though, standard birefringent phasematching fails to access d_{33} at all, and the effective nonlinearity is derived solely from the smaller coefficients:

Type I interaction $\quad d_{eff} = d_{31}\sin\theta - d_{22}\cos\theta\sin 3\phi$

$e \rightarrow e + e$ (6.2a)

Type II interaction $\quad d_{eff} = d_{22}\cos^2\theta\cos 3\phi$

$e \rightarrow o + e$

$e \rightarrow e + o$ (6.2b)

On the other hand, quasi-phasematching allows the interaction of any combination of polarisations along any direction in the crystal, as specified by the user. In PPLN, the poling direction is chosen such that when all the waves in an optical parametric interaction are chosen to have extraordinary polarisations, then the large d_{33} coefficient is accessed, according to

$$d_{eff} = \frac{2}{m\pi} d_{33} \tag{6.3}$$

where m = 1, 3, 5... is the order of the QPM interaction. Thus first order processes, with m = 1 are the most efficient, and the nonlinearity available in PPLN is approximately four times higher than the maximum available in birefringently phasematched lithium niobate.

There are no very recent measurements of the refractive indices of lithium niobate, which is perhaps surprising, given the current level of interest in PPLN. The most recent figures were published in 1993 by Schlarb and Betzler [34], who measured the indices of refraction as functions of wavelength and composition (molar percentage of LiO_2). However, the Sellmeier equations most often quoted in PPLN-related work are those of Edwards and Lawrence [35], dating from 1984. The coefficients were derived from a selection of data previously published by other authors, using the same form of equation as that used by Hobden and Warner in their measurements of 1966 [36]. These equations are generally reliable, although they are known to be less so beyond 3.235 μm, which marked the limit of the calculations.

Coefficient	Ordinary	Extraordinary
A_1	4.9048	4.582
A_2	0.11775	0.09921
A_3	0.21802	0.2109
A_4	0.027153	0.02194
B_1	2.2314×10^{-8}	5.2716×10^{-8}
B_2	-2.9671×10^{-8}	-4.9143×10^{-8}
B_3	2.1429×10^{-8}	2.2971×10^{-7}

Table 6.3 Sellmeier coefficients of lithium niobate, to fit Equation 6.4a [35].

Lithium niobate is a negative uniaxial crystal, that is to say, $n_o > n_e$. In addition, the refractive indices are temperature-dependent, so parametric devices based on

PPLN have the useful attribute of being temperature tunable. The temperature dependence is included in Edwards and Lawrence's equation, which is quoted below as Equation 6.4, with the coefficients for ordinary and extraordinary waves given in Table 6.3.

$$n^2 = A_1 + \frac{A_2 + B_1 F}{\lambda^2 - (A_3 + B_2 F)^2} + B_3 F - A_4 \lambda^2 \tag{6.4a}$$

where n is the refractive index, A_i and B_i are the coefficients, λ is the wavelength in microns, and F is the temperature dependence, given by

$$F = (T - T_0)(T + T_0 + 546) \tag{6.4b}$$

where T is the crystal temperature in degrees Celsius and T_0 is the reference temperature of 24.5°C.

The variation of ordinary and extraordinary indices with wavelength at room temperature is shown in Fig 6.4. Quasi-phasematching in PPLN uses only extraordinary waves in order to maximise the conversion efficiency, so the ordinary index is of no consequence for phasematching calculations. All phasematching data presented in this chapter are calculated from the expressions of Edwards and Lawrence. Several alternative Sellmeier expressions are given in the Handbook of Nonlinear Optical Crystals [33].

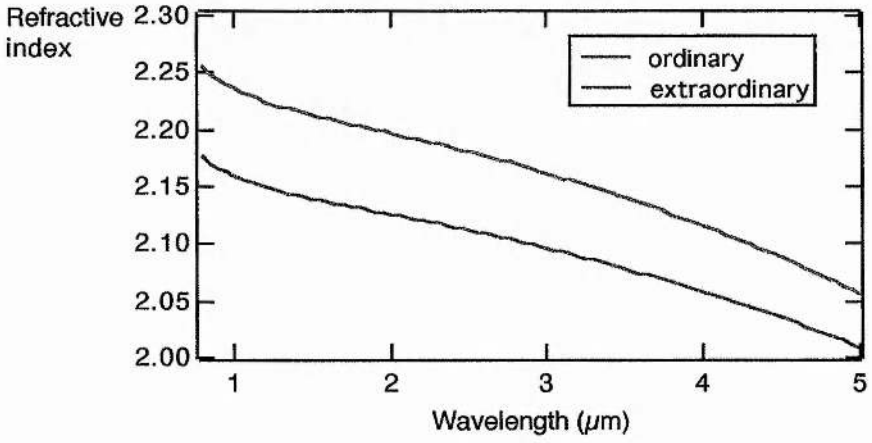

Figure 6.4 Refractive indices of lithium niobate in the infrared, calculated from the Sellmeier coefficients of Edwards and Lawrence [35].

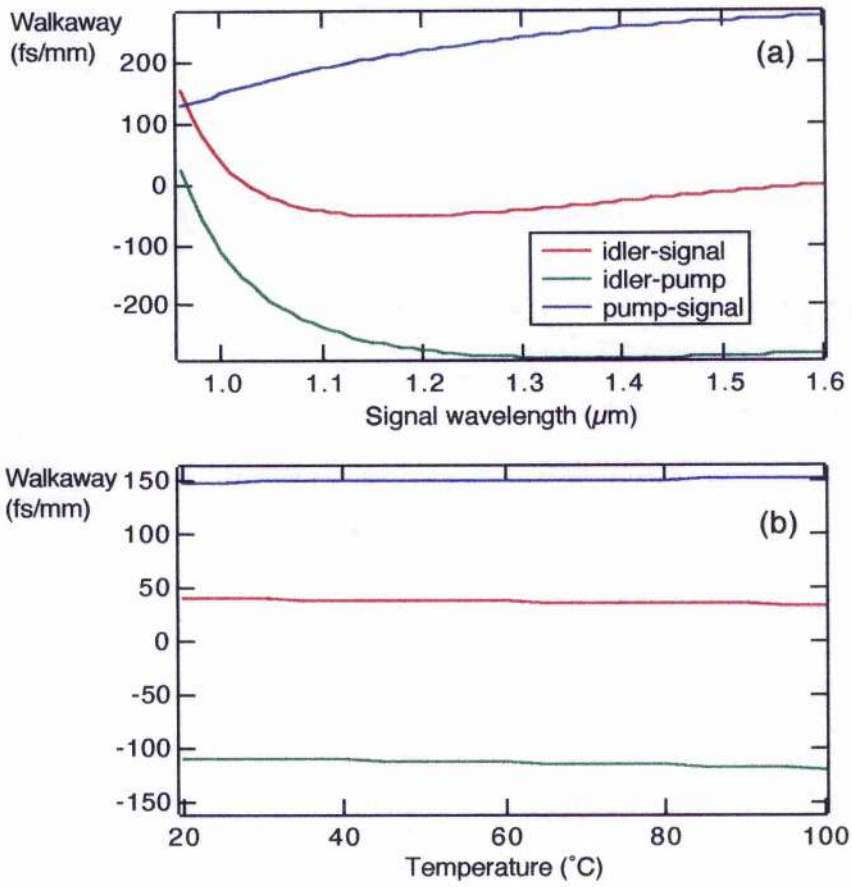

Figure 6.5 Walk-away of extraordinary waves in lithium niobate. The variation with signal wavelength is shown in (a), for a pump wavelength of 800 nm and at a crystal temperature of 25°C. The temperature dependence is shown in (b), for a pump wavelength of 800nm, a signal wavelength of 1 μm and an idler wavelength of 4 μm.

Refractive index also determines the phenomenon of walk-away, whereby the temporal overlap between interacting pulses is reduced by the wavelength-dependence of group velocity. This is of vital importance to ultrashort pulse OPOs, and the theory and significance of this parameter were discussed in Section 2.5.2. The results of calculations for the propagation of pump, signal and idler waves having extraordinary polarisations in lithium niobate, as is the case in a PPLN OPO, are presented in Fig 6.5. These graphs illustrate the walk-away in fs/mm for pump/signal, pump/idler and idler/signal pairs for variations in wavelength (Fig. 6.5a) and crystal temperature (Fig. 6.5b), under conditions given in the figure caption. It is evident that temperature tuning of an OPO has a negligible effect on walk-away, and the maximum magnitude of walk-away in the wavelength region of interest for an OPO pumped at 800 nm is less than 300 fs/mm. Poynting-vector walk-off, the

spatial equivalent of walk-away, does not occur in PPLN because all waves are propagated along a crystal axis, so it does not need to be considered when designing an OPO.

When calculating the phasematching properties of PPLN it is important to take the effects of thermal expansion into account. If temperature tuning is employed, or the crystal is heated to a constant temperature to negate the effects of photorefractive damage (see Section 6.6.3), thermal expansion will cause the grating period to increase. The overall crystal length will also change, which has an effect on efficiency calculations and the like. For the purposes of calculations presented in this chapter the thermal expansion data of Kim and Smith is used [37]. They measured expansion in all three dimensions over the temperature range 0 to 500°C. Because lithium niobate is uniaxial, expansion along the piezoelectric *X*- and *Y*-axes is equal, and since PPLN is poled along the *Z*-axis, beam propagation is in the *X*-*Y* plane. Hence it is this expansion which is relevant to the grating period, and as measured by Kim and Smith is given by

$$\Lambda_T = \Lambda_0[1 + 1.54 \times 10^{-5}(T - 25) + 5.3 \times 10^{-9}(T - 25)^2] \tag{6.4}$$

where T is the temperature in degrees Celsius, Λ_0 is the grating period at 25°C and Λ_T is the grating period at temperature T.

One final property of interest is the transparency range. At the short wavelength end, lithium niobate becomes transparent above 330 nm. However, at the long wavelength cut-off, which is of relevance to the generation of mid-infrared wavelengths, several different values have been quoted in the literature, ranging from 4 to 5.5 μm. The reason for this apparent confusion is clear from Fig. 6.6, which is reproduced from a recent paper by Myers et al [18] and shows the transmission of congruent lithium niobate in the MIR. Although the transmission drops below 100% at about 4 μm, it tails off fairly slowly and does not drop below 50% until nearly 5 μm, making it perfectly possible to generate these longer wavelengths from an OPO or difference frequency mixing device based on PPLN. Fig. 6.6 also highlights additional advantages of using extraordinary waves in PPLN (besides the enhanced nonlinearity) – an e-wave has much higher transmission than an o-wave over much of the 4 to 5.5 μm region, and also does not suffer from the large o-polarisation absorption peak at 2.9μm.

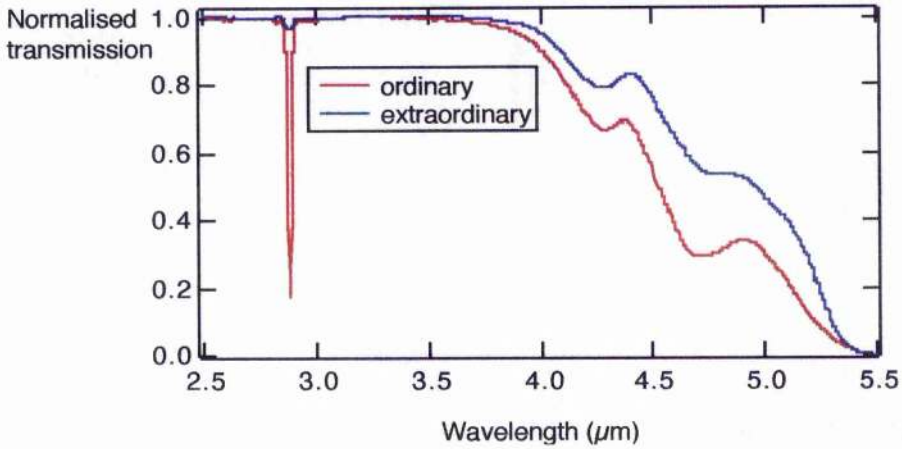

Figure 6.6 Mid-infrared transmission of lithium niobate, for ordinary and extraordinary waves [18].

The properties discussed above are all relevant to the design of a femtosecond PPLN OPO, since they determine such characteristics as phasematching, efficiency and potential operating wavelengths. A number of other properties of lithium niobate, such as the damage threshold and two-photon absorption coefficients, may be found in the Handbook of Nonlinear Optical Crystals [33].

6.4 Periodic poling

The aim of a fabrication method for periodically poled crystals is to provide a high quality, uniform grating structure on the micrometre scale, and at the same time maintain all linear and nonlinear optical properties. A variety of poling techniques have been applied to lithium niobate and other materials, with varying degrees of success. For example, chemical indiffusion can only produce shallow gratings, which are adequate for waveguides but are too small for bulk material. Electron beam writing suffers from poor reproducibility. Techniques involving a modulation of the crystal growth process, such as laser heated pedestal growth, are capable of producing very short grating periods, but can lead to unwanted axial variation in the periodicity. The technique which has so far proved most reliable, and therefore most popular, is that of electric field poling, which is described in the remainder of this section. A number of other methods are discussed in a review paper by Houé and Townsend [38].

The basis of electric field poling is to deposit an insulating mask defining the

grating structure on to the surface of the material, and then to apply an electric field across the material to reverse the polarisation only in those areas unprotected by the insulation. Several closely related methods of implementing this have been demonstrated.

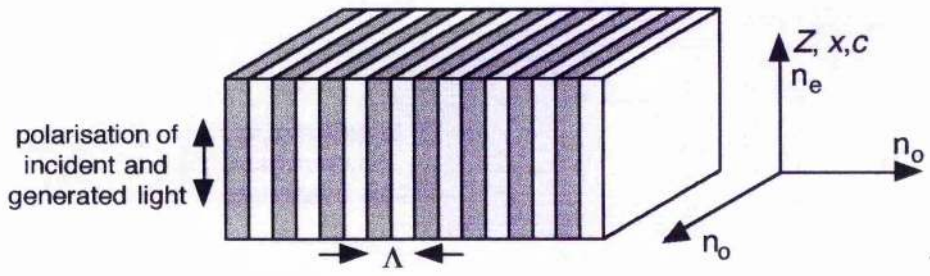

Figure 6.7 Orientation of the axes in a periodically poled lithium niobate crystal.

PPLN is generally manufactured from readily available, high quality wafers of congruently-grown lithium niobate, typically several hundred microns thick. To make use of the desirable d_{33} nonlinear coefficient, poling is carried out along the optic axis (the Z-axis in the piezoelectric frame of reference and the x-axis in the optical frame), so that a PPLN sample will have its geometry defined as shown in Fig 6.7. The mask is therefore applied to one or other of the Z faces of the sample, most often the $+Z$ side, and is patterned by lift-off lithography. One arrangement is to make the grating mask from a layer of metal, such as aluminium, typically 200 nm thick. The insulator, in the form of photoresist, is then applied over the top, to a thickness of a few microns, with a small portion of the metal left uncovered to provide electrical contact. Alternatively, the photoresist may be applied first, and lithographically patterned, with the metal layer deposited on top. To provide a uniform electric field, contact to an external circuit is provided by a layer of liquid electrolyte, frequently LiCl in deionised water, on each surface of the sample. These configurations are illustrated in Fig. 6.8. A less complex approach is to eliminate the metal altogether, by defining the grating with the photoresist mask only and sandwiching the sample between layers of filter paper soaked in electrolyte.

The electric field is then applied, either as a series of short pulses, or a single longer pulse. Reversal of the ferroelectric domains occurs when the applied field exceeds what is known as the coercive field, which is in the region of 20 kV/mm for lithium niobate at room temperature. The total duration of poling is determined by

the amount of charge, Q, which it is necessary to transfer to the sample, given by

$$Q = 2P_s A \tag{6.5}$$

where A is the area of sample to be poled, P_s is the spontaneous polarisation and the factor of 2 accounts for the polarity reversal.

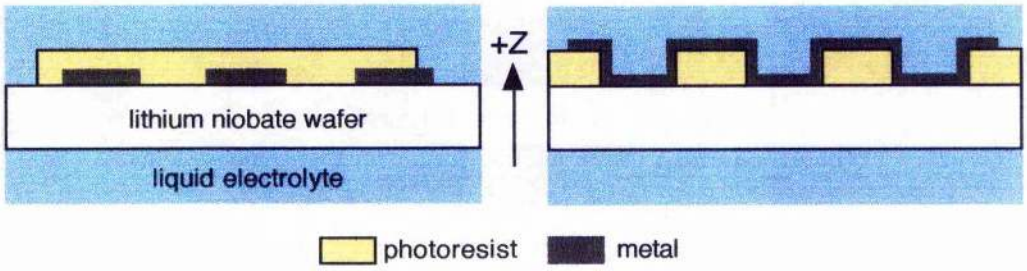

Figure 6.8 Two possible configuration of the photoresist/metal mask used in electric field periodic poling.

Any shape of grating which can be accurately defined by the lithography process can be produced. However, a mask with a precise 50:50 duty cycle will not produce a precise 50:50 grating. This is because the duration of the poling process allows the newly created domains to grow sideways to a certain extent, under the edges of the mask. This can be compensated for by appropriate adjustment of the duty cycle of the mask. The poling process can leave crystals under a certain amount of strain, which can be removed by low temperature annealing.

6.5 Design of the PPLN OPO

There were two mains aims behind the development of the PPLN OPO. The first was to exploit the noncritical geometry of quasi-phasematching and the wide transparency of lithium niobate to produce a widely tunable femtosecond mid-infrared source which would avoid the problems inherent in the critical phasematching needed to generate mid-infrared wavelengths from the majority of birefringently phasematched devices. Secondly, the large nonlinearity of PPLN suggested the possibility of a low threshold femtosecond OPO, which would potentially lead to an all-solid-state diode-pumped system. In addition, there was

also the motivation of demonstrating the first femtosecond optical parametric oscillator based on a periodically poled crystal.

The pump source available for the femtosecond PPLN OPO was the argon-ion-pumped self-modelocked Ti:sapphire laser described in detail in Chapter 3. Hence the available pump wavelengths would be between 780 and 860 nm, with average powers between 1 and 2 W. It was therefore necessary to determine what grating period or periods would provide an output in the mid-infrared.

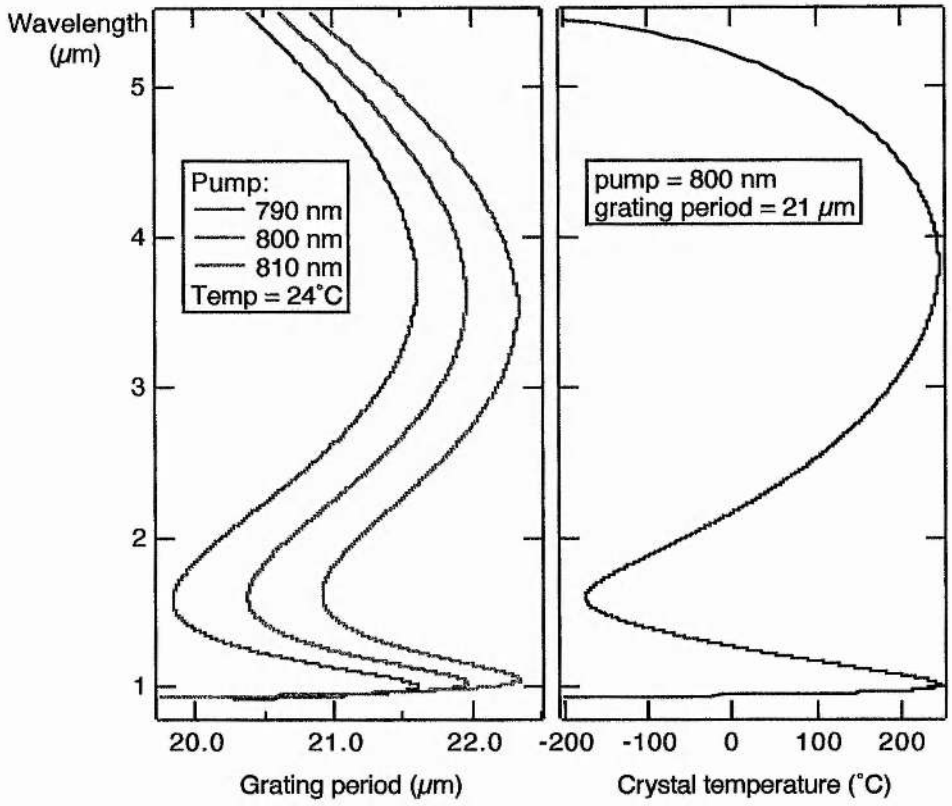

Figure 6.9 Theoretical tuning curves for a Ti:sapphire-pumped PPLN OPO, showing the possibilities available from pump tuning, grating tuning and temperature tuning.

Extensive theoretical modelling of the phasematching properties of PPLN was carried out, using the Sellmeier equations and thermal expansion data quoted in Section 6.3. The possibilities offered by grating tuning, pump tuning and temperature tuning were all considered, and the results of this are presented in Fig. 6.9. From these graphs it can be seen that for typical Ti:sapphire wavelengths near 800 nm an extensive tuning range, from below 1 μm out to the transparency edge at 5.5 μm, is

available from a very small range of grating periods between 20 and 22 μm. Of course, grating tuning from a range of discrete grating periods cannot be continuous, but the remaining spectral gaps may be covered by using pump and/or temperature tuning, both of which are quite rapid in PPLN. Thus a continuously tunable near and mid-infrared source should be possible, with tuning limited only by the bandwidth of the OPO cavity mirrors.

In the light of this, a PPLN crystal with eight gratings having periods evenly spaced between 20.5 and 22 μm was specified, and obtained via a collaboration with Crystal Technology [39]. The gratings were arranged adjacently along the crystal, leading to a size of 11 mm in that dimension, and grating tuning could be implemented simply be translating the crystal across the pump beam. The crystal was 0.5 mm thick, determined by the thickness of the wafer from which it was fabricated. A length of 1 mm in the beam propagation direction was specified. As mentioned in Section 6.3, the walk-away in lithium niobate at the wavelengths of interest can be as much as 300 fs/mm, so with pump pulses of about 100 fs duration a longer crystal would not contribute to the interaction over much of its length. The crystal is portrayed schematically in Fig. 6.10. It was coated for anti-reflection at a signal wavelength of 1.1 μm.

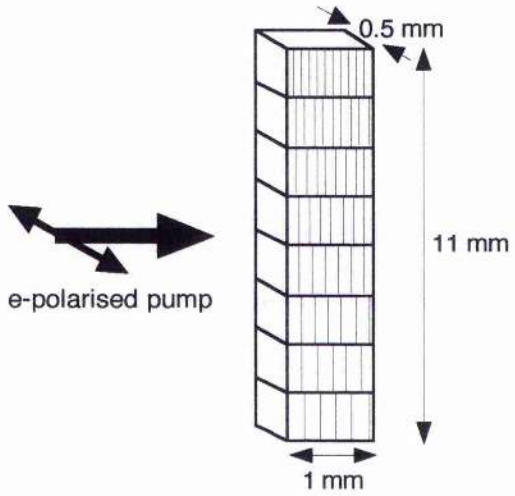

Figure 6.10 Schematic of the PPLN crystal used inthe femtosecond OPO, showing its orientation in the cavity, with respect to the pump beam.

The OPO was configured as a three-mirror cavity, thus keeping the cavity alignment as simple as possible. It was length-matched to the Ti:sapphire laser to

allow synchronous pumping, giving a cavity length of ~1.8 m. A diagram of the cavity is shown in Fig. 6.11. The isolator was included to prevent feedback of the pump reaching the Ti:sapphire cavity and destroying the modelocking.

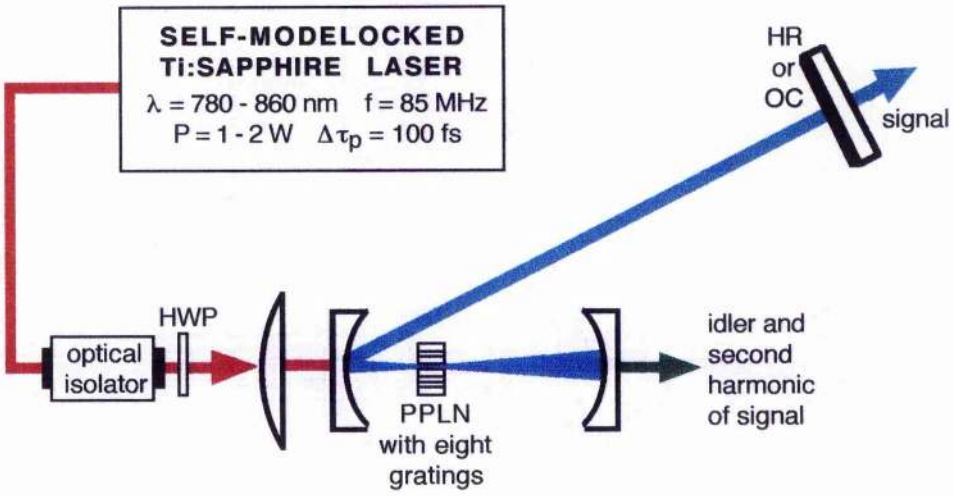

Figure 6.11 Cavity configuration of the femtosecond PPLN OPO.

The mirrors used initially were the set used previously in the KTA-based OPO described in Chapter 4. They had a reflectivity centred at 1.1 μm, with a bandwidth of ~ 200 nm. More importantly, they had calcium fluoride substrates, so the expected mid-infrared idler beam could be extracted from the cavity. The two concave mirrors had radii of curvature of -100 mm, and the end mirror was a plane high reflector. The pump beam was coupled into the cavity via a lens of focal length 50 mm.

The PPLN crystal was affixed to a small Perspex block which was in turn mounted on a xyz-translation stage to allow optimum positioning in the stability region between the curved mirrors. Rotational movement was also provided, so that the crystal could be accurately positioned normal to the incident pump beam. Translation for grating tuning was arranged in the vertical direction. This was to minimise the angle necessary between the beams at the first curved mirror that was required to provide sufficient clearance to prevent the beam from clipping the edge of the crystal. Minimising such angles reduces the effects of astigmatism. Having the crystal in such an orientation meant that the pump beam had to be polarised horizontally. This was advantageous in that it generated a horizontally polarised

signal beam which could be dispersion compensated by prisms in the horizontal plane, rather than in the vertical plane which is considerably more cumbersome to engineer and align.

Alignment of the OPO was achieved by retroreflection of the blue light generated by non-phasematched frequency-doubling of the pump beam, as described in Section 5.4.1. The PPLN crystal generated a considerable quantity of blue light so this technique was easily implemented, and oscillation was then readily achieved by translation of the OPO end mirror to length-match the cavity to the Ti:sapphire laser. Initial operation of the OPO was at room temperature only.

6.6 Experimental results

6.6.1 Tuning

For a pump wavelength of 806 nm, oscillation was achieved on all of the eight gratings. However, the tuning available from changing the grating period was far more limited than the tuning produced by varying the cavity length. Cavity length tuning in synchronously-pumped OPOs is often observed, but its effects are usually slight. As the length of the cavity is adjusted, the oscillating wavelength will shift to change the transit time through the crystal and hence maintain the same cavity round trip time. In the case of the PPLN OPO, cavity length tuning could generate wavelengths covering a large portion of the 200 nm mirror bandwidth. This resulted from a change in cavity length of less than 3 μm. Fig 6.12a shows the tuning produced by each grating, compared to a theoretical tuning curve for the same pump wavelength, while Fig. 6.12b indicates the rate of cavity length tuning. Large tolerances to variations in cavity length in a synchronously-pumped picosecond PPLN OPO have been reported by Butterworth et al [22], but no mention of tuning was made. However, cavity length tuning has been reported in a cw diode-pumped PPLN OPO, covering 100 nm on either side of degeneracy [16].

No direct measurements of the idler output were made at this stage; the signal output of 1.05 to 1.215 μm implied idler wavelengths of 2.36 to 3.14 μm. All signal wavelength measurements were made using a Rees Instruments laser spectrum analyser [40]. There were two possible methods to achieve longer idler wavelengths, either to move to a longer pump wavelength, or to shorter signal wavelengths.

Adjustment of the home-built Ti:sapphire laser to maintain a stable output at a long wavelength can be time-consuming and difficult, whereas shorter signal wavelengths could be generated by moving to different OPO cavity mirrors, so this latter method was adopted.

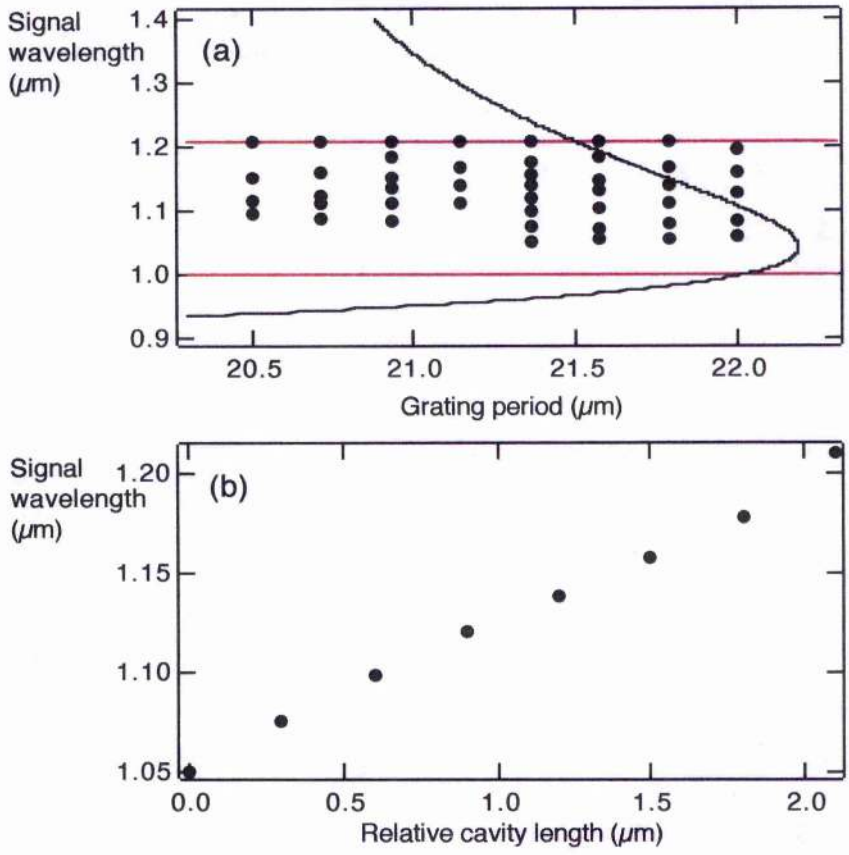

Figure 6.12 Signal wavelengths generated from the PPLN OPO with cavity mirrors centred at 1.1 μm. (a) shows the results of grating and cavity length tuning (circles), which are compared to a theoretical tuning curve (black line). The red lines indicate the mirror bandwidth. (b) shows the variation of signal wavelength with cavity length.

No custom-made OPO mirrors were readily available for operation at wavelengths below those already generated. The best alternative was a set of mirrors designed for long wavelength (1.053 μm) operation of a Ti:sapphire laser. These mirrors obviously were not optimised for transmission at ~800 nm; the pump transmission was measured to be only 40% but this proved to be sufficient. Moreover, the substrates were not calcium fluoride so would not allow extraction of the idler beam. Overall, however, the mirrors were useful enough to allow demonstration of an extension of the tuning range. A pump wavelength of 803 nm

was able to sustain operation on five gratings, those having the longer periods. Once again, cavity length tuning was significant. Signal wavelengths from 975 nm to 1.201 μm were generated, corresponding to an idler output of 2.42 to 4.55 μm, a large proportion of the desired 3 to 5 μm MIR range. The data for this tuning are shown on the composite tuning graph of Fig. 6.18.

Several other longer wavelength OPO mirror sets were available, so these were used to extend the tuning range in the other direction, towards degeneracy. Changing between mirror sets proved to be extremely straight-forward and fast, so a total of four more mirror sets were compared.

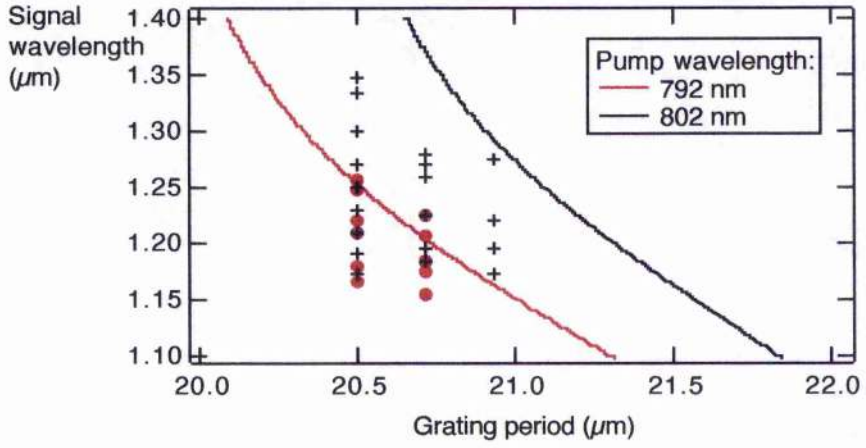

Figure 6.13 Signal wavelengths generated from the PPLN OPO with cavity mirrors centred at 1.274 μm. The results were obtained with a combination of grating and cavity length tuning, at two different pump wavelengths.

The mirrors used in the RTA-based SMURRF optical parametric oscillator of Chapter 5, with a reflectivity centred at 1.274 μm, were employed at two different pump wavelengths, 792 nm and 802 nm. The cavity length and grating tuning obtained is shown in Fig 6.13, demonstrating the extensive pump tuning available from PPLN. The bandwidth of these mirrors cuts off at ~1.4 μm, so additional mirrors would be needed to further extend the tuning range. However, problems are frequently encountered with laser systems running near 1.45 μm, caused by significant water absorption, which can be overcome by operating the laser inside a nitrogen purge to eliminate all water vapour from the surrounding atmosphere. OPO mirrors centred at 1.4 μm were available for use, but a more interesting alternative was a set of doubly-reflecting mirrors, initially designed for an intracavity OPO.

These had reflectance bandwidths centred at 1.274 μm and 1.8 μm. Pumping at 800 nm with a resonant idler wave at 1.8 μm will yield a non-resonant signal at 1.44 μm. Being non-resonant, the 1.44 μm beam would propagate only a very short distance before leaving the cavity, and consequently would not suffer unduly from water absorption. The double mirrors were inserted into the OPO cavity and oscillation was achieved. In fact, resonant waves at both the available mirror reflectivities were observed simultaneously, along with their non-resonant counterparts. Fig 6.14 presents a spectral measurement taken with a scanning monochromator and an InGaAs photodetector, showing a resonant signal wave at ~1.2 μm, its idler at ~2.2 μm, and the resonant idler at ~1.8 μm. No spectrum is seen at 1.4 μm because the measurement was taken after the plane end mirror of the OPO, and none of the 1.4 μm beam propagated that far round the cavity. All the beams showed an extraordinary polarisation, lending credence to the fact that they were all signal and idler beams, and not produced by any non-phasematched mixing processes. Operation of the OPO under these conditions was not robust, so the observations are more of a curiosity than a useful result.

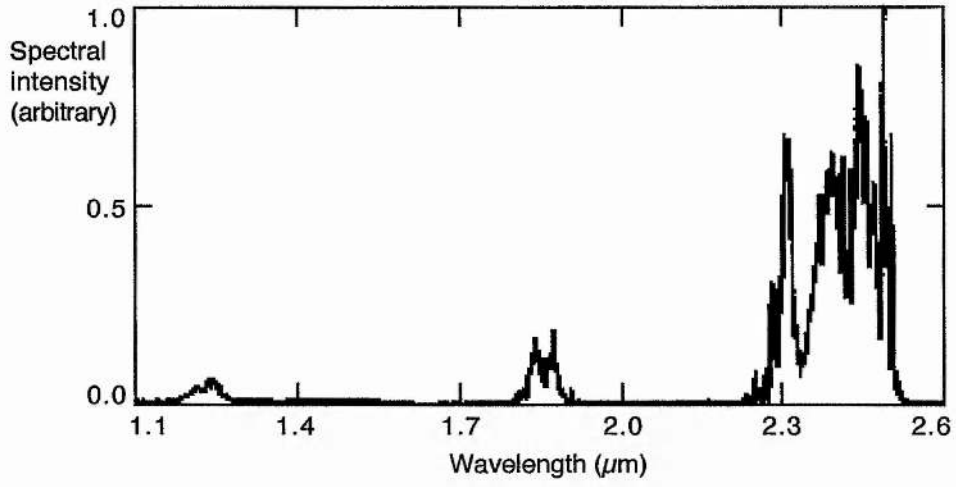

Figure 6.14 Multiple wavelength spectrum recorded from the PPLN OPO with doubly-resonant mirrors centred at 1.274 μm and 1.8 μm. The peaks are a resonant signal wave at 1.2 μm and the corresponding idler at 2.4 μm, and a resonant idler wave at 1.8 μm. The pump wavelength was ~800 nm.

The 1.4 μm OPO mirrors mentioned earlier were used next. Reflectivity data for these mirrors were not available, but the nominal centre is at 1.4 μm, and it is to be expected that the bandwidth is at least 200 nm. Cavity length tuning was achieved

on the four shortest gratings. For a pump wavelength of 803 nm, the signal output covered 1.278 to 1.535 μm, except for a large gap spanning 1.35 to 1.51 μm. Water absorption seems the likely cause of this as there are prominent absorption features over the whole of this range, as indicated in Fig 6.15, which shows the absorption spectrum of 4 m of air (taken from ref. 41). Rather curiously, though, oscillation at wavelengths from 1.444 to 1.541 μm was readily achieved using the remaining mirror set, which was centred at a reflectivity of 1.6 μm. Oscillation at 1.444 μm was right on the edge of the mirror bandwidth. Signal spectra measured at this wavelength were characterised by a number of dips, which are attributable to specific water absorption peaks. As can be seen from Fig. 6.16, many of the dips exactly match features recorded by Gilmore et al [42], who performed intracavity laser spectroscopy using a multimode Cr^{4+}:YAG laser. It was expected that oscillation at degeneracy would be possible with the 1.6 μm mirrors. Unfortunately, performance of the OPO deteriorated with tuning towards degeneracy, and operation at the degenerate wavelength of 1.6 μm was never achieved. Fig. 6.17 shows two pairs of spectra (measured with a scanning monochromator); these are signal and idler pairs recorded while tuning towards degeneracy. Fig. 6.17b shows the furthest tuning possible. The tuning may have been limited by the mirrors, because tuning stopped when the idler wavelength moved onto the long wavelength end of the mirror bandwidth so possibly the OPO was unable to support double resonance.

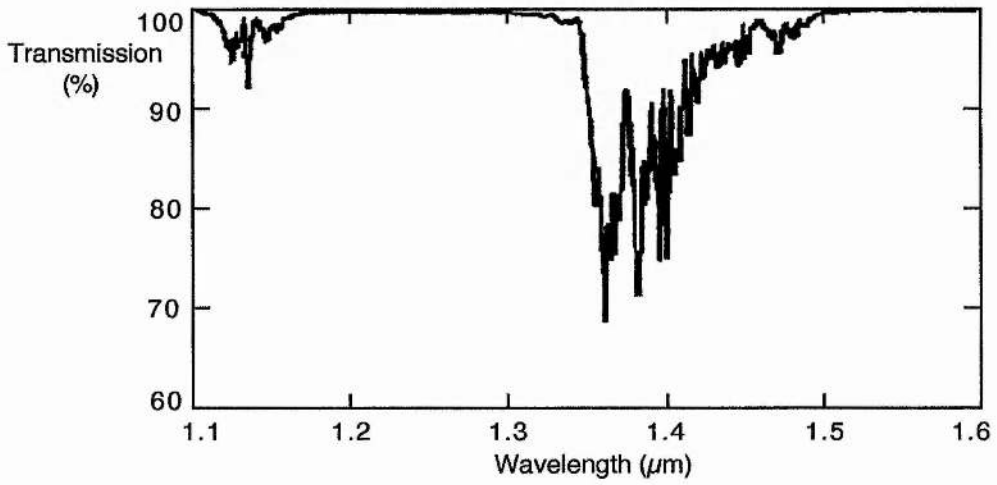

Figure 6.15 Transmission spectrum of 4 m of air, showing the prominent water absorption feature at 1.4 μm [41].

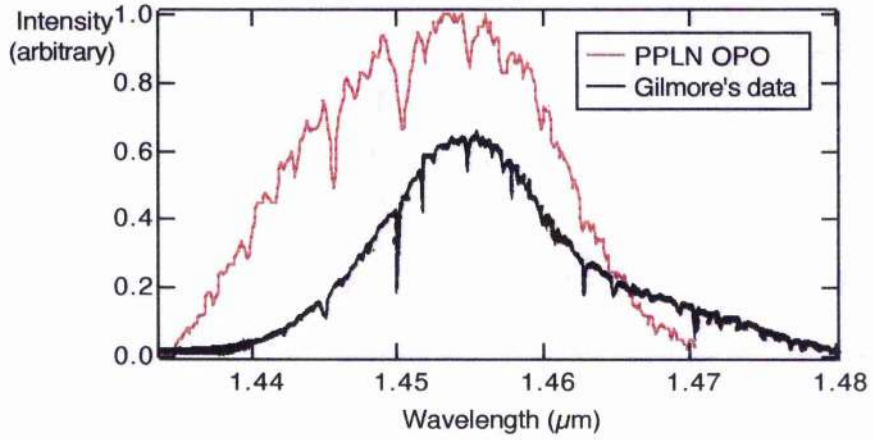

Figure 6.16 Signal spectrum from the PPLN OPO with mirrors centred at 1.6 μm (red line). A number of absorption features are visible, which correspond well with a laser spectroscopy water absorption measurment by Gilmore et al (black line)[42].

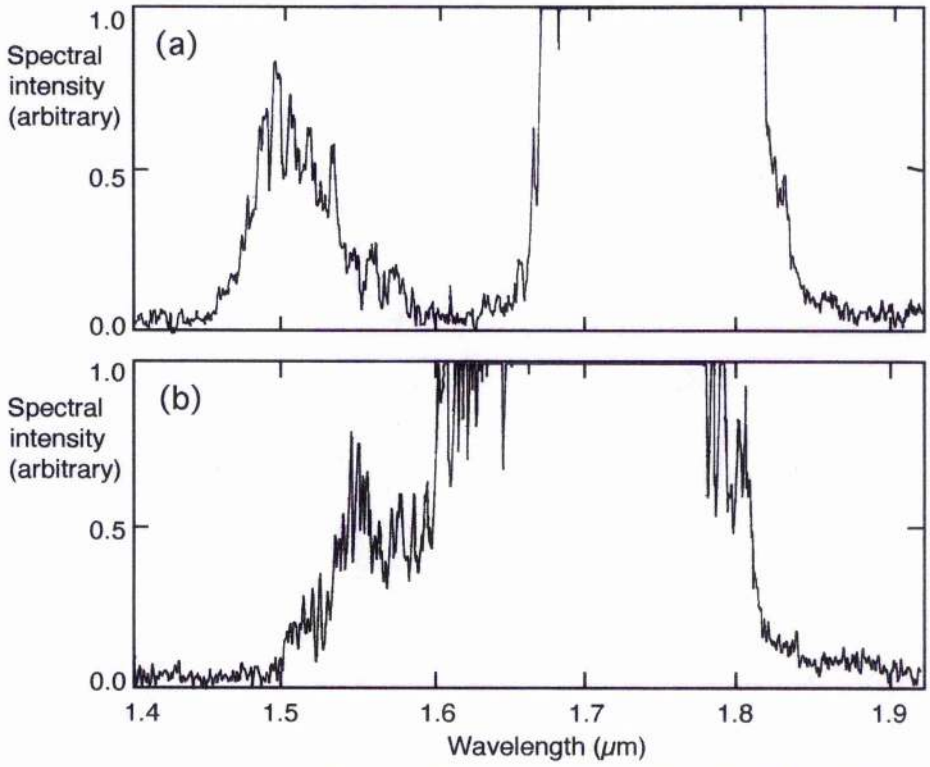

Figure 6.17 Spectra of the signal and idler output recorded from the PPLN OPO with cavity mirrors centred at 1.6 μm, as it was tuned towards degeneracy at ~1.6 μm. (b) represents the furthest tuning point reached.

Fig. 6.18 shows the majority of the aforementioned tuning data, with idler results inferred from the signal measurements. A theoretical tuning curve for a pump wavelength of 803 nm is included for comparison. With the exception of the gaps at

degeneracy and those due to absorption, tuning was continuous from 975 nm to 4.55μm, and was obtained using grating and cavity length tuning only, with five different mirror sets. Changing the mirrors was straightforward, so the PPLN OPO offers an extensively tunable ultrashort pulse source in the near and mid-infrared. Mirrors with wider bandwidths would further improve the system since fewer mirror changes would be necessary. The specifications of the five mirror sets used are summarised in Table 6.4.

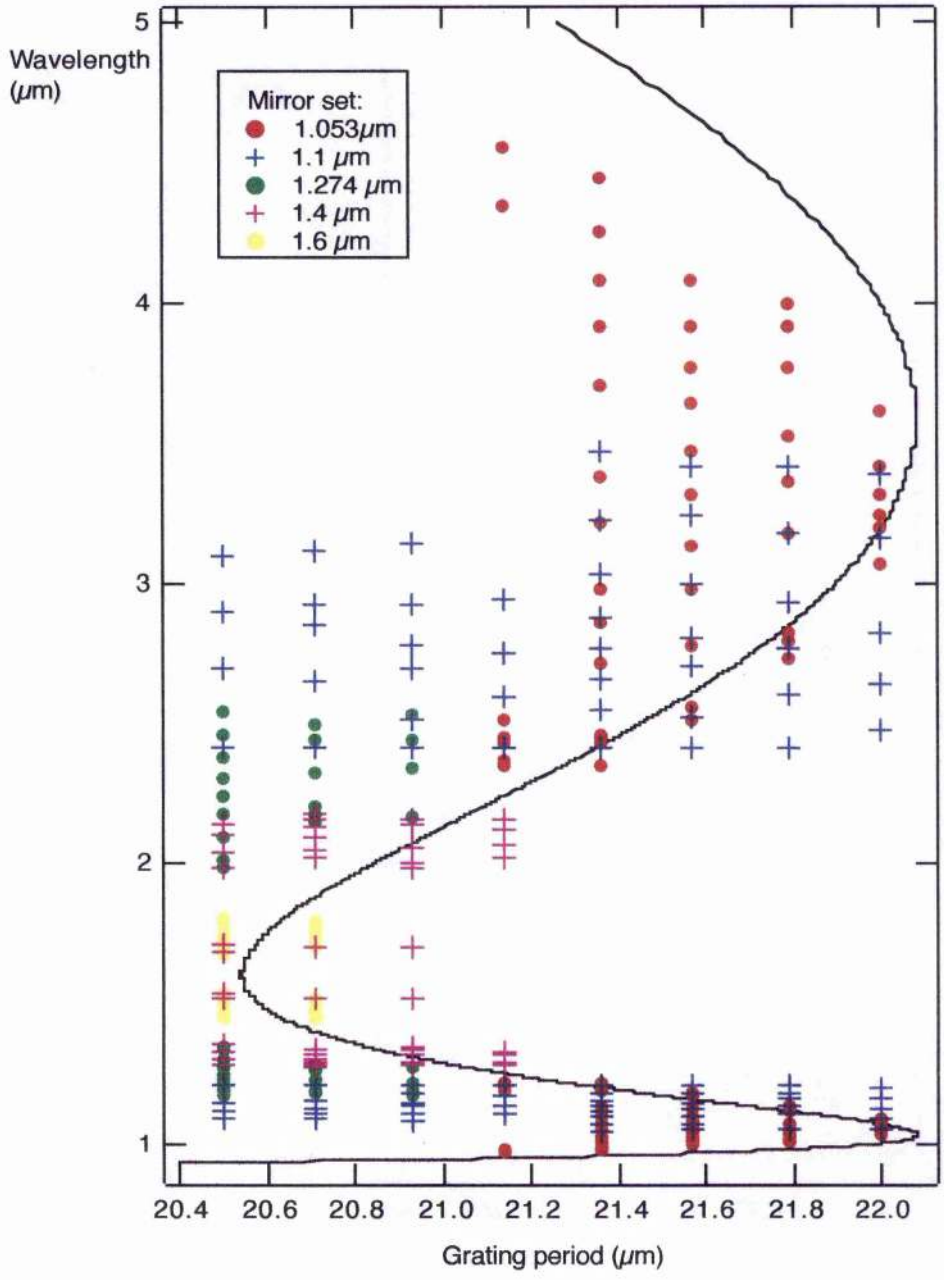

Figure 6.18 Tuning results from the PPLN OPO, from grating, cavity length and pump tuning, and five mirror sets. Idler data are inferred from signal data. The theoretical tuning curve is for a pump wavelength of 803 nm.

Mirror set	Centre wavelength (μm)	Bandwidth (μm)
Ti:sapphire	1.053	unknown
KTA OPO	1.1	1 - 1.22
RTA OPO	1.274	1.15 - 1.41
1.4 μm OPO	1.4	unknown
1.6 μm OPO	1.6	1450 - 1750

Table 6.4 Specifications of each of the mirror sets used in the PPLN OPO.

6.6.2 Gain bandwidth

It can be seen from Fig. 6.18 that a large number of experimental points lie a considerable way from the predicted curve, further than would be expected from experimental error or unreliable Sellmeier coefficients. The explanation for this can be found by considering the magnitude of the wave-vector mismatch, Δk, and the resulting variation in gain with wavelength. The particular form of this variation is a consequence of the double-valued nature of the phasematching curve; Fig 6.9a illustrates this, showing how the signal and idler branches turn back on themselves. This behaviour is seen only for pump wavelengths in the approximate range of 780 to 860 nm and occurs because for these wavelengths the resulting signal and idler span a region where the curvature of the material dispersion of lithium niobate changes sign [42]. This happens at approximately 1.6 μm, ie. near degeneracy, as shown in Fig. 6.19. An alternative way to describe this is to consider the behaviour of Δk, because the phasematching curve is merely the locus of the points where $\Delta k = 0$. For a quasi-phasematched OPO interaction Δk is given by

$$\Delta k = 2\pi\left[\frac{n_p}{\lambda_p} - \frac{n_s}{\lambda_s} - \frac{n_i}{\lambda_i} - \frac{1}{\Lambda}\right] \tag{6.6}$$

where n_j and λ_j are the refractive index and wavelength of wave j, Λ is the grating period and the subscripts p, s and i denote the pump, signal and idler, respectively. The variation of the mismatch with wavelength is of significance here, and is

calculated by taking a fixed grating period and a fixed pump wavelength and computing Δk for pairs of signal and idler wavelengths. The result of this for a pump wavelength of 803 nm and a grating period of 20.5 μm is shown in Fig. 6.20. Note that the curve of Δk crosses zero at four points, which leads to the double-valued shape of the phasematching curve. The wavelengths at which $\Delta k = 0$ vary with pump wavelength and grating period, which produces the tuning properties. Only pump/grating combinations of ~800 nm and ~20 μm give $\Delta k = 0$ in the region that gives four crossing points, so the doubling back behaviour in tuning in PPLN OPOs is seen only at pump wavelengths available from Ti:sapphire lasers, not from other common pump lasers.

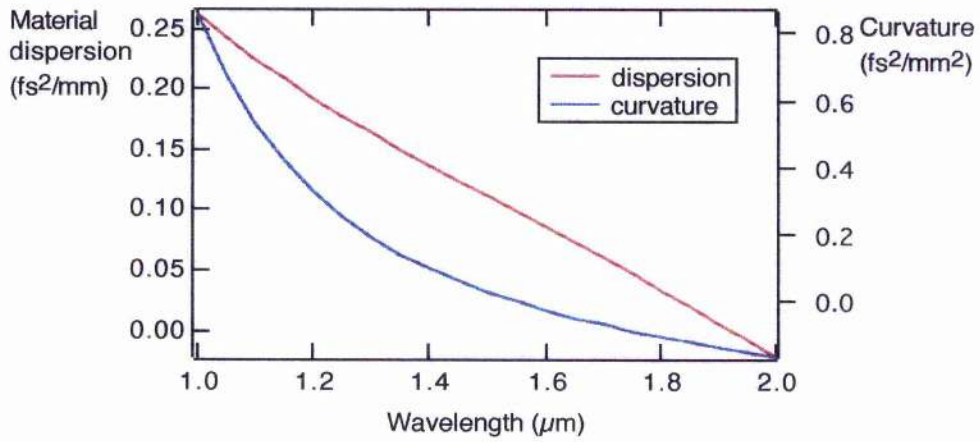

Figure 6.19 Material dispersion of lithium niobate, and its curvature, which changes sign near 1.6 μm

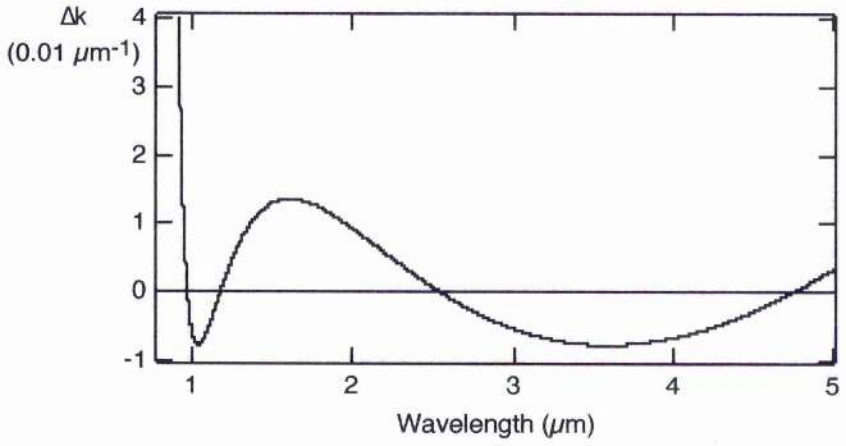

Figure 6.20 Variation with wavelength of wave-vector mismatch, Δk, in a PPLN OPO with a grating period of 20.5 μm and a pump wavelength of 803 nm.

Fig. 6.20 shows that for an extended range of signal wavelengths the value of Δk is very small. OPOs can generally tolerate small amounts of wave-vector mismatch, so it seems likely that this explains why the OPO can sustain oscillation so far from ideal phasematching. This explanation can be taken a stage further by considering the parametric gain of the system, since this depends on Δk, and oscillation can only be expected for significant values of gain. In the limit of small gain, the gain, G, of an OPO is given by

$$G(\omega_s,\omega_i) \cong \frac{\omega_s\omega_i\mu_0(\chi^{(2)})^2 l^2}{2n_p n_s n_i c} I_0(\omega_p)\frac{\sin^2(\Delta kl/2)}{(\Delta kl/2)^2} \tag{6.7}$$

where ω_j is the angular frequency of wave j, $\chi^{(2)}$ is the second order nonlinear susceptibility and l is the interaction length [44, 45]. For the purposes of the current argument it is not necessary to consider the absolute value of the gain, only its dependence on wavelength. So, given that refractive index and wave-vector mismatch are both functions of wavelength, and recalling that $\omega = 2\pi/\lambda$, Equation 6.7 can be rewritten as

$$G(\lambda) \cong \frac{1}{n_p n_s n_i \lambda_s \lambda_i}\frac{\sin^2(\Delta kl/2)}{(\Delta kl/2)^2} \tag{6.8}$$

Assuming that the parametric interaction occurs over the whole length of the crystal, the interaction length, l, may be taken to be equal to the crystal length, in this case 1 mm. The gain is therefore modulated by a sinc^2 dependence on Δk, as is evident from Fig. 6.21, which shows that a peak in gain occurs about each $\Delta k = 0$ point. Fig. 6.21 shows plots of gain against wavelength for each of the grating periods on the PPLN crystal, indicating how the bandwidths of the gain peaks are very wide and that two adjacent peaks can overlap to form a single wider peak when two $\Delta k = 0$ points are close together. These very large gain bandwidths imply that it is to be expected that oscillation could be achieved far from phasematching. The large bandwidths available in Ti:sapphire-pumped PPLN have been mentioned elsewhere [43], but no reported experimental data have demonstrated this feature. Fig. 6.22 presents a contour plot of gain against wavelength and grating period in the region of interest (a cross-section of this profile in the wavelength direction gives a curve of the type in Fig. 6.21). The experimental tuning data of Fig. 6.18 are superimposed on the plot, showing that the majority of points lie in areas of high gain. A number of points

lie outside the gain region; this is attributable to the fact that some data were recorded at pump wavelengths slightly different from the value of 803 nm used to calculate the gain model.

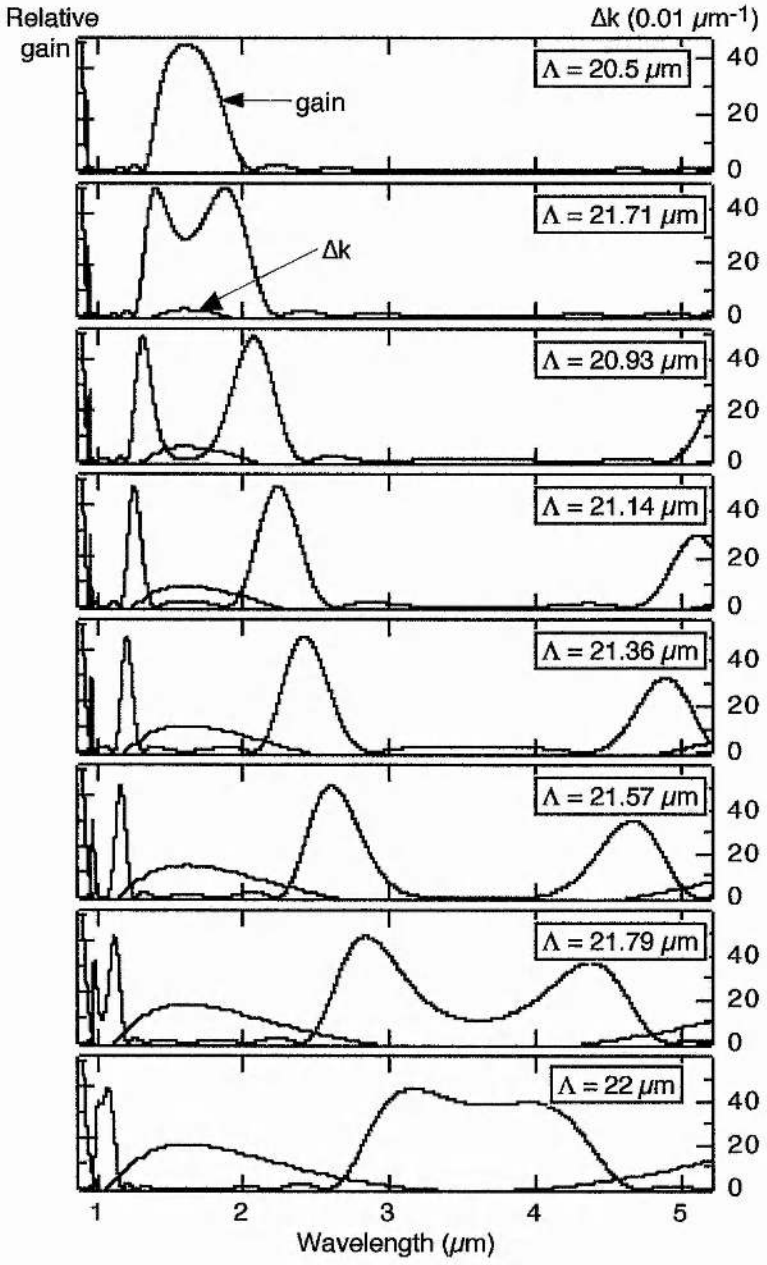

Figure 6.21 Variation of gain with wavelength for each of the gratings in the PPLN OPO crystal, for a pump wavelength of 803 nm, and calculated from Equation 6.8. The wave-vector mismatch, Δk, is included to indicate the points at which perfect phasematching occurs (Δk = 0), where the gain is consequently greatest.

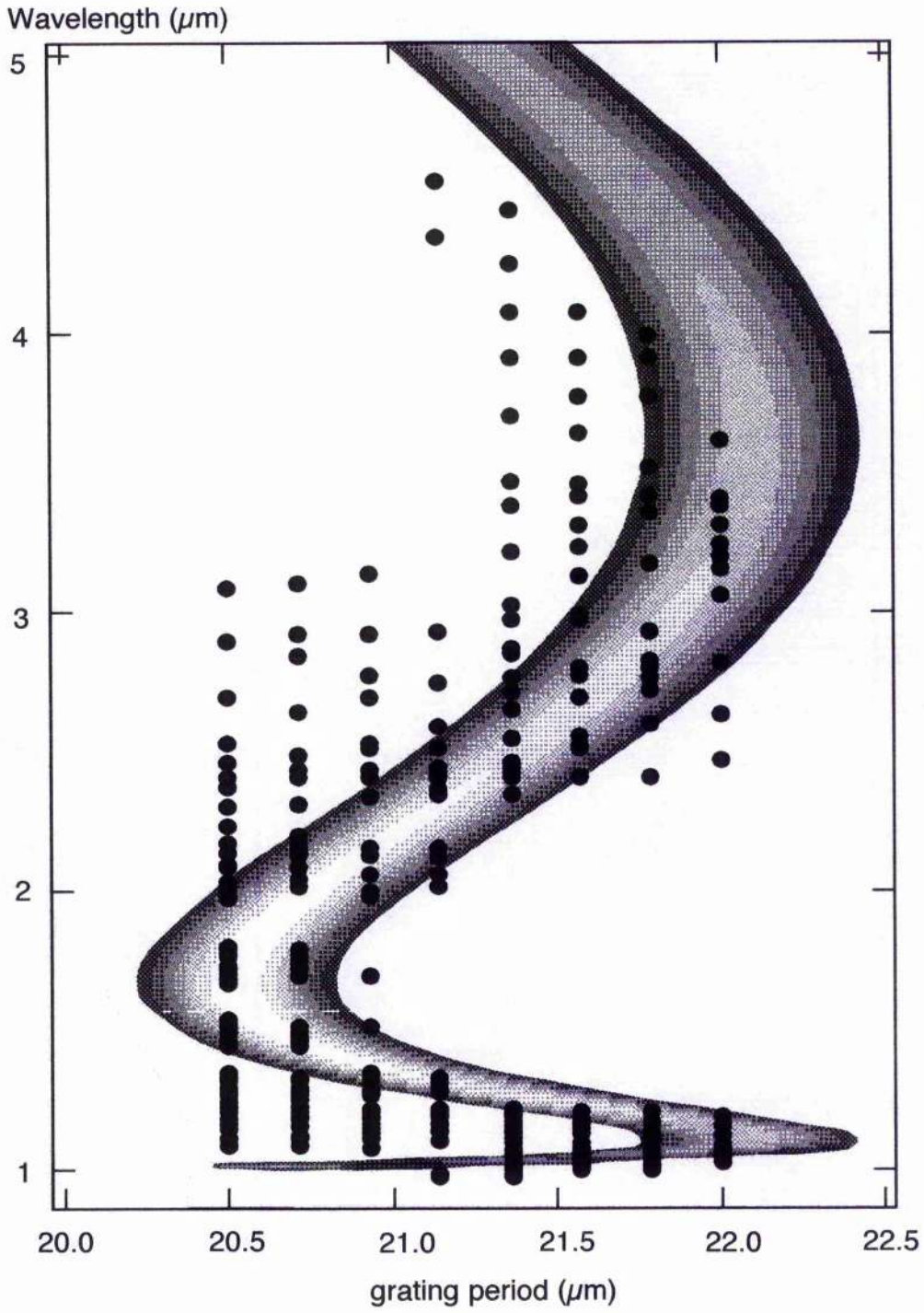

Figure 6.22 Contour plot of gain against wavelength and grating period for the PPLN OPO, calculated from Equation 6.8 for a pump wavelength of 803 nm. The white areas correspond to maximum gain, with the exception of the white background where the gain is zero or negligible. The experimental tuning data of Fig. 6.18 is included, to indicate that oscillation ocurred in areas of maximum gain.

6.6.3 Photorefractive damage

As the name suggests, the photorefractive effect [456] is a nonlinear optical effect whereby light incident on a material produces a change in the refractive index. In certain materials, called photorefractive materials, incident light of a sufficient intensity can produce free charge carriers via the process of photoionisation. The rate of production of the carriers is proportional to the local value of the intensity. The carriers diffuse through the crystal, moving away from regions of high intensity and resulting in a spatially varying charge distribution which in turn produces a spatially varying electric field distribution. This electric field produces a change in the refractive index through the linear electro-optic, or Pockels, effect. The diffusing charge carriers can result in an ever-shifting variation in refractive index throughout the material. The photoelectric effect can often be useful, as in the case of amplification by two-beam coupling, or the construction of phase conjugate mirrors. However, the effect can also be detrimental, in which case it is referred to as photorefractive damage.

The susceptibility to photorefractive damage of lithium niobate at room temperature has been acknowledged for many years [47]. However, it is generally accepted that the problem is less serious in PPLN compared to that in the unpoled material. Indeed, several reports of frequency doubling in PPLN [1, 48] state that no photorefractive damage was observed at all, despite the fact that the effect is strongest in the 400 to 700 nm region in lithium niobate [49]. Damage has been reported in a PPLN OPO [43] and was also observed during the room temperature operation of the femtosecond PPLN OPO, manifested as a constantly shifting and extensive break-up of the output beams. Fortunately, photorefractive damage can be avoided by heating. The higher temperatures cause the recombination rate of the photoionised charge carriers to exceed the rate of formation, thus eliminating the problem. Early research [47] suggested that a temperature of 170°C was appropriate to achieve this, but no mention is made in that report of behaviour at lower temperatures. More recent work [43] concluded that there was a sudden dramatic improvement in the performance of a PPLN OPO when the crystal was heated above 50°C, suggesting that temperatures as high as 170°C were unnecessary. Consequently, an oven was constructed for use in the femtosecond OPO, capable of raising the crystal temperature to 100°C, in an attempt to eliminate the observed

damage. This had the desired effect; when operated at a constant 100°C the OPO showed no sign of beam break-up, and operation became generally more stable. The design of the oven is depicted in Fig. 6.23.

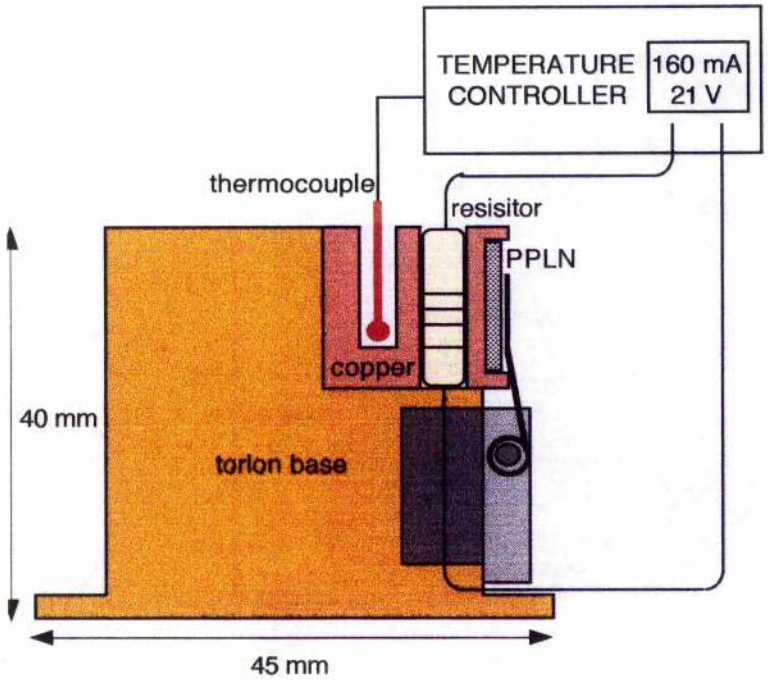

Figure 6.23 Design of the oven used to heat the PPLN crystal.

The heating element was a 150 Ω resistor, drawing a current of 0.16 A. This was placed inside a small copper block, and in good thermal contact with it. The PPLN crystal was held against the block by means of a spring-loaded lever, thus allowing thermal expansion. The copper block was surrounded on four sides by a base made of Torlon, chosen to provide good thermal insulation, which was in turn screwed to a translation stage to provide accurate positioning of the crystal. The temperature was monitored by means of a thermocouple placed in a hole in the copper block, and connected to a Marlow Industries temperature controller [50] which also provided the power supply for the resistor. It was found that the temperature as measured by the thermocouple, and displayed on the controller, was actually significantly higher than the temperature of the outer surface of the crystal, as measured by an independent temperature probe. This outside temperature was taken to be the crystal temperature, although it is likely that there was a thermal gradient across the crystal, which did not, however, seem to affect operation of the

OPO. A simple calibration of the temperature reading was conducted, so that the actual crystal temperature could be calculated from the reading on the controller. This is shown graphically in Fig 6.24. The best fit to the data is a quadratic equation:

$$T_C = 18.847 + (0.15255)T_R + (2.5898 \times 10^{-3})T_R^2 \tag{6.9}$$

where T_C is the temperature of the crystal and T_R is the temperature as displayed by the temperature controller.

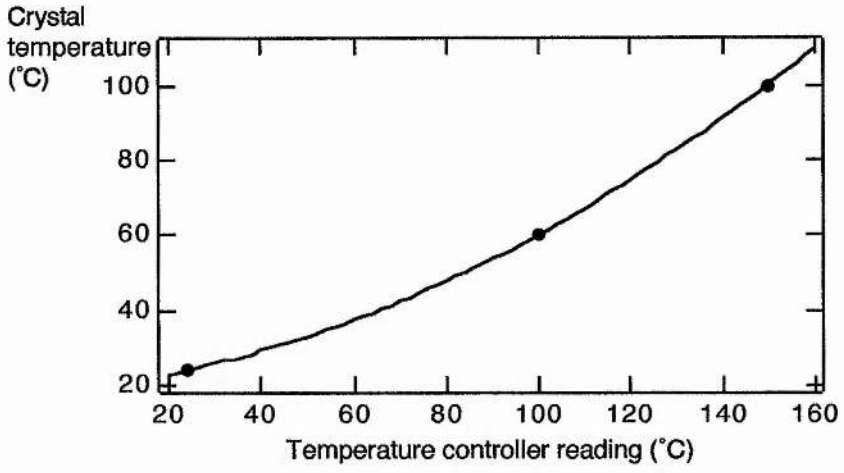

Figure 6.24 Calibration curve for the PPLN oven, relating the reading on the temperature controller to the temperature of the outer surface of the PPLN crystal. The circles are experimental results.

6.6.4 Temperature tuning

Successful temperature tuning in PPLN has been regularly reported in recent literature [15, 22, 26]. The installation of the oven meant that this facility could be added to those of pump, grating and cavity length tuning in the femtosecond PPLN OPO. This additional means of tuning is useful in providing a multi-purpose tuning capability which can allow access to a specific combination of pump, signal and idler wavelengths. Fig. 6.25 shows the results of tuning the OPO in this way, using the KTA OPO cavity mirrors, centred at 1.1 μm. Cavity length tuning is illustrated for a pump wavelength of 798 nm and a grating period of 20.71 μm, for crystal

temperatures of 24°C, 60°C and 100°C. The long wavelength end of the signal tuning is limited by the mirror bandwidth, rather than the gain. As with the grating tuning at room temperature, the tuning available from adjustment of the cavity length dwarfs the effect of temperature tuning.

Unless otherwise stated, all results reported in the remainder of this chapter correspond to a crystal temperature of 100°C, and were obtained with the 1.1 μm cavity mirrors.

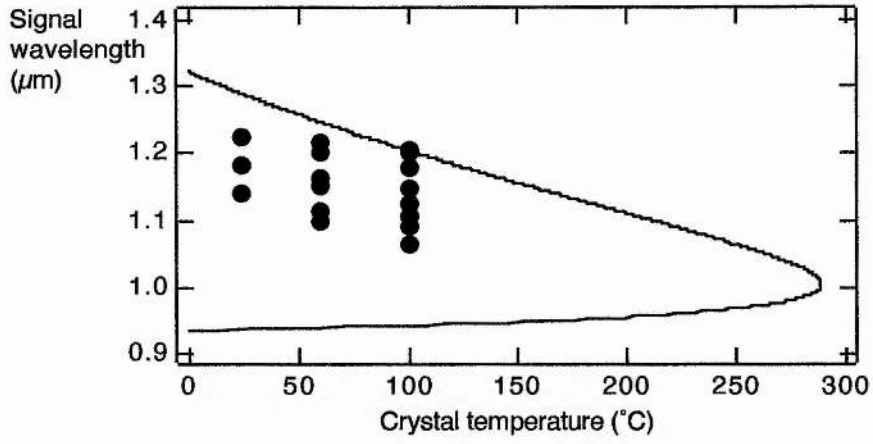

Figure 6.25 Signal wavelengths generated from temperature tuning of the PPLN OPO (circles), supplemented by cavity length tuning. The wavelength of the pump was 798 nm, the grating period was 20.71 μm, and the cavity mirrors were centred at 1.1 μm. The curve is theoretical.

6.6.5 Characterisation of the uncompensated OPO

A number of measurements were taken from the OPO with no dispersion compensation in the cavity. These are discussed in this section.

Signal power

The highly reflecting plane end mirror of the cavity was replaced with an output coupler to allow extraction of the signal beam for the purposes of characterising the pulses. The most appropriate output coupler available for use with the 1.1 μm mirrors was one giving 1% transmission at 1.2 μm, with which oscillation was readily achieved. To ascertain whether this output coupling provided near-

optimum extraction, a Brewster-angled prism was introduced into the OPO cavity, whilst running with the high reflector rather than the output coupler. A prism can be introduced into the intracavity beam by a very small amount so that part of the beam is picked off for measurement purposes while the remainder of the beam maintains oscillation. It has previously been noted that an optimal output coupler extracts 40 to 50% more power than a prism [51]. In this case the prism extracted 66% of the signal power transmitted through the output coupler, so it was concluded that the output coupling was optimised with the 1% output coupler. The variation with wavelength of signal power extracted through this output coupler is shown in Fig. 6.26. The wavelength was varied by cavity length tuning only. The graph is a fairly typical shape for the power of a resonant wave versus change in cavity length [52], except for the dip centred near 1.085 μm, the reason for which is discussed in Section 6.6.7. A maximum of 90 mW of signal power was measured, for a pump power of 1.35 W. This power level could be sustained across the tuning range by the use of pump and temperature tuning.

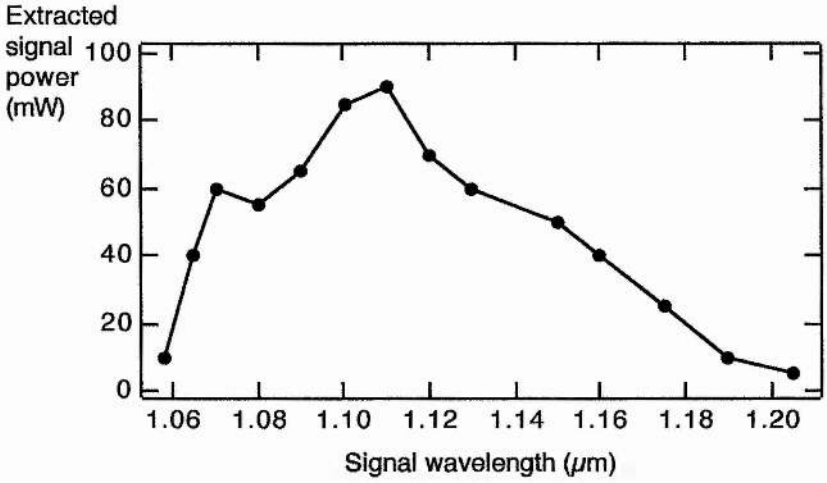

Figure 6.26 Variation of signal power with wavelength extracted from the uncompensated OPO through a 1% output coupler.

As mentioned in Section 6.6.3, photorefractive damage is claimed to be eliminated in PPLN by heating the material to temperatures greater than 50°C. This does not necessarily imply that the parametric process in PPLN is uniformly efficient at all temperatures above 50°C. To investigate this, the variation of signal power with crystal temperature was measured. For each temperature, the

performance of the OPO was optimised by optimising the cavity alignment and adjusting the crystal position and cavity length to obtain the maximum possible signal power. The results of this are shown in Fig. 6.27, and indicate that optimum performance was to be had for an operating temperature in the region of 80°C.

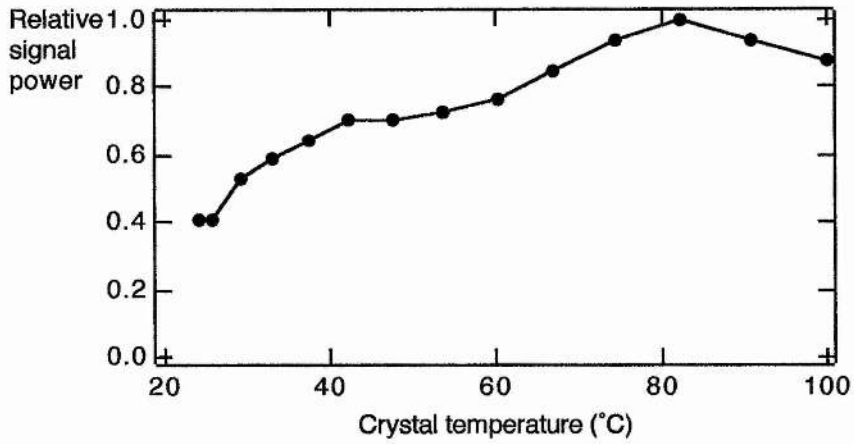

Figure 6.27 Variation with crystal temperature of maximum signal power extracted through a 1% output coupler from the optimised uncompensated OPO.

Idler power

Measurements of idler power were possible because of the calcium fluoride substrates of the cavity mirrors. A measurement was made by collecting the idler power leaving the cavity through the second curved mirror, as indicated in Fig. 6.11. Light leaving the cavity at this point was highly divergent, due to the tight focussing of the beam within the crystal, so the idler was collimated using a curved gold mirror. After optimising the performance of the OPO, a total of 53 mW of idler power was measured. This figure takes into account losses at a germanium filter used to block shorter wavelengths, but is not adjusted for transmission losses at the cavity mirrors, which may have been up to 50%.

Efficiency

Combining the stated values of signal, idler and pump powers implies the rather low extraction efficiency of 10.6%. This is somewhat disappointing, given the high nonlinearity of PPLN.

Pump depletion

A low level of pump depletion could be responsible for the poor efficiency of the OPO, so this was studied in some detail. Depletion was measured by comparing depleted pump spectra with the spectrum of the undepleted pump obtained with the OPO blocked, and calculating the percentage depletion from the relative areas under the curves. Depleted and undepleted spectra were recorded by monitoring the residual pump beam after transmission through the crystal and the second curved mirror. This was done for a range of different signal wavelengths, obtained by cavity length tuning. The results are given in Fig. 6.28, where each depleted spectrum is compared with the undepleted spectrum, and accompanied by the corresponding signal spectrum. Thus it can be seen that as the signal was tuned from short to long wavelengths, the pump was depleted at increasingly longer wavelengths. This behaviour would contribute an error to fitting experimental tuning results to a theoretical phasematching curve, because the wavelength components of the pump spectrum which interact most strongly with the signal pulses are not constant, but vary over about 10 nm. Pump tuning in PPLN is quite significant, so this could account for some of the data points that lie outwith the gain region of Fig. 6.22.

The numerical values of the pump depletion calculated from the recorded spectra are given in Fig. 6.29, as they vary with signal wavelength. The shape of the graph follows the variation of signal power with wavelength (Fig. 6.26) only very generally. Moreover, the maximum pump depletion of 60% far exceeds the 10.6% extraction efficiency, so the poor efficiency cannot be due solely to low pump depletion.

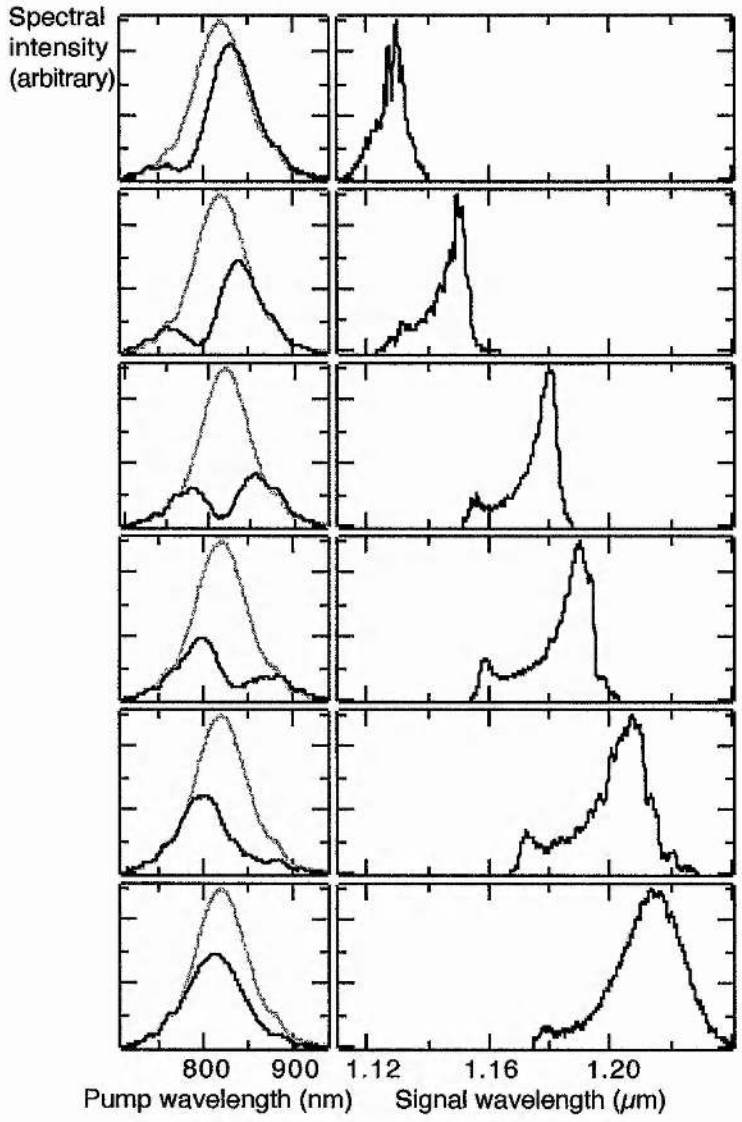

Figure 6.28 Depleted pump spectra, and their corresponding signal spectra, recorded from the uncompensated OPO during cavity length tuning. The spectrum of the undepleted pump (grey line) is included for comparison.

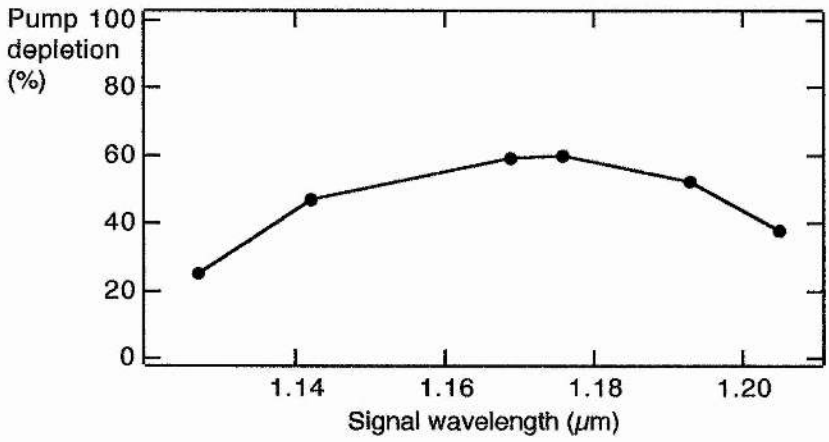

Figure 6.29 Variation of percentage pump depletion with signal wavelength, taken from Fig. 6.28.

Threshold

The oscillation threshold of the OPO was measured to be 45 mW. Given the low efficiency, this is a rather more encouraging result, implying as it does that a synchronously-pumped PPLN OPO could be pumped by a low power all-solid-state diode-pumped laser, such as a Cr:LiSAF system, producing a highly compact, highly tunable infrared ultrashort pulse source. A low threshold in a Ti:sapphire-pumped ultrashort pulse PPLN OPO has been observed before; Butterworth et al reported a threshold of only 18 mW for their picosecond device [25].

Pulse durations

The simplicity of varying the signal wavelength via cavity length tuning suggested the possibility of measuring the pulse duration for a range of wavelengths, to ascertain any effects on pulse characeteristics. Unfortunately, the lower signal powers available at the extremes of the tuning range precluded the use of an LED for interferometric autocorrelation measurements (see Section 3.2.3), so a conventional second harmonic autocorrelator was used instead. The frequency doubling was performed in an angle-tuned BBO crystal, and the resulting light recorded with a photomultiplier tube. High quality fringe-resolved autocorrelation traces were obtained in this way, and recorded at three different wavelengths, as depicted in Fig. 6.30. The longest wavelength spectrum shows the characteristic double-peaked shape indicative of self-phase modulation (SPM), as would be expected from an uncompensated OPO. This is less evident at shorter wavelengths; also, the shorter wavelength autocorrelations show a lesser degree of chirp. The cause of this is the increase in signal power with wavelength over the tuning range in question, as can be seen from Fig. 6.26. The amount of SPM in a system is proportional to intracavity power, and a high level of SPM produces increased pulse broadening. This is seen here, with the longest wavelength pulse having a significantly longer duration than the shortest. It can be difficult to precisely determine the position of the full-width half-maximum of a highly chirped autocorrelation trace, so the pulse durations were calculated by numerical averaging of the interferometric traces to produce intensity autocorrelations, from which the full-width half-maxima were easily retrieved. Thus, assuming $\mathrm{sech}^2(t)$ pulse profiles, the measured pulse durations were 335 fs at 1.067 μm (centre wavelength), 346 fs at 1.08 μm and 548 fs at 1.114 μm.

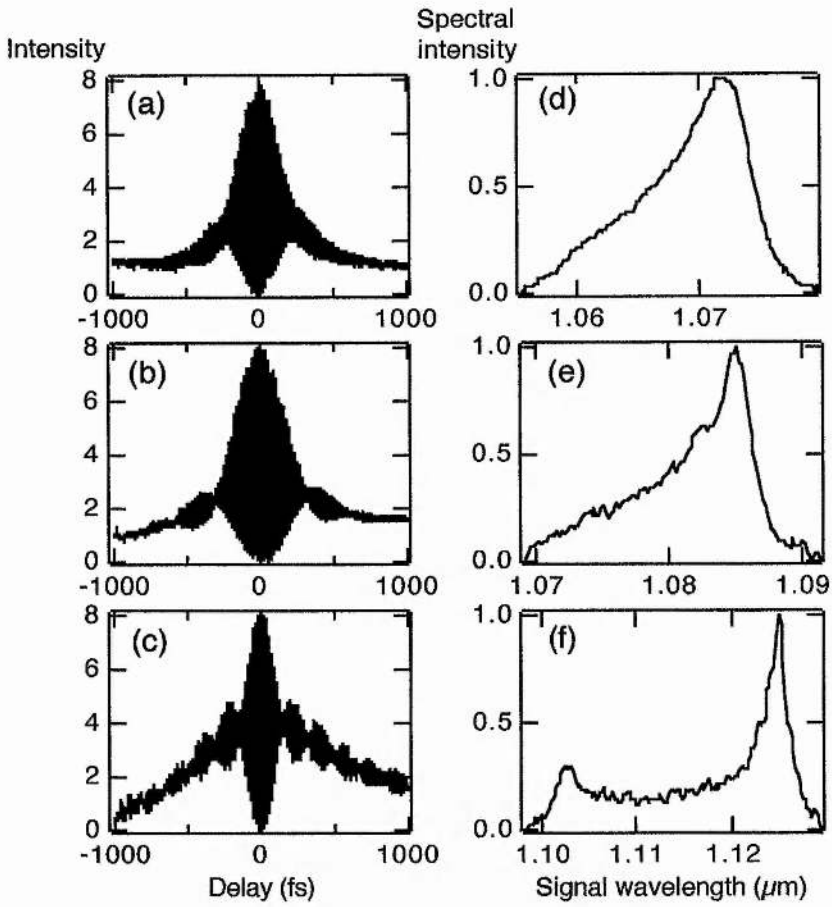

Figure 6.30 Autcorrelations and corresponding spectra of signal pulses from the uncompensated OPO, showing how the level of chirp increased with wavelength, in line with increasing signal power. The pulse durations were 355 fs (a), 346 fs (b) and 548 fs (c).

6.6.6 Characterisation of the dispersion-compensated OPO

Pulse durations

The long, highly chirped pulses generated from an OPO with no dispersion compensation can generally be improved by the addition of a prism pair to provide pulse compression and produce a net negative group velocity dispersion. To this end, a pair of SF14 prisms were inserted into the long arm of the OPO cavity, as depicted in Fig. 6.31. As discussed in Section 2.5.4, the amount of dispersion compensation provided by a prism pair depends on their apex separation. Initially, the OPO was configured with a prism separation of 150 mm, but monitoring of the pulses by

autocorrelation showed no apparent reduction in chirp. Hence, the separation was increased to 300 mm, which resulted in essentially chirp-free pulses across the signal tuning range. Fig. 6.32 shows a typical interferometric autocorrelation trace recorded at a wavelength of 1.1 μm, with its corresponding spectrum. The autocorrelation implies a pulse duration of 140 fs, assuming a $\mathrm{sech}^2(t)$ pulse shape. Combined with the bandwidth of the spectrum, 10.3 nm, this implies a time-bandwidth product of 0.35, so the pulses were near-transform-limited. Further compression of the signal pulses could have been possible by optimisation of the prism separation, but no attempt was made to do this.

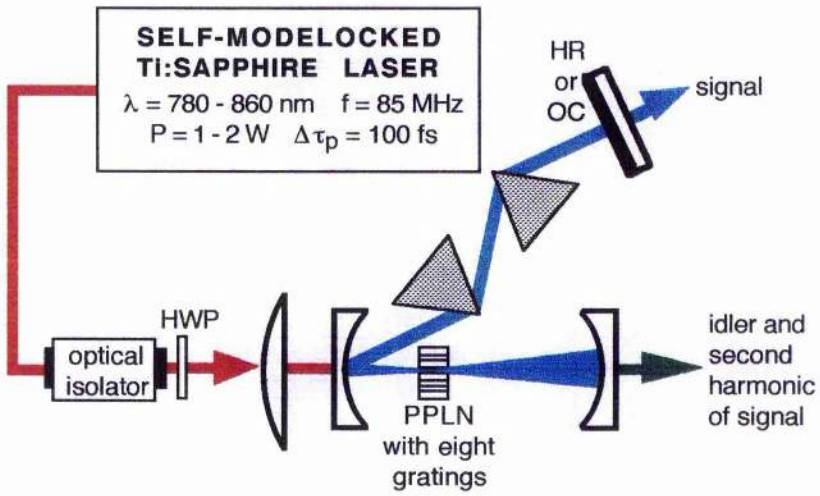

Figure 6.31 Configuration of the dispersion-compensated PPLN OPO cavity, showing the position of the intracavity prisms.

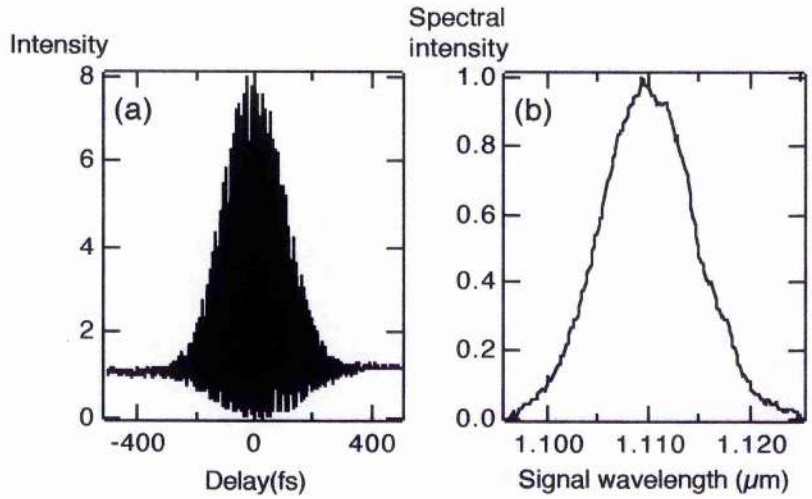

Figure 6.32 Autocorrelation (a) and corresponding spectrum (b) of signal pulses from the dispersion compensated OPO. The pulse duration was 140fs, the spectral bandwidth was 10.3 nm and the time-bandwidth product was 0.35.

Signal power

The addition of prisms to the cavity did not significantly reduce the available signal power. Only 10 mW was lost at the maximum power, as illustrated in Fig. 6.33 (c.f. Fig. 6.26). The total tuning range was reduced somewhat because the power from the compensated cavity at the shortest and longest wavelengths was too low to sustain oscillation in the presence of the losses introduced by the prisms. This small reduction in output power is in marked contrast to the large prism insertion losses reported for birefringently phasematched OPOs, which can typically reduce powers by as much as 50% [52, 53].

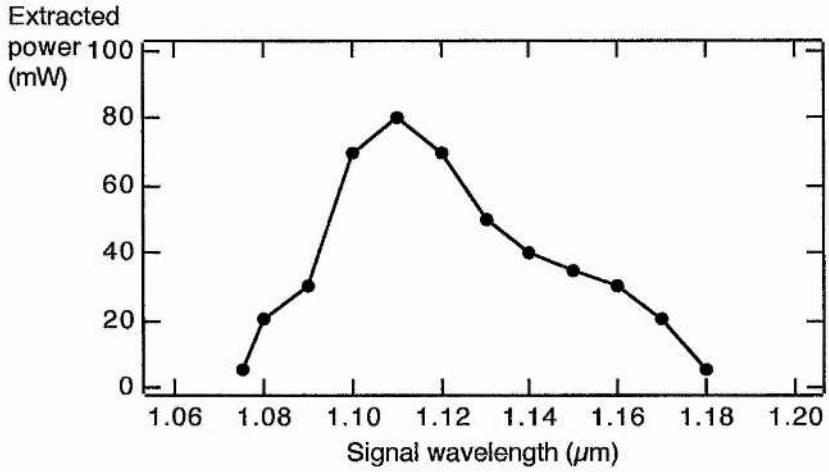

Figure 6.33 Variation of signal power with wavelength extracted from the compensated OPO through a 1% output coupler.

6.6.7 Visible output

When operated at room temperature, the OPO generated a small amount of visible light due to unphasematched mixing processes between the pump, signal and idler, as is often the case with femtosecond OPOs. The most notable of these processes were sum-frequency-mixing between the pump and signal, and frequency doubling of the signal. The wide tunability of the signal resulted in a second harmonic signal tunable from blue-green right through to red. Fig 6.34 is a photograph of the OPO generating red light in this way. Whilst useful in providing a visible indicator of oscillation, the powers at these wavelengths were negligible, as is to be expected from unphasematched interactions.

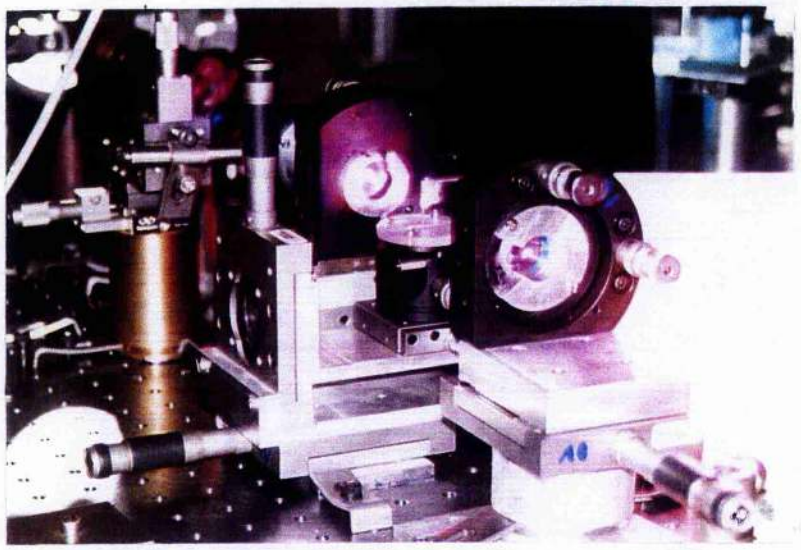

Figure 6.34 Photograph of the unphasematched visible output from PPLN OPO.The predominant red colour is due to frequency-doubling of the signal at ~1.2 μm.

However, the heating of the crystal to 100°C proved to have an additional benefit beyond that of removing photorefractive damage. The thermal expansion of the crystal was of the right magnitude to increase the periods of four of the gratings to those needed for phasematched frequency-doubling of the signal. Wavelengths from 1.075 to 1.09 μm were phasematchable in this way, producing green light between 537 and 545 nm. This is the cause of the dip in Fig. 6.26, where the signal power was depleted by generation of the green. Depletion was large, as can be seen in Fig. 6.35, which shows three signal spectra recorded as the OPO was tuned through the phasematching point.

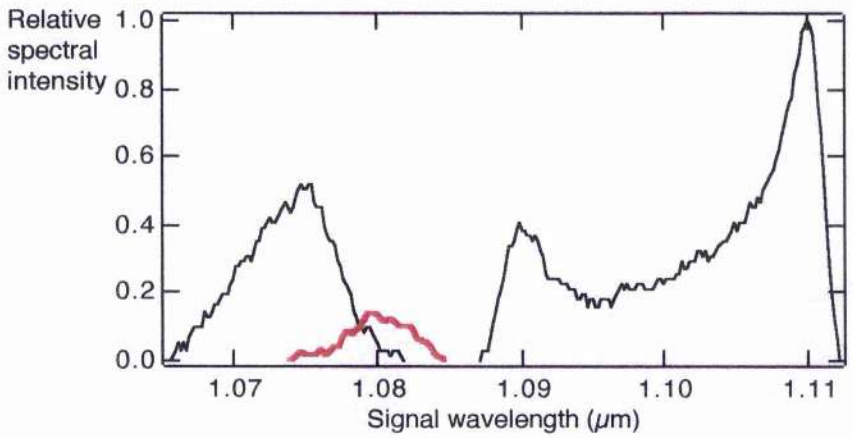

Figure 6.35 Signal spectra recorded while tuning the OPO through the point of phasematching for generation of green light via frequency-doubling of the signal. The red line indicates the depleted spectrum corresponding to maximum green generation.

As stated in section 2.2.4, the equations governing QPM are derived by inserting a grating vector, k_m, into the equations for birefringent phasematching. In this way, the equation describing QPM of second harmonic generation (SHG) becomes

$$\Lambda = \frac{m\lambda_\omega}{2(n_{2\omega} - n_\omega)} \tag{6.10}$$

where Λ is the grating period required for frequency doubling of the fundamental wave at frequency ω to generate the second harmonic at frequency 2ω. First order (m = 1) SHG of 1.08 μm in PPLN requires a grating period of ~7μm; therefore the third order process (m = 3) requires a period near 21 μm, as available in the OPO crystal. Fig. 6.36 shows the phasematching curve generated from Equation 6.10. The data points are the experimental results, where the signal wavelength observed to phasematch for a particular grating is plotted against the grating period, taking into account thermal expansion of the gratings. Best agreement between theory and experiment occurs at the longer wavelengths. The increased error at short wavelengths may be due to errors in the supposed grating periods, since any fabrication error in Λ will be more significant for shorter gratings.

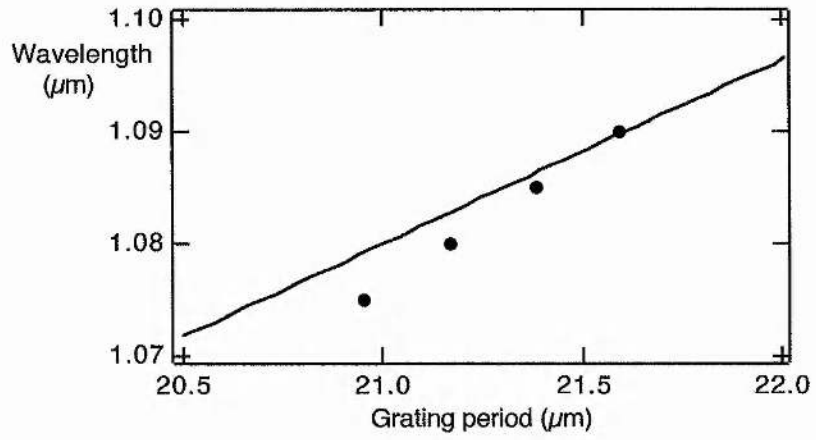

Figure 6.36 Phasematching of third-order frequency-doubling in PPLN. The line is theoretical, and the circles are represnt experimental values of the signal wavelengths observed to phasematch for each grating period. The crystal temperature was 100°C.

The amount of green light generated by this process was significant. A total of 70 mW was recorded in a single beam after the second curved mirror (Fig. 6.11); a

similar amount would be produced in the opposite direction and leave the cavity through the first curved mirror. The transmission of the mirrors in the visible is not known, so the total amount may have been much greater. A spectrum of the green output is presented as Fig. 6.37. This was recorded using a scanning monochromator and consequently the acquisition time was quite long, contributing noise to the measurement. The spectral width of 17 nm suggests that visible pulse durations of 18 fs should be attainable, as calculated from the time-bandwidth limit of a $\mathrm{sech}^2(t)$ pulse. To test that genuine SHG was occurring, measurements of green power versus cavity length were taken. This was done by mounting the end mirror on a piezo-controlled translation stage connected to a high voltage supply, which allowed very fine control over the cavity length. The results of this are shown in Fig. 6.38, and are compared with a curve showing the theoretical SHG efficiency, η, as given by the sinc^2 dependence

$$\eta \propto \frac{\sin^2(\Delta kl/2)}{(\Delta kl/2)^2} \tag{6.11}$$

While some of the experimental data are a poor fit to the curve, the general shape of a central peak and two smaller sidebands strongly suggests that the frequency doubling was genuinely phasematched. A photograph of the OPO optimised for generation of green light is given as Fig. 6.39.

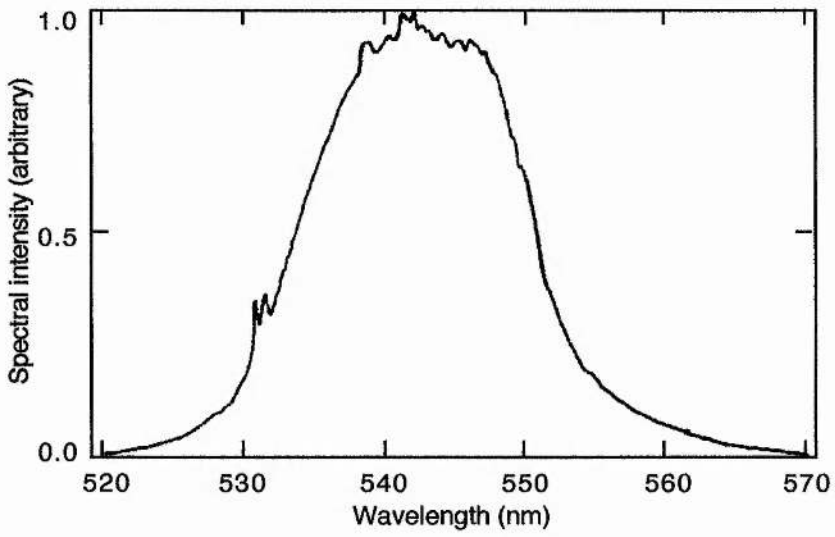

Figure 6.37 Spectrum of the green output generated by third-order phasematched frequency-doubling of the signal.

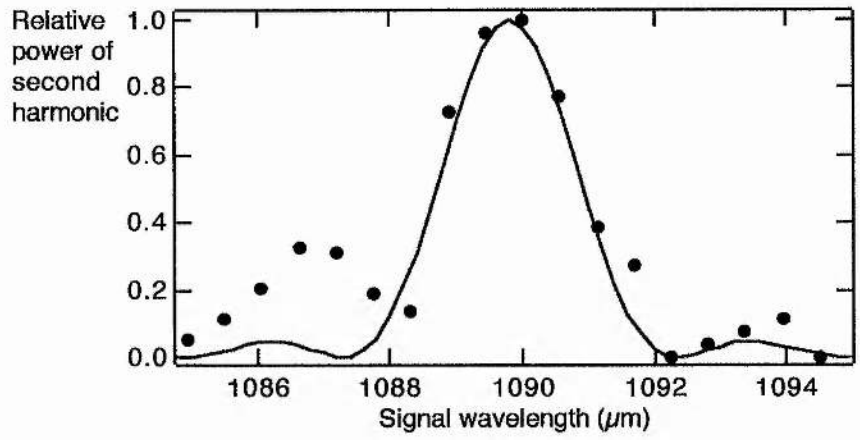

Figure 6.38 Sinc^2 dependence of the power of the generated, second harmonic, green light on the fundamental, signal wavelength. The experimental data (circles) are compared with a theoretical curve (line) calculated from Equation 6.11.

The first claimed demonstration of simultaneous phasematching of optical parametric oscillation and frequency doubling in a single crystal has recently been reported by Kartaloglu et al [54]. The system generated green light at 540 nm, and used birefringently phasematched KTP as the nonlinear medium, synchronously pumped by a femtosecond Ti:sapphire laser. The work has since been extended to produce blue light at 487 nm by simultaneous optical parametric oscillation and pump-signal sum- frequency-mixing, also in KTP [55]. This novel approach produced usable power levels of tens and hundreds of milliwatts of visible light, but the limited phasematching capabilities of a birefringent arrangement mean that these effects are unlikely to be achievable at many wavelength combinations. However, the versatility of QPM in periodically poled materials implies that many more combinations of interactions should be phasematchable. The possibilities of this were recognised by Hayata and Koshiba in 1991 [32], when practical QPM systems were still a rarity. They presented a detailed theoretical analysis of multiwave mixing in PPLN and concluded that three simultaneous visible outputs could be generated from two infrared pump sources. Devices such as this have not yet been properly realised experimentally, although a number of researchers have reported simultaneously phasematched interactions in PPLN which occurred incidentally to the main aim of their work, as is the case here. The picosecond Ti:sapphire-pumped OPO of Butterworth et al [25] generated 15 mW of light at 522 nm from sum-frequency mixing of the pump and signal. Vaidyanathan et al [27] reported a nanosecond

Nd:YAG-pumped OPO in which a secondary OPO was simultaneously phasematched and pumped by the signal of the primary OPO, with both OPOs being temperature tunable.

Thus we have the possibility of the tunable pulsed sources with synchronous outputs in the visible, near and mid-infrared, all at usable power levels. Given the pump, grating, temperature and cavity length tuning properties of PPLN demonstrated here, such a multiwavelength synchronous source could be readily tailored to the requirements of the user, and would no doubt find applications in spectroscopy.

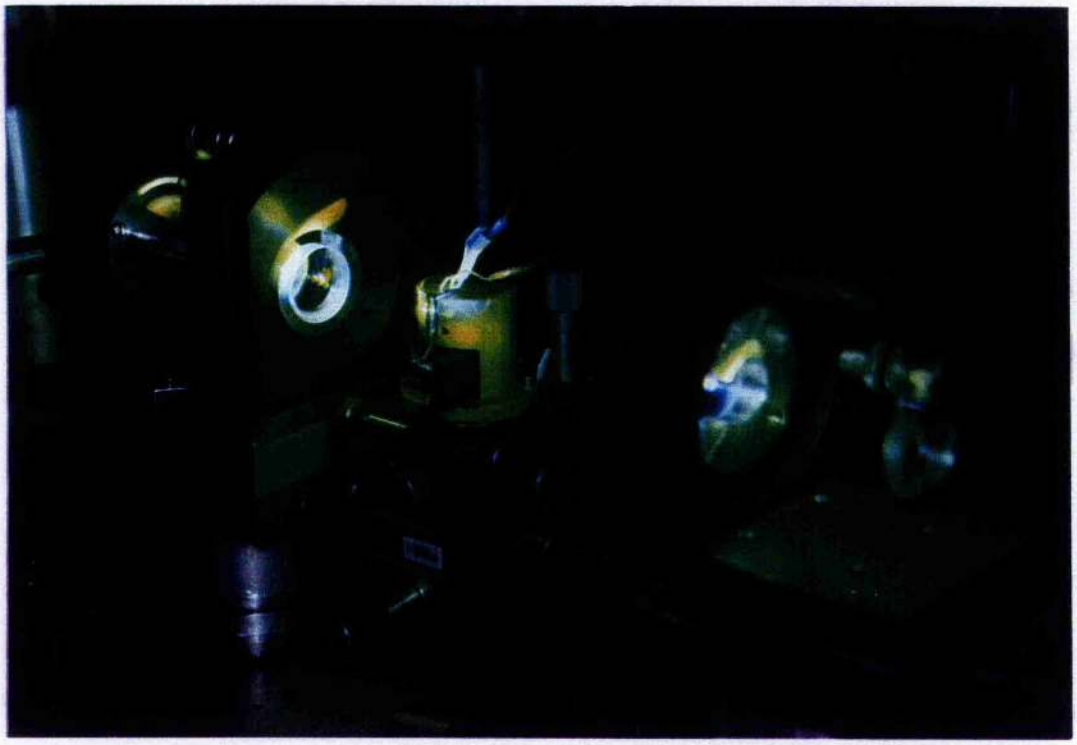

Figure 6.39 Photograph of the green output of the OPO, due to phasematching of third-order frequency-doubling of some signal wavelengths made possible by heating the PPLN crystal to 100°C.

6.7 Concluding remarks

The OPO described in this chapter is, to my knowledge, the first demonstration of a femtosecond synchronously-pumped optical parametric oscillator based on a periodically poled crystal, and more specifically, on PPLN. The device satisfied the mains aims stated at the start of Section 6.5, in that it proved to be a

widely-tunable, low-threshold, mid-infrared source. The system had a wide range of attributes which were studied in some detail, thus adding to the rapidly expanding pool of knowledge pertaining to PPLN. The principal properties are summarised below.

The main strength of the OPO was its extensive tunability, which was almost continuous over 0.975 to 1.54 μm in the signal branch and 1.67 to 4.55 μm in the idler. Thus a significant portion of the 3 to 5 μm range has been accessed, satisfying to a great extent the main aim of the work presented in this thesis – the construction of a tunable MIR femtosecond source. Cavity length tuning has been used to significantly supplement the more common methods of pump, grating and temperature tuning. Five mirror sets were used to generate the entire tuning range, in a rapid and straightforward manner. In addition to the infrared output derived from optical parametric oscillation, large quantities (>70 mW) of green light tunable about 540 nm were simultaneously generated by frequency doubling of some signal wavelengths. This approach would be applicable to the production of many combinations of infrared and visible wavelengths, given appropriate engineering of grating periods. Thus there is the possibility of PPLN being the basis of tunable, synchronous, pulsed multiwavelength sources.

Power levels of 90 mW of signal and 53 mW of idler were measured, implying an extraction efficiency of 10.6%. This is rather small, but was proved not to be due to low pump depletion, since depletion levels of up to 60% were observed. The powers generated are, however, sufficient for some applications. The oscillation threshold was only 45 mW, so such an OPO could be pumped by a diode-pumped all-solid-state laser.

Intracavity dispersion compensation was implemented to produce high quality near-bandwidth-limited signal pulses of 140 fs duration. The prism insertion loss was relatively low, just 11% at maximum power. The problems of photorefractive damage were readily overcome by heating the crystal to the relatively modest temperature of 100°C, which is significantly lower than the 170°C which has been suggested by previous work, and adopted by several researchers. The implementation of an oven to heat the crystal also introduced the option of temperature tuning.

The OPO is open to improvement and development in a variety of ways. Cavity mirrors with wider bandwidths would reduce the number of mirror sets

required to generate the entire available tuning range. Such bandwidths are available from dispersion-compensating chirped mirrors, which would also remove the need for prisms. Electronic stabilisation of the cavity length could be implemented to provide highly precise access to any required wavelength. A PPLN OPO could be constructed in the SMURRF configuration described in Chapter 5, to produce a high repetition rate ultrashort pulse MIR source, or a visible source by taking advantage of the simultaneous phasematching properties.

Most important, though, is extension of the tuning range beyond 4.55μm, possibly as far the edge of the lithium niobate transparency at 5.5 μm. One way to achieve this is to generate shorter signal wavelengths from the existing 800 nm Ti:sapphire pump source, which would require the use of cavity mirrors with reflectivities centred at shorter wavelengths than those used so far. The generation of a 5.5 μm idler from an 800 nm pump requires a signal at 936 nm. Calcium fluoride mirror substrates would be necessary to allow reasonable extraction at such long wavelengths. An alternative approach is to use longer pump wavelengths. Tuning the Ti:sapphire laser by just 20 nm to 820 nm will allow the generation of 5.5 μm from a signal of 1.03 μm, and is possible with the existing grating periods.

The overall conclusion from this work is that a femtosecond OPO based on PPLN is highly advantageous in terms of tunability. The huge spectral range easily accessible from a single system is made possible by quasi-phasematching, an exceedingly wide parametric gain bandwidth and a combination of different tuning methods. The readily available mid-infrared output implies that PPLN could become the material of choice for the generation of 3 to 5 μm. In addition, the extensive tuning capabilities at shorter wavelengths may lead to PPLN supplanting more established materials for the generation of visible and near-infrared wavelengths by frequency conversion.

References

1. G.A. Magel, M. M. Fejer and R. L. Byer, Appl. Phys. Lett. **56**, 108 (1990).
2. J. Webjörn, V. Pruneri, P. St. J. Russell, J. R. M. Barr and D. C. Hanna, Electron. Lett. **30**, 894 (1994).
3. V. Pruneri, R. Koch, P. G. Kazansky, W. A. Clarkson, P. St. J. Russell and D. C. Hanna, Opt. Lett. **20**, 2375 (1995).
4. V. Pruneri, J. Webjörn, P. St. J. Russell, J. R. M. Barr and D. C. Hanna, Opt. Commun. **116**, 159 (1995).
5. G. D. Miller, R. G. Batchko, W. M. Tulloch, D. R. Weise, M. M. Fejer and R. L. Byer, in *Conference on Lasers and Electro-Optics*,Vol. 11 of 1997 OSA Technical Digest Series (Optical Society of America, Washington, DC, 1997), p. 58, paper CTuB2.
6. V. Pruneri, S. D. Butterworth and D. C. Hanna, Opt. Lett **21**, 390 (1996).
7. M. A. Arbore, M. M. Fejer, M. E. Fermann, A. Hariharan, A. Galvanauskus and D. Harter, Opt. Lett. **22**, 13 (1997).
8. L. Goldberg, W. K. Burns and R. W. McElhanon, Opt. Lett. **20**, 1280 (1995).
9. S. Sanders, R. J. Lang, L. E. Myers, M. M. Fejer and R. L. Byer, Electron. Lett. **32**, 218 (1996).
10. G. Y. Wang, J. Zhao and M. Cronin-Golomb, in *Conference on Lasers and Electro-Optics*,Vol. 11 of 1997 OSA Technical Digest Series (Optical Society of America, Washington, DC, 1997), p. 16, paper CMD4.
11. A. Galvanauskus, M. A. Arbore, M. M. Fejer, M. E. Fermann and D. Harter, Opt. Lett. 22, 105 (1997).
12. D. J. Lovering, J. A. Levenson, P. Vidakovic, J. Webjörn and P. St. J. Russell, Opt. Lett. **21**, 1439 (1996).
13. J. J. Zayhowski, Opt. Lett. **22**, 169 (1997).
14. *Model 110*, Aculight Corporation, 11805 North Creek Parkway, S., Suite 113, Bothwell, WA 98011, USA.
15. L. E. Myers, G. D. Miller, R. C. Eckardt, M. M. Fejer, R. L. Byer and W. R. Bosenberg, Opt. Lett. **20**, 52 (1995).
16. L. E. Myers, R. C. Eckardt, M. M. Fejer, R. L. Byer and J. W. Pierce, Electron. Lett. **31**, 1869 (1995).
17. V. Pruneri, J. Webjörn, P. St. J. Russell and D. C. Hanna, Appl. Phys. Lett. **67**, 2126 (1995).
18. L. E. Myers, R. C. Eckardt, M. M. Fejer, R. L. Byer and W. R. Bosenberg, Opt. Lett. **21**, 591 (1996).
19. W. R. Bosenberg, A. Drobshoff, J. I. Alexander, L. E. Myers and R. L. Byer, Opt. Lett. **21**, 713 (1996).
20. T. P. Grayson, L. E. Myers, M. D. Nelson and V. Dominic, Electron. Lett. **32**, 1136 (1996).
21. W. R. Bosenberg, A. Drobshoff, J. I. Alexander, L. E. Myers and R. L. Byer, Opt. Lett. **21**, 1336 (1996).
22. S. D. Butterworth, V. Pruneri and D. C. Hanna, Opt. Lett. **21**, 1345 (1996).

23. L. P. Gonzalez,V. Dominic, L. E. Myers and R. C. Eckardt, in *Conference on Lasers and Electro-Optics*,Vol. 11 of 1997 OSA Technical Digest Series (Optical Society of America, Washington, DC, 1997), p. 18, paper CMD7.
24. D. Chen, D. Hinkley, J. Pyo, J. Swenson and R. Fields, in *Conference on Lasers and Electro-Optics*,Vol. 11 of 1997 OSA Technical Digest Series (Optical Society of America, Washington, DC, 1997), p. 17, paper CMD6.
25. S. D. Butterworth, P. G. R. Smith and D. C. Hanna, Opt. Lett. **22**, 618 (1997).
26. R. G. Batchko, D. Weise, T. Plettner, G. D.Miller, M. M. Fejer and R. L. Byer, in *Conference on Lasers and Electro-Optics*,Vol. 11 of 1997 OSA Technical Digest Series (Optical Society of America, Washington, DC, 1997), p. 340, paper CThG2.
27. M. Vaidyanathan, L. E. Myers and T. P. Grayson, in *Conference on Lasers and Electro-Optics*,Vol. 11 of 1997 OSA Technical Digest Series (Optical Society of America, Washington, DC, 1997), p. 456, paper CThY5.
28. F. Jona and G. Shirane, *Ferroelectric Crystals* (Pergamon Press, Oxford, 1962).
29. B. T. Matthias and J. P. Remeika, Phys. Rev. **79**, 1886 (1949).
30. R. W. Boyd, *Nonlinear Optics* (Academic Press, San Diego, 1992), p. 45.
31. Ibid., p. 52.
32. K. Hayata and M. Koshiba, Opt. Lett. **16**, 560 (1991).
33. V. G. Dmitriev, G.G. Gurzadyan and D. N. Nikogosyan, *Handbook of Nonlinear Optical Crystals* (Springer-Verlag, Berlin, 1991).
34. U. Schlarb and K. Betzler, J. Appl. Phys. **73**, 3472 (1993).
35. G. J. Edwards and M. Lawrence, Opt. Quantum Electron. **16**, 373 (1984).
36. M. V. Hobden and J. Warner, Phys. Lett. **22**, 243 (1966).
37. Y. S. Kim and R. T. Smith, J. Appl. Phys. **40**, 4637 (1969).
38. M. Houé and P. D. Townsend, J. Phys. D **28**, 1747 (1995).
39. Crystal Technology Inc., 1040 E. Meadow Cir., Palo Alto, CA 94303, USA.
40. Rees Instruments Ltd., Thornbrook, Weyside Park, Catteshall Lane, Godalming, Surrey, GU7 1XE.
41. J. D. Kafka, M. L. Watts and J. W. Pieterse, J. Opt. Soc. Am. B **12**, 2147 (1995).
42. D. A. Gilmore, p. Vujkovic Cvijin and G. H. Atkinson, Opt. Comm. **103**, 370 (1993).
43. L. E.Myers, R. C. Eckardt, M. M. Fejer, R. L. Byer, W. R. Bosenberg and J. W. Pierce, J. Opt. Soc. Am. B **12**, 2102 (1995).
44. M. Ebrahimzadeh, "Pulsed parametric oscillators", *Laser Sources and Applications: Proceedings of the Forty Seventh Scottish Universities Summer School in Physics*, A. Miller and D. M. Finlayson, ed. (SUSSP Publications and Institute of Physics Publishing, Bristol, 1996) p. 235.
45. E. Harris, Proc. IEEE **57**, 2096 (1969).
46. R. W. Boyd, *Nonlinear Optics* (Academic Press, San Diego, 1992), p. 409.
47. A. Ashkin, G. D. Boyd, J. M. Dziedzic, R. G. Smith, A. A. Ballman, J. J. Levinstein and K. Nassau, Appl. Phys. Lett. **9**, 72 (1966).
48. D. H. Jundt, G. A. Magel, M. M. Fejer and R. L. Byer, Appl. Phys. Lett. **59**, 2657 (1991).
49. R. W. Boyd, *Nonlinear Optics* (Academic Press, San Diego, 1992), p. 411.

50. *Model SE5020*, Marlow Industries, 7 Laura House, Jengers Mead, Billinghurst, West Sussex, RH14 9NZ.
51. D. T. Reid, C. McGowan, M. Ebrahimzadeh and W. Sibbett, IEEE J. Quantum Electron. **33**, 1 (1997).
52. J. M. Dudley, D. T. Reid, M. Ebrahimzadeh and W. Sibbett, Opt. Comm. **104**, 419 (1994).
53. W. S. Pelouch, P. E. Powers and C. L. Tang, Opt. Lett. **17**, 1070 (1992)
54. T. Kartaloglu, K. G. Köprülü and O. Aytür, Opt. Lett. **22**, 280 (1997).
55. K. G. Köprülü, T. Kartaloglu and O. Aytür, in *Conference on Lasers and Electro-Optics*,Vol. 11 of 1997 OSA Technical Digest Series (Optical Society of America, Washington, DC, 1997), p. 457, paper CThY6.

chapter seven

CONCLUSIONS

The aim of the research which has been presented in this thesis was to address the current demand for femtosecond pulses in the mid-infrared. The laser gain media best suited to the generation of ultrashort pulses via modelocking have spectral outputs limited to the near-infrared, so it is necessary to turn to nonlinear optical frequency mixing to produce longer wavelengths. In this case, the technique of optical parametric oscillation was successfully used to generate a range of widely-tunable femtosecond pulses in the near to mid-infrared spectral region. These pulses were characterised using novel arrangements of the two principal pulse diagnostic methods: autocorrelation and frequency-resolved optical gating.

The scene was set in Chapter 1, which included reviews of the applications of mid-infrared ultrashort pulses, and of recent research pertaining to pulsed sources in the near and mid-infrared, and a discussion of the state of the art of femtosecond mid-infrared pulse generation. This served to place into context the experimental work described later in the thesis.

A summary of some relevant linear and nonlinear optical concepts was given in Chapter 2, to explain many of the subjects referred to in subsequent chapters. The origin of optical nonlinearities was described, leading to a discussion on optical parametric oscillation, and the factors to be considered when designing an optical parametric oscillator (OPO) for a specific purpose. Some of the parameters which affect the propagation of ultrashort pulses, in both lasers and OPOs, were also described, because these can have an important bearing on OPO construction.

Each of the OPOs presented here was synchronously-pumped by a self-modelocked Ti:sapphire laser, which was described at the beginning of Chapter 3, along with a brief discussion of self-modelocking and the properties of Ti:sapphire.

Ultrashort pulse measurement techniques were dealt with in the remainder of the chapter. The subject of autocorrelation was addressed in some detail, because it was a measurement method used extensively to characterise the outputs of the femtosecond OPOs. In addition, a novel advance in autocorrelator design was presented, whereby the frequency-doubling crystal and photomultiplier tube of a conventional autocorrelator was replaced by either a photodiode or an ultrahigh brightness light-emitting diode (LED). The advantages of such an arrangement are manifold, and the devices were used successfully to record interferometric autocorrelation traces of laser and OPO pulses. The alternative and more detailed pulse measurement technique of frequency-resolved optical gating (FROG) was then discussed. FROG is a relatively new technique, but yields complete characterisation of pulses and so is an attractive complement to autocorrelation, and is consequently the subject of much research interest at the present time. A development in FROG design was then presented, which used a modified autocorrelator in conjunction with a spinning mirror and a CCD camera to provide a real-time second harmonic generation FROG system, which allowed continuous monitoring of a pulsed output. It was used to determine detailed phase and intensity information about OPO pulses.

A noncollinear critically phasematched OPO based on $KTiOAsO_4$ (KTA) was presented in Chapter 4. Tuning out to 4.1 μm was demonstrated, thus covering half of the desired 3 to 5 μm mid-infrared range. Suggestions for ways to extend the tuning were given. The mid-infrared idler pulses were measured by autocorrelation based on an InGaAs photodiode, and represented the longest wavelength pulses to be characterised by interferometric autocorrelation at that time, to the best of my knowledge. The OPO was operated with and without a pair of prisms to provide dispersion compensation, and the idler pulse measurements indicated that dispersion compensation was not required to obtain essentially chirp-free idler pulses. In addition, two theoretical models were presented which were used to predict the optimum noncollinear propagation angle, and produced values which agreed well with experiment. Alignment of noncollinearly phasematched OPOs is notoriously difficult, and these models represent a useful contribution to the pool of practical knowledge on the subject.

An OPO novel in its design rather than its output was presented in Chapter 5. A unique semi-monolithic cavity design was used to produce a highly compact device, based on noncritical birefringent phasematching in $RbTiOAsO_4$ (RTA), and

operating at harmonics of the pump laser repetition rate. Extraction efficiencies as high as 55%, and a pulse repetition rate of 344 MHz at the signal wavelength (the fourth harmonic of the pump laser repetition frequency) were demonstrated. The design is open to ready modification for higher repetition rates, at the signal or idler wavelengths, and alternative nonlinear crystals could increase the tuning range beyond the 1.2 to 1.3 μm and 2.1 to 2.5 μm available from Ti:sapphire pump tuning of RTA.

The objective of a 3 to 5 μm femtosecond source was best met by the OPO described in Chapter 6, which was a quasi-phasematched device based on periodically poled lithium niobate (PPLN). This had remarkably wide tunability, covering 0.975 to 1.54 μm in the signal branch, and 1.67 to 4.55 μm in the idler branch, from a combination of cavity length tuning, grating tuning, pump tuning and temperature tuning. A theoretical model indicated that a very wide gain bandwidth was responsible for the tuning properties. Simultaneous phasematching of frequency doubling of the signal was observed, producing a green output at ~540 nm. An oscillation threshold of 45 mW was recorded, which was sufficiently low to suggest that PPLN could be a good candidate for an all-solid-state device pumped by a diode-pumped Cr:LiSAF laser, for example. Techniques for extending the idler tuning out to the transparency edge of lithium niobate, at 5.5 μm, were discussed.

The three femtosecond OPOs provided examples of the main types of phasematching – critical and noncritical birefringent phasematching, and quasi-phasematching, and thus highlighted the advantages and disadvantages of each technique. Birefringent phasematching, upon which OPO researchers have relied for so long, has a limited tuning range when used in a noncritical configuration, and extending the tuning via critical phasematching leads to the problems of Poynting vector walk-off and noncollinear geometries. Quasi-phasematching, on the other hand, is always noncritical, but allows tuning over the entire transparency range of a nonlinear crystal, as well as allowing access to higher nonlinearities. After being disregarded for so many decades, quasi-phasematching is now coming into its own, thanks to a tremendous investment and effort currently being put into the development of periodically poled materials. As poling techniques become increasingly advanced and are applied to a wider range of materials, it is now possible to tailor a periodically poled crystal to the precise needs of the user. This was not possible with birefringent crystals, so that, to a great extent, researchers had to

"make do" with the properties of the crystals available, and resort to ingenious pump laser and OPO material combinations to produce the required output.

Thus, quasi-phasematching in periodically poled crystals looks set to change the face of OPO research for ever. Consequently, the PPLN OPO presented here, being the first demonstration of femtosecond optical parametric oscillation in a periodically poled material, is an important contribution to the field, as a device in its own right and not only as a tunable ultrashort pulse mid-infrared source.

It seems likely that quasi-phasematching will lead to a shift in the emphasis of OPO research. Previously, the constraints of birefringent phasematching have meant that much effort has been expended on finding nonlinear materials which would generate desired wavelengths from convenient pump sources, at various pulse durations. In other words, the primary focus was on the output of OPOs, and on demonstrations of new materials. Now, however, quasi-phasematching has made it possible to generate a much broader range of wavelengths from a single material, with a limit set only by the transparency, which can cover the visible, near and mid-infrared, so does not represent too much of a limit. With wavelengths therefore more readily attainable, researchers should become more able to devote time to the development of OPO cavities, with objectives such as reducing oscillation thresholds or increasing tuning bandwidth. This is a subject which has perhaps been somewhat neglected in the past, so an increased interest in it would surely be beneficial.

The semi-monolithic ultrahigh repetition rate femtosecond (SMURRF) RTA-based OPO of Chapter 5 is an example of such a development, although it was not motivated by the advent of periodically poled crystals. The cavity design is unique, allowing as it does the flexible focussing arrangement needed for shortening the cavity length of a synchronously-pumped OPO. This decrease in cavity size is very much in the spirit of a great deal of current laser research, since there is such an emphasis on the use of diode-pumping to reduce the size and cost of laser systems. The combination of an all-solid-state diode-pumped laser pump source and a SMURRF OPO could result in a highly compact and robust tunable source, especially if a periodically poled crystal, such as lithium niobate, KTP or RTA, were incorporated in the OPO to maximise the tuning capabilities. The simultaneous phasematching properties of PPLN, as demonstrated in Chapter 6, could produce a multi-wavelength source, with outputs in the visible, near and mid-infrared, one or more of which could have an ultrahigh repetition rate. The increasing prevalence of chirped

mirrors, originally introduced to facilitate pulse compression but which also remove the need for bulky prisms, and have a wider bandwidth than conventional mirrors, should be an important factor in compact tunable source development. They have recently been applied to OPOs, and would be of particular relevance to a SMURRF design, where the compactness and simplicity is compromised by a prism pair to provide dispersion compensation.

Continuing the theme of miniaturisation, I feel that the importance of the LED autocorrelator of Chapter 3 should not be underestimated. Compact laser sources should ideally be accompanied by compact measurement devices, and utilising an LED is an excellent way to achieve this aim. The combination of small size and extremely low cost suggests the possibility of commercial modelocked laser systems of the future being supplied with integral autocorrelators. The robustness of an LED-based device would also lend itself to use in a battery-operated, fully portable autocorrelator, useful for laser service engineers and at trade-show demonstrations.

Thus, in my opinion, the most relevant and useful developments to emerge from the research presented in this thesis are the photodiode/LED-based autocorrelator, the SMURRF OPO cavity design and the demonstration of femtosecond quasi-phasematched optical parametric oscillation. A combination of these last two would prove very interesting and useful, especially as new and better periodically poled crystals become available, and if chirped mirrors were incorporated. The high power, highly compact, high repetition rate, widely-tunable source which could result would be fascinating, and I hope that such a device is realised in the near future.

Of course, it is not at all a certainty that the application of LEDs and photodiodes to autocorrelation measurements will have the impact that I think it should, and the SMURRF cavity design may be usurped by something completely different, but periodically poled crystals and quasi-phasematching are surely here to stay. They have attracted so much recent interest, and have proved to be so successful and widely applicable that I feel it is a safe bet to say that they represent the future of nonlinear optics.

appendix a

Calculation of the walk-off angle of an extraordinarily-polarised signal beam in KTA

Propagation in *xz*-plane, at angle $\theta = 39° \equiv 0.681$ rads and $\phi = 0$ rads

Define signal wavelength: $\lambda = 1.2\ \mu m$

Define Sellmeier coefficients* for refractive index:

$A_x = 1.90713$	$A_y = 2.15912$	$A_z = 2.14912$
$B_x = 1.23522$	$B_y = 1.00099$	$B_z = 1.29559$
$C_x = 0.19692$	$C_y = 0.21844$	$C_z = 0.22719$
$D_x = 0.01025$	$D_y = 0.01096$	$D_z = 0.01436$

Calculate refractive indices:

$$n_x = \sqrt{A_x + \frac{B_x}{[1-(C_x/\lambda)^2]} - D_x\lambda^2} \qquad n_x = 1.778$$

$$n_y = \sqrt{A_y + \frac{B_y}{[1-(C_y/\lambda)^2]} - D_y\lambda^2} \qquad n_y = 1.783$$

$$n_z = \sqrt{A_z + \frac{B_z}{[1-(C_z/\lambda)^2]} - D_z\lambda^2} \qquad n_z = 1.863$$

Ω = angle between optic axis and z-axis, defined for positive biaxial crystal as

$$\Omega = \arcsin\left(\frac{n_z}{n_y}\sqrt{\frac{n_y^2 - n_x^2}{n_z^2 - n_x^2}}\right)$$

---

* D. L. Fenimore, K. L. Schepler, U. B. Ramabadran and S. R. McPherson, J. Opt. Soc. Am. B **12**, 794 (1992).

δ = polarisation angle, defined as

$$\delta = \frac{\arctan\left(\dfrac{\sin 2\phi \cos\theta}{\sin^2\phi - \cos^2\theta\cos^2\phi + \cot^2\Omega\sin^2\theta}\right)}{2}$$

Walk-off angle :

$$\rho = \arccos(\hat{E}.\hat{D})$$

so calculate unit vectors:

$$\hat{D} = \begin{bmatrix} -\cos\theta\cos\phi\cos\delta + \sin\phi\sin\delta \\ -\cos\theta\sin\phi\cos\delta - \cos\phi\sin\delta \\ \sin\theta\cos\delta \end{bmatrix} = \begin{bmatrix} \hat{D}_1 \\ \hat{D}_2 \\ \hat{D}_3 \end{bmatrix}$$

E and D unit vectors related by:

$$\hat{E}_s = \begin{bmatrix} \frac{1}{n_x^2} & 0 & 0 \\ 0 & \frac{1}{n_y^2} & 0 \\ 0 & 0 & \frac{1}{n_z^2} \end{bmatrix} . \hat{D} = \begin{bmatrix} \hat{E}_1 \\ \hat{E}_2 \\ \hat{E}_3 \end{bmatrix}$$

Therefore, walk-off angle, in radians, is

$$\rho = \arccos\left(\frac{\hat{D}_1\hat{E}_1 + \hat{D}_2\hat{E}_2 + \hat{D}_3\hat{E}_3}{\sqrt{\hat{D}_1^2 + \hat{D}_2^2 + \hat{D}_3^2}\sqrt{\hat{E}_1^2 + \hat{E}_2^2 + \hat{E}_3^2}}\right)$$

Convert to degrees: $\rho = \rho(180/\pi)$ therefore $\rho = 2.595°$

appendix b

Parameters used in the modelling of gain in noncollinearly pumped optical parametric oscillators, as shown in Fig. 4.11[1]

Pulse duration

pump	100 fs
signal	800 fs
idler	100 fs

Focussed spot size

pump	15 μm
signal	20 μm
idler	20 μm

λ_p (nm)	θ_p (°)	λ_s (μm)	λ_i (μm)	d_{eff} (pm/V)	walk-off (°)	walkaway[2] (fs/mm)		
						p - s	p - i	i - s
816	38.8	1.064	3.5	2.25	2.6	-10.9	+92.1	-103
800	47	1.374	1.92	2.63	2.6	+0.4	+167	-167
800[3]	90	1.145	2.66	3.6	0	+121	-137	+258

[1] Calculated from the Sellmeier data given in D. L. Fenimore, K. L. Schepler, U. B. Ramabadran and S. R. McPherson, J. Opt. Soc. Am. B **12**, 794, (1995).

[2] Positive value implies that first wave lags, negative value implies that first wave leads.

[3] Noncritical, collinear phasematching situation used to calculate relative gain for the noncollinear geometries.

appendix c

PUBLICATIONS

Journal publications

'Continuously tunable femtosecond pulses covering 2.1 to 2.5 μm from an optical parametric oscillator based on $RbTiOAsO_4$'

C. McGowan, D. T. Reid, M. Ebrahimzadeh and W. Sibbett

Journal of Modern Optics **43**, 913 - 918 (1996)

'Femtosecond pulses tunable beyond 4 microns from a KTA-based optical parametric oscillator'

C. McGowan, D. T. Reid, M. Ebrahimzadeh and W. Sibbett

Optics Communications **134**, 186 - 190 (1997)

'Characterisation and modelling of a noncollinearly phasematched femtosecond optical parametric oscillator based on KTA and operating to beyond 4 μm'

D. T. Reid, C. McGowan, M. Ebrahimzadeh and W. Sibbett

IEEE Journal of Quantum Electronics **33**, 1 - 9 (1997)

'Light-emitting diodes as measurement devices for femtosecond pulses'

D. T. Reid, M. Padgett, C. McGowan, W. E. Sleat and W. Sibbett

Optics Letters **22**, 233 - 235 (1997)

'Compact, efficient 344 MHz repetition-rate femtosecond optical parametric oscillator'

D. T. Reid, C. McGowan, W. Sleat, M. Ebrahimzadeh and W. Sibbett

Optics Letters **22**, 525 - 527 (1997)

'A real-time FROG-trace acquisition system for non-amplified femtosecond oscillators'

D. T. Reid, C. McGowan, W. E. Sleat and W. Sibbett

'Engineering and Laboratory Notes', *Optics and Photonics News* **8** (5) (1997)

'Femtosecond optical parametric oscillator based on periodically poled lithium niobate'

C. McGowan, D. T. Reid, Z. E. Penman, M. Ebrahimzadeh and W. Sibbett

Journal of the Optical Society of America B (accepted for publication) (1997)

'Broadly-tunable infrared femtosecond optical parametric oscillators based on periodically poled lithium niobate'

Z. E. Penman, C. McGowan, D. T. Reid, P. Loza-Alvarez, M. Ebrahimzadeh and W. Sibbett

Journal of Modern Optics (accepted for publication) (1997)

Conference presentations

'Powerful femtosecond pulses covering 2.1 - 2.6 μm from an optical parametric oscillator based on $RbTiOAsO_4$'

D. T. Reid, C. McGowan, M. Ebrahimzadeh and W. Sibbett

in *Technical Digest of the Twelfth UK National Quantum Electronics Conference*, Southampton, 1995, poster P1-3

'Mid-infrared femtosecond pulses from a critically phase-matched optical parametric oscillator based on $KTiOAsO_4$'

C. McGowan, D. T. Reid, M. Ebrahimzadeh and W. Sibbett

in *Conference on Lasers and Electro-Optics*, vol. 9, 1996 OSA Technical Digest Series (Optical Society of America, Washington, D. C., 1996) p 342, paper CThA5

'Semi-monolithic compact resonator geometry high-repetition-rate femtosecond optical parametric oscillator'

D. T. Reid, C. McGowan, M. Ebrahimzadeh and W. Sibbett

in *Technical Digest of the 1996 Conference on Lasers and Electro-Optics Europe*, IEEE Catalog Number 96TH8161, Postdeadline Papers, paper CPD1.4

'Light-emitting diodes as measurement devices for femtosecond pulses'

D. T. Reid, C. McGowan, M. J. Padgett, W. E. Sleat, J. W. Allen and W. Sibbett

in *Technical Digest of the 1996 Conference on Lasers and Electro-Optics Europe*, IEEE Catalog Number 96TH8161, Postdeadline Papers, paper CPD2.8

'Light-emitting diodes as measurement devices for femtosecond pulses'

D. T. Reid, C. McGowan, M. Padgett, W. E. Sleat and W. Sibbett

in *Conference on Lasers and Electro-Optics*, vol. 11, 1997 OSA Technical Digest Series (Optical Society of America, Washington, D. C., 1997) p 164, paper CTuS3

'Compact semi-monolithic ultrahigh repetition rate femtosecond optical parametric oscillator'

C. McGowan, D. T. Reid, M. Ebrahimzadeh and W. Sibbett

in *Conference on Lasers and Electro-Optics*, vol. 11, 1997 OSA Technical Digest Series (Optical Society of America, Washington, D. C., 1997) p 376, poster CThL32

'Femtosecond opticalparametric oscillator based on periodically poled lithium niobate'

C. McGowan, D. T. Reid, Z. E. Penman, M. Ebrahimzadeh and W. Sibbett

in *Technical Digest of the Thirteenth UK National Quantum Electronics Conference*, Cardiff, 1997

acknowledgements

A big thank you to:

my supervisor, Professor Wilson Sibbett, for his endless support and advice;

Majid Ebrahimzadeh, who contributed a great deal to this work;

Miles Padgett, for his collaboration on the Wollaston autocorrelator;

Derryck, who taught me so much;

Zoe, for all her help with the PPLN OPO;

Matthew, for being my careers advisor, and for being so gloriously disorganised;

Gordon, for helpful discussions on a myriad of subjects;

Bill, for his electronic know-how;

David Birkin, who took the photos of the PPLN OPO;

the rest of the ever-changing W-Squad, for assorted help, hindrance and hilarity: Gareth (sorry for shouting at you), David, Karen, Peter, Carl, David, John-Mark, Pablo, Paul and Edik;

Mark and Neil – my thesis writers' support group;

the guys in the workshop, for making so many bits and pieces;

and of course Doms, who didn't want an acknowledgement.
Thanks for the Hebrew.

I am indebted to the Engineering and Physical Sciences Research Council for financial support, and to Dieter Jundt of Crystal Technology, Inc. for supply of the PPLN crystal.